Alma Mater Studiorum - Università di Bologna

DOTTORATO DI RICERCA IN

IL FUTURO DELLA TERRA, CAMBIAMENTI CLIMATICI E SFIDE SOCIALI

Ciclo 35

Settore Concorsuale: 04/A4 - GEOFISICA

Settore Scientifico Disciplinare: GEO/10 - GEOFISICA DELLA TERRA SOLIDA

MONITORING TIME-DEPENDENT DEFORMATION PATTERNS THROUGH GEODETIC TECHNIQUES

Presentata da: Eugenio Mandler

Coordinatore Dottorato

Silvana Di Sabatino

Supervisore

Maria Elina Belardinelli

Co-supervisore

Enrico Serpelloni

Esame finale anno 2023

Alma Mater Studiorum · Università di Bologna

PhD Program
Future Earth, Climate Change and Societal Challenges

MONITORING TIME-DEPENDENT DEFORMATION PATTERNS THROUGH GEODETIC TECHNIQUES

Settore Concorsuale: 04/A4 - GEOFISICA
Settore Scientifico Disciplinare: GEO/10 - GEOFISICA DELLA TERRA SOLIDA

Supervisor:
Prof. Maria Elina Belardinelli

Co-supervisor:
Dott. Enrico Serpelloni

PhD director:
Prof. Silvana Di Sabatino

Presented by:
Eugenio Mandler

Cycle XXXV
Final exam year 2023

Abstract

In this thesis we focus on the analysis and interpretation of time dependent deformations recorded through different geodetic methods. Firstly, we apply a variational Bayesian Independent Component Analysis (vbICA) technique to GPS daily displacement solutions, to separate the postseismic deformation that followed the mainshocks of the 2016-2017 Central Italy seismic sequence from the other, hydrological, deformation sources. By interpreting the signal associated with the postseismic relaxation, we model an afterslip distribution on the faults involved by the mainshocks consistent with the co-seismic models available in literature. We find evidences of aseismic slip on the Paganica fault, responsible for the Mw 6.1 2009 L'Aquila earthquake, highlighting the importance of aseismic slip and static stress transfer to properly model the recurrence of earthquakes on nearby fault segments. We infer a possible viscoelastic relaxation of the lower crust as a contributing mechanism to the postseismic displacements. We highlight the importance of a proper separation of the hydrological signals for an accurate assessment of the tectonic processes, especially in cases of mm-scale deformations. Contextually, we provide a physical explanation to the ICs associated with the observed hydrological processes.

In the second part of the thesis, we focus on strain data from Gladwin Tensor Strainmeters, working on the instruments deployed in Taiwan. We develop a novel approach, completely data driven, to calibrate these strainmeters. We carry out a joint analysis of geodetic (strainmeters, GPS and GRACE products) and hydrological (rain gauges and piezometers) data sets, to characterize the hydrological signals in Southern Taiwan.

Lastly, we apply the calibration approach here proposed to the strainmeters recently installed in Central Italy. We provide, as an example, the detection of a storm that hit the Umbria-Marche regions (Italy), demonstrating the potential of strainmeters in following the dynamics of deformation processes with limited spatio-temporal signature.

Contents

Chapter 1

Introduction

The two end-member modes through which faults can release accumulated tectonic stress are *seismic slip* and *aseismic slip*. Seismic slip refer to that specific class of events that occur when the velocity of slip is sufficiently high for dynamic forces to radiate energy in the form of seismic waves. On the other hand, we talk about aseismic slip when fault slip is so slow that inertial forces and the radiation of seismic waves is negligible. The classical theory through which we represent the seismic cycle of a given fault predicts that stress is accumulated, along plate boundaries, on long time periods, which are referred to as the *interseismic deformation phases*. When an earthquake occurs, faults release suddenly the accumulated stress during the *coseismic phase*, which is afterwards followed by a *postseismic relaxation* of stress. Several mechanisms are generally responsible for the stress relaxation in the postseismic phase of the seismic cycle. In particular an aseismic creep of the areas surrounding the main coseismic ruptures (e.g., Perfettini and Avouac, 2007), a viscoelastic deformation associated with the bulk flow of the deepest portion of the crust and/or the shallower portion of the mantle (e.g., Pollitz et al., 2000), and a poroelastic rebound associated with fluid redistribution after the stress perturbation induced by the mainshocks (e.g., Fialko, 2004). When the stress induced by the earthquake has been fully relaxed, the situation goes back to the interseismic situation and the cycle starts again. Interseismic and postseismic phases occur over long time scales and are typically aseismic, coseismic phases occur over time scales of $\sim$ seconds/minutes during which seismic waves are radiated. A schematic representation of the seismic cycle described above is given in Figure 1.1. It is important to stress that this behaviour has to be intended as representative of reality only on average over long time scales, and that the occurrence of earthquakes does not show any periodical signature.

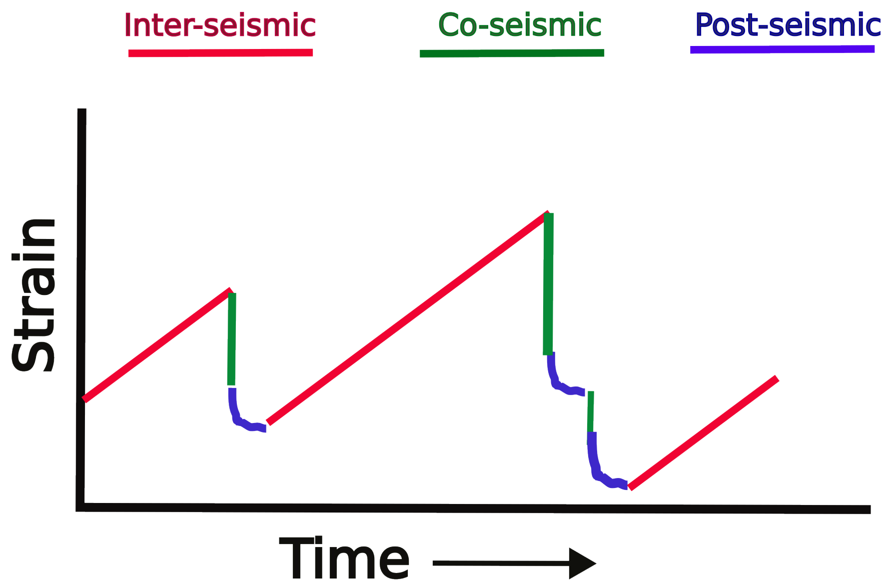

Figure 1.1. Figure shows strain evolution during a seismic cycle in the inter-seismic phase (red lines), co-seismic phase (green lines) and post-seismic phase (blue lines)

However, over the past decades, the number of different slip's manifestation increased together with the accuracy and the amount of the observational methods. It is now clear that creep of faults during interseismic phases and slow postseismic relaxations represent only roughly the possible slip manifestations. The augmented capability of our observational methods populated the slip spectrum of several phenomena, and such a variability reflects a suit of unique fault characteristics. A summary of slip events is given by figure 1 of Peng and Gomberg (2010) and here reported (Figure 1.2). We can imagine that regular ("fast") earthquakes occur when the slip velocity is high enough for shear stresses carried by the wavefronts to overcome friction on faults and cause large displacements. However, in other cases, dynamic velocity is not reached and seismic waves are radiated with low frequency and small amplitudes. We refer to such a phenomenon as to "non volcanic tremor", or just tremor. Seismic signals with limited rupture speed and source duration are referred to as Low Frequency Earthquakes (LFEs) or Very Low Frequency earthquakes (VLFS). When slip on faults is so slow that seismic radiation is negligible we talk about aseismic signals. Many slip manifestations fall under the umbrella of these slow slip phenomena: examples are afterslip on faults, repeating earthquakes (i.e., seismic ruptures embedded in a predominantly aseismic fault segment), swarms, creep and aseismic slip in general. The importance of aseismic slip has been recognized relatively late, thanks to the GPS continuous recordings of the last three decades, and in more recent times with the increasing contribution of strainmeters and tiltmeters.

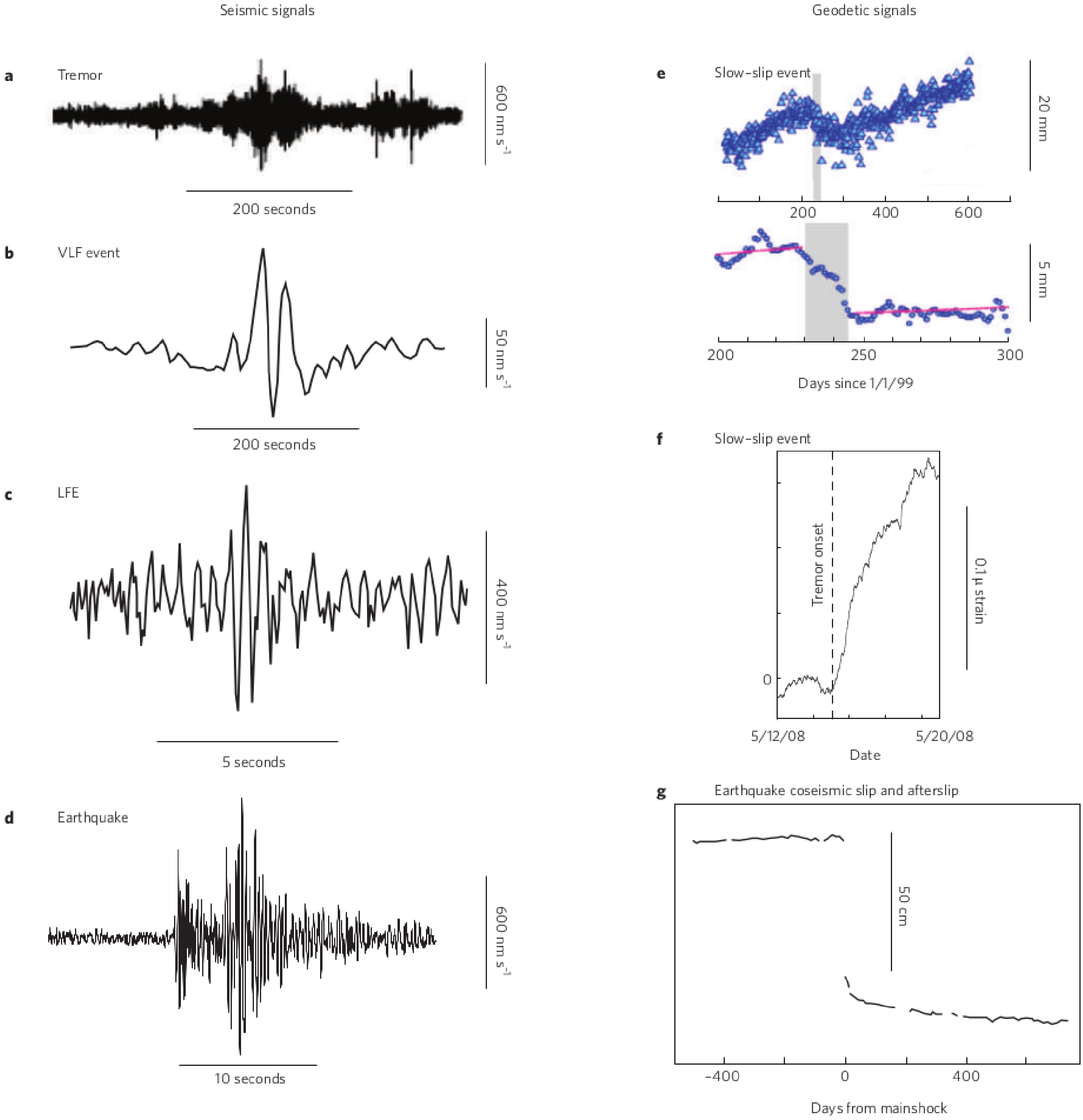

Figure 1.2. In Figure a representation of the slip phenomena, recorded either through seismological (left column) or geodetical (right column) methods/observations. In particular: (a) example of a tremor; (b) Very Low Frequency (VLF) earthquake recording; (c) Low Frequency Earthquake (LFE) recording; (d) recording of a regular earthquake; (e) Slow Slip Event (SSE) as recorded by the GPS; (f) SSE as recorded by a strainmeter; (g) coseismic offset rercorded by the GPS. Figure is taken from Peng and Gomberg (2010) and references are therein.

Nowadays, a key question is whether slow-slip events (SSEs) can be framed as a component of the slip's spectrum or they are a distinct mode of fault slip (Scuderi et al., 2020). Since the slip mode of faults is representative of the mechanical features of the fault itself, an affirmative answer to such a question would imply that even SSEs are governed by the same frictional laws as regular slip events (Scuderi et al., 2020). In other words: do slip modes span a continuum of the spectrum or are they rather separated in different classes (Peng and Gomberg, 2010)? In the former case SSEs could be governed by the same constitutive laws as regular earthquakes, implying that they can be interpreted through frictional instability described by a given class of physical mechanisms. The question whether the slip spectrum can be considered as continuous is still largely debated, with many studies in favor of this hypothesis (e.g., Frank and Brodsky, 2019; Gomberg et al., 2016; Hawthorne and Bartlow, 2018; Wech et al., 2010), although two distinct failure modes (i.e., fast and slow) are observed (Ide et al., 2007) and the mechanics underlying SSEs is still unclear. As a matter of fact, many authors (e.g., Peng and Gomberg, 2010; Gomberg et al., 2016; Frank and Brodsky, 2019) suggest that the different failure mode of slipping events has to be associated with limitations to our instruments' observational capability and accuracy.

We may ask ourselves: is the spectrum of slip events actually not continuous or gaps may rather be imputed to a limitation of the instrumentation? Geophysical observational means may be distinguished in two main classes, seismological and geodetic, which are sharply separated in terms of the duration of the observable phenomena. As acknowledge by Frank and Brodsky (2019), if on the one hand slow slip can be efficaciously constrained through continuous GPS measurements, on the other hand, episodic slip occurring on time scales of minutes to hours, which for instance is known to accompany LFEs and tremors, is invisible to standard geodetic techniques. Hence what is missing is a measure of motion which can link the seismically and geodetically recorded slip events. As a matter of fact, no single geophysical instrument can measure with the needed accuracy the whole slip spectrum, leaving blind spots on a general comprehension of the mechanics ruling faults' behaviour. Highly sensible surface and borehole strainmeters prove to be a valuable help to tackle this problem, allowing somehow to fill the instrumental gap existing between traditional seismological and geodetic methods (Figure 1.3) as they record, in continuous and with high accuracy, on time scales of seconds to months. Strainmeters, which made possible the first observations of time dependent deformations (e.g., Bilham, 1989; King et al., 1975; Lienkaemper et al., 2012), helped, for example, to clearly constrain rupture propagation features of slow slip events in Cascadia (McCausland et al., 2008) and to relate them with seismic activity in Japan (Fukuda et al., 2008), thanks to their high sensitivity (in the order of 10^{-11} strains on time scales of hours to months) which outperforms that of traditional geodetic observations (the GPS, for instance, reaches accuracies of 10^{-7} strains on sub-diurnal time scales, Reuveni et al., 2012). Therefore, if on the one hand GPS is critical to resolve slip events with long characteristic times (in the order of months to years), on the other hand, on shorter time scales borehole strainmeters are essential. As a matter of fact, by downscaling our observational capability we are able to detect the strain signature of creep events with periods of minutes to months, which encompasses the time scale of repeating earthquakes. Moreover, the improved geodetic observational capability of strainmeters allows us to detect low-intensity swarms and microseismicity which is usually invisible to GPS, or not easy to detect. This is fundamental in order to give an answer to questions about the relationship between creep, slow slip, dynamic earthquake rupture, and tectonic faulting, especially with the goal of detecting and resolving the faint aseismic deformation that can anticipate the nucleation of large earthquakes (e.g., Dresen et al., 2020).

However, if on the one hand the downscaling of observations is essential for a thorough understanding of faults' behaviour, on the other it brings along an increased level of "noise" in our data. Strainmeters time series are highly affected by the presence of numerous signals of environmental (e.g., barometric effects and human activities) and hydrological origins. The recognition of such processes is important from many points of view. Alongside with the already mentioned issue of lowering the level of noise when we are interested in detecting small tectonic deformation signals, evidences of how hydrological and tidal deformation can modulate seismicity are getting more and more abundant (e.g., Hainzl et al., 2006; Devoti et al., 2015,; D'Agostino et al., 2018; Serpelloni et al.,2018; Pintori et al., 2021). An hydromechanical coupling, namely a relationship among slip events (Kodaira et al., 2004), aftershocks (Nur and Booker, 1972; Miller et al., 2004), the triggering of earthquakes (Prejean et al., 2004) and hydrological processes, is now largely recognized by the scientific community. It has been shown that seasonal groundwater variations can trigger and modulate seismicity in the Southern Apennines (D'Agostino et al., 2018) and on the Southern Alps (Pintori et al., 2021), thanks to the non-negligible stress perturbation that they induce in the Earth's crust at seismogenic depth. In other cases, pore fluid pressure perturbations induced by rainfall at depths as far as ~ 4 km have been demonstrated to trigger earthquake activity through the mechanism of fluid diffusion (Hainzl et al., 2006). Therefore, our increased capability of detecting faint signals opens the perspective of further investigating the occurrence of seismic activity related to non-tectonic sources, which is crucial in the light of a deep understanding of the earthquake cycle and assessment of seismic hazard (Johnson et al., 2017).

Lastly, the investigation of hydrological processes has a certain importance itself. Water resources management and hydrological hazard assessment is a societal key problem, especially now that it has become clear that climate change is a primary issue to tackle (Taylor et al., 2012). GPS (Bawden et al., 2001; Ji and Herring, 2012; King et al., 2007) and Interferometric Synthetic-Aperture Radar (InSAR) (Chaussard et al., 2017; Galloway and Hoffmann, 2007; King et al., 2007) applied to the observation of groundwater level changes have already proven to be valuable means of monitoring groundwater levels. In this sense strainmeters, with their high temporal resolution, can significantly help to integrate the observations, providing local communities with more detailed information about the dynamics of underground water reservoirs.

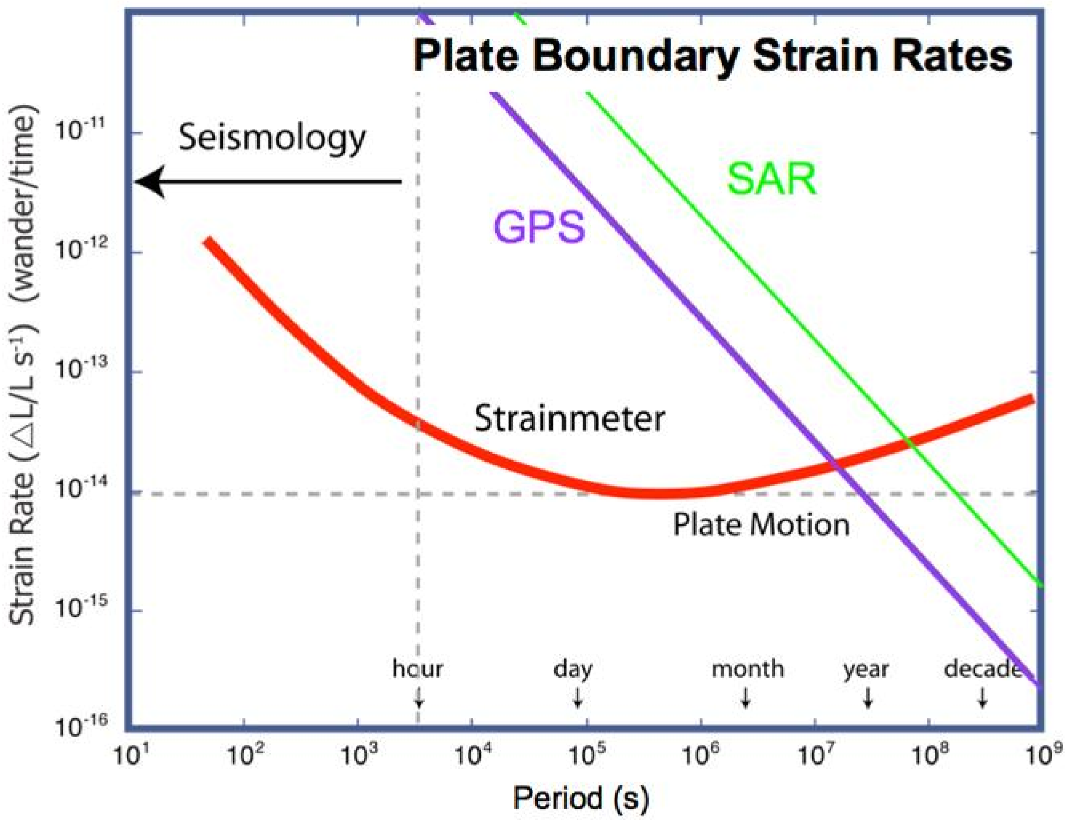

Figure 1.3. In figure the frequencies encompassed by seismometers, strainmeters, GPS and InSAR.

To sum up, with the progression of the geophysical measurement techniques, it has become clear that faults release accrued stress in a wide range of slip manifestations (Figure 1.2), which occur both seismically and aseismically. Recent studies (Frank and Brodsky, 2019; Gomberg et al., 2016; Hawthorne and Bartlow, 2018; Wech et al., 2010) point towards a continuum of the slip's spectrum, therefore implying that there is not a substantial difference between the mechanics describing regular earthquakes and the more recently discovered family of slow slip events (Jolivet and Frank, 2020). A clear understanding of the relationship among all the slip manifestations is limited by the lack of a unique geophysical instrument which allows us to observe the whole spectrum. Hence the need of a joint analysis which includes both seismological and classical geodetic data, whose connection is represented by strainmeters. A part from bridging the two end-members of the traditional geophysical instrumentation, strainmeters enhance of $\sim 3-4$ order of magnitude our capability of detecting deformation signals with characteristic times of hours to months. This will help us to address questions concerning seismic activity of both tectonic and non-tectonic origin, which has largely remained unexplained so far.

In this dissertation we exploit different geodetic techniques and hydrological data to study and interpret transient deformation signals of both tectonic and non-tectonic origin. In Chapter 2 we study the postseismic deformation following the 2016-2017 earthquakes that struck Central Italy exploiting GPS daily displacement time series. In particular, we try to answer to questions about the possible sources of aseismic deformation which are known to follow the stress perturbation induced by the mainshocks. In doing so, we study the occurrence of afterslip on the main faults active during the coseismic phase and we investigate the possible role played by nearby structures, thus reflecting on faults interaction. Furthermore, we try to address the question of whether multiple postseismic mechanisms concurred in the displacement field that the GPS network recorded, finding evidences of a viscoelastic relaxation of the lower crust as well. Since GPS, on the time scales considered for this study, provides results with mm-scale precision, an investigation of the hydrological processes, clearly affecting our time series, has come up to be essential for an accurate analysis of the tectonic processes ongoing in the area. Such a study resulted in the published article *Post-Seismic Deformation Related to the 2016 Central Italy Seismic Sequence From GPS Displacement Time-Series* (Mandler et al., 2021) from which Chapter 2 is basically taken. In Chapter 3 we introduce the reader to a specific type of strainmeter, the Gladwin Tensor one, and we provide the motivations and the general information concerning the calibration of these instruments. In Chapter 4 the original methodology we propose to calibrate these strainmeters is presented and applied to the array deployed in Taiwan. Contextually, an application of a joint analysis of various data sets to investigate deformation due to hydrological processes at different temporal and spatial scales in Taiwan is presented. As already mentioned, due to the high sensitivity of strainmeters, hydrological signals are relevant in strain time series, and they can mask tiny tectonic signals. In Chapter 4 we show that for some sites they can get to be the dominant source of deformation, thus highlighting the importance of a characterization of such non-tectonic processes. Finally, in Chapter 5, the same methodology of Chapter 4 is applied to the strainmeters recently installed in the Northern Apennines, across the Alto Tiberina Fault. Contextually, we provide an example of the potential role of these instruments in following the dynamic of a storm that hit the Umbria-Marche regions (Central Italy) in 2022. Such a source of deformation is clearly visible in the strain time series, and provides us with the opportunity of showing the relevance of the detection and interpretation of faint signals in the light of future analysis of tectonic sources.

Chapter 2

Amatrice-Visso-Norcia Seismic Sequence

2.1 Introduction to the seismic sequence

The 2016-2017 Amatrice-Visso-Norcia (AVN) seismic sequence began with a Mw 6.0 earthquake on August 24, located near the town of Amatrice (Figure 2.1), in a sector of the Central Apennines characterized by a narrow band of measurable geodetic and seismic deformation rates (D'Agostino, 2014; Sani et al., 2016; Barani et al., 2017). The Amatrice earthquake caused hundreds of deaths, while the nearby towns and surroundings were considerably damaged (Pucci et al., 2017). As Chiaraluce, Di Stefano, et al. (2017) show, the mainshock was followed by seismicity which was recorded both northwestwards and southeastwards of the epicenter, with decreasing magnitude and frequency, until October 26, when a second shock of Mw 5.9 occurred near the town of Visso (Figure 2.1). The epicenter of this second event has been located about 25 km to the NW of Amatrice's earthquake one. Four days after, on October 30, the largest shock of the whole sequence (Mw 6.5) nucleated close to the town of Norcia, on a section of the fault system between the two preceding earthquakes that had been left unbroken until that moment (Cheloni et al., 2017). Three months after, on January 18 2017, four $5 \leq Mw \leq 5.5$ earthquakes occurred in an area southeast of the Amatrice event rupturing the Campotosto fault (Xu et al., 2017 ; Cheloni et al., 2017).

This sector of the Apennines is characterized by a SW-NE extension of $\sim$ 3-4 mm/yr (D'Agostino, 2014; Barani et al., 2017; Devoti et al., 2017), accomodated by several NW-SE trending active normal faults (Boncio et al., 2004; Galli et al., 2008; Pizzi and Galadini, 2009). Consistently, all the main events of the 2016-2017 seismic sequence show focal mechanisms in agreement with such a tectonic setting (http://cnt.rm.ingv.tdmt.it; Figure 2.1).

A considerable amount of geodetic (Cheloni et al., 2017; Huang et al., 2017; Lavecchia et al., 2016; Walters et al., 2018; Wang et al., 2018; Xu et al., 2017), seismological (Chiaraluce, Di Stefano, et al., 2017; Papadopoulos et al., 2017; Pizzi et al., 2017; Scognamiglio et al., 2018; Tinti et al., 2016), and geological (e.g., Civico et al., 2018; EMERGEO Working Group, 2016; Falcucci et al., 2016; Galadini et al., 2018; Pizzi et al., 2017; Villani et al., 2018) observations highlight how each mainshock ruptured a different, slightly off-axis, segment of a SW dipping normal fault system parallel to the Apennines mountain chain, and in particular the main fault systems of the area, namely the Mt. Vettore-Mt Bove to the north and the Mt. della Laga (also known as the Gorzano fault) to the south, which are separated by the Pliocene Sibillini thrust (Figure 2.1).

In the past four centuries, several $5.2 < \mathrm{Mw} < 6.2$ earthquakes nucleated in this section of the Apennines (Rovida et al., 2019; Figure 2.1). The faults responsible for the mainshocks of the 2016-2017 seismic sequence are part of a 80 km long system (Figure 2.1; Michele et al., 2020), and are confined by the structures responsible for the Colfiorito 1997 seismic sequence to the north (Chiaraluce et al., 2003; Amato et al., 1998; Boncio and Lavecchia, 2000; Ferrarini et al., 2015), and by the one responsible for the 2009 L'Aquila earthquake to the south (Chiaraluce, 2012; Lavecchia et al., 2012; Valoroso et al., 2013). Hence, the 2016-2017 seismic sequence can be framed in the wider context of a 150 km long normal fault system, which consists of 10-30 km long segments separated by crosscutting compressional structures inherited from the pre-Quaternary compressional tectonics (Pizzi and Galadini, 2009).

Although the segmentation of the fault system is not unequivocally determined, the faults that ruptured during the Amatrice-Visso-Norcia sequence are rather well defined. Most of the studies (Chiaraluce, Di Stefano, et al., 2017; Cheloni et al., 2017, Cheloni et al., 2019; Xu et al., 2017; Walters et al., 2018) suggest the activation of a fault system $\sim 60 - 70$ km-long, $157° - 164°$ striking and $39° - 50°$ dipping. Some studies (Xu et al., 2017; Cheloni et al., 2019) propose coseismic slip models on a single plane for the main fault, while others (Chiaraluce, Di Stefano, et al., 2017; Cheloni et al., 2017; Walters et al., 2018) divide such fault plane into 3-4 segments which are consistent in terms of strike and dip. The Amatrice event was characterized by a bilateral rupture (Lavecchia et al., 2016; Tinti et al., 2016; Cheloni et al., 2017; Xu et al., 2017; Chiaraluce, Di Stefano, et al., 2017) on the southern portion of the Amatrice-Visso-Norcia fault system between the M. Vettore and the Gorzano faults, with maximum slip $\sim$ 1m . Such event may have possibly activated the Campotosto fault in the area struck by the January 2017 earthquakes (Xu et al., 2017). The Visso earthquake nucleated on the northernmost portion of the Amatrice-Visso-Norcia fault system with a maximum slip of $\sim 0.6 - 1$ m occurring at a depth of 3-6 km (Xu et al., 2017; Chiaraluce, Di Stefano, et al., 2017; Cheloni et al., 2017; Walters et al., 2018). The Norcia earthquake filled the gap on the fault system left by the previous events with ruptures extending southwards up to the area already activated during the Amatrice event (Xu et al., 2017; Cheloni et al., 2019; Scognamiglio et al., 2018). As regards the coseismic slip distributions, most of the studies (Cheloni et al., 2017, 2019; Chiaraluce, Di Stefano, et al., 2017; Walters et al., 2018; Xu et al., 2017; Scognamiglio et al., 2018) present similar solutions in terms of slip location (Cheloni et al., 2019) and peaks of maximum slip ($\sim 2.5 - 3$ m) in the shallower portion of the fault ($\sim 0 - 6$ km), consistently with the observed surface ruptures (Xu et al., 2017); nevertheless some of them (Cheloni et al., 2017, 2019) allow considerable slip deeper than that. Cheloni et al. (2017, 2019), Walters et al. (2018), Scognamiglio et al. (2018) invoke for the Norcia earthquake the activation of multiple secondary faults. Specifically, a fault antithetic to the M. Vettore fault, well highlighted by the seismicity (Chiaraluce, Di Stefano et al., 2017) with a steep dipping angle ($\sim 65°$), striking $\sim 336°$ N (Cheloni et al., 2017, 2019; Walters et al., 2018). Cheloni et al. (2017), Walters et al. (2018) and Scognamiglio et al. (2018) include in their solution a $\sim 210° - 220°$N striking, $\sim 35° - 40°$ dipping additional secondary fault, possibly connecting in its deepest part with the Sibillini thrust and suggesting its reactivation (Scognamiglio et al., 2018; Cheloni et al., 2017). However, more recent studies (Cheloni et al., 2019; Pousse-Beltran et al., 2020) suggest that requiring the activation of such an oblique structure to explain the seismic sequence is an unnecessary addition of complexity, as the main fault system plus a series of antithetic faults is sufficient to explain the complex displacement pattern observed.

A comparison between seismological data and subsurface geology (e.g., Porreca et al., 2018) has pointed out that most of the instrumental background seismicity that followed the 1997 and 2009 earthquake sequences is recorded within the sedimentary succession, as suggested by Chiaraluce, Barchi, et al. (2017). Remarkably, the extension at depth of the normal faults of the area is confined into the first 8-10 km of the upper crust, being bounded by $\sim 2 - 3$ km thick, east-dipping, layer of seismicity, which hosted a series of small to moderate aftershocks (Mw $\simeq 4$). It has been argued that the higher angle faults might be loaded by this layer of seismicity which, moreover, could mark the decouplement between the upper and lower crusts (Chiaraluce, Di Stefano, et al., 2017; Vuan et al., 2017). However, the relationship among this layer of seismicity, the sudden cut-off of seismicity at depth, and the position of the overlying basement (between a depth of 8 and 11 km) is still unclear. Following previous authors (e.g. Chiaraluce, Di Stefano, et al., 2017; Vuan et al., 2017; Michele et al., 2020) we will refer to such a thick layer of seismicity as *shear zone*.

To the best of our knowledge, the postseismic phase of the 2016 Central Italy sequence has been studied only by Pousse-Beltran et al. (2020), who used Interferometric Synthetic Aperture Radar (InSAR) time-series to detect and model the early postseismic deformation (i.e., first six months), focusing on the near-field response (< 50 km). In such study, two subsidence areas are detected: the first one in the Castelluccio basin and the second one nearby the town of Arquata. Due to inconsistencies between the observed and the modeled displacement, poroelasticity and viscoelasticity are ruled out as the main mechanisms responsible of the postseismic displacement pattern (Pousse-Beltran et al., 2020). However, due to a poor explanation of the subsidence observed in the Castelluccio basin by afterslip only, Pousse-Beltran et al. (2020) do not completely exclude their contribution, and/or those of the shear zone, to the displacement observed in this area. On the other hand, the logarithmic-like evolution of the displacement in the InSAR time-series in the Arquata area validates the hypothesis of afterslip as the driving mechanism (Pousse-Beltran et al., 2020). The best slip distribution they retrieve requires the activation of the M. Vettore fault (as modeled by Cheloni et al., 2017) and of an antithetic fault (as modeled by Cheloni et al., 2019; Maubant et al., 2017).

In this study, on the other hand, we consider ground displacement time-series obtained from the analysis of GPS stations distributed over a wider region ($\leq$ 100 km), thus including also far-field stations, over a longer time period (up to 2.3 years). We apply a blind-source-separation algorithm to characterize the temporal evolution and spatial features of the postseismic deformation signal across the 2016-2017 epicentral area. The longer time span and wider area here considered allow us to investigate, beside afterslip, a contribution of the viscoelastic relaxation, which has already been demonstrated to follow $M >\sim 6$ earthquakes (e.g., Bruhat et al., 2011). For a thorough analysis, particular attention has been given to a proper separation of tectonic signals present in the data set from non-tectonic ones, as they may be mask preventing a good interpretation (e.g. Michel et al., 2018; Gualandi et al., 2020).

The chapter is organized as follows: in Section 2.2 we describe the GPS data set used and the results of the Independent Component Analysis (ICA) applied to the GPS displacement time-series; in Section 2.3 we interpret the retrieved non postseismic signals as due to hydrological sources; in Section 2.4 we obtain, by inverting the GPS time series, the distribution of afterslip and show a possible viscolastic contribution to the measured geodetic, far field, displacements; in Section 2.5 we discuss the findings of this study and in Section 2.6 conclusions are drawn.

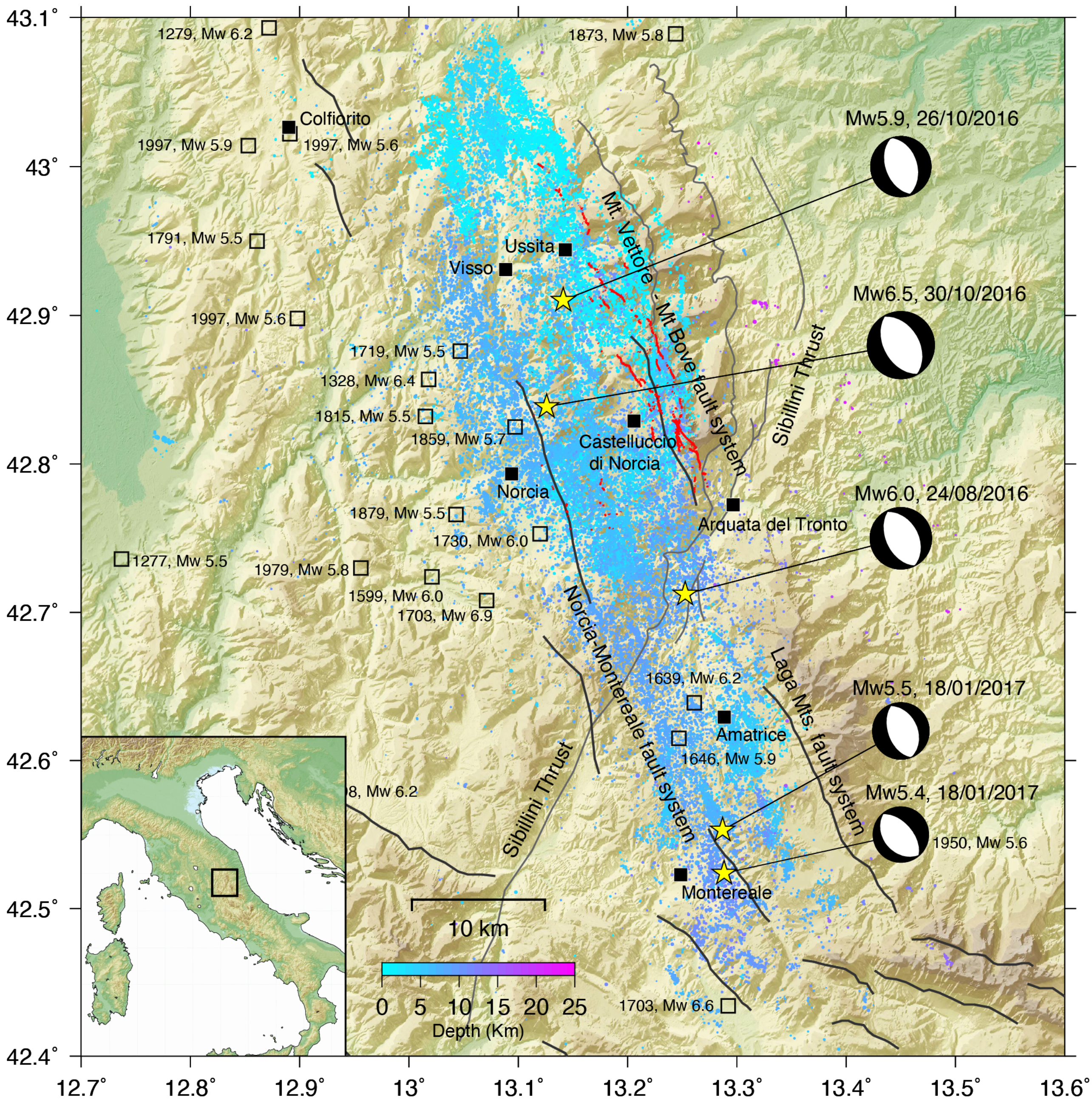

Figure 2.1. Map showing the major events of the 2016-2017 Central Italy sequence (yellow stars), the focal mechanism (from Michele et al., 2020) and the historical seismicity (squares), for earthquakes with equivalent $5.4 \leq Mw$ (from CPTI15, V.2.0, https://emidius.mi.ingv.it/CPTI15-DBMI15). Colored dots represent the seismicity recorded after August 24 (from Michele et al., 2020), plotted as a function of depth. The red lines represent ground ruptures associated with the Amatrice and Norcia mainshocks (from Civico et al., 2018). The black and grey lines show the trace of the major normal faults and of the Sibillini thrust, respectively.

2.2 GPS data and time series analysis

Figure 2.2 shows the GPS stations considered in this work. Since we are interested in measuring the continuous slow deformation process occurring after the Amatrice mainshock, we have considered mainly GPS stations with almost continuous data in the time-interval 2012-2019, which have been integrated by a few campaign-mode stations, belonging to the CaGeoNet network (Galvani et al., 2013), that have been occupied almost continuously after the Amatrice mainshock (see Cheloni et al., 2016 for details). We also included a few stations in the Adriatic off-shore, which are managed by ENI S.p.a. (https://www.eni.com) and presented by Palano et al. (2020). This data set also includes new continuous stations installed as emergency response soon after the Amatrice and Norcia events.

We followed the procedure described in Serpelloni et al. (2006, 2013, 2018) in order to get the position time series, namely we: reduce raw phase data; we combine loosely constrained network solutions and we define the reference frame; we analyze time series, estimating velocities, carrying out the spatial filtering of common mode errors, and removing co-seismic and instrumental offsets. The details of the processing and post-processing procedures are described in the supplementary material of Mandler et al. (2021) Section S1.1. The time series used in this work are part of a continental-scale geodetic solution, including >3500 continuous GPS stations and the spatial filtering has been applied at a continental-scale, following Serpelloni et al. (2013, 2018), excluding all GPS stations affected by earthquakes, thus preventing the removal of the localized geophysical signals recorded by the GPS stations in the study area.

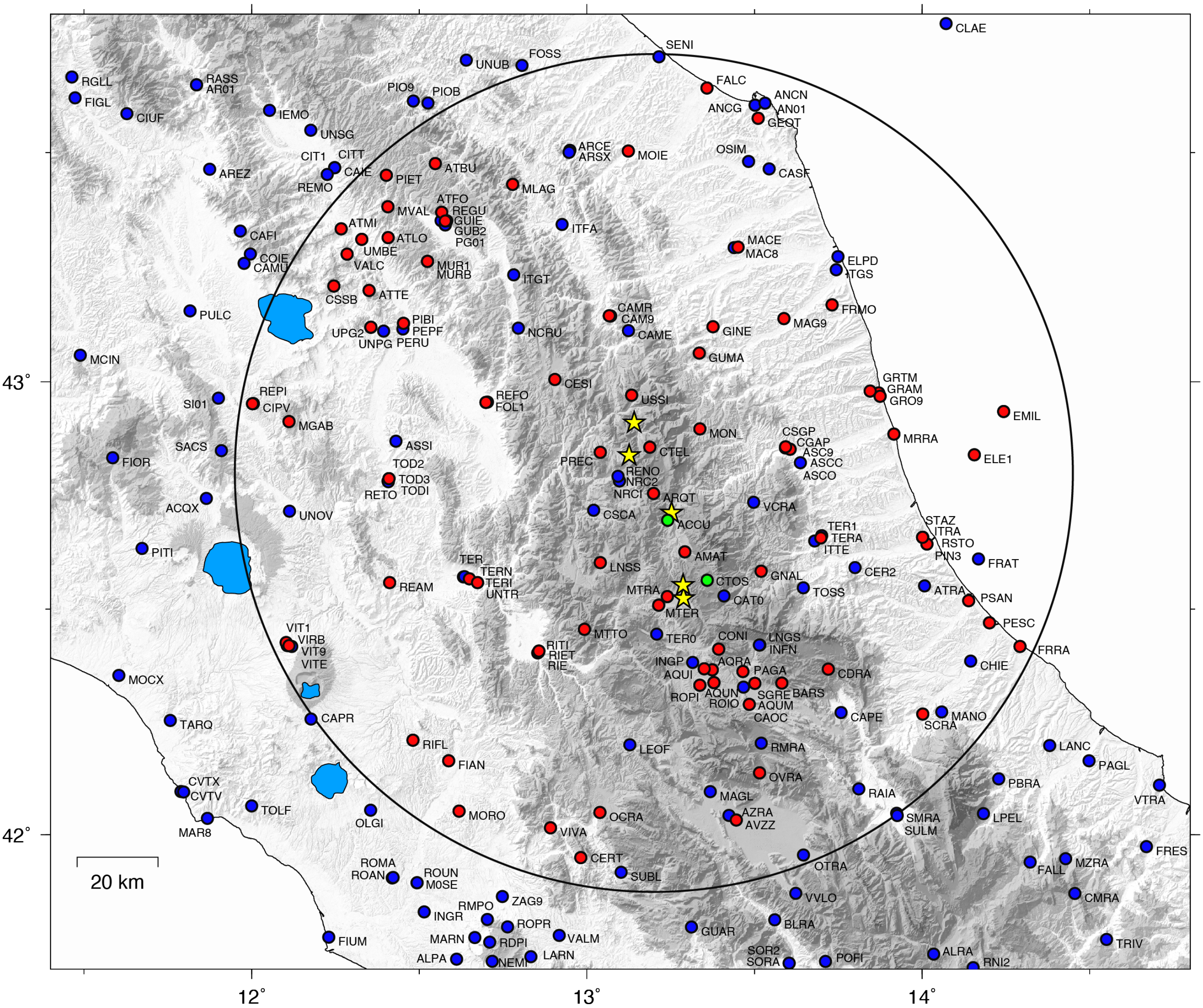

Figure 2.2. Colored circles show the GPS stations considered. The blue circles show the positions of the continuous GPS stations present in this area and for which we analyze the raw data as described in Section 2.2. Among the whole GPS network, the red circles show the position of the continuous GPS stations used in the blind source separation analysis with the vbICA method (Section 2.2.1), namely stations within a of radius = 100 km from the epicentral area having almost continuous observations after the Amatrice earthquake. The green circles show the position of the two non-permanent GPS stations, belonging to the CaGeoNet network, included also in the vbICA. The yellow stars show the epicenters of the mainshocks of the 2016-2017 seismic sequence, as in Figure 2.1.

2.2.1 Independent Component Analysis

In this Section we will provide the reader with the basic principles of the Independent Component Analysis (ICA) technique, while the results of its application to our data set will be presented in Section 2.2.2.

Our data consist of the displacement time series recorder by the 85 GPS sites between 2012 and 2019, with a daily sampling. As we are dealing with 3D records (east, north and vertical), the total number of time series will be $M = 3 \times 85 = 255$ for a total number of days $T = 2525$. We can organize the data into a spatio-temporal matrix $X_{M \times T}$, in which each column represents the record at a given time or epoch while each row is a different time series. Our measurements consist of surface displacement originating from different processes acting together on different spatio-temporal scales. Our goal is to separate them in order to properly model and interpret the sources of deformation. However, as in principle such sources are unknown, we are facing a so-called blind source separation problem. Multivariate statistical approaches that try to maximize the independence of the sources producing the observations are well established techniques, belonging to the *Independent Component Analysis*, and generally consisting in a linear decomposition of the data into the so-called mixing matrix A (MxL) and source matrix S (LxT). L is the number of sources (components) of which we maximize the independence. We can formulate the problem as follows:

$$X = AS + N \tag{2.1}$$

where N is noise (typically Gaussian). The equality in equation 2.1 would hold if we decomposed our data with a number of components L sufficient to span the whole original space where the data X live. However, we generally perform a truncation, i.e. $L < \min\{M, T\}$, and the right hand side is a low-rank approximation of the left hand side (e.g., Kositsky and Avouac, 2010). As we are carrying out a linear decomposition, we can separate the spatial information content to the temporal one, respectively in the matrices A and S. The ICA tries to find L sources of deformation, requiring statistical independence, which are encoded in the matrix S. In our case, we perform the decomposition in the so-called T-mode, i.e. with sources that are independent in the time domain. As we are dealing with a blind-source separation technique we do not need to impose any functional form to the sought sources of deformation. In fact, ICA techniques belong to the so-called unsupervised learning approaches to pattern recognition.

In general, in order to build the cost function to maximize (or minimize) we need to introduce some approximations, as the independence condition is not straightforward. Among the possible approaches we follow here a *variational Bayesian ICA* (vbICA), which has proven to be more flexible in the description of multimodal sources and it allows to take into account missing data (e.g., Roberts and Choudrey, 2003; Chan et al., 2003). In particular, we employ the version described in Gualandi et al. (2016) following a similar notation. Accordingly, each independent component is described by its temporal evolution (V) and a certain spatial distribution (U). As U and V are adimensional, weighting coefficients Σ (in mm) are needed to fully explain the contribution of each IC to the displacement observed. Since the vbICA belongs to the field of linear decompositions, we can write the result of the decomposition of the data matrix X as:

$$X_{M\times T} = U_{M\times L}\Sigma_{L\times L}V_{L\times T}^{T} \tag{2.2}$$

where $V_{L\times T}$ contains the temporal evolution of the L sources; $U_{M\times L}$ contains the spatial response of the M components of the GPS network to the L sources of displacement; $\Sigma_{L\times L}$ is a diagonal matrix embedding the relative importance of each IC in explaining the measured displacement (in mm). As we are carrying out the decomposition in the T-mode, we seek independent sources in the time domain. Namely we can correspond V matrix and the product $U\Sigma$ of equation 2.2 respectively with the source S matrix and the mixing matrix A of equation 2.1. The probability density function of each source is modeled, in the vbICA algorithm, through a mix of Gaussian distributions (4 in this case, as suggested by Choudrey, 2002), obtaining the sought U and V (i.e., the spatial and temporal information) of the ICs. In our study, all stations without data after the Amatrice earthquake and stations with large chunks of missing data ($> 90\%$) across the 2016-2017 earthquake sequence are not considered. As we are carrying out a blind separation analysis, the number L of independent sources in not known. Statistical tests such as the χ^2, F-test (Kositsky and Avouac, 2010) or the ARD test (Choudrey, 2002; Gualandi et al., 2016) can be adopted to seek the best decomposition. We test the case of a number of ICs L = 3, 4, 5, 6, and the ARD test limited $L \leq 5$. An estimation of the goodness of the decomposition is given by the χ^2_{red} which is respectively 1.53, 1.48 and 1.50 for L = 3, 4, 5. In order to assess if these values are significantly different one another we perform the F-test on the χ^2. The F-test between the 3 ICs and 4 ICs provides F=1.66, while between 4 and 5 components it provides F=0.79. The comparison between these values and the critical value at a 95% level of confidence (F-critical= 1.02) suggests to retain 4 components, and such configuration is the one we investigate.

vbICA algorithm provides us with an estimate of the uncertainty associated with each independent component. However, they are generally found to be underestimated. In this study, we implement a novel approach to better assess them. In practice we run 100 Monte Carlo simulations generating synthetic data sets and randomly perturbing the original GPS time series assuming a nominal Gaussian uncertainty at each available epoch. We perform 100 ICA decompositions and we refer to them as to ICA_{rand}. Differently from the more common Principal Component Analysis (PCA), a problem with the ICA is that the ordering of the ICs is not well defined. Fortunately, the extracted ICs are sufficiently robust with respect to the random perturbations imposed, and we can thus sort the ICs ordering them on the base of the correlation between their temporal sources and the original sources obtained not perturbing the data. We estimate the uncertainty on the spatial pattern U, the weights Σ and the temporal functions V considering how spread their values are across the 100 ICA_{rand}. In practice, we calculate the sample variance for each element of each matrix. This procedure provides larger uncertainties with respect to those outputted by the vbICA code, and we consider them to reflect more realistically the uncertainty in the data.

2.2.2 ICA results

Aim of this Section is to provide the reader with the results of the vbICA performed on the GPS data set described in Section 2.2. In Figure 2.3 we report the temporal evolution of the four ICs (V) (panel (a)), together with their corresponding power spectral density (panel (b)). The components resulting from the decomposition described in Section 2.2.1 are: (i) a postseismic relaxation signal (IC1); (ii) two components with annual periodicity (IC2 and IC4); (iii) a multiannual component (IC3). It can be noticed, from the spectral analysis, that low frequencies dominate IC1 and IC3, namely the postseismic and the multiannual IC, and that IC2 and IC4 are dominated by a periodical signal with characteristic time ~ 1 year. However the IC4 spectral density shows a low frequencies content as well. The spatial response of the four ICs (U) is shown in Figure 2.4. Figure 2.4 shows the NE-SW main direction of the U1 spatial pattern, in agreement with the extensional mechanisms of the seismic sequence. The second component (U2) mainly affects the vertical component of GPS, with all stations experiencing coherently uplift and subsidence with annual periodicity, whereas U3 and U4 show more complex horizontal, and secondly vertical, spatial patterns. In the Section 2.3 a physical explanation for the IC2, IC3 and IC4 will be provided, whereas the IC1 will be discussed in detail in Section 2.4.

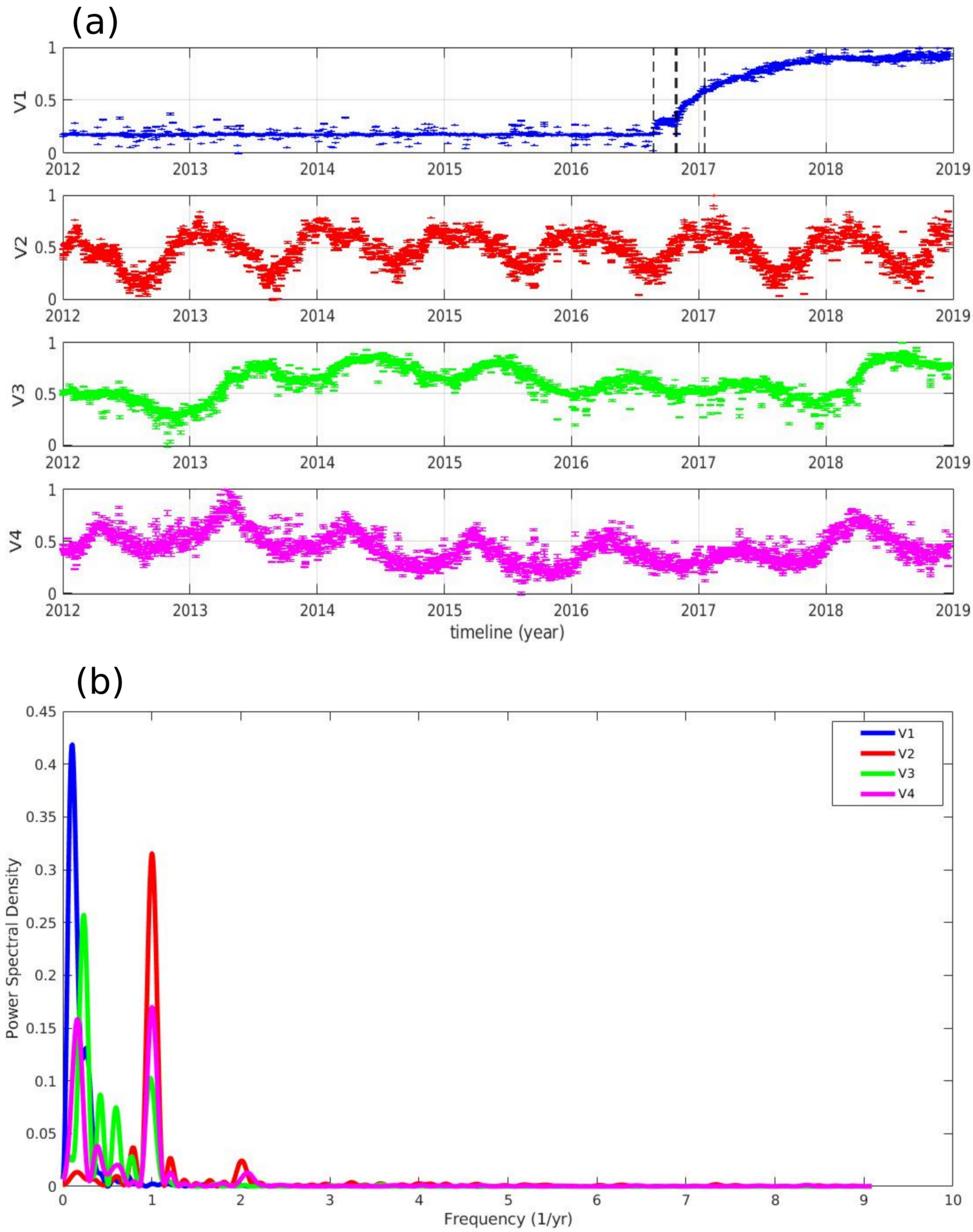

Figure 2.3. (a) The temporal evolution V of the four independent components (vertical dashed lines for V1 mark the Amatrice, the Visso-Norcia and the January 2017 Campotosto earthquakes) and (b) their corresponding power spectral density plots.

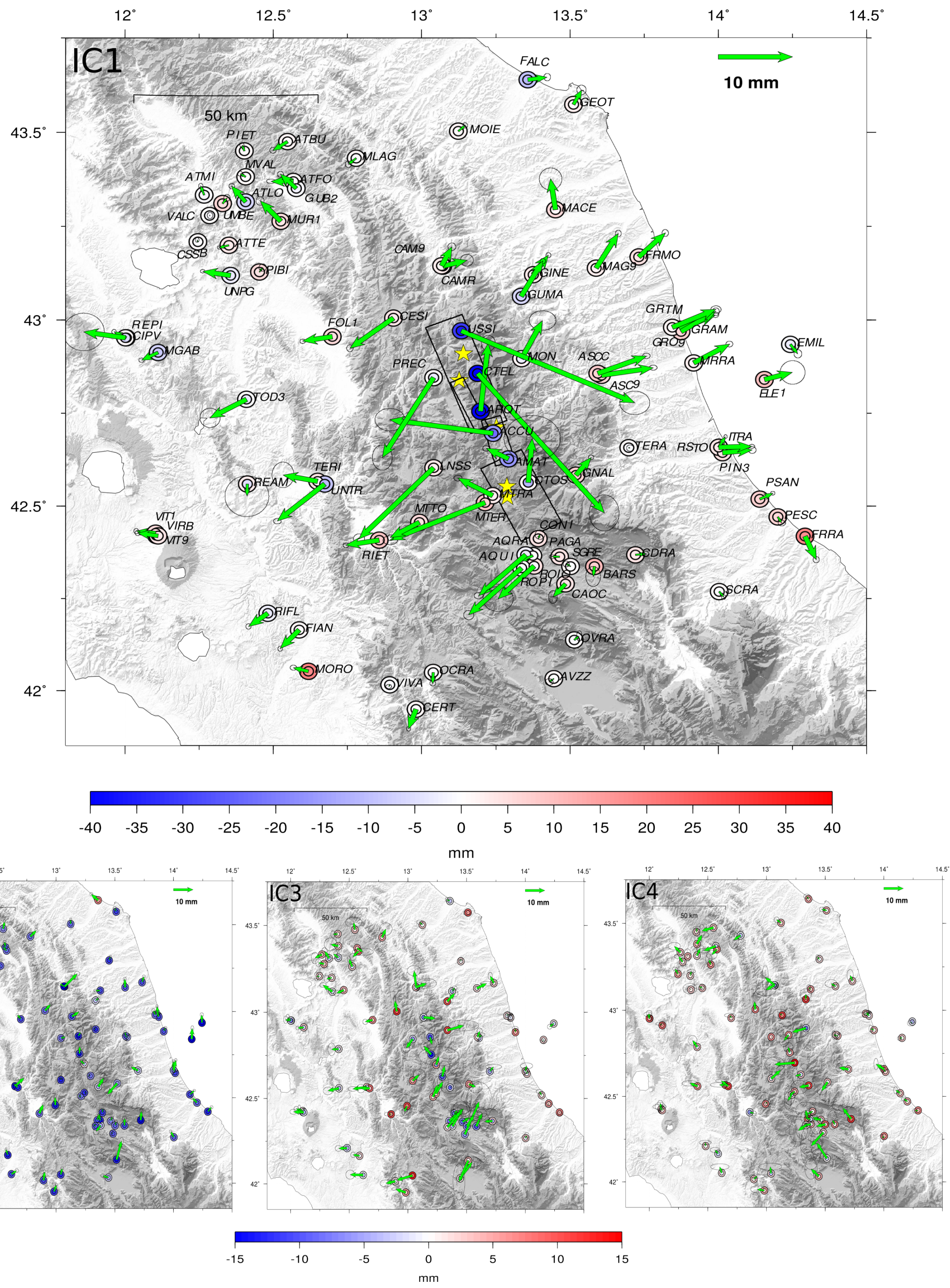

Figure 2.4. In Figure the dimensional spatial components (Σ U) of the IC1, IC2, IC3, IC4, with the corresponding temporal functions being normalized between 0 and 1 (Figure 2.3a). Green arrows mark the horizontal response in mm; outer colored circles mark the vertical response $+\sigma$ while inner colored circles mark the vertical response $-\sigma$ of the GPS stations (in mm). Error ellipse shows the uncertainty associated with the ICs at 2σ. Yellow stars mark the location of the mainshocks of the seismic sequence (as in Figure 2.1), while the black boxes in IC1 show the location of the faults responsible for the 2016-2017 sequence as in Cheloni et al. (2017, 2019).

2.2.3 ICA on the pre-seismic phase

In order to present a complete overview of the 2016-2017 Central Italy seismic sequence we briefly investigate its pre-seismic phase, performing an ICA on the time interval 2015-2016.64 (i.e. the 24^{th} of August), as already done in Vičič et al. (2020). Aim of this analysis is to highlight some possible deformation that can be associated with the preparatory phase of the 2016 earthquake sequence. We considered the same GPS network as for the postseismic analysis (see Figure 2.2) and, according to an F-test, L=4 components provides the most suitable decomposition. In Figure 2.5 we present the results: none of the V shows the occurrence of a geodetic transient anticipating the mainshock of the 24^{th} of August, and spatial parts U are generally sparse and do not support the presence of any ongoing localized tectonic process in the preparatory phase of the 2016-2017 seismic sequence. Our analysis does not point out any localized deformation that can be associated with a clear tectonic strain transient such as the sudden rise at the beginning of 2016 described by Vičič et al. (2020).

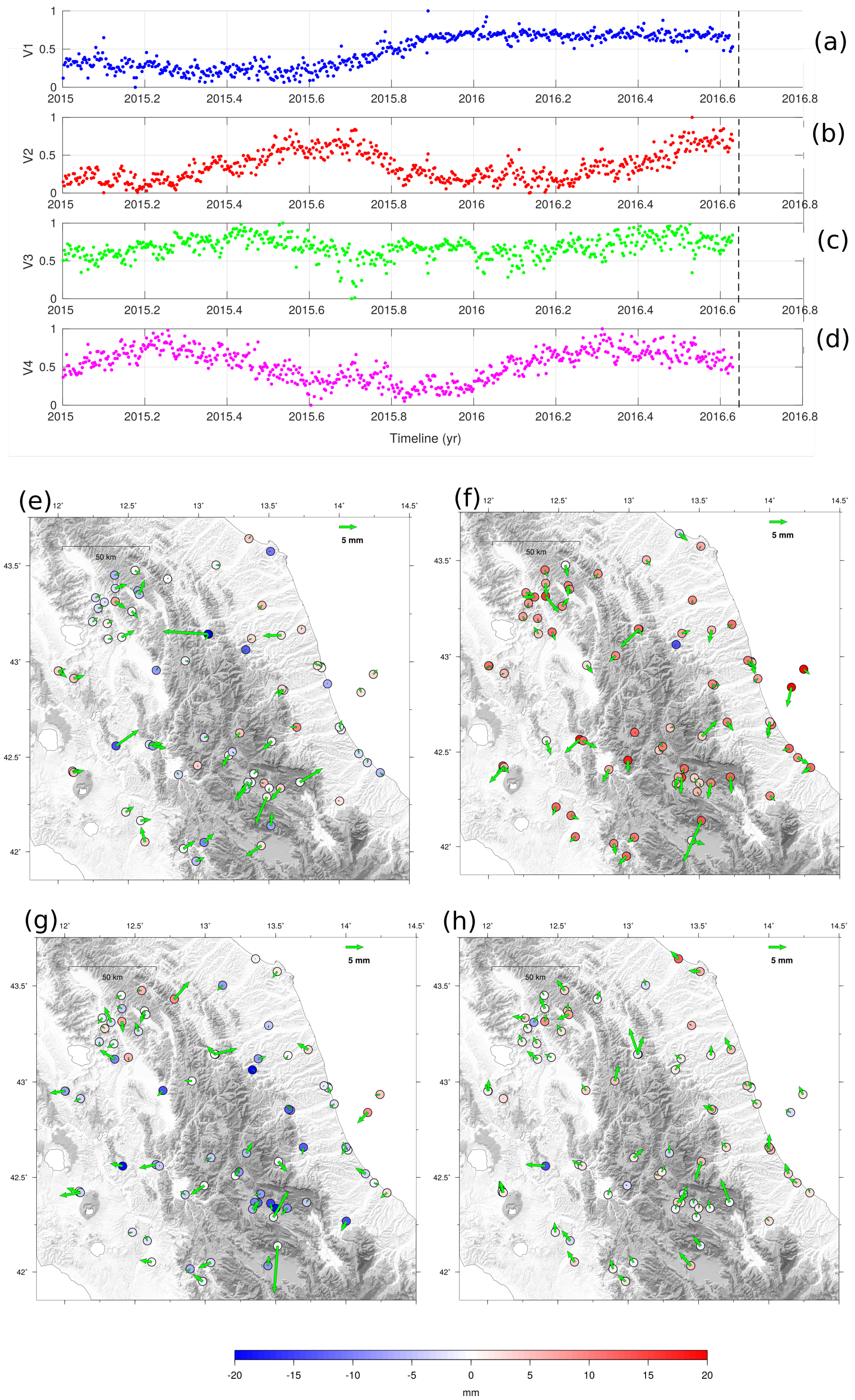

Figure 2.5. Temporal evolution and dimensional spatial response of IC1 (a, e), IC2 (b, f), IC3 (c, g), IC4 (d, h) of the analysis on the pre-seismic phase (time span 2015-2016.64). Vertical dashed lines in panels (a, b, c, d) mark the 24th of August mainshock. In the lower panels the spatial responses to the sources of deformation are given in mm.

2.3 Hydrological components

In this section the sources of deformation associated with the IC2, IC3 and IC4 (Figure 2.3 and 2.4) are discussed, and a physical explanation for these signals is provided. In particular, we test the hypothesis that these ICs are associated with hydrological processes. Such processes act on different spatial scales, either affecting the entire GPS network or being very dependent on the local geological features, and impacting the vertical and horizontal components with variable intensity. Moreover, as we showed in Figure 2.3b, low frequencies dominate the spectral density of the multi-annual component IC3, similar to those of the postseismic relaxation. For this reason, discerning the IC3 and IC1 contributions to the recorded deformation is crucial in order to improve the accuracy of the retrieved postseismic displacements, especially in case these are expected to be rather small. This is particularly true for the GPS sites in the Paganica area as we will discuss in Section 2.3.3.

2.3.1 IC2

IC2 represents a vertical common mode annual signal, with a uniform spatial response (i.e., all the GNSS stations move coherently upwards and downwards). Seasonal vertical displacements are related in the literature to loading due to mass redistribution in the shallow Earth crust and surface (e.g., Amos et al., 2014; Argus et al., 2014; Borsa et al., 2014; Dong et al., 2002; Tregoning, 2005). Vertically, the IC2 describes large seasonal displacements, with median amplitude of ~ 6.3 mm, whereas horizontally the IC2 shows much smaller annual displacements, with median amplitudes ~ 1.1 mm and 0.7 mm in the N-S and E-W direction, respectively.

The second IC vertical effect on the GNSS network is to produce uplift as temperature rises, and subsidence when the temperature decreases. Since the the temporal evolution of IC2 (the V2) is in phase with temperature (see Figure 2.6) we do not exclude that monument thermal expansion may also have an effect on GPS height changes.

We compare the V2 with products of global reanalysis models that estimate the redistribution of fluids at the Earth's surface. Figure 2.6 shows V2 compared to the temporal evolution of hydrological loading displacements estimated from the ERA-interim (European Centre for Medium-Range Weather Forecasts, ECMWF reanalysis) model (Berrisford et al., 2009; Dee et al., 2011), using predictions provided by http://loading.u-strasbg.fr (Gegout et al., 2010; see also Serpelloni et al., 2018 for a similar application), and with the sum of the soil moisture and the snow water equivalent in the first 2 m, estimated by GLDAS-Noah (Rodell et al., 2004). Clearly, V2 is temporally correlated with ERA-interim displacements and anti-correlated with soil moisture, suggesting that IC2 is associated with surface hydrological mass loading (SHL) processes.

A strong agreement between vertical displacements associated with IC2 and the ones calculated from the ERA-interim data set is observed (Figure 2.6) both in terms of temporal evolution (Pearson correlation coefficient = 0.8, with no significant time lags between the two curves), and amplitude. In fact, the mean seasonal amplitude of the vertical displacements caused by surface hydrological loading according to the ERA-interim model is 5.1 mm, which is just 1.2 mm less than the median value of the seasonal displacement associated with IC2. Regarding the horizontal displacements, the north component of the displacements associated with IC2 still well correlates with predictions from the ERA-interim model. On the other hand poorer correlations are found for the east-west displacements, as already observed in Serpelloni et al. (2018). This difference can likely be imputed to limitations of the underlying assumptions of the model (i.e., an elastic and spherical Earth), which do not account for lateral heterogenities of the Earth's elastic properties (Chanard et al., 2018).

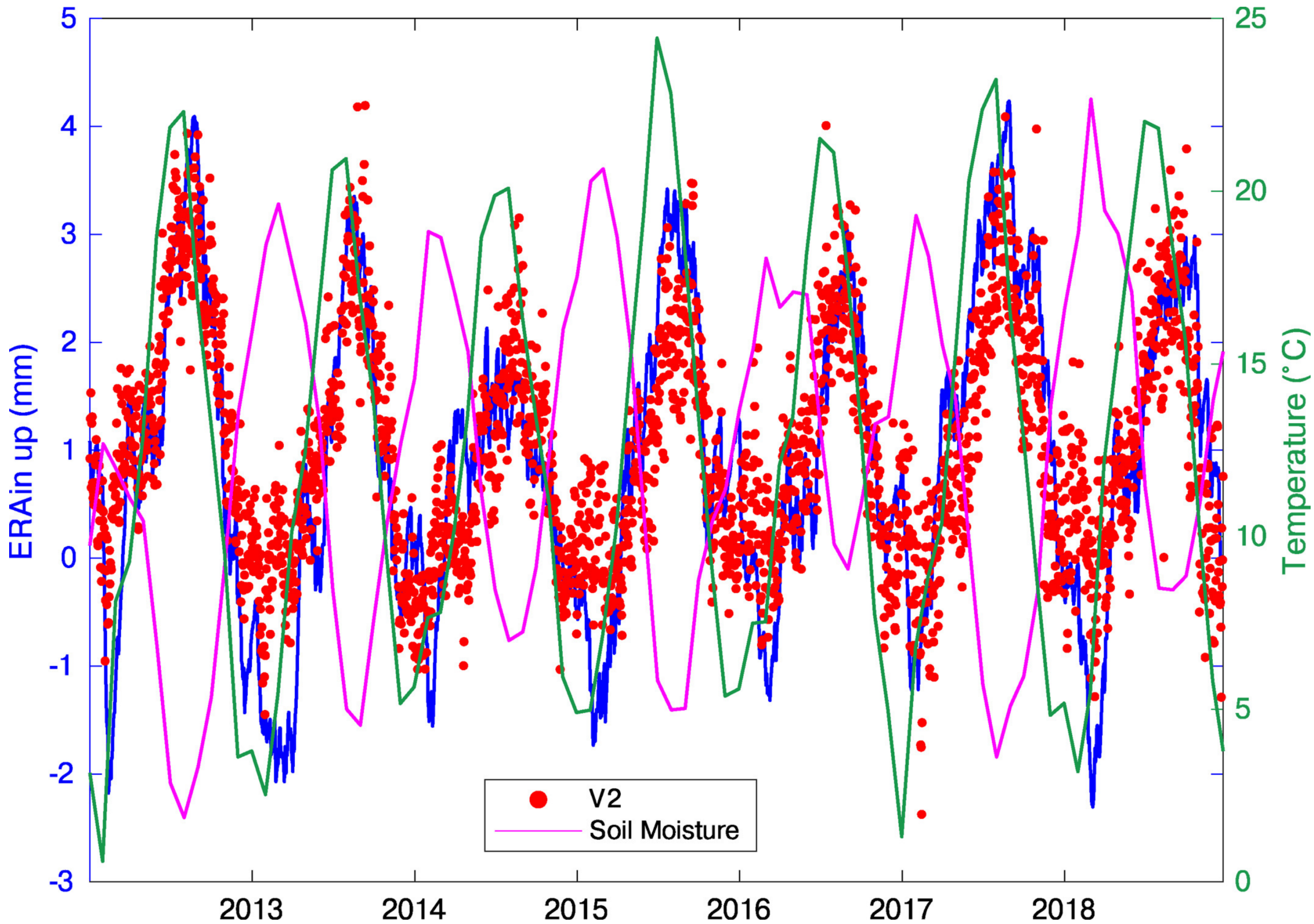

Figure 2.6. Red: V2 (sign reversed to indicate maximum uplift/subsidence during positive/negative peak values); Blue: mean vertical displacements caused by surface hydrological loading using the ERA-interim model (http://loading.u-strasbg.fr); magenta: soil moisture in the first 2 m estimated by GLDAS-Noah (Rodell et al., 2004); green: mean monthly temperature (GHCN Gridded data provided by the NOAA/OAR/ESRL PSL, Boulder, Colorado, USA, from their Web site at https://psl.noaa.gov/; (Fan and van den Dool, 2008). For all the data sets, we considered mean values in a box with limits: lon. 12.00° – 14.50° E; lat. 42.00° – 44.00° N

2.3.2 IC3 and IC4

Regarding the third IC, we test the hypothesis that this multi-annual deformation signal is associated with changes in groundwater content. As already observed in literature (e.g., Silverii et al., 2016; Serpelloni et al., 2018), deformations associated with groundwater variations affect the horizontal components of displacement with particular temporal and spatial signatures. We use the lumped parameter hydrological model GR5J (Pushpalatha et al., 2011) to quantify daily total water storage (TWS) changes of 5 hydrological basins, namely the Tevere, Nera, Tronto, Aterno and Pescara basins, shown in Figure 2.7. In Figure 2.8b,c,d we show TWS changes estimated for the 5 basins considered compared with temporal evolution of the IC3, while in Table 2.1 we report the estimated Pearson correlation coefficients and time lags. In Figure 2.8a we compare the V3 with liquid water equivalent thickness (LWE), estimated by GRACE measurements processed at JPL using the Mascon approach (Version2/RL06, Watkins et al., 2015). Since there are only 5 GRACE-FO data available during the time period covered by GNSS time series, and the gap between GRACE and GRACE-FO is about 1 year, we do not consider GRACE-FO data to compute correlations between GRACE and V3.

LWE and TWS estimates do not take into account only the superficial water accumulation, as SHL models do, but also consider the effect of the deep waters. While SHL is almost spatially uniform, since it is mainly caused by the soil moisture, the accumulation of water at depth is much more heterogeneous, especially in carbonatic mountainous regions where significant groundwater flows are present. A possible interpretation of IC2 and IC3 is that precipitation water, once removed the runoff and the evapotranspiration contributions, is partially absorbed by the first 1-2 m of soil, causing the displacements associated with IC2, which, in fact, are not significantly delayed with respect to the displacements caused by SHL. The remaining portion of precipitation may penetrate, depending on the hydro-geological properties of the subsurface, hundreds of meters until reaching a less permeable layer, accumulating water and causing the ground displacements associated with IC3. The duration of this percolation process causes a temporal delay between TWS variations and the displacements associated with IC3 (see also Table 2.1 for the time lag values), which occurs when the water level of the aquifer eventually increases.

Regarding the IC4, its interpretation is less straightforward. We notice that the TWS calculated in the Tevere basin is the one that differs the most from the others (Figure 2.8d): it has the lowest correlation with V3 among the basins considered (Table 2.1), but the highest one, when considering V4 (Table 2.2). Our interpretation is that IC3 alone is not sufficient to well reproduce the displacements associated with TWS changes in all the basins considered, in particular in the Tevere one, which includes a significant number of GNSS stations so that IC4 is needed.

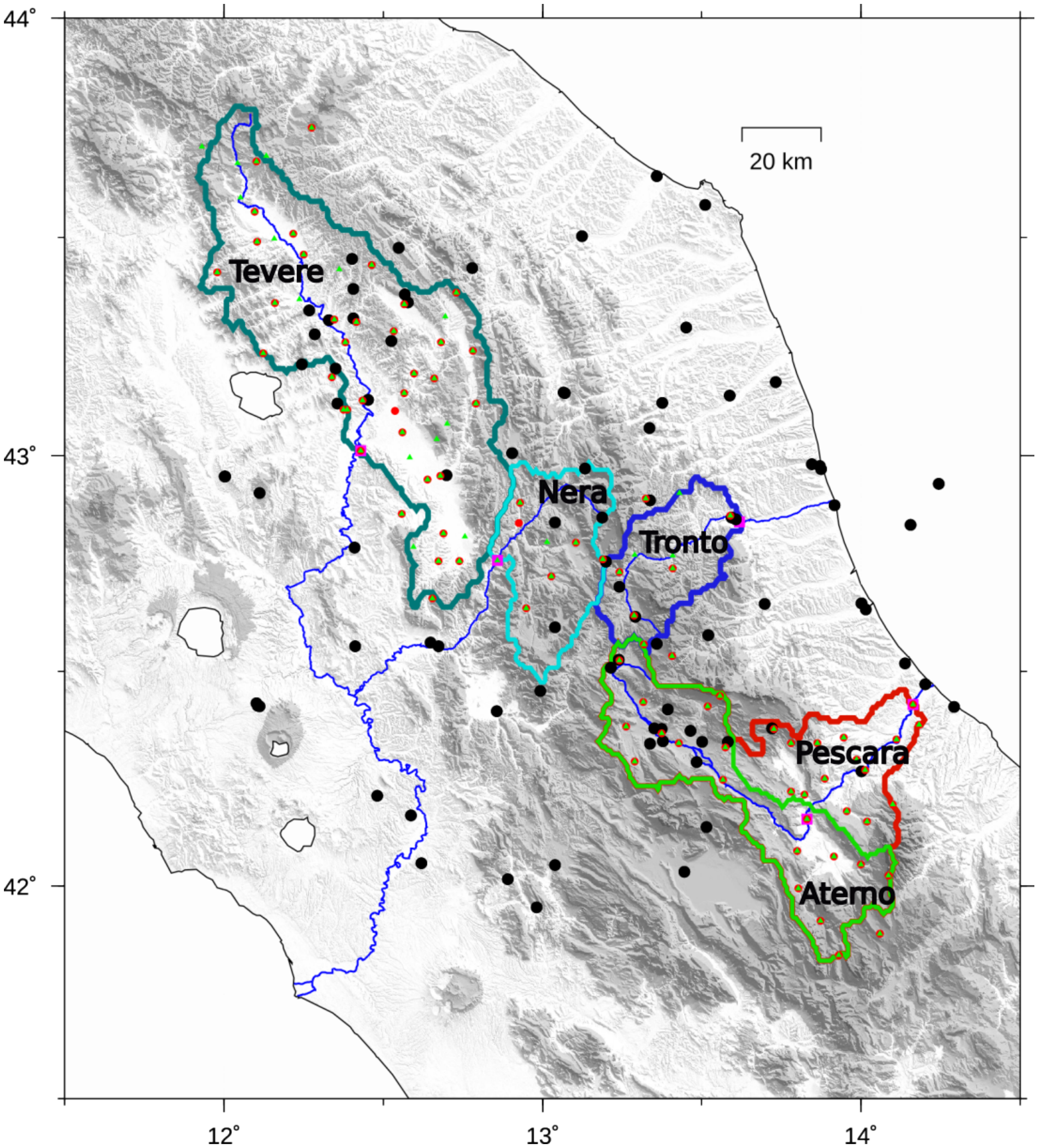

Figure 2.7. Hydrological basins of the Tevere (dark green), Nera (cyan), Tronto (blue), Aterno (light green), Pescara (red) rivers. Black dots: GNSS stations; purple squares: river gauging stations; green triangles: pluviometers; red circles: thermometers. The Tables 2.1 and 2.2 show the cross-correlation between TWS and V3, V4 (Figure 2.8) respectively. The time lag that maximizes the correlation is reported, too.

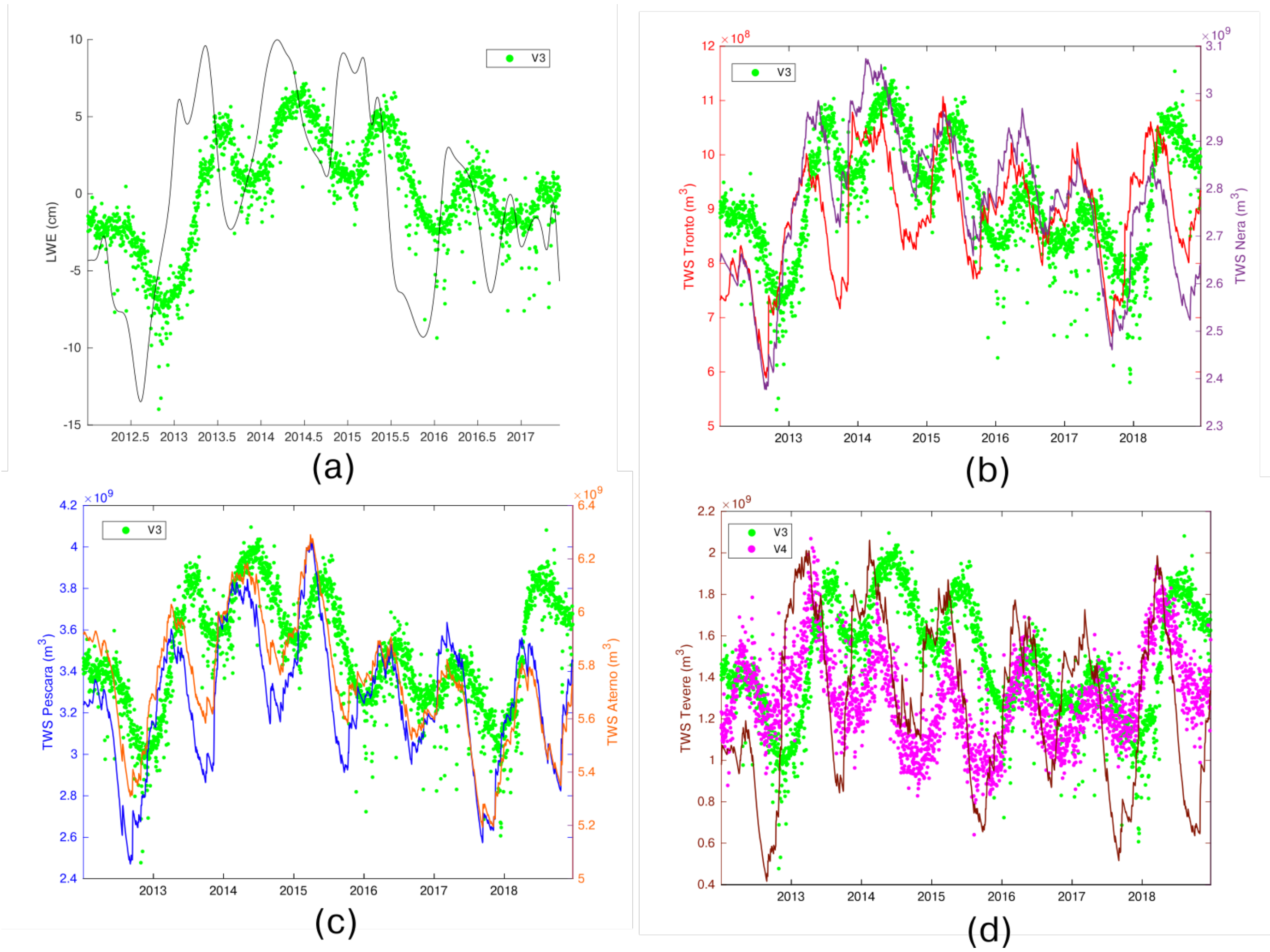

Figure 2.8. a) Comparison between LWE (in grey) from GRACE data and V3 (in green). Comparison between V3 and TWS changes computed in the hydrological basins (Figure 2.7) of Tronto (in red) and Nera (in purple) (b), Pescara (in blue) and Aterno (in orange) (c). d) Comparison among TWS changes (in brown) computed in the Tevere basin and V3 (in green), V4 (in magenta).

Hydrological basin	Pearson Correlation Coefficient TWS - V3	Lag (days)
Tevere	0.7077	110
Tronto	0.7528	93
Pescara	0.7374	79
Aterno	0.7606	63
Nera	0.7404	82

Table 2.1. Pearson cross-correlation coefficient between TWS computed in the hydrological basins and V3 (Figure 2.8). TWS anticipates V3 by a number of days estimated in the third column. Both TWS and V3 have been detrended.

Hydrological basin	Pearson Correlation Coefficient TWS - V3	Lag (days)
Tevere	0.4831	20
Tronto	0.4144	8
Pescara	0.3043	6
Aterno	0.2128	9
Nera	0.2163	10

Table 2.2. Pearson cross-correlation coefficient between TWS computed in the hydrological basins and V4 (Figure 2.8). TWS anticipates V4 by a number of days estimated in the third column. Both TWS and V4 have been detrended.

2.3.3 Paganica sites IC1 - IC3 separation

In this section we show the importance of a correct separation among tectonic and non-tectonic sources for the sites in the Paganica area. As we will see in the Section dedicated to the postseismic relaxation, a good separation of IC1 and IC3 in the area deeply affects our afterslip models (i.e., Section 2.4.2).

GPS stations in the Paganica area are heavily affected by the IC3 (Figure 2.4) as it is quite clear from the raw time-series (Figure 2.9); however to neglect a postseismic contribution to the total displacement leads to a bad data modelization (Figure 2.9). To double check this fact we subtracted the hydrological ICs from the raw data. The residuals show a mm-scale postseismic transient (Figure 2.10) consistent with the spatial displacement associated with the IC1 (Figure 2.4a).

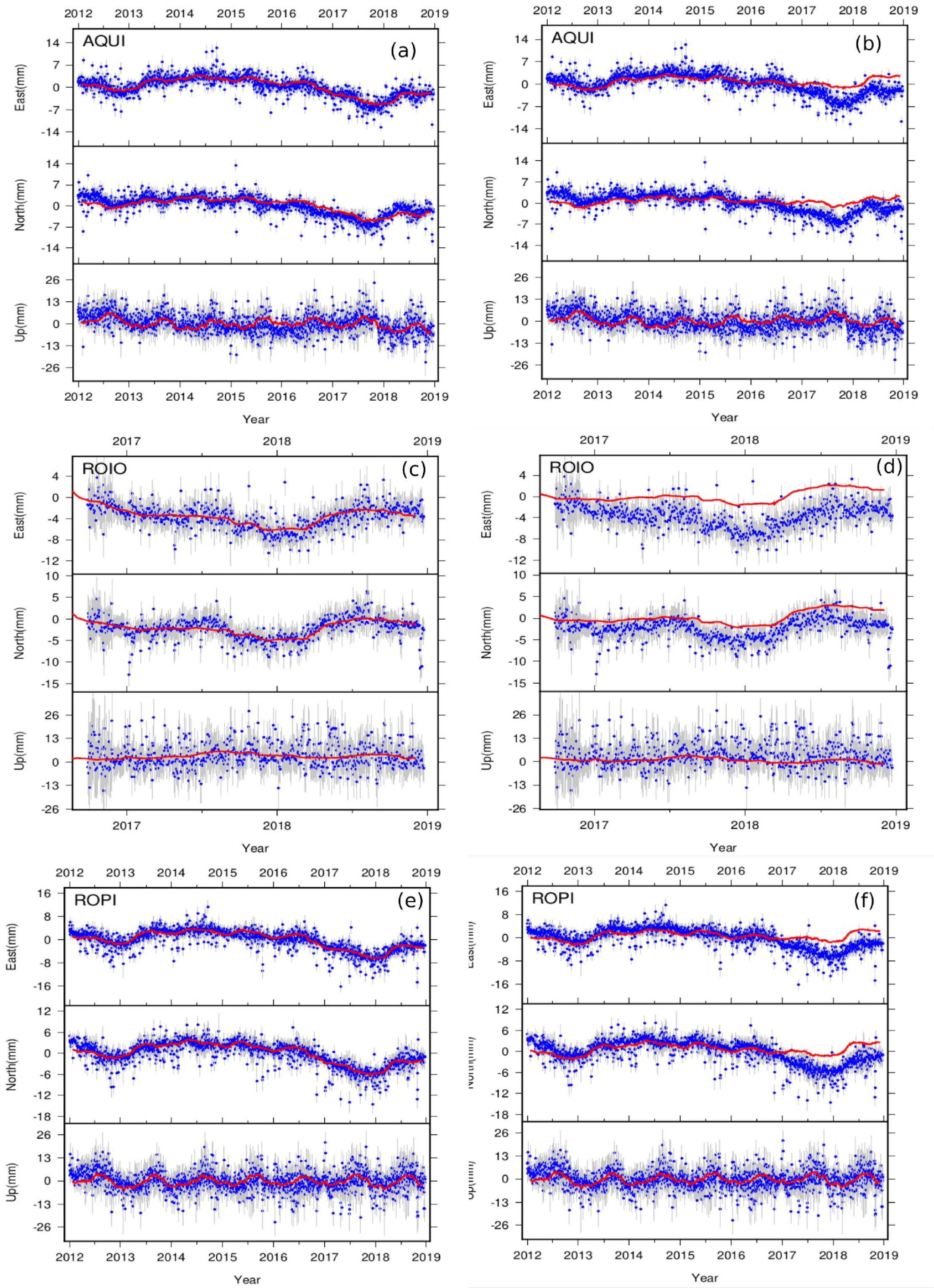

Figure 2.9. Comparison of AQUI, ROIO, ROPI time-series reconstruction using all of the ICs (panels a, c, e) and using only the non-tectonic components (panels b, d, f). Blue dots show the raw data while red lines the ICA modelization.

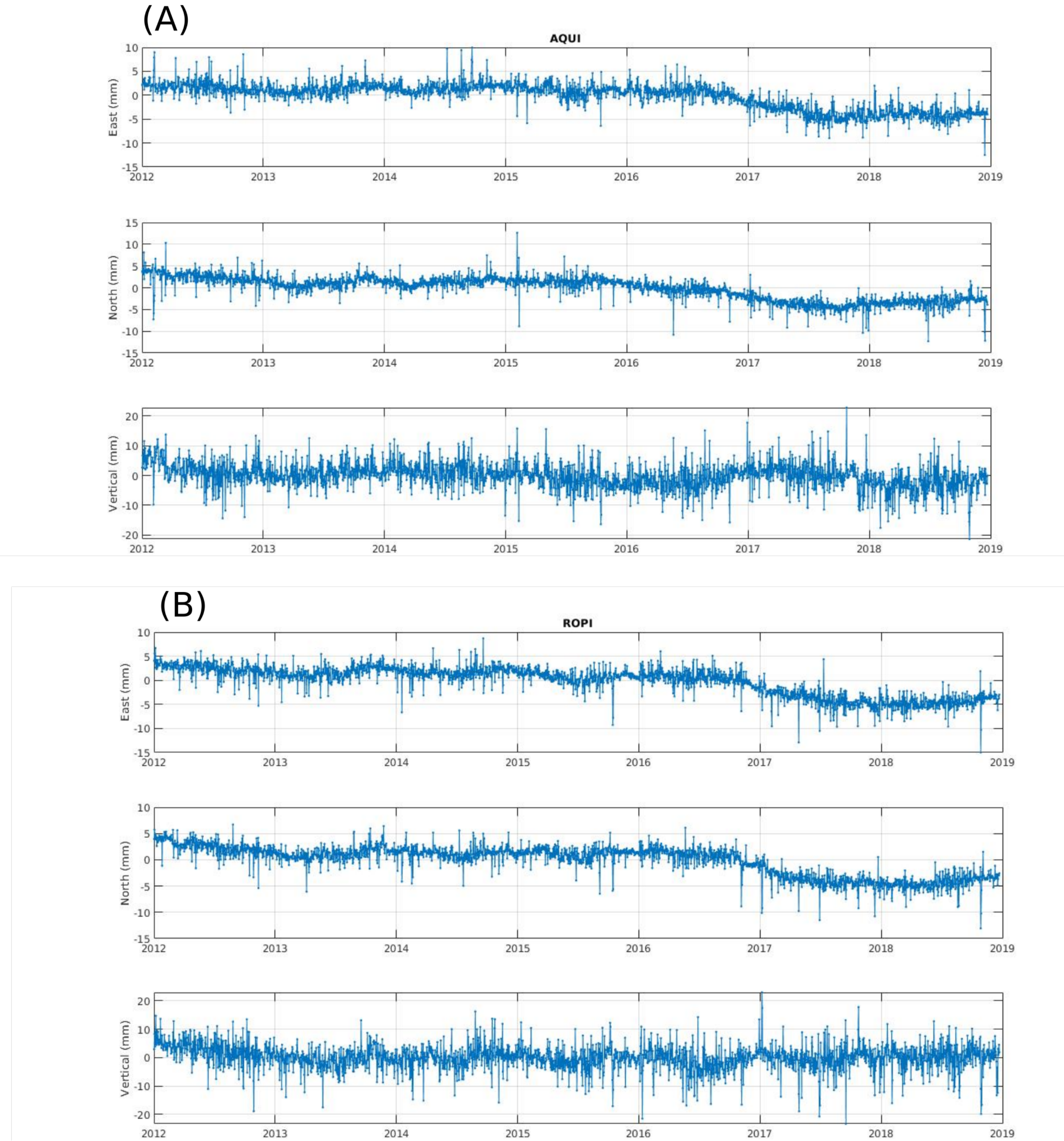

Figure 2.10. In Figure the residuals among the raw time series and the IC 2, 3, 4, for the GPS stations AQUI (A), ROPI (B). In the postseismic phase they show a mm-scale deformation prevalently SW-oriented, consistent with the direction and intensity of the spatial part of the IC1.

2.4 Postseismic relaxation

As it is shown in Figures 2.3a and 2.11, the relaxation following the mainshocks of the seismic sequence is represented by the first independent component with two distinct decays, the first following the Amatrice event and the second one following the Visso and Norcia events. The fact that we explain the whole postseismic phase through a single component indicates a limitation of the signal separations. As a matter of fact, from a physical point of view, three independent regions surrounding the corresponding mainshocks distributions are expected to be subjected to afterslip. As discussed in Section 2.3, an accurate separation among hydrological components and tectonic components is crucial. In order to separate the postseismic transients that we expect to follow the three mainshocks, we filter the time series removing the seasonal ICs (see Section 2.3) retrieved in the first analysis. Since we are focusing our attention on the postseismic phase only, we analyze the time span 2016-2019, and the vbICA is performed by fixing the number of ICs L=3 as suggested by an F-test. In the following images we show the results of this decomposition: the postseismic relaxation is still clear (IC1, Figure 2.12) and it explains the majority of the variance of the data ($\Sigma_1 = 1523$ mm); the second component (IC2, Figure 2.13) shows a non monotonic evolution that does not match with what we observe in the postseismic time series. Moreover its relative importance in explaining the data variance is limited ($\Sigma_2 = 403$ mm), therefore we neglect it as a contributing source of the postseismic relaxation. The IC3 (Figure 2.14) shows a periodical behaviour in its temporal part and for this reason we consider it as due to incomplete correction of the hydrological signals.

The re-analysis on the time series filtered from the hydrological components does not lead to a further extraction of postseismic ICs. Bearing in mind the limits of having only one IC representative of the whole postseismic relaxation, the first IC will be deeply analyzed in this Section and discussed in Section 2.5.

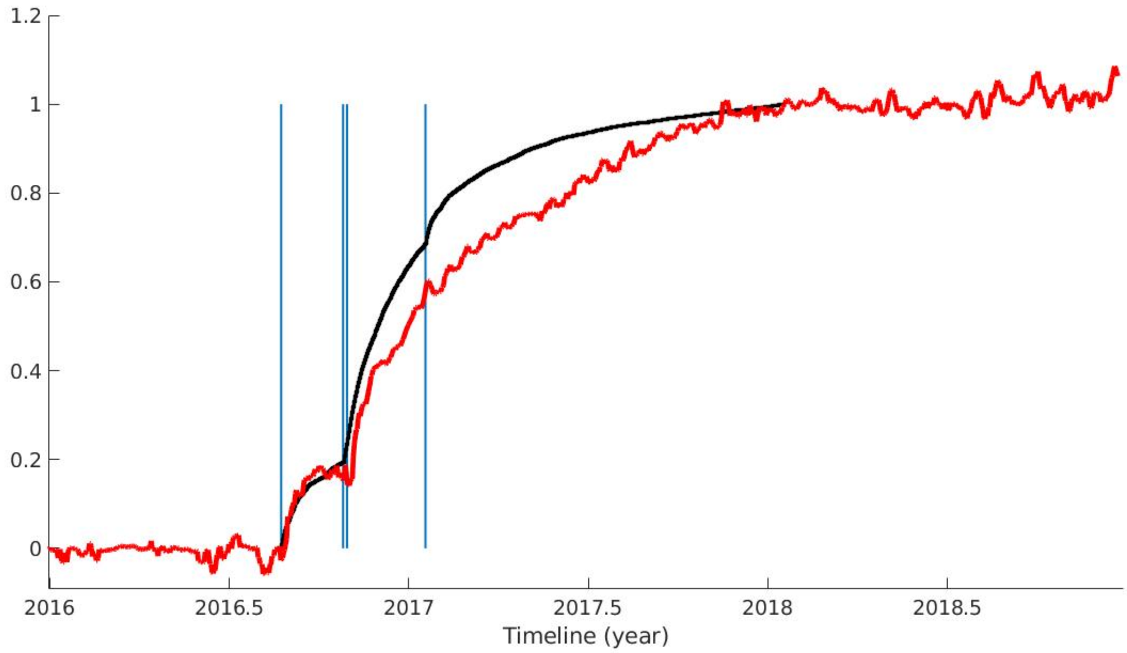

Figure 2.11. In Figure the normalized cumulative number of aftershocks from the catalogue described in Michele et al. (2020) (black line) and the normalized filtered postseismic evolution (red line). Vertical lines mark the epochs respectively of the Amatrice, Visso, Norcia and the January 2017 Campotosto earthquakes.

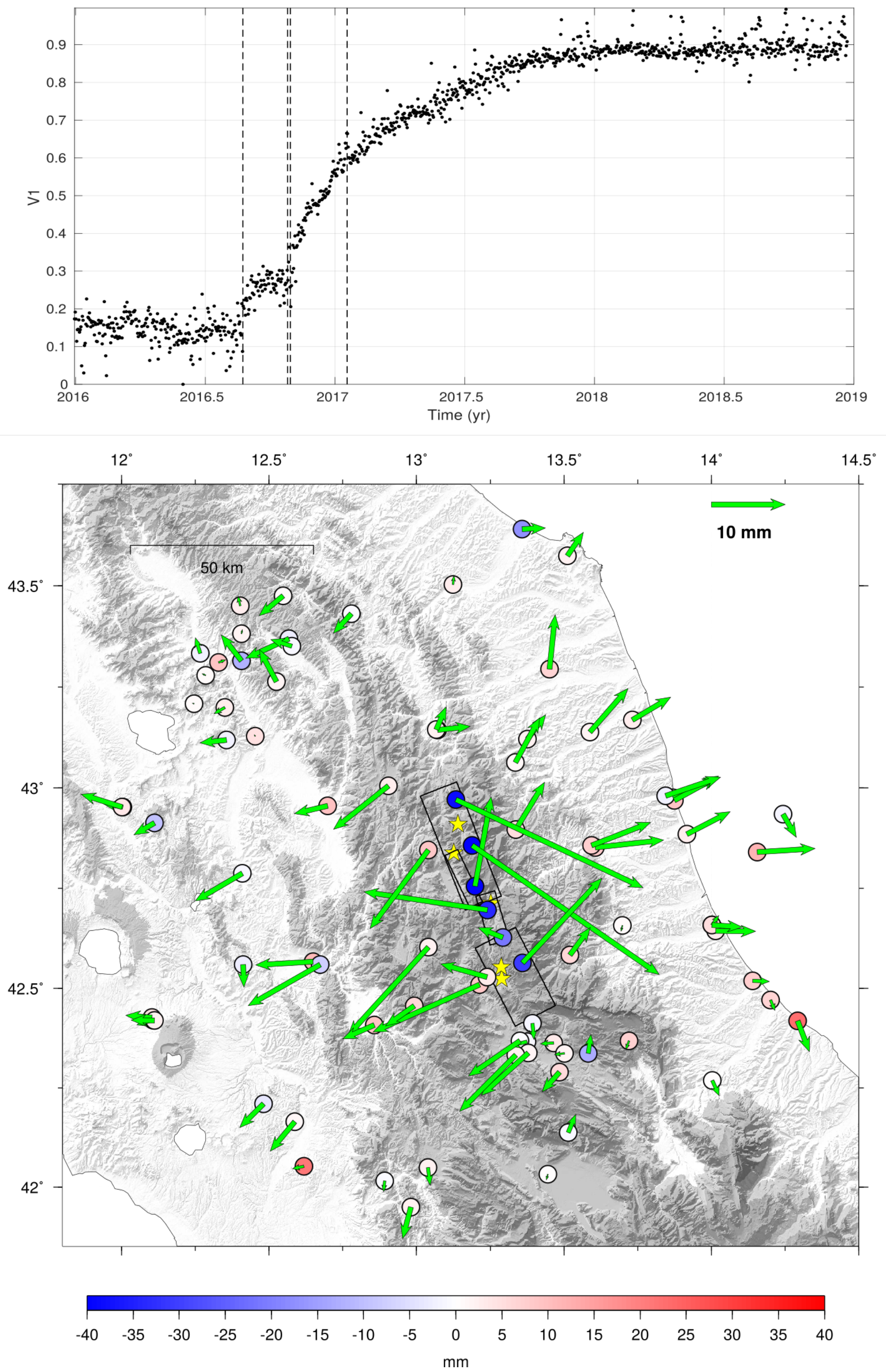

Figure 2.12. The IC1 (upper panel = temporal evolution, lower panel = spatial pattern) of the analysis on the postseismic phase of the time series filtered from the hydrological components. Yellow stars show the epicenters of the mainshocks while the black boxes show the location of the faults responsible for the 2016-2017 sequence as in Cheloni et al. (2017, 2019).

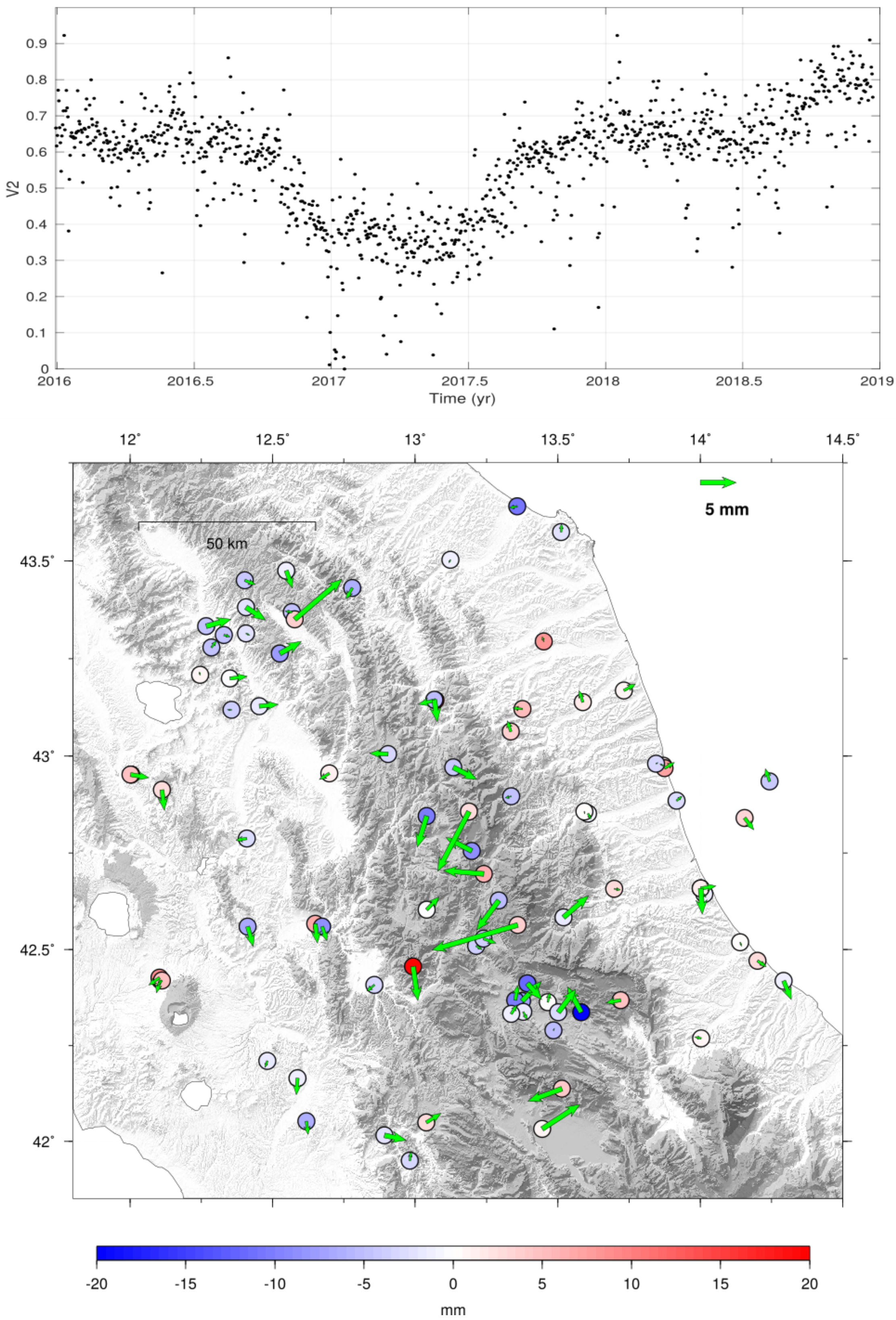

Figure 2.13. The IC2 (upper panel = temporal evolution, lower panel = spatial pattern) of the analysis on the postseismic phase of the time series filtered from the hydrological components.

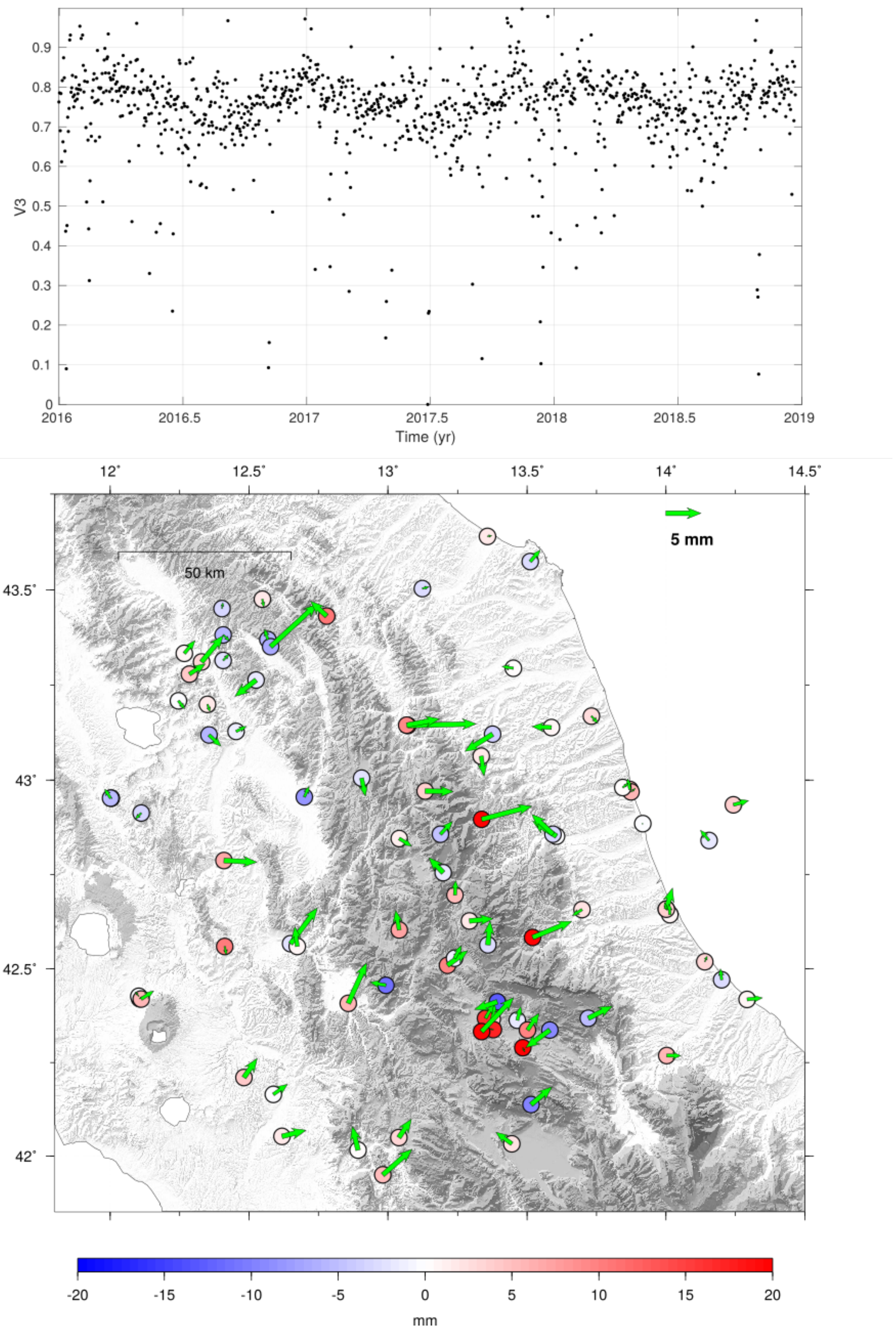

Figure 2.14. The IC3 (upper panel = temporal evolution, lower panel = spatial pattern) of the analysis on the postseismic phase of the time series filtered from the hydrological components.

2.4.1 Inversion method

A possible explanation of a postseismic relaxation process is given by the occurrence of afterslip on faults. Here we consider as primary faults those structures already introduced in Section 2.1, namely the M. Vettore fault, a fault antithetic to it, and the Laga Mountains fault (see also Figure 2.1). However, as already mentioned in Section 2.1, a univocal segmentation of this fault system does not exist in literature with some authors proposing co-seismic slip on just one fault plane (Cheloni, Falcucci and Gori, 2019; Xu et al., 2017), whereas others suggest the activation of multiple segments (Chiaraluce, Di Stefano, et al., 2017; Cheloni et al., 2017; Walters et al., 2018). Bearing also in mind the number of GNSS stations available, we follow the principle of finding the simplest solution, namely to keep the faults' geometry as simple as possible. Since in this study we are taking into account the four earthquakes of January 2017, we include in our model the Campotosto fault. We take as dip angles of the faults those of Cheloni et al. (2017, 2019), Walters et al. (2018). The northern master fault we consider, is similar to the M. Vettore fault from Cheloni et al. (2019), however it is furtherly extended northwards along the strike as seismicity suggests. We will refer to such a structure as to *M. Vettore fault*. As more recent studies (Cheloni, Falcucci, and Gori, 2019; Pousse-Beltran et al., 2020) suggest, the complex displacement pattern observed is better explained if we include in the modelization a fault antithetic to the M. Vettore. Hence we also include such fault, which shares the same dip and strike angles as in Cheloni et al. (2017, 2019) and Walters et al. (2018) but is extended northwards as suggested by seismicity. The southern master fault, modeled to include the four January 2017 events, gathers the Laga fault of Walters et al. (2018) (i.e., the Gorzano fault of Cheloni et al., 2017) and the Campotosto fault from Gualandi et al. (2014). We will refer to it as *Campotosto fault*. Vuan et al. (2017) and Michele et al. (2020) have shown that the extension at depth of these faults is bounded by a sub-horizontal thick layer of seismicity (i.e., the shear zone presented in Section 2.1) at about 10 km depth, which is in agreement with the thickness of the brittle crust estimated by Boncio et al. (2004) for this area. All the faults are discretized in grids of patches of about $2 \times 2\ km^2$.

The inversion approach we follow is the one proposed in Kositsky and Avouac (2010) and adapted to the ICA decomposition by Gualandi et al. (2016). In practice, we invert the spatial pattern relative to the postseismic IC and then we recombine the retrieved spatial slip distribution with the corresponding weight Σ and temporal function V. The linear system we are dealing with is described by the relation

$$d = U_1 = Gm \tag{2.3}$$

where the data vector d is the spatial deformation associated with the IC1, G stands for the Green's functions for the fault system, $m = (m_{strike}\ , m_{dip}\ )$ is the afterslip spatial distribution along the strike and the dip directions. For the inversion we follow the least squares formulation of Tarantola (2005) for linear problems:

$$m = m_0 + C_{m0}G^T(GC_{m0}G^T + C_d)^{-1}(d - Gm_0) \tag{2.4}$$

$$C_m = C_{m0} - C_{m0}G^T(GC_{m0}G^T + C_d)^{-1}GC_{m0} \tag{2.5}$$

where m_0 and C_{m0} represent respectively the a priori model (which is taken null as in Radiguet et al., 2011) and its covariance matrix, G are the Green's functions for a homogeneous elastic half-space, d is the data vector, and C_d the corresponding covariance matrix. Bearing in mind the tectonic setting of the area, we also impose a positivity constraint to account for a dip-slip mechanism ($m_{dip} \leq 0$). We follow, for the a priori model covariance matrix, the formalism of Radiguet et al. (2011), which considers the spatial correlation of slip on patches to decay exponentially: given two fault patches A and B at a distance d_{AB}:

$$C_{m0}^{AB} = \left(\sigma_m \frac{\lambda_0}{\lambda}^2\right) e^{-\frac{d_{AB}}{\lambda}} \tag{2.6}$$

where λ is the characteristic decay length, λ_0 is a scaling length factor fixed to the root square of the average of the patches' area, σ_m is a standard deviation of the a priori model parameters. The inversion needs to be regularized, namely we need to add information to artificially make the problem overdetermined, determining the values (λ , σ_m). Since (λ , σ_m) associated with each fault depend on the dimension of the fault itself, we can't find a unique pair of values representative of the whole fault system. Therefore we determine them seeking the best compromise between a physically acceptable solution (i.e., compatible with the tectonic setting) and the misfit with the data, and they resulted in a $\lambda = 2\lambda_0$ and a priori standard deviation σ_m= 0.71 for the M. Vettore and its antithetic fault and σ_m=1 for the Campotosto faults.

2.4.2 Inversion results

A first inversion attempt, carried out following the geometry and the methodology presented in Section 2.4.1, is reported in Figure 2.15. Here we notice a strong concentration of slip (up to 35 cm) on the southern edge of the Campotosto fault which is likely driven by the position of the GPS sites in the Paganica area with respect to the fault. Despite the presence of such concentration of slip, we notice that our model is not capable of reproducing the observations at the Paganica sites, which remain largely underestimated (Figure 2.15b). Hence, once the postseismic displacement associated with the sites in the Paganica area has been carefully checked (Section 2.3.3), we find that such displacement requires the inclusion of the Paganica fault in the inversion.

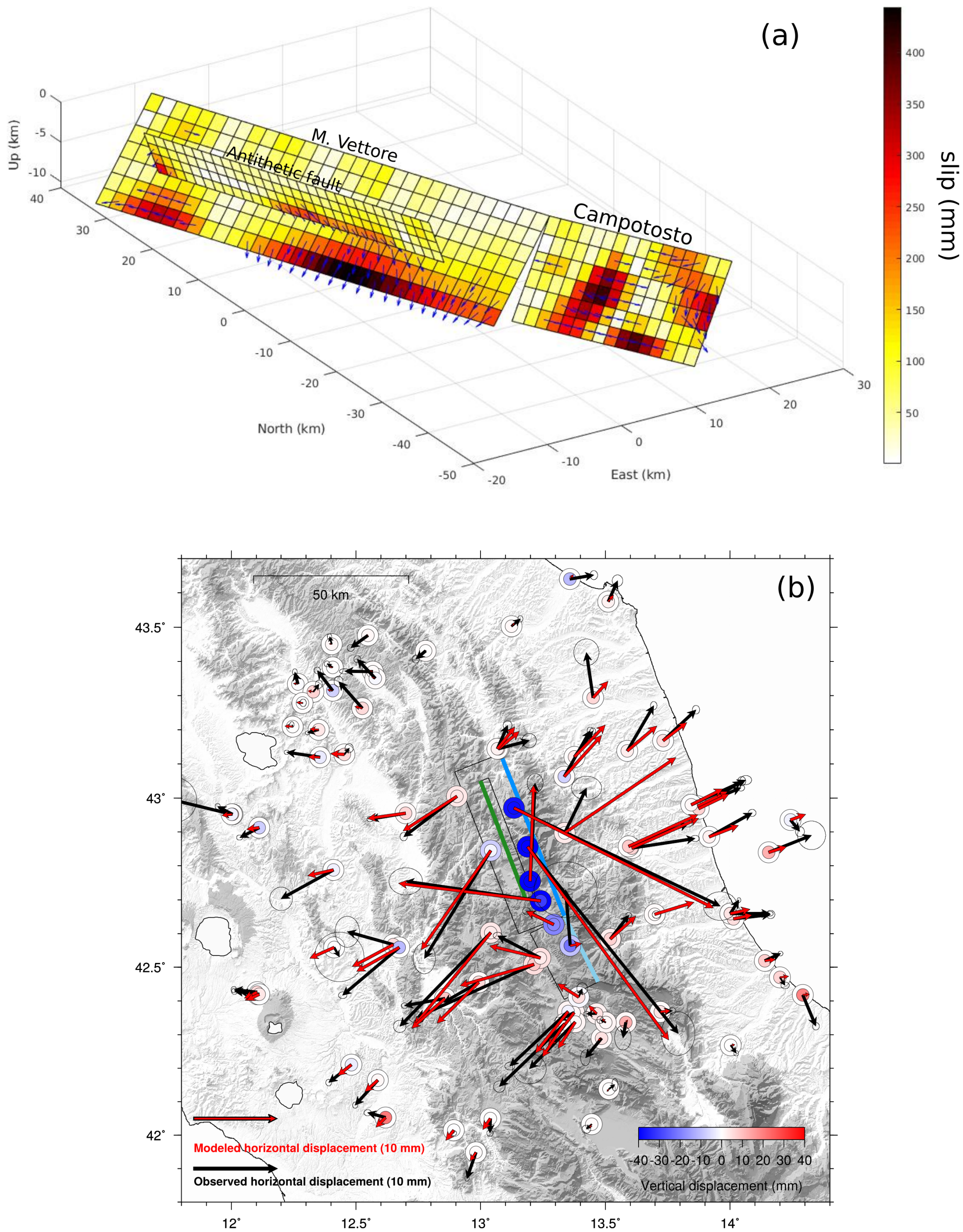

Figure 2.15. (a): Slip distribution on the M. Vettore fault, the antithetic fault and the Campotosto fault; (b): map of the data modelization for the inversion with the Paganica fault not included.

The included Paganica fault follows the Gualandi et al. (2014)s' geometry, and we choose the same regularization parameters as for the Campotosto fault (see Section 2.4.1).

In Figure 2.16 we report the afterslip distribution obtained. We notice a generally satisfying data reproduction, with an almost perfect reconstruction of the displacement pattern in the epicentral area, and a weaker agreement at farther GPS sites. This model shows the occurrence of slip on the deepest portion of the M. Vettore fault below the co-seismic ruptures of the Amatrice and Norcia events, with slip up to 40 cm and a prevalent normal mechanism (Figure 2.16a), while below the Visso area transcurrent slip reaches up to $\sim 25 - 30$ cm. Contextually the antithetic fault, where a Mw 5.4 event occurred one hour after the Amatrice main event (Chiaraluce, Di Stefano, et al., 2017), accommodates normal slip (~ 25 cm) in its deepest part, at the intersection with the M. Vettore main fault. The Campotosto fault accommodates up to 25 cm of slip about 10 km south of the town of Amatrice and, with a similar intensity, about 10 km southwards. Interestingly, this model suggests the presence of aseismic slip on the northernmost edge of the Paganica fault, which ruptured during the 2009 L'Aquila earthquake in a different area as shown in Figure 2.16d (Gualandi et al., 2014; Ragon et al., 2019).

We notice from Figure 2.16 that afterslip on the faults considered is not sufficient to explain the ~ 2.3 years cumulative displacement recorded by the whole GPS network. In fact, although the postseismic displacement measured at stations farther from the epicentral area seems to have a signal to noise ratio > 1 (see error ellipse in Figure 2.4), they generally result to be underestimated by this model. In order to better point out such a general underestimation, we proceed as follows. We solve the forward problem relative to a 60 km long, 10 km deep, rectangular fault plane uniformly slipping by 1 m and embedded in a homogeneous elastic half-space. This dislocation represents an along-strike extension of the major structures described in Cheloni et al. (2017, 2019), centered on the seismicity pattern that followed the seismic sequence (Figure 2.17). The calculated displacement at the GPS locations basically consists in the Green's function response, and it is made of a three components vector per station j: $G_j = [G_{je}, G_{jn}, G_{ju}]^T$, $j = 1, ..., N_{stn}$. We compare the L2 norm of such vector normalized by the maximum value retrieved for all the stations, $g_j = \frac{|G_j|}{max\{|G_i|\}_{i=1}^{Nstn}}$ for $j = 1, ..., N_{stn}$, with the normalized L2 norm relative to the spatial postseismic response at the studied stations, $u_j = \frac{|U_j|}{max\{|U_i|\}_{i=1}^{Nstn}}$ for $j = 1, ..., N_{stn}$. In order to better identify the GPS sites that are most affected by the slip on the fault (i.e. near field stations) we consider a local reference frame with origin in the center of the rectangular plane used for the forward model. We define the horizontal plane by the x-axis parallel to the fault strike and the y-axis perpendicular to it. In Figure 2.17b we plot g (blue) and u (orange) with respect to the distance (from the origin) normalized to a characteristic length for x-axis (the half length of the fault trace, i.e. 30 km) and the y-axis (two times the depth of fault, i.e. 20 km). This normalization is chosen to take into consideration not only the main deformation signal along the extensional direction, but also a possible heterogeneous elastic response along the strike direction due to the complex faults system involved. We observe that the two signals show spatial decays that differ from each other for normalized distances greater than 2. For such distances u is systematically higher than the elastic response g, suggesting that the displacement recorded at these GPS sites cannot be described solely by afterslip. We therefore consider this threshold value of normalized distance equal to 2 in order to distinguish GPS sites into two groups: i) the near field group, for distances less than the threshold value and ii) the far field group, for greater distances (Figure 2.17). Displacement at GPS sites belonging to the latter group cannot be explained purely by an elastic mechanism, and this fact remains true despite the strong concentration of afterslip on the deepest patches of the high angle faults (Figure 2.16).

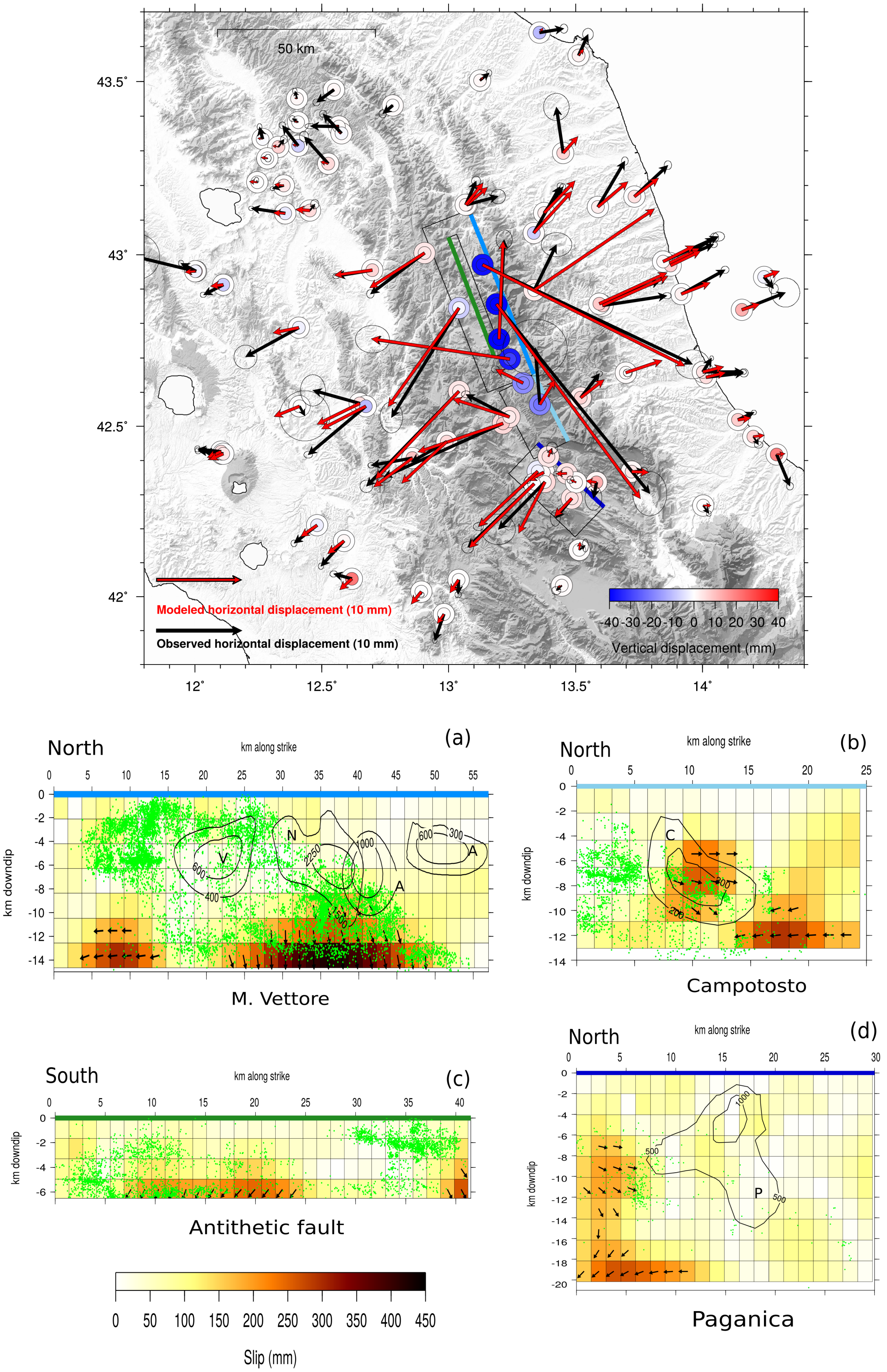

Figure 2.16. (Caption next page.)

Figure 2.16. Map: black and red arrows represent respectively the observed and the modeled horizontal postseismic cumulative displacement on the 24^{th} of August 2016 - January 2019 time interval, whereas inner and outer circles represent respectively the observed and the modeled vertical postseismic cumulative displacement. Solid lines show the surface projection of the high faults described in Section 2.4.1. The faults' traces are coloured as in panels (a, b, c, d) which show the afterslip distribution on the M. Vettore, Campotosto, antithetic and Paganica faults, respectively, in a strike-dip reference system (slip in mm). Co-seismic contours on the M. Vettore fault are from Cheloni et al. (2017, 2019), on the Campotosto fault from Cheloni et al. (2019a), on the Paganica fault are from Gualandi et al. (2014).

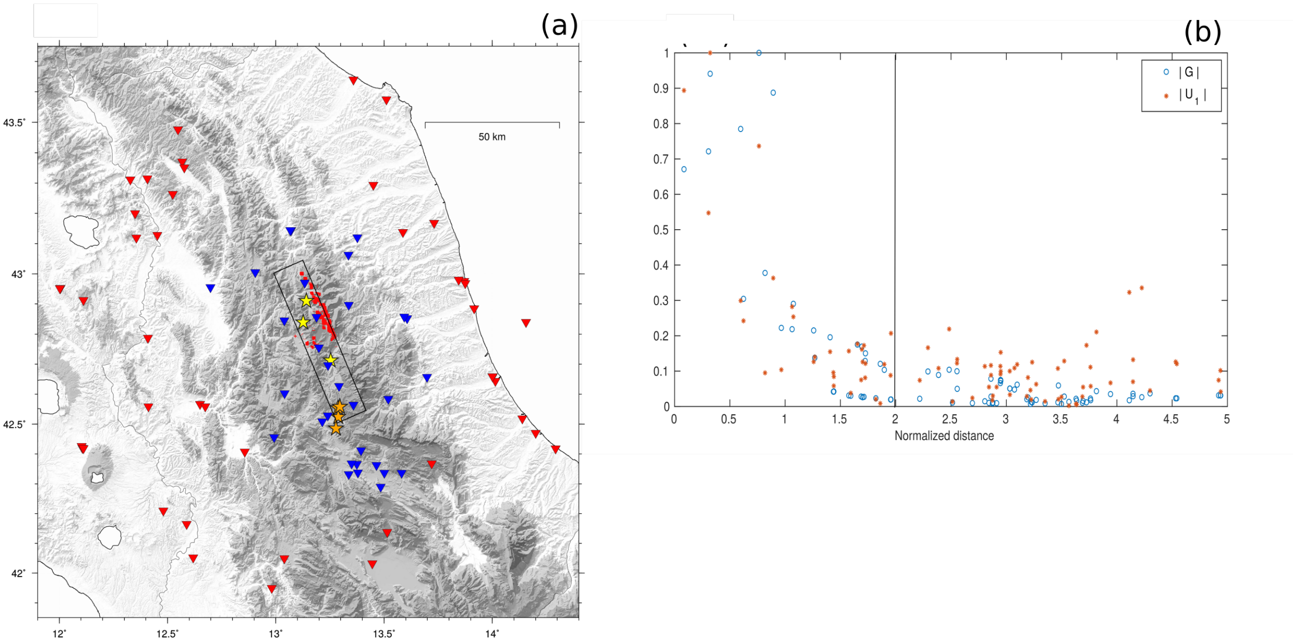

Figure 2.17. Panel (a) shows the near field and far field GPS stations' position (respectively blue and red triangles), the Amatrice, Visso and Norcia earthquakes (yellow stars) and the January 2017 Campotosto events (orange stars). The black rectangle represents the fault used to distinguish stations in the near field from those in the far field. Panel (b) shows g (blue circles) and u (orange dots) vs the normalized distance. The vertical line marks the threshold distance.

2.4.3 Afterslip on the Shear zone

As many authors show (e.g., Chiaraluce, Di Stefano, et al., 2017; Michele et al., 2020), the $\sim 2-3$ km-thick subhorizontal layer of seismicity (i.e., the shear zone) played an important role during the seismic sequence. Vuan et al. (2017) suggest that aftershocks nucleating within such volume may be triggered by afterslip and Pousse-Beltran et al. (2020) infer a possible contribution of the shear zone to the displacement field, though eventually they do not include it in their model. To further investigate the role played by the shear zone during the postseismic phase, we repeat the procedure to invert the displacement data described in Section 2.4.1, taking into account the shear zone modeled as two planar surfaces. We follow the model proposed in figure 10b of Michele et al. (2020) and in figure 1 of Vuan et al. (2017). Accordingly, the shear zone consists of a ramp-flat fault divided in a low-angle east dipping plane and an almost flat detachment, respectively east and west of the Apennines chain, and the two surfaces are discretized into patches of about 3x3 km^2 (Figure 2.18e, f; Figure 2.19b)

Taking into account the shear zone in the inversion of the data, slip on the four high angle faults (Figure 2.16) does not result to be concentrated on the deeper patches only but it is found on shallower patches as well, around the areas co-seismically activated. This proves to be particularly true for the M. Vettore and its antithetic fault (Figure 2.18a and c), where afterslip is more distributed and its maximum intensity is reduced to ~ 20 cm. On the other hand, according to this second model, the Campotosto and Paganica faults accommodate a smaller amount of slip, but the inclusion of the shear zone in the inversion does not substantially change the areas that slipped aseismically (Figure 2.18b and d). In Figure 2.20 we directly compare the slip distribution retrieved in Section 2.4.1 and 2.4.3.

The western, flat, part of the shear zone accommodates slip in an area coinciding with the down-dip prosecution of the M. Vettore fault slipping area, reaching up to ~ 10 cm of slip on its deepest border (Figure 2.18e). We observe an afterslip concentration on the deepest portion of the eastern part of the shear zone as well (Figure 2.18f) with maximum slip $\sim 18-20$ cm.

Regarding the capability of this model of reproducing the data measured (Figure 2.19a) we observe a slight better reproduction of the displacement for some near field sites. A direct comparison between the data reconstruction of this model and the model presented in Section 2.4.2 is shown in Figure 2.21. As regards the far-field stations, on the Adriatic side we observe an improvement in the fit (WRMSE improvement $\sim 16.5\%$, see Table 2.3) while a much lower improvement is observed for far-field sites on the Thyrrenian side (WRMSE improvement $\sim 0.5\%$, Table 2.3). If on the one hand the fit to the data on the whole data set results to be globally improved (WRMSE improvement $\sim 6\%$, Table 2.3), on the other hand the resolution matrix is generally low. As Figure 2.22 shows, we obtain values > 0.2 only on patches close to the GPS sites, as expected. Computing the restitution matrix, we observe that the majority of patches has values

> 1 (Figure 2.23). We can conclude that the postseismic displacement pattern cannot be explained even by complicated models such as the one presented in this Section. Keeping in mind the structural constraints imposed on the geometry of the tectonic structures, we believe that our results indicate a possible viscoelastic relaxation to contribute to the geodetic displacement.

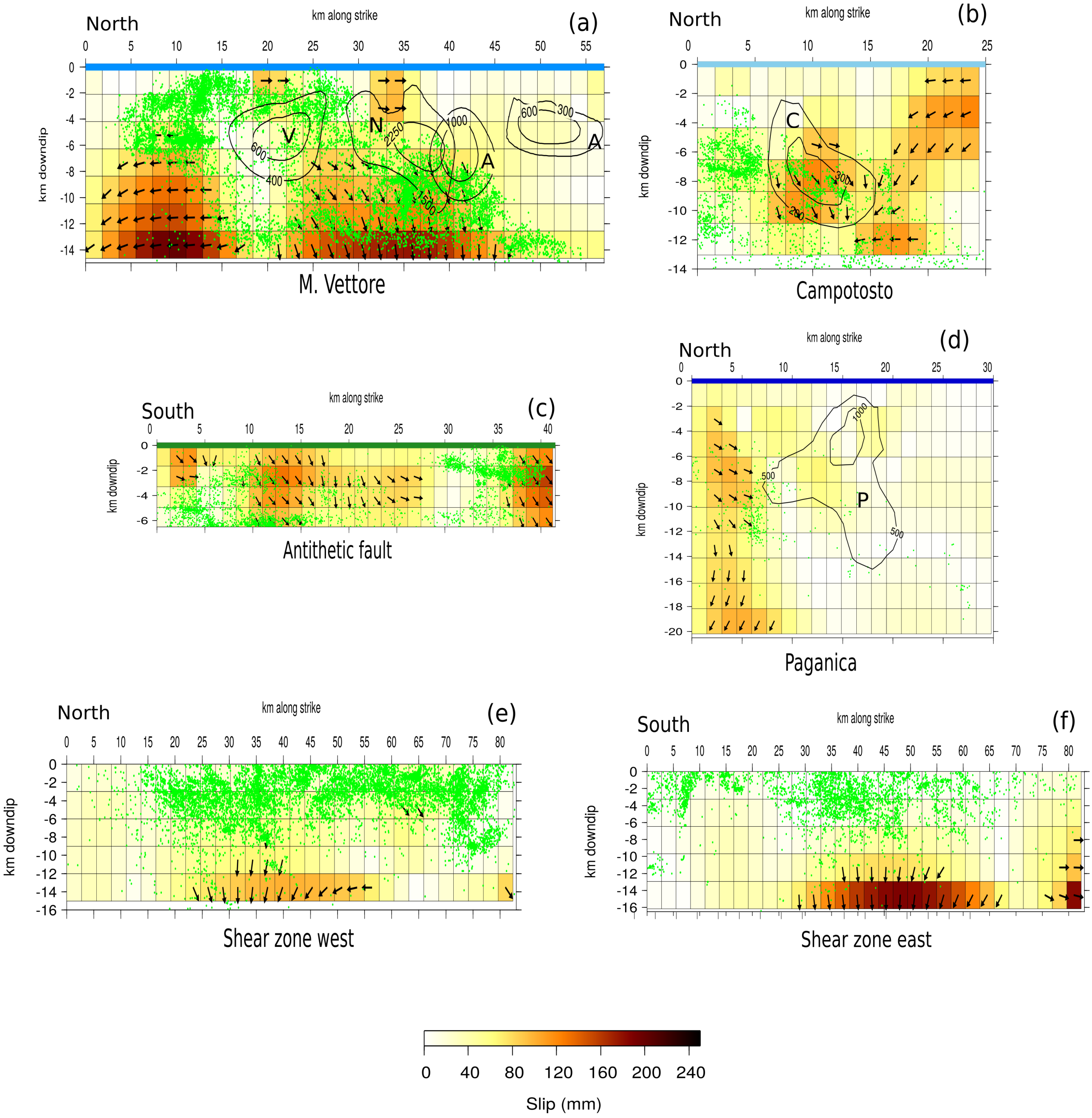

Figure 2.18. Panels (a, b, c, d) show the afterslip distribution respectively on the M. Vettore, Campotosto, antithetic and Paganica faults in a strike-dip reference system. Panels (e) and (f) show the afterslip distribution on the western and eastern segments of the shear zone (slip in mm). Co-seismic contours on the M. Vettore fault are from Cheloni et al. (2017, 2019), on the Campotosto fault from Cheloni et al. (2019a), on the Paganica fault are from Gualandi et al. (2014).

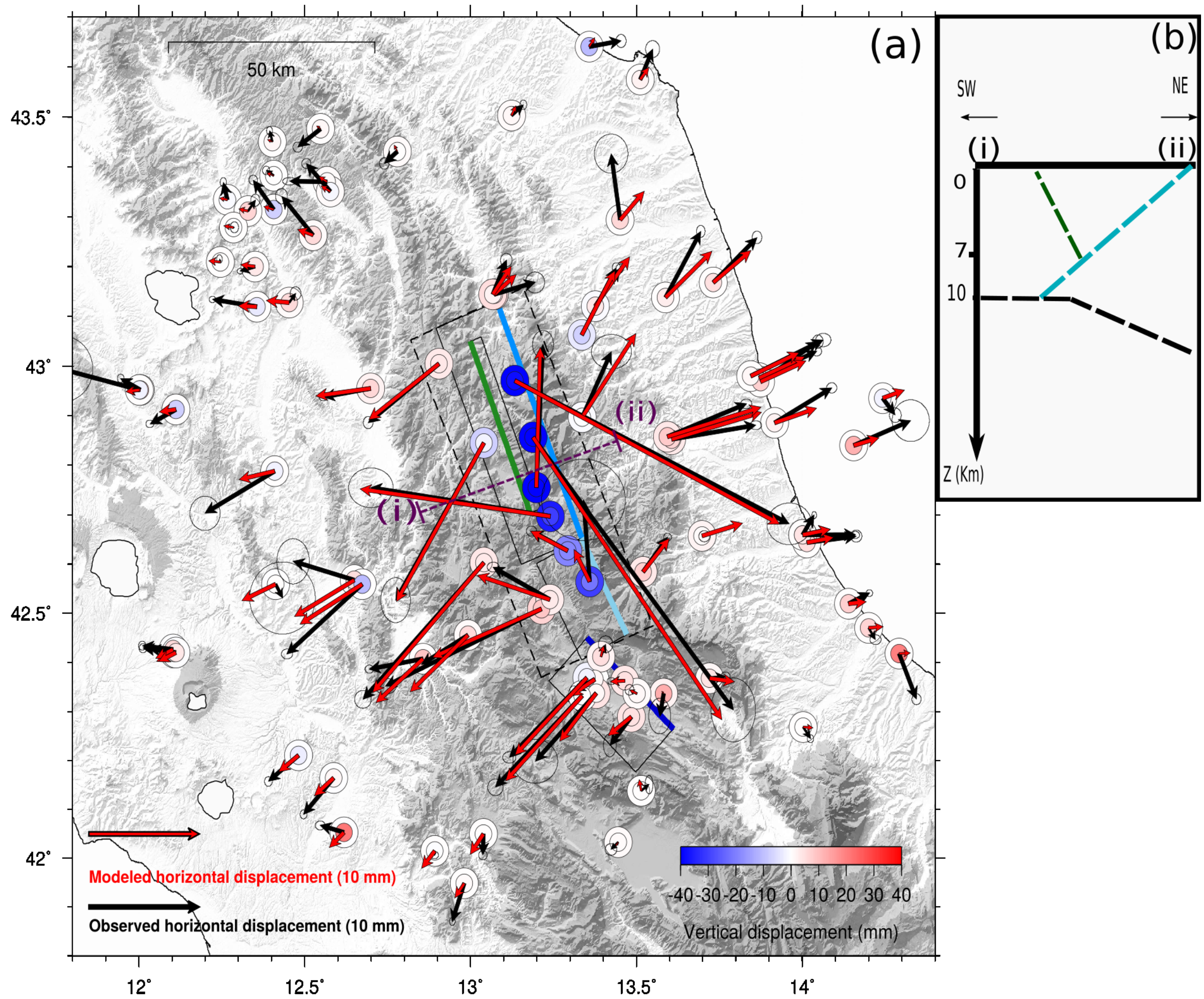

Figure 2.19. (a): black and red arrows represent respectively the observed and the modeled horizontal postseismic cumulative displacement, whereas inner and outer circles represent respectively the observed and the modeled vertical postseismic cumulative displacement. Solid lines show the surface projection of the high faults described in Section 2.4.1 and dashed lines the surface projection of the shear zone as described in this Section. The faults' traces are coloured as in panels (a, b, c, d) of Figure 2.18. (b): we show a cross-section of the fault system along the (i)-(ii) line.

Model	$WRMSE_{tot}$	$WRMSE_E$	$WRMSE_W$	$WRMSE_{N.F.}$
Section 2.4.2	429 mm	181 mm	181 mm	67 mm
Section 2.4.3	405 mm	151 mm	180 mm	74 mm

Table 2.3. Weighted root mean square error (WRMSE) for the two afterslip models described in Section 2.4.2 and 2.4.3. WRMSE are computed on the cumulative postseismic displacement in the time span 25^{th} of August 2016 - 2019 on the whole dataset ($WRMSE_{tot}$), on the two subsets of GPS stations east and west of the fault system (respectively $WRMSE_E$ and $WRMSE_W$) and on the near field GPS stations $WRMSE_{N.F.}$.

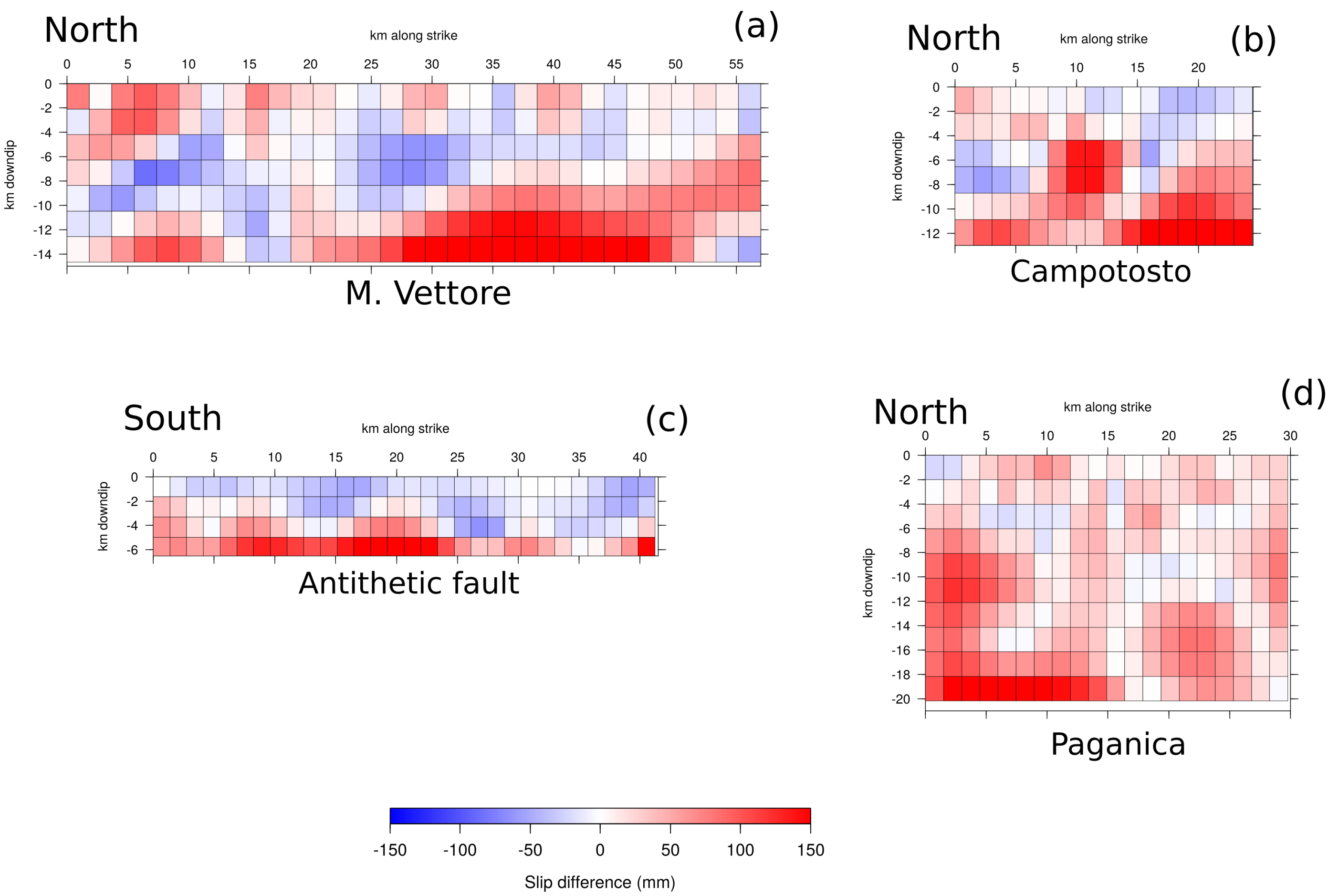

Figure 2.20. Figure shows the difference of slip magnitude (in mm) between the afterslip solutions of Section 2.4.1 and 2.4.3 in a strike-dip reference system for (a) the M. Vettore, (b) the Campotosto, (c) the antithetic fault and (d) the Paganica fault.

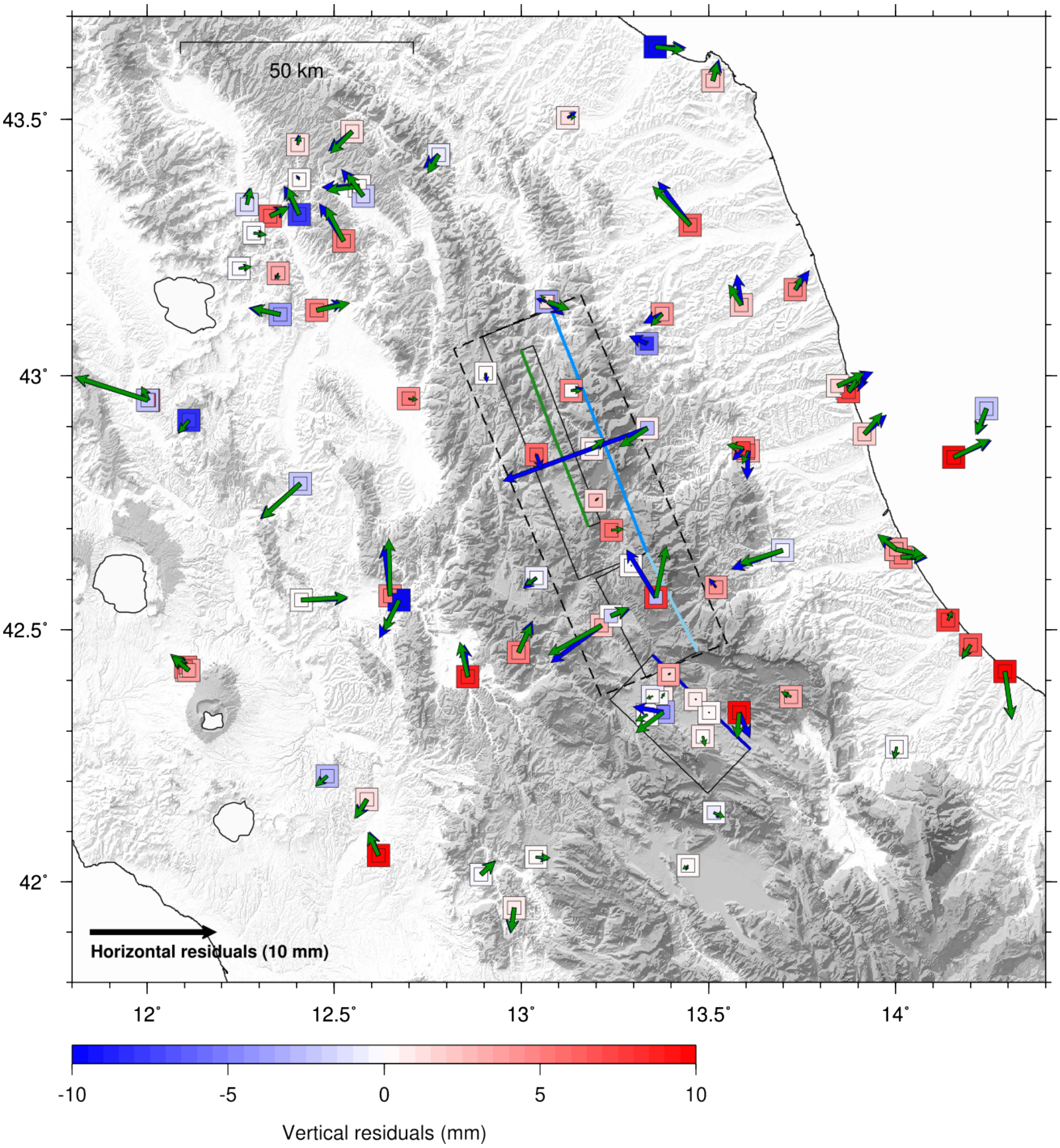

Figure 2.21. In map the residuals between the observed and the modeled horizontal (arrows) and vertical (squares) components of the postseismic cumulative displacement are shown. Blue arrows and inner squares represent the model without the shear zone; green arrows and outer squares represent the model with the shear zone included.

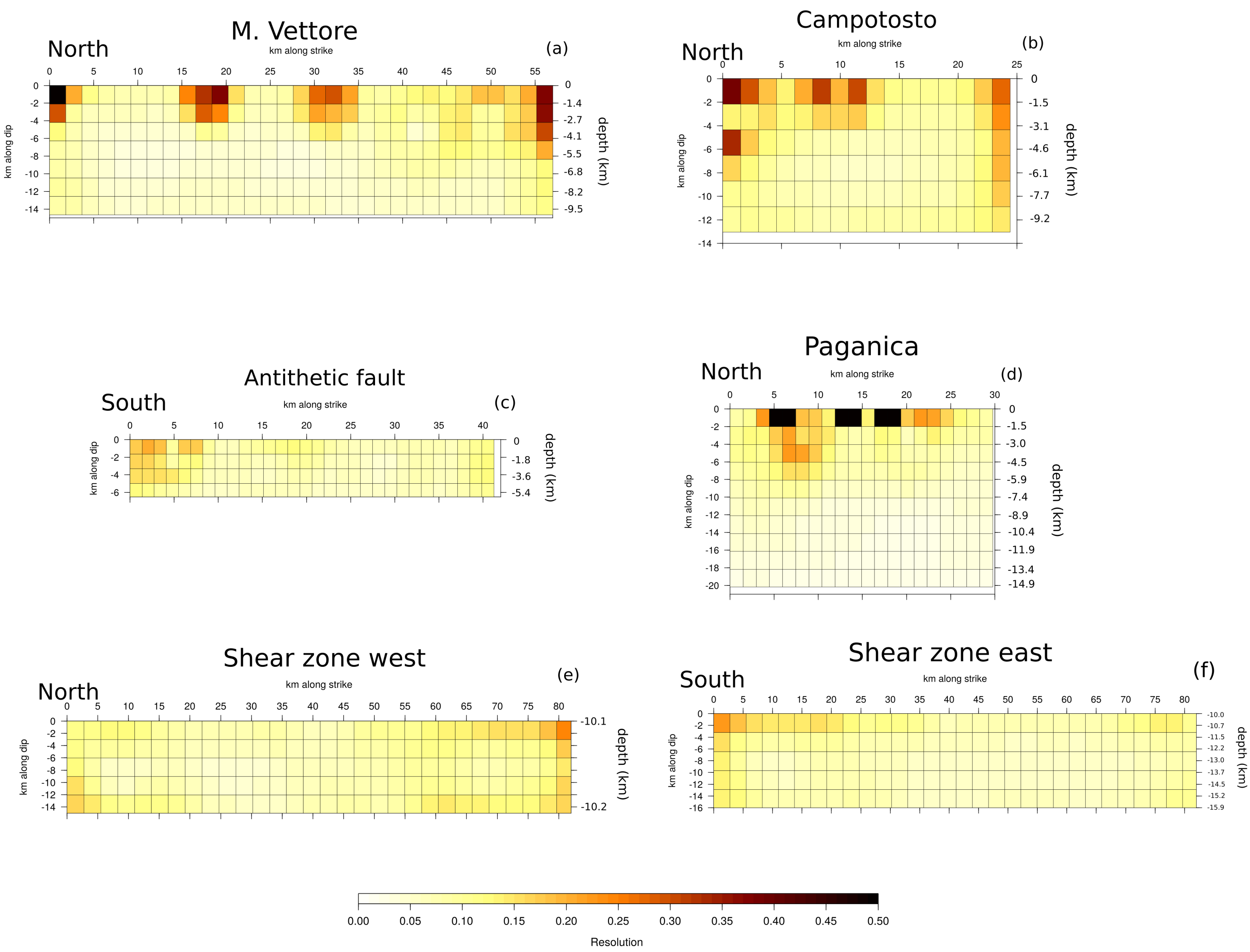

Figure 2.22. The resolution of the inversion of Section 2.4.3 for the M. Vettore fault (a), Campotosto fault (b), antithetic fault (c), Paganica fault (d), western (e) and eastern (f) side of the shear zone.

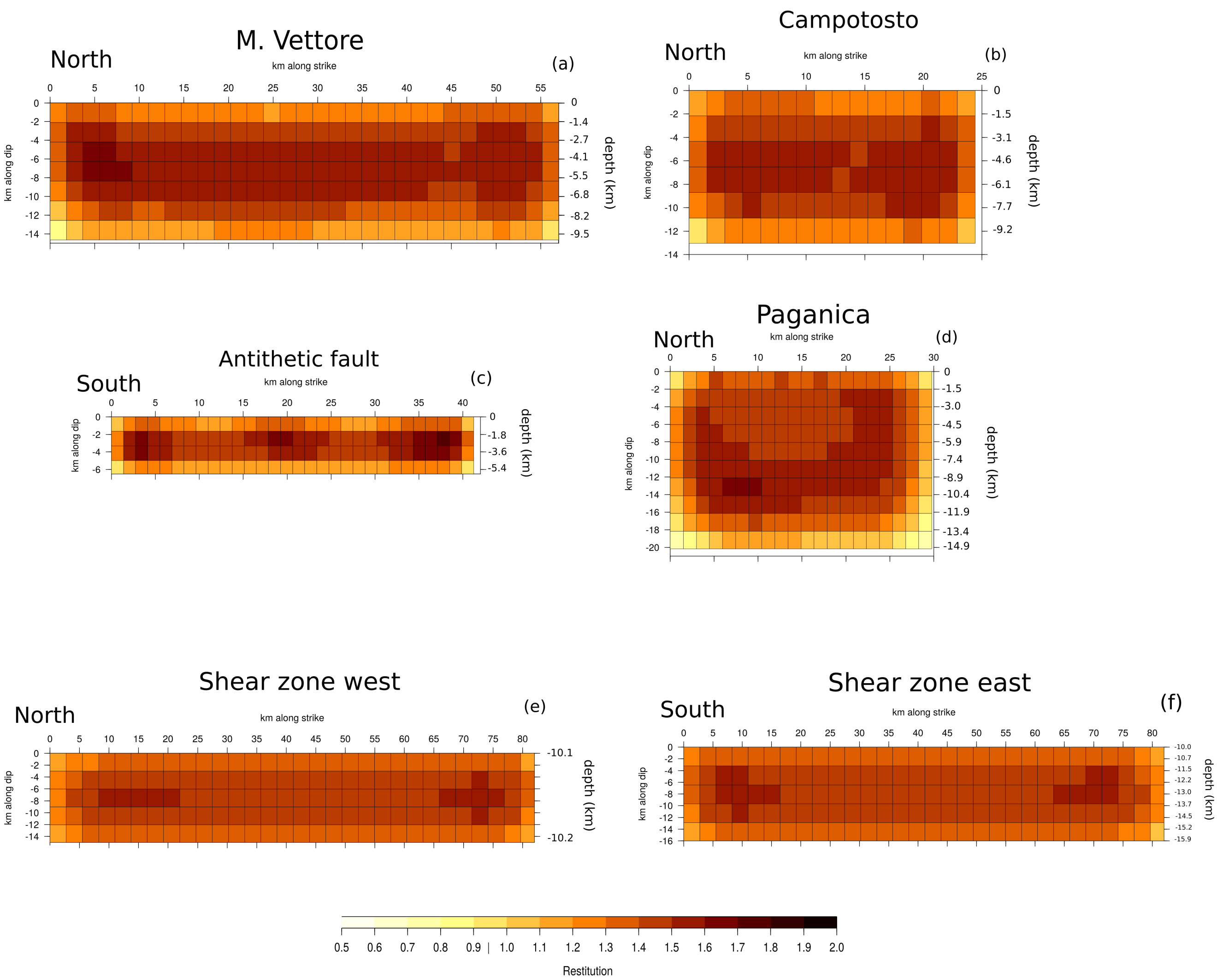

Figure 2.23. The restitution of the inversion of Section 2.4.3 for the M. Vettore fault (a), Campotosto fault (b), antithetic fault (c), Paganica fault (d), western (e) and eastern (f) side of the shear zone.

2.4.4 Viscoelastic relaxation

As we showed in Section 2.4.3, displacement at far-field GPS sites results to be generally underestimated (Figure 2.19b), and large amount of slip occurs on the deepest patches of the fault planes (Figure 2.19a). As claimed for the Colfiorito seismic sequence investigated by Riva et al. (2007), afterslip occurring at the base of the seismogenic layer might be symptomatic of a rheological discontinuity between the brittle upper crust and the underlying layers. We will refer to such a it as to *brittle-ductile transition*. Moreover, as it has already been described in literature (e.g. Perfettini and Avouac, 2007) a correlation in time between afterslip and the cumulative number of aftershocks exists. Looking at Figure 2.11, for the A-V-N seismic sequence, this correlation holds up to a few months after the 30^{th} of October earthquake only, thus supporting the hypothesis of further postseismic mechanisms acting after the Norcia earthquake besides afterslip.

Hence, following also previous authors (Pousse-Beltran et al., 2020), we study the contribution of the viscoelastic lower crust and upper mantle to the displacement field. In order to do that, we employ the open-source software RELAX 1.0.7 (Barbot and Fialko, 2010), modeling the simplified case of an initial stress perturbation produced solely by the Norcia Mw 6.5 event. We here consider the coseismic slip distribution as modeled by Cheloni et al. (2019). Considering the length of the time series available ($\sim$ 2 years after the mainshocks), and the few mm per year relaxation rates typically induced by moderate earthquakes (Riva et al., 2007), we test a viscoelastic model described by Maxwell rheologies, being aware of the relevance of power-law rheologies in controlling viscoelastic relaxation (e.g. Freed and Burgmann 2004). We implement a profile consisting of a brittle upper crust characterized by the elastic parameters $\lambda = \mu = 30$ GPa, which is situated over a viscelastic lower crust and upper mantle (this latter at 33 km depth, Pousse-Beltran et al., 2020). A key problem when using stress-driven viscoelastic relaxation models to investigate surface deformations is to match the observed far field data without overestimating the near field data. As showed by Freed et al. (2006), too low viscosities and/or too thick viscoelastic layers can easily match the far field data but they easily overshoot the near field observations (and vice versa). We show in Figure 2.24 the temporal evolution predicted by a forward model which takes $\eta_{lc} < 10^{18}$ Pa s, for (a) CAMR, (b) PREC, (c) FOL1 and (d) CESI sites. Low viscosities produce non-monotonic displacement time series, that are not representative of the postseismic evolution observed. Furthermore, the relaxation time in the order of 0.1 yr would produce a cm-scale postseismic relaxation, which is not justified by our data. Therefore we infer, for the lower crust, viscosity values in the range of $10^{18} < \eta_{lc} < 10^{19}$ Pa s, and we fix it to the average value of $\eta_{lc} = 5 \times 10^{18}$ Pa s. As already found by Riva et al. (2007), due to its deep position and high viscosity, the effect of the mantle on our surface measurements is hardly observable. We fix the viscosity for this layer to $\eta_m = 10^{21}$ Pa s.

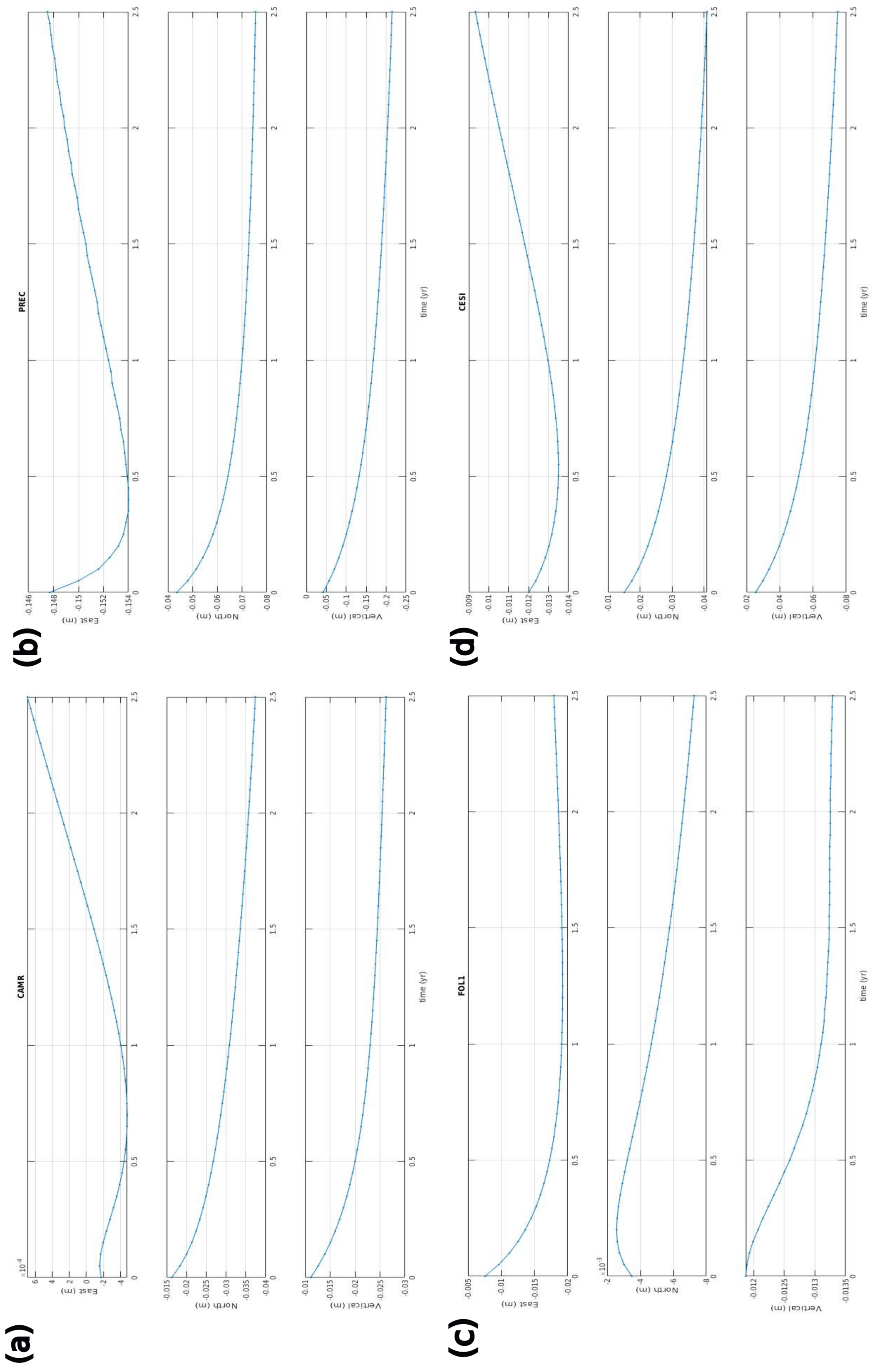

Figure 2.24. (Caption next page.)

Figure 2.24. In Figure the east, north and vertical displacement time series (respectively upper, central and lower panels) produced by the model with $\eta_{lc} = 10^{17}$ for (a) CAMR, (b) PREC, (c) FOL1 and (d) CESI GPS sites. Displacement is in meters while time is in years measured from the Norcia earthquake epoch.

As it is proposed by various seismological studies (e.g. Tesauro et al., 2008; Di Stefano et al., 2009; Molinari and Morelli, 2011; Molinari et al., 2015), the upper crust in the central portion of the Apennines gets thicker moving eastwards, i.e. moving from the Tyrrhenian side up to the Adriatic side. This is in agreement with the eastward deepening of the brittle-ductile transition proposed by Carminati et al. (2001), Carannante et al. (2013), Vuan et al. (2017), and modeled by Albano et al. (2020). We try to model this characteristic, implementing a second model with variable thickness of the upper crust: we fix the brittle-ductile transition at a depth of 11 km on the western side of the Apennines, below which it increases to 15 km of depth, affecting the entire eastern side (Figure 2.25b). The map in Figure 2.25 shows the horizontal displacement field that the viscoelastic lower crust produces, for a variable (red arrows) and constant (blue arrows) brittle-ductile transition depth. Notably, in the $\sim$ 2 years after the mainshock the cumulative vertical displacement resulting from these models ($\sim$ 3 mm) is below the threshold of detection of GPS for all the sites away from the epicentral area and it is therefore not represented in Figure 2.25. As it can be observed, the two models are equivalent on the Adriatic side and consistently they produce the same effect at far field GPS sites. The displacement produced is consistent with the direction of the IC1. On the other hand, on the west of the M. Vettore fault the constant-thickness model provides smaller displacements both in near and far field, coherently with a less thick lower crust. From our modeling, we can conclude that the simplest model (i.e., the one with the constant brittle-ductile transition) provides the best compromise between the near field and the far field observations, namely to justify the missing displacement at far field stations while not overshooting near field data which are satisfactorily reproduced through afterslip (see Figure 2.19). In Figure 2.26 we show the summation of the displacement produced by the afterslip model (as in Figure 2.18) and the viscoelastic model with constant brittle-ductile transition depth (Figure 2.25a). Even though a fully coupled afterslip-viscoelastic inversion would produce more accurate results, we find that such a simple model explains a relevant part of the total elastic plus viscoelastic displacement at far field stations, accounting for a mean value of the ratio of displacement modeled through viscoelastic relaxation and total displacement = 22%.

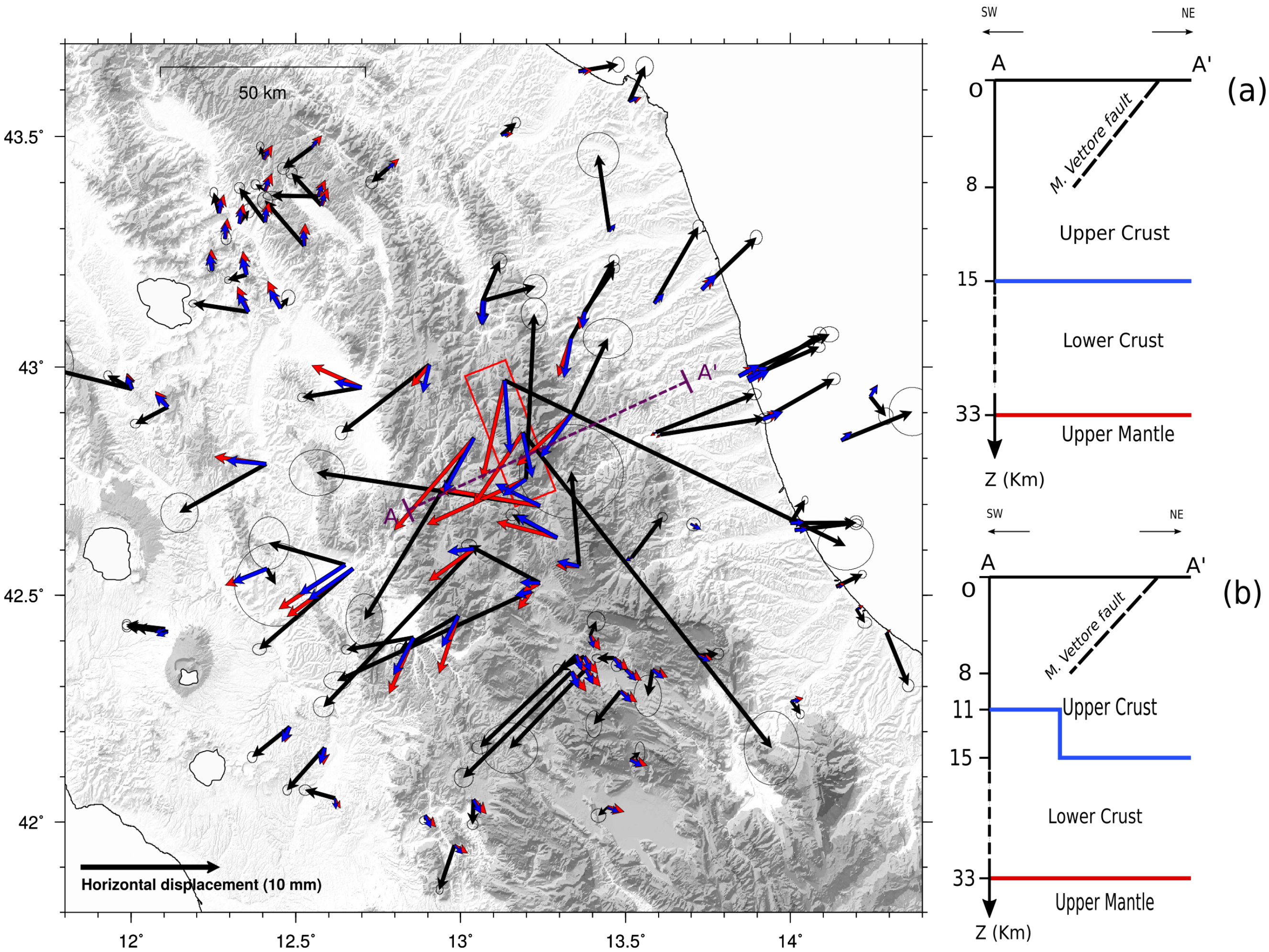

Figure 2.25. In map we compare the postseismic IC (black arrows) and the viscoelastic relaxation field after 2.1 years from the 30^{th} of October Norcia mainshock (blue arrows for the model with a constant brittle-ductile transition's depth, red arrows for the model with a variable transition depth). The red box marks the surface projection of the (Cheloni et al., 2019)s' masterfault. (a) and (b): cross sections along the AA' line respectively for the model with constant and variable brittle-ductile transition's depth.

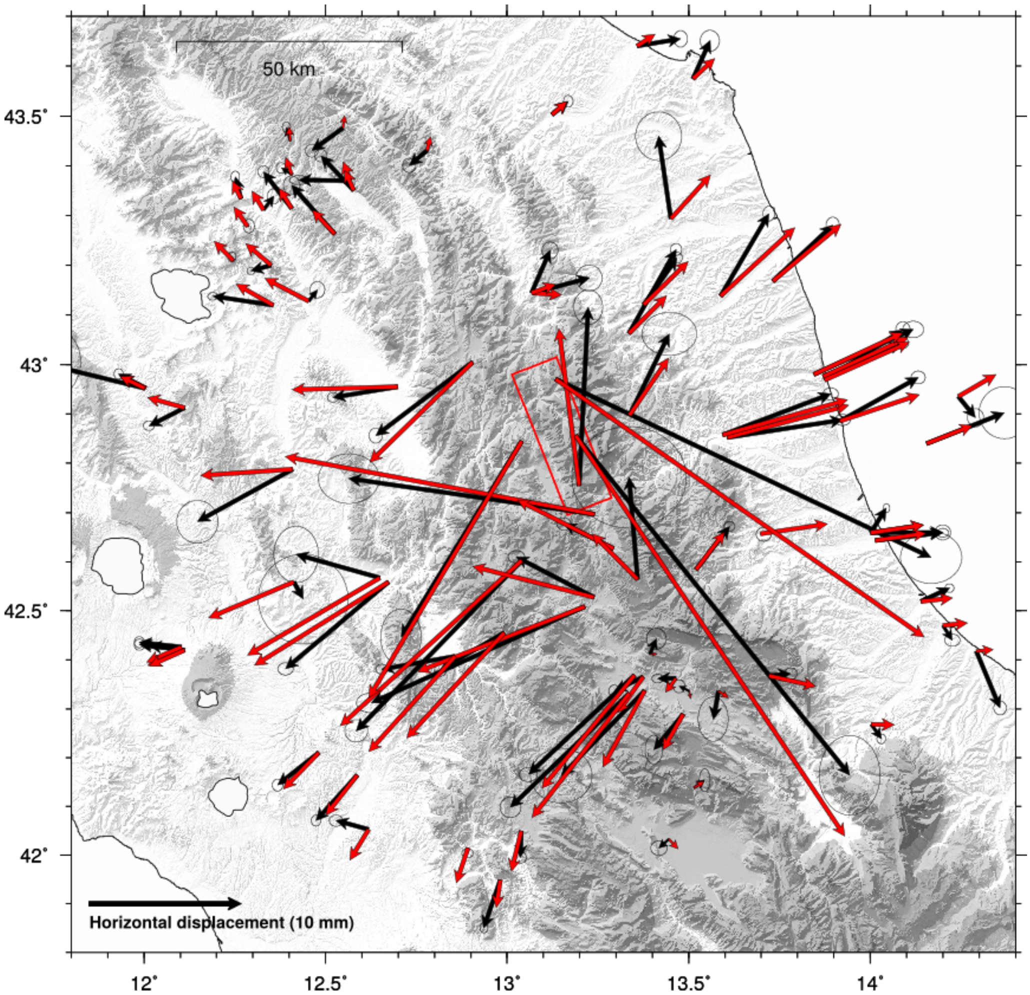

Figure 2.26. Map showing the sum (red arrows) of the displacement associated with afterslip (from model shown in Figure 2.18) and the displacement associated with the viscoelastic contribution obtained with uniform depth of the brittle-ductile transition. Black arrows as in Figure 2.25. Error ellipses as in Figure 2.4.

2.5 Discussion

In this work we analyze the displacement time-series of GPS sites active during and after the 2016-2017 Central Italy seismic sequence, employing a blind-source-separation algorithm based on variational bayesian ICA (vbICA) to analyze the 2012-2019 time-span. We highlight one postseismic component (IC1, Figure 2.3) plus three hydrological, seasonal, components (IC 2, 3, 4; Figure 2.3).

In the IC2 (Figure 2.4) a spatially-uniform vertical displacement signal is mapped. In agreement with previous findings, it generally represents the largest source of non-tectonic seasonal deformation (Michel et al., 2018, Serpelloni et al., 2018). Underground water content variations, mapped in the IC3 and IC4, produce mm-scale horizontal displacements as already observed by Silverii et al. (2016) and Devoti et al. (2018) in the Apennines, and by Devoti et al. (2015), Serpelloni et al. (2018) and Pintori et al. (2021) in the Southern Alps. The deformation processes associated with the hydrological ICs (Section 2.3) were not detected by Pousse-Bertrand et al. (2020) in their InSAR data analysis on the pre-seismic phase of the 2016-2017 seismic sequence. On the other hand, the decomposition we carried out on the pre-seismic time-span (Section 2.2.3) does not highlight any IC related to a transient deformation that we can associate with the preparatory phase of the Amatrice earthquake, as it is done in Vičič et al. (2020).

As we showed for the GPS sites in the Paganica area (Section 2.3.3), the distinction of tectonic and non-tectonic signals is crucial, in particular when dealing with mm-scale postseismic displacements. As a matter of fact, for such GPS sites, the IC3 has a main SW-NE horizontal deformation pattern, similar to the direction of the tectonic deformation in this area (Figure 2.4), and might prevent us from a proper assessment of the displacement related to the postseismic relaxation. However, the vbICA has proven to be capable of an accurate separation as we discussed in Section 2.3.3: as we show in Figure 2.9, not considering the effect of a postseismic relaxation on the Paganica sites leads to a poor modelization of the time series after the Norcia earthquake. Once the postseismic displacement at Paganica GPS sites has been validated, we find the necessity of including the Paganica fault in the inversion, since not considering it leads to a concentration of afterslip on the southern edge of the Campotosto fault (Figure 2.15), as close as possible to the GPS stations position. We deem such a high concentration of slip to be unlikely, mainly due to the difference in magnitude between the earthquakes occurred on the M. Vettore fault and those occurred on the Campotosto fault. Moreover, considering only the Campotosto fault in the inversion we are not capable of fully reproducing the displacement pattern at GPS sites in the Paganica area (Figure 2.15b). The Paganica fault was acknowledged as the main structure responsible for the 2009 L'Aquila earthquake, but no mainshock nucleated on this fault during the 2016-2017 seismic sequence. Nevertheless our results suggest that it may have accommodated a few centimeters of afterslip in the three years following the main events. In Figure 2.27 we show the stress perturbation, in terms of Coulomb Failure Function variation (DCFF), owing to the mainshocks of the seismic sequence, as proposed by Cheloni et al. (2017, 2019, 2019a) on the six fault planes of Figure 2.18. We find positive values for the Paganica fault ($DCFF \sim 0.02-0.05$ MPa) favoring slip on this structure. This finding highlights how faults interaction needs to be taken into account if we want to attempt a deterministic modelization of the seismic cycle.

As discussed in Section 2.4, our analysis isolated only one postseismic component for the whole time span considered. An attempt to increase the accuracy of the decomposition has been made through an iterative application of the vbICA algorithm (Section 2.4), as in Michel et al. (2018). However, no further tectonic components were highlighted during this re-analysis. The fact that the postseismic relaxation is described solely by IC1 brings along some limitations:

1. Concerning the afterslip model, several mainshocks occurred during the Central Italy seismic sequence, however only one component is representative of the whole postseismic relaxation. Hence, we are not capable of getting any hint on the possible spatial migration or different activation times of the various segments of the fault system involved. Therefore our results are limited to a stationary spatial response of the slip, not allowing us to determine when the different parts of the faults actually began to slip.

2. Three mechanisms primarily drive the postseismic relaxation of stress: poro-elastic rebound, afterslip and viscoelastic flow. Here we deemed at least two of them (afterslip and viscoelastic flow) to act, but we are not able to distinguish them as instead achieved in similar studies (e.g., Mw 7.2 El Mayor-Cucapah earthquake, Gualandi et al., 2020).

Usually afterslip and poro-elastic rebound effects are the dominant mechanisms relaxing stress in the postseismic phase (e.g., Nespoli et al., 2018). For the Central Italy seismic sequence, Tung and Masterlark (2018) suggested that poroelasticity affected the seismicity while Pousse-Bertrand et al. (2020) suggest that poro-elastic rebound does not account for a substantial contribution to the observed surface displacements. This is in agreement with the results here presented, since the GPS sites that are affected the most by the third and fourth IC (which may be partially associated with fluid migration) are located in the Paganica area, far from the epicenters. Moreover, the density of the GPS network does not allow to identify and limit an aquifer generating poro-elastic deformations.

The simultaneous action of afterslip and viscoelasticity is also supported by the different temporal evolution of the postseismic transient and the decay describing the cumulative number of aftershocks (Figure 2.11). We believe that the reason why the vbICA is not capable of separating such mechanisms may be related to the short time span here considered, and longer time-series will help to address this problem in the future. As a consequence we cannot exactly establish the relative contribution of the various deformation mechanisms to the total measured displacement field.

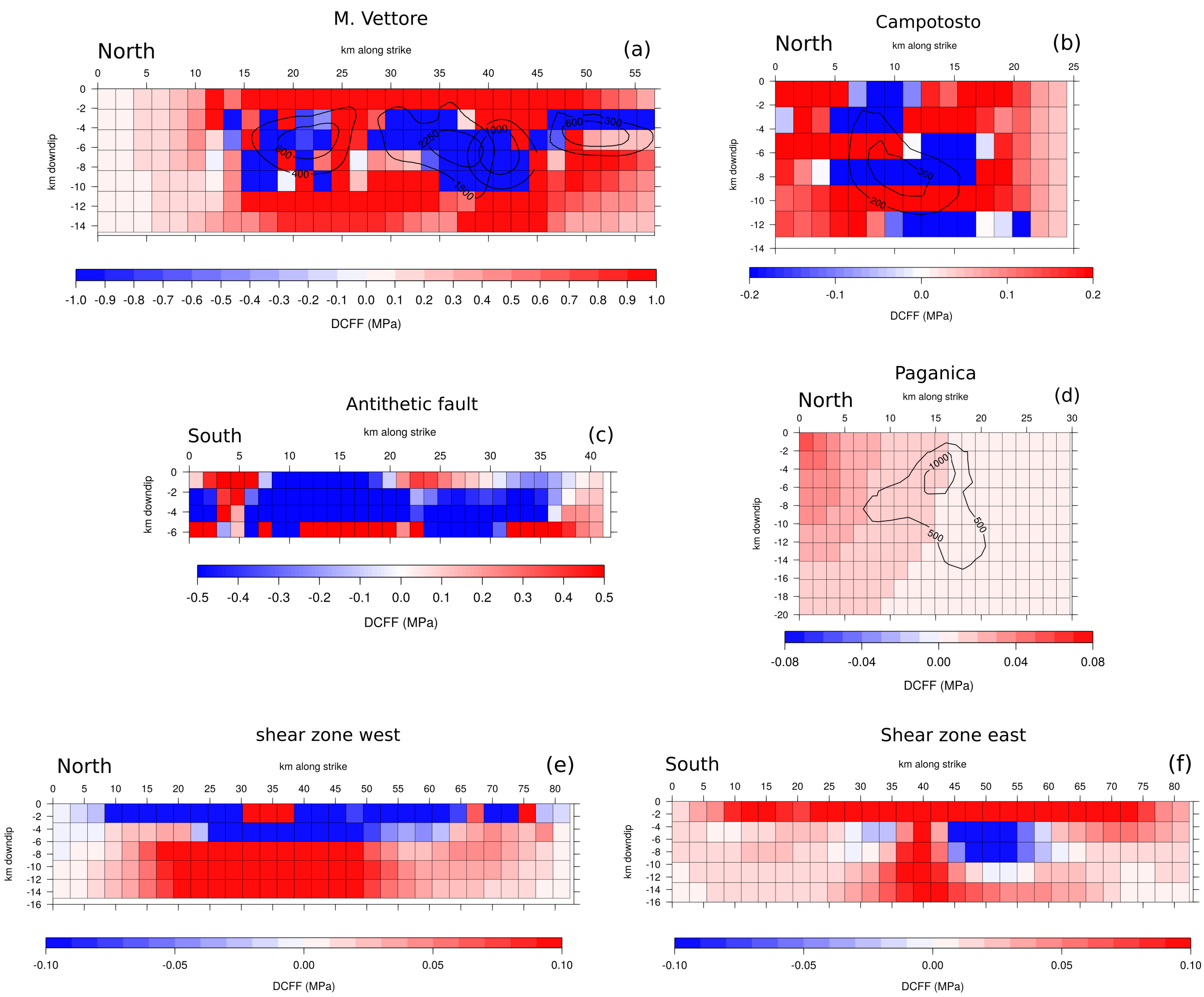

Figure 2.27. The Coulomb failure function variation (DCFF) on the M. Vettore fault (a), Campotosto fault (b), antithetic fault (c) , Paganica fault (d), western (e) and eastern (f) side of the shear zone, related to the main events of the 2016-2017 sequence (Section 2.1) as modeled by Cheloni et al. (2017, 2019, 2019a). Co-seismic contours are as Figure 2.18. Note the different scale below each fault plane (units of MPa).

2.5.1 Afterslip remarks

As Figure 2.16 shows, including the four high angle faults only in our afterslip model leads to a strong slip concentration on the bottom edge of faults. However, this is not enough to explain the displacement recorded at sites away from the epicentral area (red triangles of Figure 2.17a). As shown in Section 2.2.1, far-field stations measured statistically significant postseismic displacements. Hence we choose to add complexity to our model, first investigating the role of the shear zone in the postseismic phase, as suggested by

Vuan et al. (2017) and Pousse-Beltran et al. (2020). This second inversion model brings a better fit of the far field stations and to a different afterslip distribution: we observe lower intensities of slip at the bottom edges of the high angle faults (Figure 2.10), which is probably compensated by the afterslip occurring on the deepest portion of the shear zone itself (Figure 2.18e and 2.18f).

We may compare the afterslip model of Figure 2.18 with the one proposed by Pousse-Beltran et al. (2020). This latter exploited InSAR measurements and near-field GPS sites to retrieve the afterslip distribution on the M. Vettore and its antithetic fault with a geometry similar to that of Cheloni et al. (2019). Since the faults employed in our study, and in particular the M. Vettore fault and its antithetic fault, share the same orientation (dip and strike), we can directly compare the Pousse-Beltran et al. (2020)s' slip distribution (figure S21 in Pousse-Beltran et al., 2020s' supplementary material) and the afterslip we retrieve on the four high angle faults (namely the M. Vettore, the Campotosto, the Paganica and the antithetic fault). Pousse-Beltran et al. (2020) found two main slipping areas, one below Arquata del Tronto and one in the Castelluccio area. This latter partially involves areas that ruptured co-seismically during the Amatrice and the Norcia mainshocks and it is less certain, as claimed by the authors themselves.

The model presented in Figure 2.18 does not show the same overlapping in the Castelluccio area, as afterslip on the M. Vettore fault is mainly accommodated outside the co-seismic areas (Figure 2.18a). We also find significant slip in the shallow portion of the M. Vettore fault, $\sim$ 10 km NE of the slipping area beneath Arquata del Tronto indicated by Pousse-Beltran et al. (2020). Furthermore, in Pousse-Beltran et al. (2020)s' model, slip reaches maximum values of $\sim$ 16 cm, which is less than our data suggest ($\sim$ 24 cm). This may be justified: (i) noting that Pousse-Beltran et al. (2020) analyzed a shorter time span (from November 1 2016 to February 11 2017); (ii) by the smaller area covered by the interferograms used in Pousse-Beltran et al. (2020) with respect to the coverage of the GPS network employed by us; (iii) by the smoothing method adopted to regularize the inversion.

We can observe from Figure 2.18b that the northern slipping patches on the Campotosto fault overlap with the co-seismic slip distribution retreived by Cheloni et al. (2019a). Since the solution they obtain is based on InSAR inferograms that encompassed the displacement of the 1^{st} month after the January 2017 earthquakes, we estimate about 8% of the moment released in that time period (i.e. up to February 11) to be related to a postseismic relaxation. Regarding the shear zone, a few cm of slip occur on its eastern, slightly E-dipping, side (Figure 2.18f). Afterslip on those patches, located far from where slip occurred during the co-seismic phase, is probably driven in the inversion by displacements measured at sites towards the Adriatic coast. However, we notice from Figure 2.27f that the stress perturbation owing to the earthquakes of sequence on this deep portions of the shear zone are slightly>0 ($DCFF \sim 0.05 - 0.1$ MPa), therefore in principle we cannot rule out the occurrence of slip in that area.

We estimate the equivalent seismic moment associated with the ~ 1 year postseismic relaxation (i.e., up to January 2018) to be $M_0^{geodetic} = 6.25 \times 10^{18}$ Nm (for a rigidity modulus = 30 GPa), which would correspond to a Mw 6.5. Exploiting the seismic catalogue described by Michele et al. (2020), we may compare the $M_0^{geodetic}$ with the seismic moment released by aftershocks. We convert the reported ML into Mw using the relation Mw-ML proposed by Munafò et al. (2016) for small events, and we find a moment released by aftershocks during the first year of the postseismic phase (i.e., up to January 2018) $M_0^{aftershocks} = 4.60 \times 10^{17}$ Nm. This suggests that the postseismic deformation was dominated by aseismic motion. Concerning the spatial relation among co-seismic slip, afterslip and aftershocks, we observe that aftershocks on the Campotosto and antithetic faults overlap only partially with the areas undergoing postseismic slip (Figure 2.18b and c). On the M. Vettore fault (Figure 2.18a) a first cluster of aftershocks is located on the bottom edge of the Amatrice and Norcia co-seismic ruptures where a large amount of afterslip is accommodated; whereas a second cluster is located in the shallower portion of the fault around the Visso slipping area. The majority of the aftershocks of this second cluster occurs outside the patches undergoing afterslip, which might be due to a lack of GPS coverage in that area.

2.5.2 Viscoelastic remarks

As it can be observed from Figure 2.18, the maximum value of afterslip occurs at the base of the high-angle faults. According to Riva et al. (2007)s' results on the 1997 Umbria-Marche seismic sequence this may point out a rheological discontinuity decoupling the seismogenic upper crust from a viscoelastic lower crust. According to Boncio et al. (2004), the active faults in the seismogenic layer of this sector of the Apennines detach into a layer dominated by aseismic plastic flow passing through a broad transition zone. Such detachment is illuminated by a high seismicity rate discussed by Vuan et al. (2017) and interpreted as the top of the brittle-ductile transition by Chiaraluce, Barchi, et al. (2017). The brittle-ductile transition may be marked by flat detachments within the crust (Carcione et al., 2014; Fayon et al., 2000; Jolivet et al., 2010; Platt et al., 2015; Rabillard et al., 2018). Following also Nespoli et al. (2019), the fault dip angle is expected to drastically decrease just below the brittle-ductile transition. Below the detachments, which can be interpreted as ductile shear zones (Rabillard et al., 2018), an elasto-plastic rheology can be assumed and rocks behave like viscoelastic materials (Carcione et al., 2014; Fayon et al., 2000). As suggested, for instance, by Carminati et al. (2001) and Carannante et al. (2013), beneath this part of the Apennines the brittle-ductile transition deepens moving eastwards. Fixing $\eta_{lc} = 5 \times 10^{18}$ Pa s and about 18-22 km of thickness for the lower crust, we model a displacement field consistent with the geodetic observations. This rheological model (Figure 2.25b) is in agreement with model LC18 proposed in Riva et al. (2007). Simplifying such model and taking a uniform brittle-ductile transition depth at 15 km (Figure 2.25a), we are capable of matching the near- and far-field postseismic displacements slightly better. Taking η_{lc} below 10^{18} Pa s causes the displacement reproduction to worsen, in agreement with what Riva et al. (2007) showed. On the other hand, in Riva et al. (2007) a slightly thinner viscoelastic layer (about 12 km) is suggested. This is likely compensated by the lower viscosity ($\eta = 10^{18}$ Pa s) they infer. In fact, a trade-off between the thickness of the viscoelastic layer and its viscosity exists. An attempt to model a viscoelastic relaxation following the Norcia event was made by Pousse-Beltran et al. (2020) as well. However, their results suggested an inversion of vertical polarity (i.e. uplift) and therefore discharged viscoelasticity as a mechanism contributing to the postseismic deformation. We believe this is due to the rheological profiles they implemented, which takes a $\dfrac{\partial \eta}{\partial z} < 0$. In case of a high viscosity layer in between the elastic layer and the underlying substrates, the vertical postseismic and co seismic deformations show an opposite polarity (Hetland and Zhang, 2014). We assume in our viscoelastic models the thick layer of seismicity that bounds the high-angle normal faults to be elastic on the time scale we considered. As it is suggested by Hetland and Zhang (2014), if the co-seismic rupture does not entirely break the seismogenic layer then the unruptured portion behaves like a viscoelastic material with very high viscosity. The tests we run indicate that the lower bound for the viscosity of the volume of seismicity described by Vuan et al. (2017) is 10^{20} Pa s, and lowering such value would produce unobserved effects at near-field GPS stations.

In light of the considerations here discussed, we propose the viscoelastic relaxation of the lower crust as a mechanism contributing to the observed postseismic displacements, but a deeper understanding is limited by several factors. In this study we exploited short time series (~ 2 years) compared to the typical characteristic times of viscoelastic processes (~ 5 years for the viscosity here inferred). We should also keep in mind that moderate earthquakes, such as the Mw 6.5 Norcia event, produce small deformation rates (in the order of few mm/yr), as suggested by Riva et al. (2007). Moreover, a key issue while studying the postseismic response of the lithosphere to an earthquake is the uniqueness of the explanation. Since the vbICA highlights a single postseismic IC, a clear separation between the viscoelastic relaxation and the afterslip contribution proved to be a challenging task. We suggest that both afterslip and viscoelastic relaxation acted during the postseismic phase of the sequence and one should be careful in preferring one mechanism to the other because of the good agreement with the observations (Freed et al., 2006). The good reproduction of GPS displacements by afterslip is not surprising, as the inversion is not constrained by physical processes such as coseismic stress changes, whereas the misfit produced by the viscoelastic model can be explained by the simplifications made in our forward models to the real Earth's case.

2.6 Conclusion

In this study we use GPS ground displacement time-series to characterize the postseismic phase of the Amatrice-Visso-Norcia seismic sequence. Applying a vbICA algorithm, we distinguish the postseismic tectonic source of deformation from other hydrological deformation sources, the former being represented by a single IC in spite of the occurrence of at least three main events. GPS stations as far as ~ 90 km from the epicentral area clearly recorded displacements associated with a postseismic relaxation. Taking advantage of the the high accuracies and temporal resolution offered by continuous GPS observations we investigate the relaxation processes that drove the postseismic ground deformation. Our results suggest that the largest part of the cumulated displacement observed in the ~ 2.3 years after the Amatrice earthquake is due to an afterslip mechanism. We infer the occurrence of aseismic slip on the Paganica fault during the postseismic phase of the seismic sequence, since the data inversion accounting for the faults that hosted the main events of the sequence only leads to a bad reproduction of the measurements at GPS stations in the Paganica area and at far-field sites. Interestingly, the Paganica fault (unruptured in the co-seismic phase of the sequence) accommodated some centimeters of afterslip during the postseismic phase of this seismic sequence, pointing out the importance of accounting for the interaction among faults while attempting a deterministic modelization of the earthquake cycle. Given the afterslip concentration at the bottom edge of the seismogenic faults, the discrepancy between the temporal evolution of the postseismic transient and the cumulative number of aftershocks, and the differences between the measured and the modeled afterslip displacements, we cannot exclude a viscoelastic contribution to the total displacement. In particular, we infer the relaxation of the lower crust to be a contributing postseismic mechanism in the 2 years following the 2016-2017 seismic sequence. Keeping in mind the limits of the data and of our interpretation, we propose an afterslip model that is consistent with the co-seismic slip solutions for the faults involved in this seismic sequence. Furthermore, we provide some preliminary values of the viscosity and thickness of the lower crust, leaving further investigations to future studies, which might consider an afterslip + viscoelastic joint inversion of possibly longer time series.

Chapter 3

Gladwin Tensor Strain Monitor

The Gladwin Tensor Strain Monitor (*GTSM*) is a type of strainmeter designed to measure strain in the Earth. GTSMs belong to the class of multi-component (tensor) and they were developed, during the 1970's, to perform in deep boreholes. GTSMs can measure the horizontal principal components of the strain field with high precision and high stability, detecting deformations with intensities up to 10^{-11} on time scales of minutes to months (for comparison, GPS sub-diurnal accuracy is $\sim 10^{-7}$, Reuveni et al., 2012). Owing to these features, GTSMs met with the favours of the scientific community and, since the first deployment in 1975, they have gone through a wide spread diffusion around the world. In fact, GTSMs have been installed in the US for the Plate Boundary Observatory (PBO) project, in Australia, Japan, Turkey and Korea. Between 2003 and 2010, thirteen instruments were installed in Taiwan and they will be presented in Chapter 4, and in more recent times (2021-2022) six were deployed in Central Italy and will be presented in Chapter 5. In the last decades GTSMs have contributed to the analysis of episodic tremor and slip events, aseismic creep, coseismic deformation, seismic wave propagation, the study of the normal modes and in hydrogeodesy. A short overview of the observations and scientific results made possible through strainmeters will be given in Section 3.1.

The aim of this Chapter is to introduce the reader to the basic features of GTSMs, and to review the necessary assessments for a correct functioning and calibration of these instruments. Finally, in Section 3.4 we present the original methodology that has been developed during this work of thesis.

3.1 Strainmeters scientific outcomes

Since their first deployment in California in the early 1980's (Gladwin et al., 1987), strainmeters have contributed in many fields of the geophysical research.

Strainmeters are capable of measuring even the most fiable strain variation in the rock, allowing us to detect both the dynamic of earthquakes (e.g., Cao et al., 2018 ; Barbour et al., 2021) and slow events with longer characteristic times (e.g., Hawthorne and Rubin, 2010 ; Durand et al., 2022). Although examples of how strainmeters have helped to constrain faults source parameters are well documented in literature (e.g., Canitano et al., 2015), these instruments find their best application in the study of transient slip. Thanks to their high sensitivity, which is maintained over time scales that range from minutes to months, strainmeters have successfully contributed to the observation of aseismic slip either anticipating earthquakes nucleation (e.g., Gladwin et al., 1991), occurring in concomitance with seismic swarms (e.g., Martinez-Garzon et al., 2019) or following the mainshock (e.g., Hawthorne et al. 2016). A precise characterization of the aseismic behaviour of faults is necessary to achieve a thorough assessment of seismic hazard, especially in highly vulnerable areas (e.g., Bohnhoff et al., 2013). Aseismic slip may release accrued stress, therefore postponing and/or preventing the nucleation of large earthquakes (Gualandi et al., 2017; Rolandone et al., 2018; Vaca et al., 2018). On the other hand, examples of seismicity triggered by slow slip events are present in literature as well (e.g., Durand et al., 2022). It is clear that aseismic slip events participate to the total budget of moment release. Whether they occur repeatedly, releasing stored energy, or they favour the nucleation of moderate and large earthquakes, is still an open question, which is nowadays being tackled through borehole strainmeter observations.

Moreover strainmeters have led to a downscaling of our observational capability, allowing us to highlight the interaction between seismic activity and hydrological processes. Liu et al. (2009) noted that typhoons hitting Taiwan produced strain changes consistent only with barometric forcing, hence suggesting a relationship between slow slip events and sudden changes in barometric pressure. Periodical forcing such as Earth tides are known to have induced tremors in Nankai (Shelly et al., 2007) and Cascadia (Rubinstein et al., 2008). Furthermore strainmeters deployed in the Sea of Marmara (Turkey) highlighted how the sea level variations can be linked to enhanced seismicity rates (Martínez-Garzón et al., 2023).

Strainmeters have also contributed to the study and characterization of hydrological processes, allowing investigating how solid Earth and surface processes interact. For instance in Mouyen et al. (2017) borehole strainmeter data have been used to study the elastic response of the crust in response to heavy storms hitting Taiwan, as well as to quantify the large amount of rainwater brought by typhoons or episodic heavy rainfalls. Further examples of this, will be provided in Section 4.5 and 5.4.

3.2 Instrumentation

A Gladwin Tensor Strain Monitor consists of four moduli (CH_i, Figure 3.1(a)), each one containing an extensiometer, that are usually referred to as "*gauges*". The gauges are oriented at different angles, and in particular three of them are spaced by 120° (CH_0, CH_1, CH_2), while the fourth one (CH_3) is 90° away from channel 1 (Figure 3.1(b)).

Since the GTSM is designed to measure the horizontal strain field, having four gauges provides redundancy as well as a back-up channel in case of malfunctioning. Moreover, tensor strainmeters allow us to measure shear strains beside the areal (volumetric) strain.

Each gauge hosts a Stacey-type differential capacitance bridge (Stacey et al., 1969) which allows us to measure the change in the instrument diameter as a result of deformation processes. In Figure 3.1(c) a schematic representation of this transducer element is provided: it consists of a series of two capacitors, one of which has its plates fixed (i.e. the capacitance is constant) and works as a reference, whereas the third plate is free to move in response of external forcing (Gladwin et al., 1984). The differential capacitance can be related to the elongation (e) of the instrument, namely the uniaxial strain in the direction of the specific gauge, through the relation:

$$e = \left[\frac{R(t) \times 10^{-}8}{1 - R(t) \times 10^{-}8} - \frac{R(t_0) \times 10^{-}8}{1 - R(t_0) \times 10^{-}8} \right] \times \frac{\text{Reference Gap}}{\text{Diameter}} \tag{3.1}$$

where $R(t)$ is the raw capacitance measurement and $R(t_0)$ is a reference measurement. Reference gap of the Stacey-type differential capacitance bridge and diameter of the cylinder are as in Figure 3.1(c).

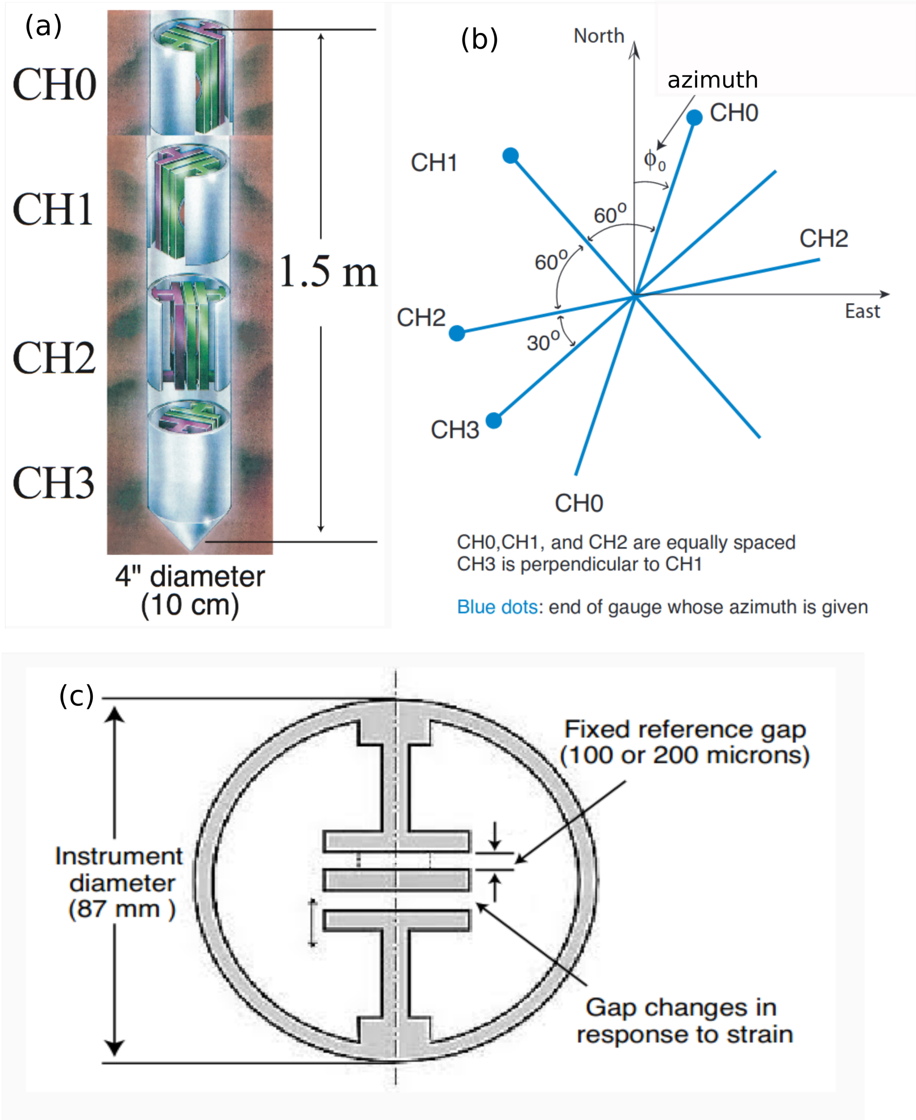

Figure 3.1. (a) Representative image of a GTSM; (b) orientation of the gauges; (c) cross-section of a transducer.

The first step when installing a GTSM is the choice of the site, and the criteria used to assess the goodness of the location are:

- the presence of competent rocks at depths of $\sim 150 - 250$ m, and with a $\sim 3 - 6$ m section.
- The absence of fractures that can allow water flow.
- The absence of pumping that can perturb the strain field.

- A safe place for the instrument with access to power supply and telemetry.

Provided these general guidelines, when selecting the strainmeter location, it is important to bear in mind the geophysical relevance of the site, namely its scientific interest. A typical installation starts with the drilling of a 15 cm wide, $\sim$ 200 m deep (depending on the location of the desirable rock) borehole, at the bottom of which the strainmeter is placed. The GTSM is coupled to the surrounding medium through a special expanding grout which keeps the instrument in compression where it is designed to operate optimally. Ideally, the instrument should be installed in rocks which share its same elastic properties. Practically this would imply to design each strainmeter specifically for the borehole it is intended for. The ideal rock formation would be massive, unfractured, non-layered intrusive granites. However, in real world cases we are often forced to compromise and igneous, metamorphic, and sedimentary rocks are all possible. The more horizontally layered the rock formation the better. Water pumped in wells in the proximity of the strainmeter can produce effects hard to characterize, and therefore reduce the data quality. Other sources of anthropogenic noise (highways, railroads ...) nearby the instrument are also undesirable. The ideal location of installation would be in the middle of a plain on a low terrain far from any river. Topography can perturb the measured strain field depending on where the strainmeter is located (Harrison 1976). Other features to bear in mind when selecting the site are a good sky view and the absence of obstacles for good telemetry and GPS measurements, as well as an accessible site (heavy machines are usually employed in the drilling of the borehole).

Three are the criteria to be met in order to assess the data quality of the installed instrument:

1. the instrument shows a long term contraction;
2. the instrument records Earth (and oceanic) tides;
3. the instrument records signals in the seismic band;

In particular, the long term contraction depends on the grout used to cement the GTSM, and on the strain released on the edge of the borehole by the rock formation which tends to close in.

Strainmeters find their optimal employment in the observation of the short term (minutes to months) strain changes. On such time-scales, which are not encompassed by seismometers, strainmeters outperform GPS. As a matter of fact, strainmeters fill the gap between seismology and geodetic techniques such as GPS and SAR (see also Figure 1.3). GTSM can detect variations in the borehole diameter in the order of the 10^{-12} meters, i.e. deformations in the order of 10^{-2} nanostrain. The sensitivity is limited by the ambient noise, however short term signals (such as seismic waves) are measured to about 0.1 nanostrain and daily signals (such as tides) are measured to about 1 nanostrain.

3.3 Calibration: theoretical background

GTSMs are coupled to the rock through a cementing grout. However the instrument and the grout do not have the same elastic moduli as the surrounding medium. Moreover, the borehole, the grout and the instrument itself perturb the local strain field forming an inhomogeneity in the ground, therefore each gauge responds to deformations perpendicular and parallel to its axis that do not correspond to those of an unperturbed medium (Roeloff et al., 2010). The elongation measured by each gauge is not exactly, but is related to, the rock formation strain. Hence the necessity to *calibrate* the strainmeters, namely to assess the coefficients that describe the measured elongation as a combination of the strain components.

Two ways are possible to calibrate a strainmeter: the first one consists in estimating the coefficients directly from the inclusion elastic parameters; the second one consists in comparing the instrument response to a known reference signal. The former approach has been followed, for instance, by Gladwin and Hart (1985) and Shimada et al. (1987). However, as Hart et al. (1996) have shown, the parameters of the inclusion are hard to estimate and are affected by large uncertainties. Therefore the second approach is the most widely used and the common reference signals used are tides (Earth and/or oceanic) and teleseismic waves. The calibration through teleseismic waves has, for instance, been achieved by Bonaccorso et al. (2016) for the dilatometers installed on the Mount Etna volcano. This reference signal is less commonly used and it requires the availability of high frequency strain recordings.

3.3.1 Tides

We refer to tides as to the motion induced by tidal forces on either the fluid part of the Earth, in which case we are dealing with oceanic tides, or the solid part in which case we will have Earth tides. Tides are well known phenomena, generally well recorded by borehole strainmeters, and for these reasons they are the most commonly used reference signals for these instruments calibration. The Earth is more rigid than the oceans and its shape is easier to model, and this makes the computation of Earth tides more accurate and less dependent on fine details.

We refer to *theoretical tides* as to those derived from some gravitational model. The first step when computing the tidal effect consists in finding the tidal forces or *equilibrium tidal potential*. Such tidal forces originate from celestial bodies (mainly the Moon and the Sun) and their derivation belongs to the field of astronomy. This step substantially requires to compute the ephemeris of the Moon and the Sun (and of other planets if needed). The better our capability of modeling the ephemeris the more accurate the equilibrium tidal potential is going to be. Once the equilibrium potential is known we can proceed with the computation of the theoretical tides. This step can be split into two parts: in the first one we compute the *body tides*, namely the tides we would observe in a oceanless (but realistic) Earth, then we add the effect of the motion of the oceans (i.e. the *load tides*). The sum of this two contributions will give the theoretical tide.

Theoretical tides are usually found numerically from the knowledge of celestial bodies' orbits. Following Thomson and Darwin works in the 1870's and 1880's, the tidal equilibrium, that is given by the tidal potential V_{tid} divided by the gravitational acceleration of the earth g and represents the change in elevation of the geoid, is usually expressed through the spherical harmonics $Y_{nm}(\theta, \phi)$, whose individual sinusoids are called *tidal constituents* of degree n and order m (D.C. Agnew, 2005):

$$\frac{V_{tid}}{g} = r_{eq}\frac{M_a}{M_e}\sum_{n=2}^{\infty}\frac{4\pi}{2n+1}\left(\frac{r_{eq}}{R}\right)^{n+1}\sum_{m=-n}^{n}Y^*_{nm}(\theta', \phi')Y_{nm}(\theta, \phi) \tag{3.2}$$

where r_{eq} is the Earth's equatorial radius and M_e its mass; R the distance of the attractor body and M_a its mass; θ and ϕ are respectively colatitude and longitude of the point on the Earth we are considering. The second summation of equation 3.2 separates the *tidal species* with a frequency $m = 0, 1, 2, ..n$ cycles per day. The most relevant are: the diurnal ($m = 1$), which is largest at midlatitudes and vanishes towards the equator; the semidiurnal ($m = 2$), which is the largest at the equator; and the long-period ($m = 0$), which is the only one acting at the poles. If we consider $n = 2$, since V_{tid} scales as $\frac{GM_a}{R^3}$ we can just consider the lunisolar tides: if the Moon's potential is taken as a reference $\left(\text{i.e. } \frac{GM_a^{moon}}{R^3_{moon}} = 1\right)$, then the solar contribution would be $= 0.46$, the Venus contribution $\sim 10^{-5}$ and Jupiter's $\sim 10^{-6}$.

As it can be observed from Figure 3.2, the amplitudes of the tidal species can significantly differ (upper panel). Moreover, from central and lower panels of Figure 3.2, we can observe that each species' constituent is separated in different bands called *groups*. In particular, in central panel of Figure 3.2 we can observe the groups separation of the diurnal species, whereas in lower panel the separation of the semidiurnal one.

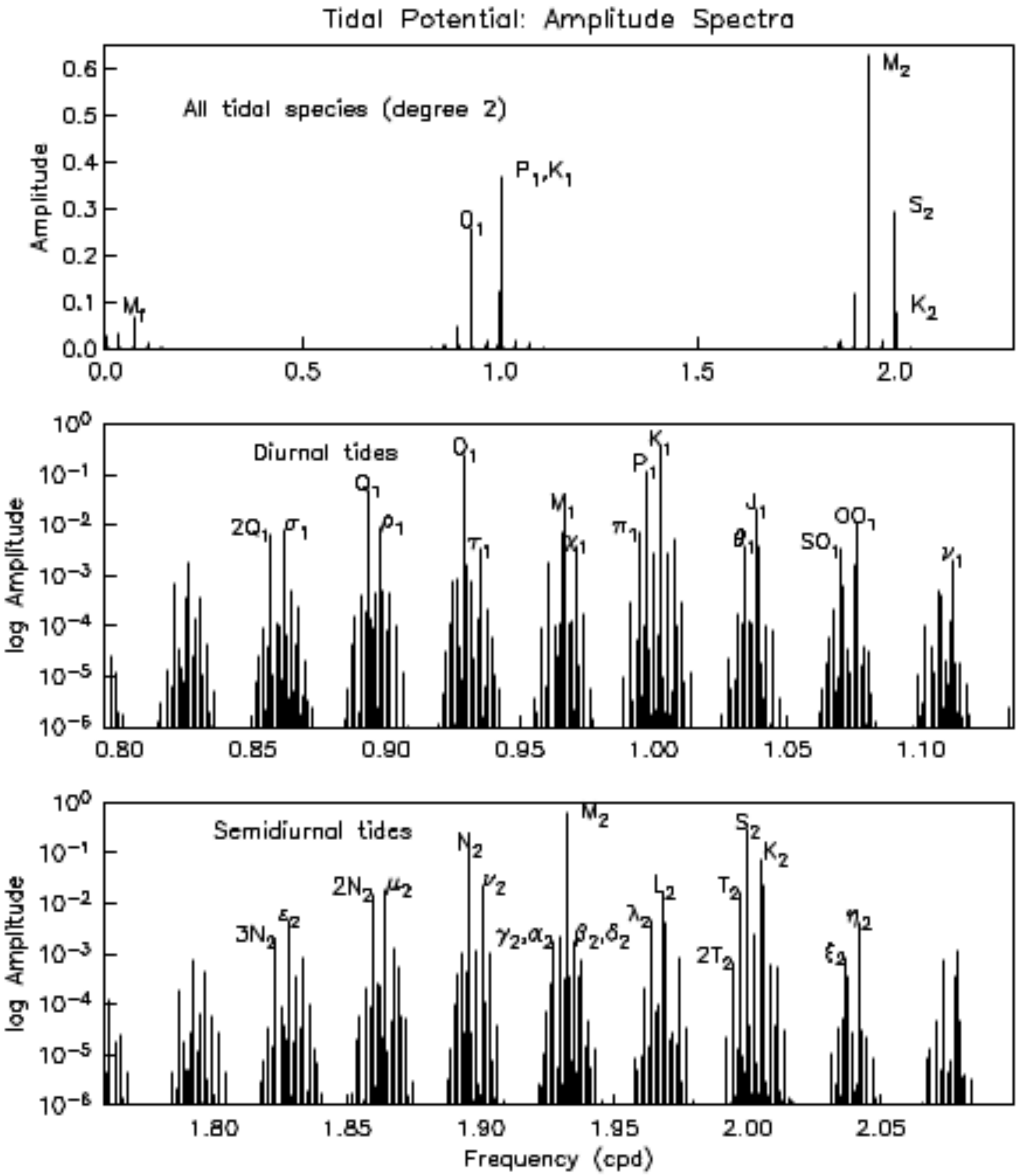

Figure 3.2. Plot of the frequency VS amplitude for some tidal constituents.

In order to compute the Earth's response to the tidal forcing we usually make some simplifications. In particular it is assumed a Spherical, Non-Rotating, Elastic, Isotropic and Oceanless (SNREIO) Earth. We use a quasi-static theory, which implies that the forcing has a much longer period than any normal mode of the Earth. This latter assumption is quite true for the solid Earth but not for the oceans. Given a certain model for the Earth (for instance the PREM model), and fixed a certain degree (i.e. n) for the tidal equilibrium, it is possible to compute the resulting vertical displacement as $h_n \frac{V}{g}$ and the horizontal displacement as $l_n \frac{\nabla V}{g}$, where h_n and l_n are the appropriate *Love numbers*. Love numbers are dimensionless parameters that describe the mechanical properties of a planetary body, and they are assumed to be known.

Limitations of this approach are given by: (i) the Earth in not SNREIO, the largest difference being the presence of the oceans; (ii) the Earth is not perfectly spherical, its ellipticity extending down to the core-mantle boundary; (iii) the mantle is not perfectly elastic. Accounting for these differences can be made through corrections in the computation of Love numbers with more accurate modelizations of the Earth. The largest correction accounts for (i), with the addition of load tides to our theoretical prediction, which implies an adequate modelization of the effects of tidal forces on the oceans.

3.3.2 Calibration of GTSM

In order to calibrate a strainmeter, we need to compare the strain as measured by the instrument against the one actually occurring in the ground (which is assumed to be known theoretically). Following Jaeger and Cook (1976), the strain in the rock formation (i.e. in far-field, namely far enough from the borehole for the strain field to be in an unperturbed state) is related to the radial strain, s^i_{par}, measured by the transducer with azimuth θ_i by the following equation

$$s^i_{par} = \frac{1}{2}\Big[\epsilon^F_A + \gamma^F_1 cos(2\theta_i) + \gamma^F_2 sin(2\theta_i)\Big] \tag{3.3}$$

where $\epsilon^F_A = \epsilon^F_{xx} + \epsilon^F_{yy}$ is the *areal strain* in the rock formation; $\gamma^F_1 = \epsilon^F_{xx} - \epsilon^F_{yy}$ and $\gamma^F_2 = 2\epsilon^F_{xy}$ are the shear components of the strain field (respectively the *differential* and *engineering strain*). However, when a gauge is installed in the ground it is also subject to s^i_{per}, the strain perpendicular to its axis

$$s^i_{per} = \frac{1}{2}\Big[\epsilon^F_A - \gamma^F_1 cos(2\theta_i) - \gamma^F_2 sin(2\theta_i)\Big] \tag{3.4}$$

Provided that gauges have different sensitivity to strain parallel ($w_{par} > 0$) and perpendicular ($w_{per} < 0$) to their axis (Hodgkinson et al., 2013), the total strain felt by the sensor is

$$e_i = w_{par}S_{par} - w_{per}S_{per} \tag{3.5}$$

namely

$$e_i = \frac{1}{2}\Big[(w_{par} - w_{per})\epsilon_A^F + (w_{par} + w_{per})\gamma_1^F cos(2\theta_i) + (w_{par} + w_{per})\gamma_2^F sin(2\theta_i)\Big] \quad (3.6)$$

or in Hart et al. (1996)s' formulation,

$$e_i = \frac{1}{2}\Big[C\epsilon_A^F + D\gamma_1^F cos(2\theta_i) + D\gamma_2^F sin(2\theta_i)\Big] \quad (3.7)$$

C and D are the *areal and shear coupling coefficients* that relate the observations of the strainmeter to strain in the surrounding rock. An underlying assumption here is that the medium is isotropic.

We can take into account the possibility that gauges have different mechanical gains and we can include them by multiplying by some g_i both sides of the previous equation. Without any loss of generality, we can subsume the weights in the coupling coefficients of the right hand side of equation 3.7

$$g_i e_i = \frac{1}{2}\Big[C\epsilon_A^F + D\gamma_1^F cos(2\theta_i) + D\gamma_2^F sin(2\theta_i)\Big] \quad (3.8)$$

As already recognized in the 1990's by Hart et al. (1996) the isotropic case does not always reconcile with the theoretical tides, and possible sources for the observed differences are non-isotropic properties in the rock and/or grout, irregularities in the borehole and the topography. From inspection of equation 3.6, Roeloff et al. (2010) suggested that shear coupling coefficients may differ if the strainmeter responds also to other components of the strain field in coordinates parallel and perpendicular to each gauge. In such cases, the isotropic case may be seen as the large scale, unperturbed strain field. Following Hart et al. (1996)s' terminology, we refer to such a case as to the *cross-coupled* one, namely the strain measured by the instrument is a combination of the remote strain in the rock formation. Therefore, we relax the condition of a fully isotropic medium, and allow for a certain degree of anisotropy. We firstly imagine that common calibration coefficients for the four gauges exist, but shear coupling coefficients might differ. Hence equation 3.8 becomes:

$$g_i e_i = \frac{1}{2}\Big[C\epsilon_A^F + D_{dif}\gamma_1^F cos(2\theta_i) + D_{eng}\gamma_2^F sin(2\theta_i)\Big] \quad (3.9)$$

We may also imagine a medium in which the isotropy condition is fully relaxed, this means that each gauge can have different coupling coefficients, but also that for each gauge the shear strain coefficients may not coincide. Recasting the problem in the more general form:

$$\begin{pmatrix} e_0 \\ e_1 \\ e_2 \\ e_3 \end{pmatrix} = \begin{pmatrix} c_0 & d_{01}cos(2\theta_0) & d_{02}sin(2\theta_0) \\ c_1 & d_{11}cos(2\theta_1) & d_{12}sin(2\theta_1) \\ c_2 & d_{21}cos(2\theta_2) & d_{22}sin(2\theta_2) \\ c_3 & d_{31}cos(2\theta_3) & d_{32}sin(2\theta_3) \end{pmatrix} \begin{pmatrix} \epsilon_A^F \\ \gamma_1^F \\ \gamma_2^F \end{pmatrix} \quad (3.10)$$

As it was claimed, the widest spread approach consists in comparing the measured strain components against the theoretical ones. Each tidal consituents can be expressed in a sinusoidal form:

$$f(t) = a\,cos(\omega t - \phi) \tag{3.11}$$

or, more practically:

$$f(t) = Acos(\omega t) + Bsin(\omega t) \tag{3.12}$$

where $a = \sqrt{A^2 + B^2}$ and $\phi = atan(B/A)$. A and B are usually referred to as "in-phase" or "real part" and "quadrature" or "imaginary part". Therefore each tidal constituent usually carries two information, namely the amplitude and the phase, and the M_2 and O_1 tides are the most used since they are the less affected by local thermal effects. Equation 3.10 can be written for practical purposes:

$$\begin{pmatrix} e_0^{M_2,R} & e_0^{M_2,I} & e_0^{O_1,R} & e_0^{O_1,I} \\ e_1^{M_2,R} & e_1^{M_2,I} & e_1^{O_1,R} & e_1^{O_1,I} \\ e_2^{M_2,R} & e_2^{M_2,I} & e_2^{O_1,R} & e_2^{O_1,I} \\ e_3^{M_2,R} & e_3^{M_2,I} & e_3^{O_1,R} & e_3^{O_1,I} \end{pmatrix} = \begin{pmatrix} c_0 & \tilde{d_{01}} & \tilde{d_{02}} \\ c_1 & \tilde{d_{11}} & \tilde{d_{12}} \\ c_2 & \tilde{d_{21}} & \tilde{d_{22}} \\ c_3 & \tilde{d_{31}} & \tilde{d_{32}} \end{pmatrix} \begin{pmatrix} \epsilon_A^{M_2,R} & \epsilon_A^{M_2,I} & \epsilon_A^{O_1,R} & \epsilon_A^{O_1,I} \\ \gamma_1^{M_2,R} & \gamma_1^{M_2,I} & \gamma_1^{O_1,R} & \gamma_1^{O_1,I} \\ \gamma_2^{M_2,R} & \gamma_2^{M_2,I} & \gamma_2^{O_1,R} & \gamma_2^{O_1,I} \end{pmatrix} \tag{3.13}$$

where the coupling coefficients c_i and $\tilde{d_{ij}}$ correspond to those in equation 3.10, and the apexes R and I indicate respectively the real and imaginary part of the tides.

However, as it is pointed out by Langbein (2015), usual calibration can lead to poor results for shear components. In fact, Hart et al. (1996) showed that shear strains are more subjected to cross coupling originating from internal inhomogeneities. A calibration approach that has proven to be more robust, is the one proposed in Canitano et al. (2018). In such study, tidal waveforms were reconstructed (instead of adjusting the coefficients to the predicted amplitudes and phases) to calibrate Sacks–Evertson (Sacks et al. 1971) SES-3 borehole strainmeters installed in eastern Taiwan.

In this thesis, we tested an original procedure to carry out the calibration of the Gladwind Tensor strainmeters, starting from the state of art of the traditional calibration techniques available in literature (e.g., Roeloff et al., 2010; Hodgkinson et al., 2013), and following the tidal waveform reproduction proposed by Canitano et al. (2018). As it will be shown in the dedicated Section (i.e., Section 3.4), the developed approach is completely data driven and proposes a new workflow to get the calibrated horizontal strain components starting from the raw measurements.

3.4 Calibration methods

In this section the two methodologies followed to calibrate the Gladwin Tensor strainmeter type, i.e. to find the set of coefficients that relate strain inside the instrument to the actual strain field of the rock formation, will be detailed. The simplest scenario, namely the calibration of strainmeters installed in an isotropic medium (equation 3.8) proved to be unsuitable for all of the instruments taken in consideration during this work of thesis, and common shear coupling coefficients could never be found. We directly admit a certain degree of cross-coupling and allow the shear coupling coefficients to differ. Secondly, we will present the more general situation of a non-isotropic medium. In this section we will provide the reader with the flowchart (Figure 3.3) we follow to calibrate the strainmeters. A more detailed theoretical description of each passage will be presented in Sections 3.4.1 and 3.4.2, and examples, for what concerns the array in Taiwan will be presented in Sections 4.2.1 and 4.2.2, and in Section 5.2, for what concerns the array in Central Italy.

Independently from the methodology adopted, the first step to take consists in separating the tidal response of the gauges among all of the different sources of deformation (Figure 3.3). To this aim we exploited the well documented *Baytap08* software (Tamura et al., 1991), to compare them with the theoretical predictions computed through, for instance, *GOTIC2* (Matsumoto et al., 2001). *Baytap08* exploits a Bayesian modeling procedure to fit time series which contain tidal signals (e.g. tidal gravity, ocean tides, and strain and tilt data) in a least square sense. This software uses the Akaike Bayesian Information Criterion (ABIC) (Ishiguro et al.,1981; Ishiguro, 1981; Ishiguro et al.,1984; Ishiguro and Tamura, 1985) to find the best tidal and crustal deformation model, and separate it from other signals that might be present in the time series (e.g., the long term trend, the effects of atmospheric pressure). *Gotic2* computes solid Earth and ocean tidal loading effects at the surface of an elastic spherical Earth using Green's function based on Gutenberg-Bullen Earth model (Farrell, 1972). Having checked the robustness of the extracted tidal components, thanks to the redundancy of the observations (Section 3.2), we can run preliminary tests on the measured areal strain and differential strain (e.g., *consistency check*). Results of the consistency check suggest whether or not a weighting of the gauges of the GTSM is necessary. Starting off with the simplest method, we carry out the calibration assuming the *quasi-isotropy* of the medium (i.e., a cross-coupling between the shear components of strain field). We check the azimuth of the instrument (i.e., *orientation check*), by rotating the observed shear components, to bring them in the same reference system as the theoretical ones. Lastly we compare the theoretical and measured waveforms of the areal, differential and engineering components.

In case the comparison provides poor results, we further relax the isotropic condition of the medium, and we proceed with the second methodology. In this case, we find the (coupling) coefficients that relate the horizontal strain components in the rock formation to the observed elongation of each gauge. Organizing the coupling coefficients in a matrix as in equation 3.13, namely the *coupling matrix* which is representative of a certain instrument, we can invert it to obtain the *calibration matrix.* Applying such matrix to our data, we can check whether the retrieved coefficients correctly relate our observations to the modeled theoretical strain for the site. Comparisons of the waveforms provide us with an assessment of the correctness of the calibration coefficients retrieved.

As we mentioned in Section 3.3.2, the calibration procedure here presented represents a new data-driven approach which relies on the design of the Gladwin strainmeters. As the methods are completely data driven, they do not require any further information than the precise coordinates of the instrument for a proper modelization of the theoretical Earth's tides. Moreover, we propose, rather than a simple phase and amplitude comparison between observed and theoretical tides, a full waveform one which is supposed to provide robust results as acknowledged by Canitano et al. (2018). As a matter of fact, modeling the whole waveform, rather than seeking for the set of coefficients that reduces the misfit among the tidal measured and predicted constituents (i.e., Roeloff et al., 2010), should yield more accurate results and should allow us to have a better control on the estimated parameters.

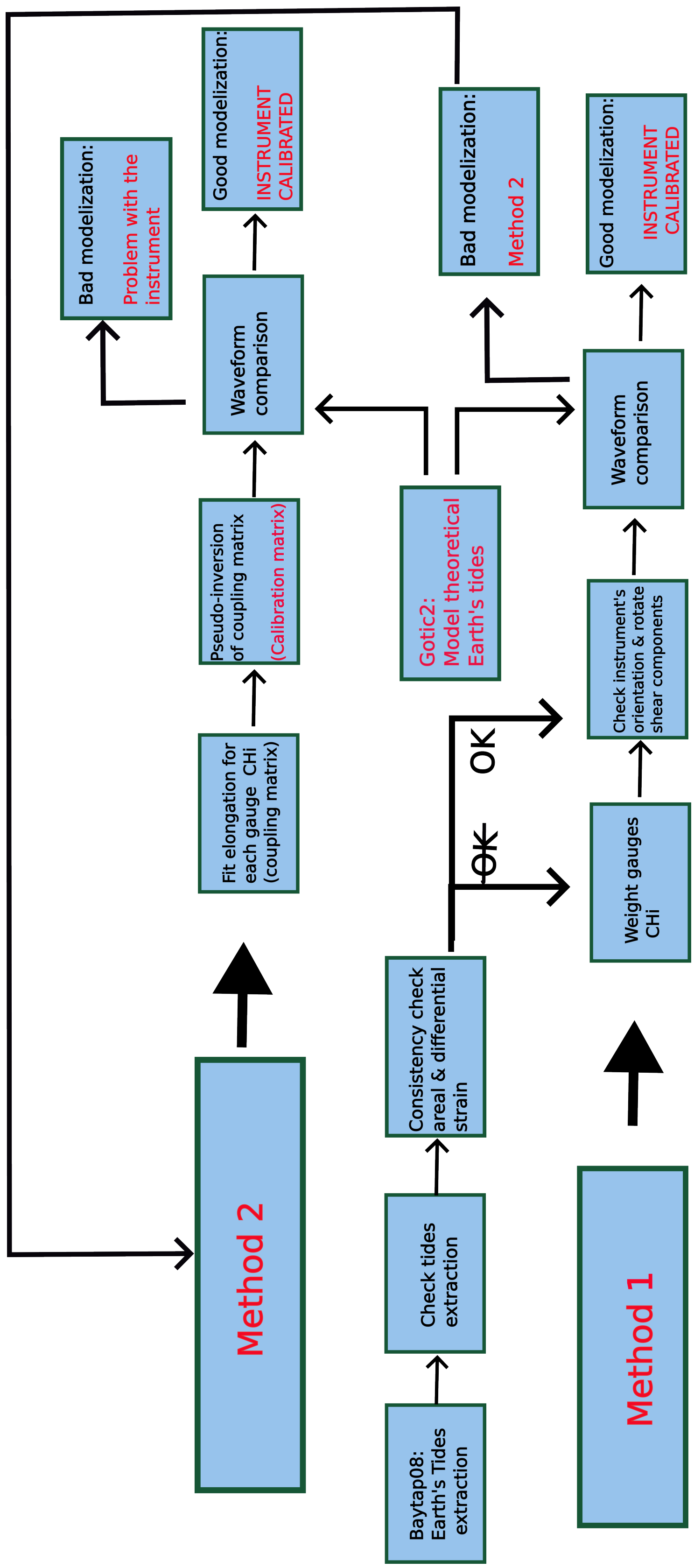

Figure 3.3. In Figure the flowchart of the calibration methodology proposed in this work. The procedure to follow is detailed in Sections 3.4.1 and 3.4.2.

3.4.1 Method 1: Quasi-isotropic calibration

As already mentioned in Section 3.4, our tests suggest that a unique shear coupling coefficient cannot be found for any strainmeter here considered. Therefore, in order to calibrate the GTSMs, we start modeling a cross-coupled medium which we consider representative of a quasi-isotropic situation, hereinafter we refer to such a case as to **Method 1** (equation 3.8). Under this assumption, thanks to the relative orientation of gauges (Figure 3.1), the redundancy of observations of the GTSMs provides two relations for the areal strain and we will refer to them as AR and AR_0:

$$AR = \frac{2}{3} \times (g_0 e_0 + g_1 e_1 + g_2 e_2) \quad = \quad \epsilon_A^I \tag{3.14}$$

$$AR_0 = \quad g_1 e_1 + g_3 e_3 \quad = \epsilon_A^I \tag{3.15}$$

and differential strain, referred to as ED and ED_0:

$$ED = \frac{2}{3} \times (2 g_1 e_1 - g_0 e_0 - g_2 e_2) \quad = \quad \gamma_1^I \tag{3.16}$$

$$ED_0 = \quad g_1 e_1 - g_3 e_3 \quad = \quad \gamma_1^I \tag{3.17}$$

as detailed in Roeloffs et al. (2010) work. The engineering strain (ES) can be obtained through the combination of CH0 and CH2 (here the notation CH_i and e_i is used indifferently):

$$ES = \frac{2}{\sqrt{(3)}} \times (g_0 e_0 - g_2 e_2) \quad = \quad \gamma_2^I \tag{3.18}$$

It should be stressed here that the apex "I" stands for the strain inside the instrument, and that the shear components γ_1 and γ_2 are to be intended in the reference system defined by CH1 and CH3 (i.e. with the E-W axis rotated parallel to to CH1 azimuth).

We first run a consistency check on the two ways of computing areal (equations 3.14 and 3.15) and differential (equations 3.16 and 3.17) strain. Following Roeloff et al. (2010), results obtained using the two (AR_0 and ED_0, equations 3.15, 3.17) and three (AR and ED, equations 3.14, 3.16) gauges-combination should yield the same time history and amplitudes. Differences between the phases and amplitudes point towards an anisotropic medium and different gauges sensitivities (Hodgkinson et al., 2013). Moreover, the differential strain gives a strong indication on the actual azimuth of the instrument, as it will be shown below. As already acknowledged by previous studies (e.g., Canitano et al., 2018) through site tests, although orientation is checked during the installation process, it may not be resolved well enough. This is mainly due to magnetic properties of rocks and/or a malfunctioning of the instrument compass (Hodgkinson et al., 2013). An accurate estimate of the azimuth is a fundamental step for multi-component strainmeters.

In order to correctly weight the four gauges, we seek for a unique set of parameters (g_i in equation 3.8) for both areal and differential strain. g_1 is fixed $= 1$ and subsumed in the coupling coefficients, therefore weights for CH0, CH2, CH3 are expressed relatively to CH1. Having the shear strains correctly re-scaled, we can assess the orientation of the instrument, i.e. the azimuth of CH1 (see Figure 3.1, relative orientations among gauges are assumed to be correct), through the following procedure:

(1) using *Gotic2* software, we compute the strain tensor ϵ_{ij} in the E-W, N-S reference system:

$$\epsilon_{ij} = \begin{pmatrix} \epsilon_{EW} & \epsilon_{EN} \\ \epsilon_{EN} & \epsilon_{NS} \end{pmatrix} \tag{3.19}$$

(2) we iteratively rotate such vector by an angle θ with steps of 1° applying the rotational matrix R:

$$\epsilon_{i'j'} = R^T \epsilon_{ij} R = \begin{pmatrix} \epsilon_{x'x'} & \epsilon_{x'y'} \\ \epsilon_{x'y'} & \epsilon_{y'y'} \end{pmatrix} \tag{3.20}$$

with

$$R = \begin{pmatrix} \cos(\theta) & -\sin(\theta) \\ \sin(\theta) & \cos(\theta) \end{pmatrix} \tag{3.21}$$

and $\epsilon_{i'j'}$ the strain tensor rotated by the angle θ.
(3) at each step we compute the shear strain components:

$$\gamma_1^{x'y'} = \epsilon_{x'x'} - \epsilon_{y'y'} \tag{3.22}$$

$$\gamma_2^{x'y'} = \epsilon_{x'y'} \tag{3.23}$$

(4) we correlate $\gamma_1^{x'y'}$ and $\gamma_2^{x'y'}$ respectively with the two-ways differential strain of equations 3.16 and 3.17, and with the engineering strain of equation 3.18. We seek for the angle which gives the highest Pearson correlation coefficient R (Figure 4.6), and we assume such angle to be the azimuth of CH1.

Once the gauge weights have been adjusted, the (unique) calibration coefficient for areal strain (C in equation 3.9) is found comparing the theoretical waveform and the observations (equations 3.14 and 3.15). Similarly, the shear strain calibration coefficients (D_{dif} and D_{eng} in equations 3.9) can be found once the theoretical deformation in the E-W, N-S reference system has been rotated in the system defined by CH_1 and CH_3.

3.4.2 Method 2: Non-isotropic calibration

As already mentioned in Section 3.3.2, deviations from the isotropic case can emerge from variations in the rock elastic properties and if the strainmeter responds to other components of the strain field. A more complicated situation than the isotropic one can be spotted by inspecting the raw strain time series. The lack of the long term contraction originating from the expanding grout and the borehole itself (Section 3.2) in one or more gauges, together with strong differences among the gauges time series, may point towards the need of a more complex model.

A non-isotropic calibration (hereinafter referred to as **Method 2**) consists in resolving the linear system of equation 3.13, namely finding for each gauge the coefficients that relate elongation e_i and the horizontal strain components in the rock formation (with apex "F"):

$$e_i = c_i \epsilon_A^F + \tilde{d_{i1}} \gamma_1^F + \tilde{d_{i2}} \gamma_2^F \tag{3.24}$$

Once the coupling coefficients are known for every gauge, it is possible to invert the coupling coefficients matrix to obtain the calibration matrix. As the coupling matrix is non-squared, some approximation are needed and a Moore-Penrose pseudoinverse is used. The linear system can be recast in the following fashion:

$$\begin{pmatrix} \epsilon_A^F \\ \gamma_1^F \\ \gamma_2^F \end{pmatrix} = \begin{pmatrix} C_{non-iso}^0 & C_{non-iso}^1 & C_{non-iso}^2 & C_{non-iso}^3 \\ D_{non-iso}^{(0)dif} & D_{non-iso}^{(1)dif} & D_{non-iso}^{(2)dif} & D_{non-iso}^{(3)dif} \\ D_{non-iso}^{(0)eng} & D_{non-iso}^{(1)eng} & D_{non-iso}^{(2)eng} & D_{non-iso}^{(3)eng} \end{pmatrix} \begin{pmatrix} e_0 \\ e_1 \\ e_2 \\ e_3 \end{pmatrix} \tag{3.25}$$

in which the elements of the calibration matrix are explicitly expressed. Applying such matrix to our observations (e_i, $i = 0, 1, 2, 3$), we obtain the strain field components that can be compared with the theoretical ones to check the correctness of the coefficients estimation.

Chapter 4

Taiwan GTSM array

4.1 Seismotectonic setting and installation environment

The island of Taiwan is situated between the Eurasian Plate and the Philippine Sea Plate (Figure 4.1), the former subducting eastward beneath the Philippine Sea Plate in Southwestern Taiwan with a contraction rate of $\sim$ 80 mm/yr (Yu et al., 1997; 1999). In Northeast Taiwan we observe an opposite polarity of subduction, with the Philippine Plate undergoing the Eurasian Plate with an extension rate of $\sim$ 30-40 mm/yr (Shyu et al., 2005). In Eastern Taiwan we find two different geological regions, respectively the Coastal Range to the east and the Central Range to the west, which are separated by the Longitudinal Valley (Canitano et al., 2015). Deformation there is accommodated by two main structures, the Longitudinal Valley Fault and the Central Range Fault (Shyu et al. 2006). The former shows a prevalent oblique slip mechanism on its Southern portion, and left-lateral strike-slip mechanism on its Northern portion (Shyu et al. 2005; Yu and Kuo 2001); whereas the latter shows a prevalent thrust mechanism (Canitano et al., 2015), associated with the Central Range mountain building process at a rate of $\sim$ 17 mm/yr (Huang et al., 2000). In Western Taiwan the collision of the Eurasian Plate and the Philippine Sea Plate results in a fold-and-thrust belt, deformation here is accommodated by a series of thrust faults and lateral faults (Shyu et al., 2005).

Due to its pivotal position at the junction of the Eurasian Plate and the Philippine Sea Plate, Taiwan is in one of the most active seismic regions in the world (Zhuang et al., 2005), with numerous destructive earthquakes striking in recent times (e.g., Hsu, 1980. See also map in Figure 4.2), including the well documented 1999 Chi-Chi M_w 7.6 earthquake (e.g., Shin et al., 2000; Wang et al., 2000; Shin, 2004). Studies of background seismicity rates conducted in the area, which allow to separate the island into five seismotectonic zones (Zhuang et al., 2005; Figure 4.1), highlight how Taiwan is mainly characterized by minor, light and moderate earthquakes (i.e., $M_w \sim 4$ - 6, Obi et al., 2017). After the major 1999 Chi-Chi earthquake, several institutions started a project to enhance the observational network of Taiwan, including 11 Gladwin Tensor strainmeters.

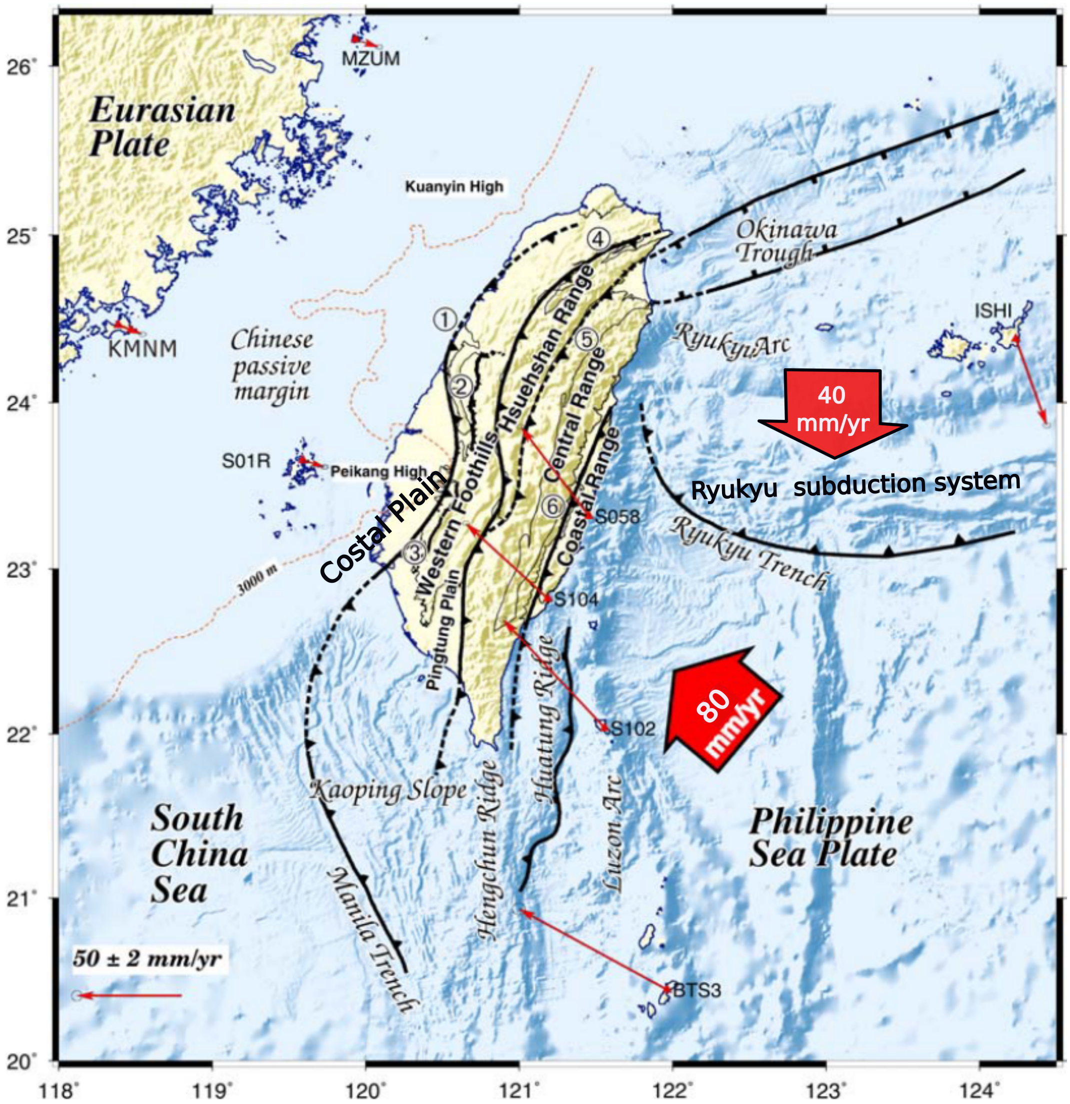

Figure 4.1. In Figure the seismotectonic map of Taiwan. Subduction zones are indicated through solid line with triangles on the overriding plate. Numbers from 1-6 indicate the traces of the major structures of the area (respectively the Chelungpu fault, the Chuchih fault, the Lishan fault and the Longitudinal Valley fault). Large red arrows show the direction and intensity of the subducting plates. Small red arrows show the GPS velocity with respect to Euroasian Plate from Yu et al. (1999). The five seismotectonic regions are also indicated: 1) the Coastal Plain; 2) the Western Foothills and Hsuehshan Range; 3) the Central Range; 4) the Ryukyu subduction system; 5) the Coastal Range (Zhuang et al., 2005). the Figure has been modified from figure 1 of Lin et al. (2010).

The first GTSMs were installed in 2003 in southwestern Taiwan as an attempt to intensify the earthquakes monitoring project of the Central Geological Survey (CGS) after the 1999 Chi-Chi mainshock. The first instruments were installed in the Tsengwen reservoir (Figure 4.2) and were followed, respectively two and three years later, by the installation of further instruments in the Hsinchu region and Nantou county. These strainmeters are supposed to enhance the GPS arrays capability of monitoring the plate boundary tectonics of Taiwan.

The first instruments, namely RNT and RST (table 4.1 and Figure 4.2), were installed on the opposite side of the Tsengwen reservoir where topographic effects are particularly significant. Topography is steep for GTSMs in the Hsinchu area (table 4.1 and Fig. 4.2) and landslides have affected these sites. Instruments deployed in the Nantou county (DARB, TAIS and TSUN, table 4.1) are located on a high topography close to escarpments. Installation in steep areas is often necessary, however it has to be kept in mind that this affects the noise level in the data. The last instruments were installed in the Taipei area on a flat terrain but in an highly antrophized area.

Station	**long (°)**	**lat (°)**	**alt(m)**	**dep(m)**	**Array name**	**Environment**
RNT	120.70	23.33	252	200	Tsengwen reservoir	hill / mountain
RST	120.50	23.24	110	224	Tsengwen reservoir	hill / mountain
DARB	120.74	23.46	953	199	Nantou county	nerby Zengwun river
TAIS	120.63	23.54	790	200	Nantou county	hill / mountain
TSUN	120.70	23.48	1370	198	Nantou county	hill / mountain
PFMT	121.20	24.68	496	166	Hsinchu region	hill / mountain
BMMT	121.05	24.68	195	199	Hsinchu region	hill / mountain
SANS	121.36	24.99	80	200	Taipen area	plain / low terrain
JING	121.48	24.99	19	192	Taipen area	plain / low terrain
SLIN	121.37	24.97	***	183	Taipen area	***
CINT	121.24	24.73	505	198	Hsinchu region	nerby river

Table 4.1. Detailed informations of the GTSM arrays deployed in Taiwan.

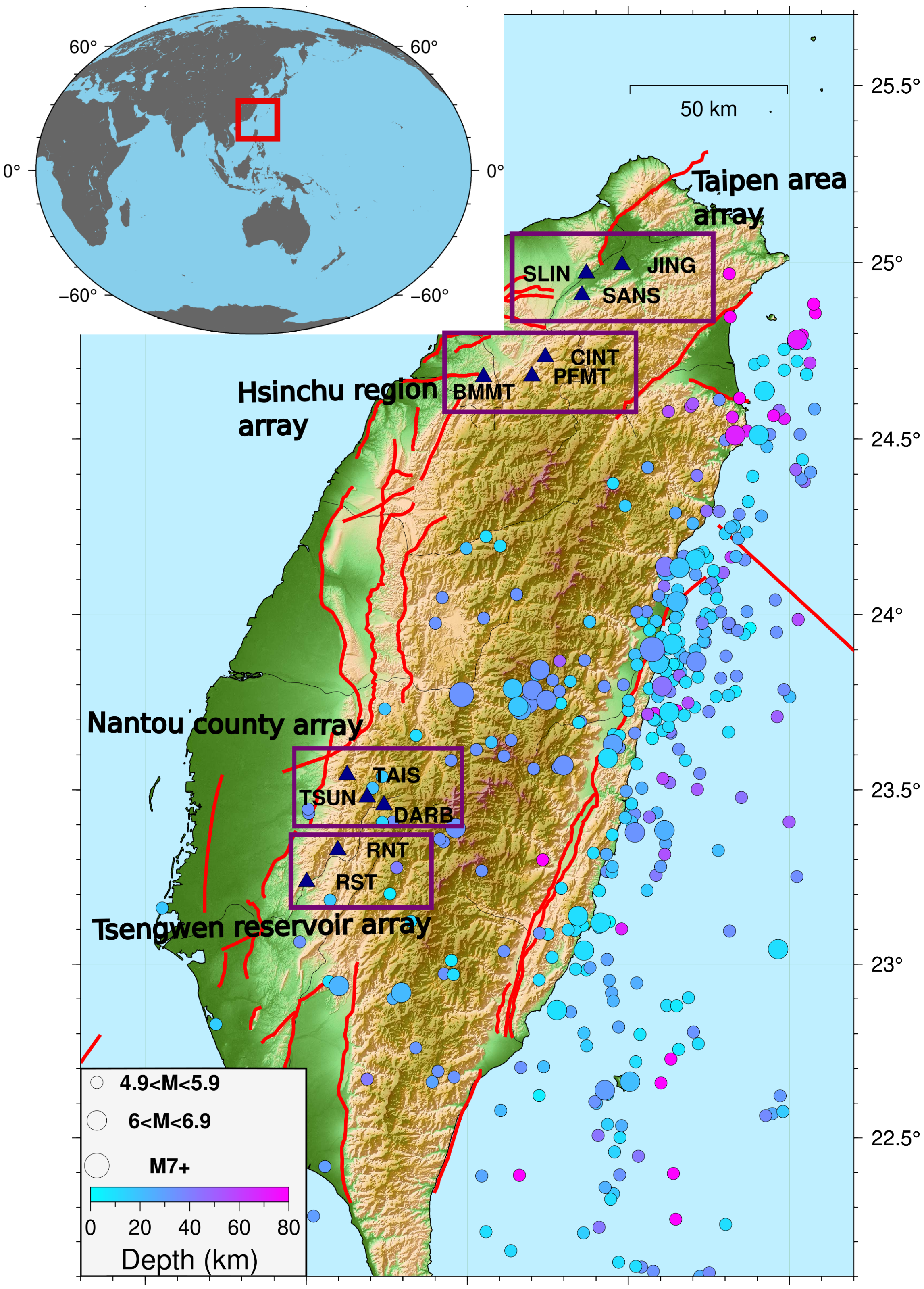

Figure 4.2. In Figure the Taiwanese strainmeter arrays (blue triangles) considered for the calibration. Purple rectangles separate the different arrays. Red lines mark the traces of the principal documented faults in the area. Colored circles show the events with $5 \leq M$ in the time span 1980-2023, from USGS catalogue (https://earthquake.usgs.gov/earthquakes/search/).

4.2 Taiwan GTSMs calibration results

In this section the results of the procedure detailed in Subsections 3.4.1 and 3.4.2 will be provided. As we are using the tidal waveforms present in the strain time series to calibrate the strainmeters, independently from the methodology adopted, the first step concerns the separation of such signals from the others present in the strain time series. To this aim, as already mentioned in Section 3.4, we exploit the well-known software Baytap08 to retrieve the tidal constituents into the total strain signal (Figure 4.3). The specific time span analyzed for each GTSM is reported in Table 4.2. Analyzed periods are chosen in order to consider the longest time series with no significant ($\sim days$) data gaps. As a matter of fact, about $\sim 3-4$ months of data are needed in order to carry out a robust tidal analysis. On these time scales barometric pressure plays a key role in strain measurements, therefore we aim at separating this component in the total deformation time series (lower panles of Figure 4.3). Although Baytap08 tidal analysis proves to be very robust, including the effect of air pressure helps to retrieve more accurate tidal related deformations. Observing that the residuals do not contain significant signals with 12 or 24 hours period, we can assume that tides have been properly separated. This is also confirmed by the spectral analysis carried out (Figure 4.4), which clearly shows the reduction in the content of signals with periods of 12h and 24h (vertical lines) after the tidal analysis with Baytap08. In order to double check the correctness of the tidal extraction, we apply a pass-band filter around the 12 and 24 hours to the raw data. At these time scales, we expect the tidal signal to be the dominant one, and hence the filtered data and Baytap08's output to be consistent (small differences can arise as Baytap08 models only specific tidal constituents. On the other hand, raw data contain also both further tidal constituents and other sources of strain, e.g. thermal effects). As shown in Figure 4.5, Baytap08's results are consistent with pass-band filtered raw data.

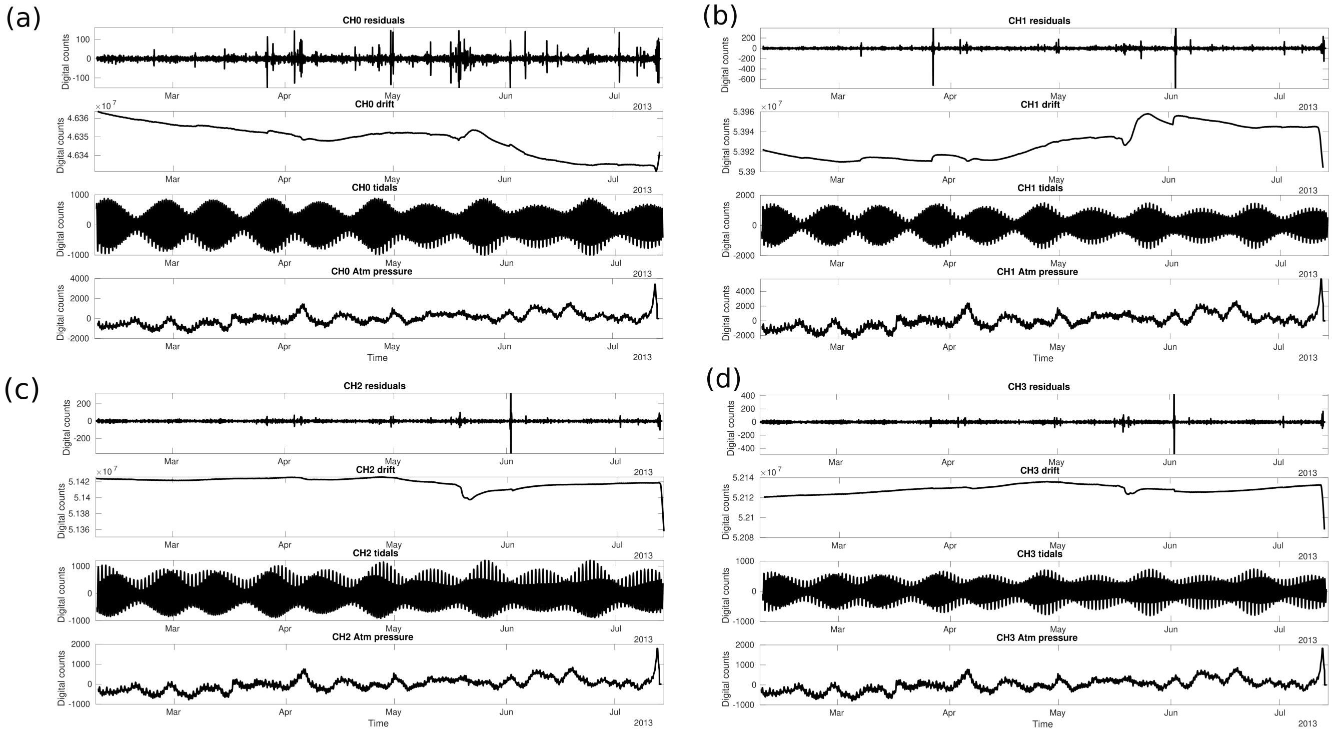

Figure 4.3. Example of the Baytap08 analysis results for DARB's four gauges CH_0, CH_1, CH_2, CH_3 (respectively panels (a), (b), (c), (d)). For each of the four gauges, plots represent, from top to bottom, respectively the residuals, the estimated long term trend, the recorded Earth's tides and the response to barometric pressure. The residual is given by the original time series removed of the long term, the tidal content and the effect of barometric pressure.

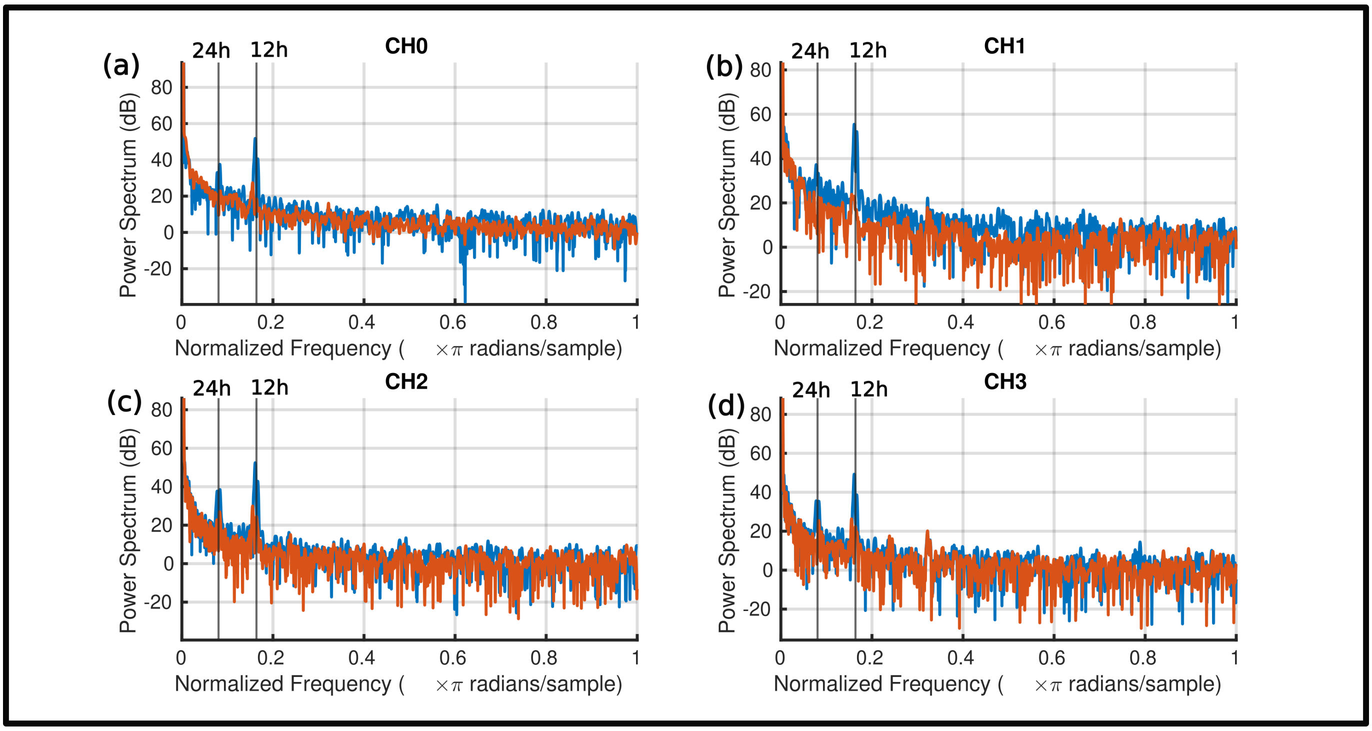

Figure 4.4. Power spectrum of the Baytap08 analysis results for DARB's four gauges CH_0, CH_1, CH_2, CH_3 (respectively panels (a), (b), (c), (d)). For each panel, in blue the raw deformation measurements, and in orange the residuals after removing the tides. Vertical lines mark the normalized frequency corresponding to the 12h and 24h.

Station	1^{st} **- last epoch analyzed**	**Number of days**
RNT	25/3/2012-8/7/2012	135
RST	7/12/2004-10/4/2005	124
DARB	8/2/2013-14/7/2013	156
TAIS	12/9/2013-10/7/2014	301
TSUN	20/11/2006-15/11/2007	360
PFMT	26/12/2009-22/11/2010	331
BMMT	26/1/2017-17/10/2017	264
SANS	12/10/2011-3/6/2012	235
JING	12/6/2013-22/7/2014	400
SLIN	12/3/2016-14/9/2016	186
CINT	1/8/2013-16/3/2014	227

Table 4.2. Details of the time span analyzed through Baytap08 for each GTSM in Taiwan.

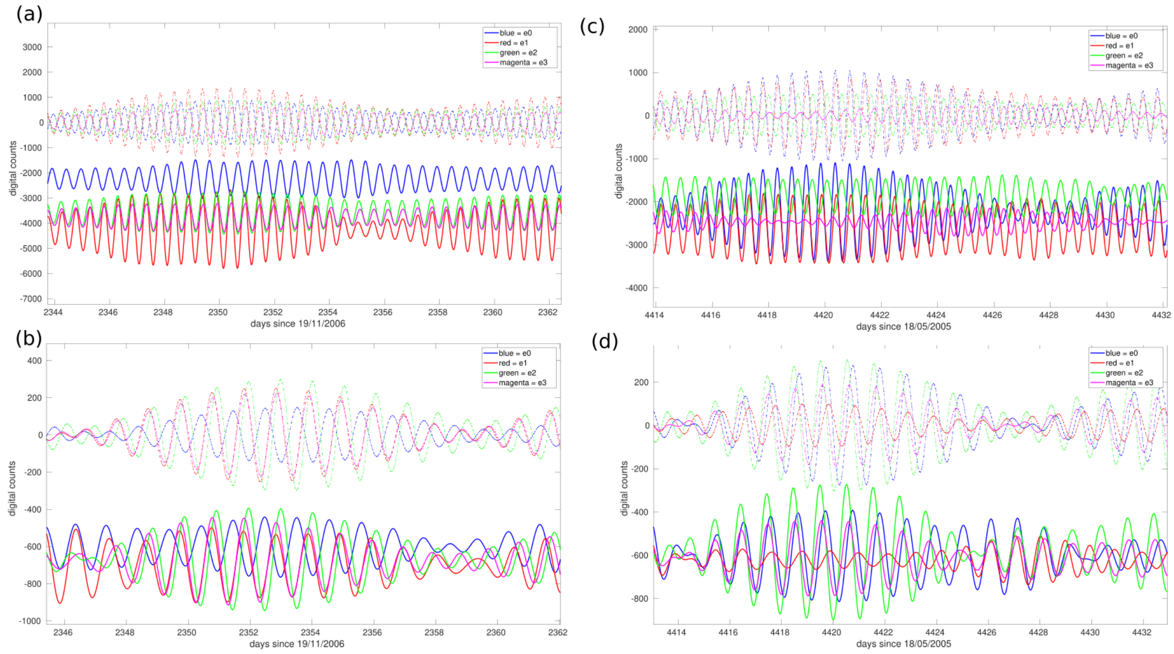

Figure 4.5. (a) and (c) comparison of a 12h pass-band filter applied to raw data (solid lines) and to tidal signals outputted from Baytap08 (dashed lines) respectively for DARB and BMMT GTSMs. (b) and (d) same as (a) and (c) for a 24h pass-band filter.

4.2.1 Method 1

In order to carry out the calibration of the GTSMs under the quasi-isotropic assumption, we firstly need to assess whether the two expressions for the areal (equations 3.14 and 3.15) and differential strain (equations 3.16 and 3.17) yield the same time history (Hodkinson et al., 2013). The correlation between AR and AR_0, and ED and ED_0 results to be generally significant ($> 90\%$) for most of the GTSMs, except areal strain for $PFMT$ and $JING$, and differential strain for $SANS$ (Table 4.3). However only two strainmeters (RNT and RST) also show similar amplitudes (Figure 4.7(a,b)), i.e. equal gains of the gauges. To properly weight the strainmeters channels we exploit the redundancy of observations of GTSMs. Equalizing equations 3.14 and 3.15 (or equivalently equations 3.16 and 3.17), we obtain:

$$e_1 = 2 \times g_0 e_0 + 2 \times g_2 e_2 - 3 \times g_3 e_3 \tag{4.1}$$

through a least square minimization, gauge weights g_0, g_2, g_3 relative to g_1 can be found (the gain of CH_1 will be subsumed into the calibration coefficients). A re-scaling of CH_i can significantly reduce the variance of the differences between the 2 ways of computing the areal strain (and equivalently the differential strain), for 9 of the 11 strainmeters analyzed (Table 4.3), as shown for instance in Figure 4.7(b-j) for JING and SANS. Once

AR and AR_0 have properly been readjusted with the weights g_i, the quasi-isotropic calibration coefficient for areal strain C_{iso} can be found simply comparing them with the theoretical waveforms computed through *Gotic2*. Results for the 11 GTSMs are summarized in Table 4.5 and examples are provided for TSUN, DARB and RST (Figure 4.8). Contextually, uncertainties are assessed using the redundancy of the measurement of the GTSMs, namely through the semi-difference between the calibration coefficient from AR and AR_0.
As already discussed (Section 3.4.1), instruments orientation is generally checked after installation. Following the procedure of Section 3.4.1, we can thus have an estimation of CH_1 azimuth θ_1 (Figure 4.6) and, assuming the relative orientation of gauges to be correct, the azimuth for all gauges (see Figure 3.1). Having the orientation adjusted (namely having theory and observations in the same reference system), the measured shear strains and the theoretical ones are related by the simple calibration coefficient D^{dif}_{q-iso} and D^{eng}_{q-iso} (Table 4.5). Again, uncertainties associated with D^{dif}_{q-iso} are estimated as the semi-difference between the calibration coefficient from ED and ED_0. Results of the calibration of the strain components for TSUN, DARB and RST are reported in Figure 4.8.

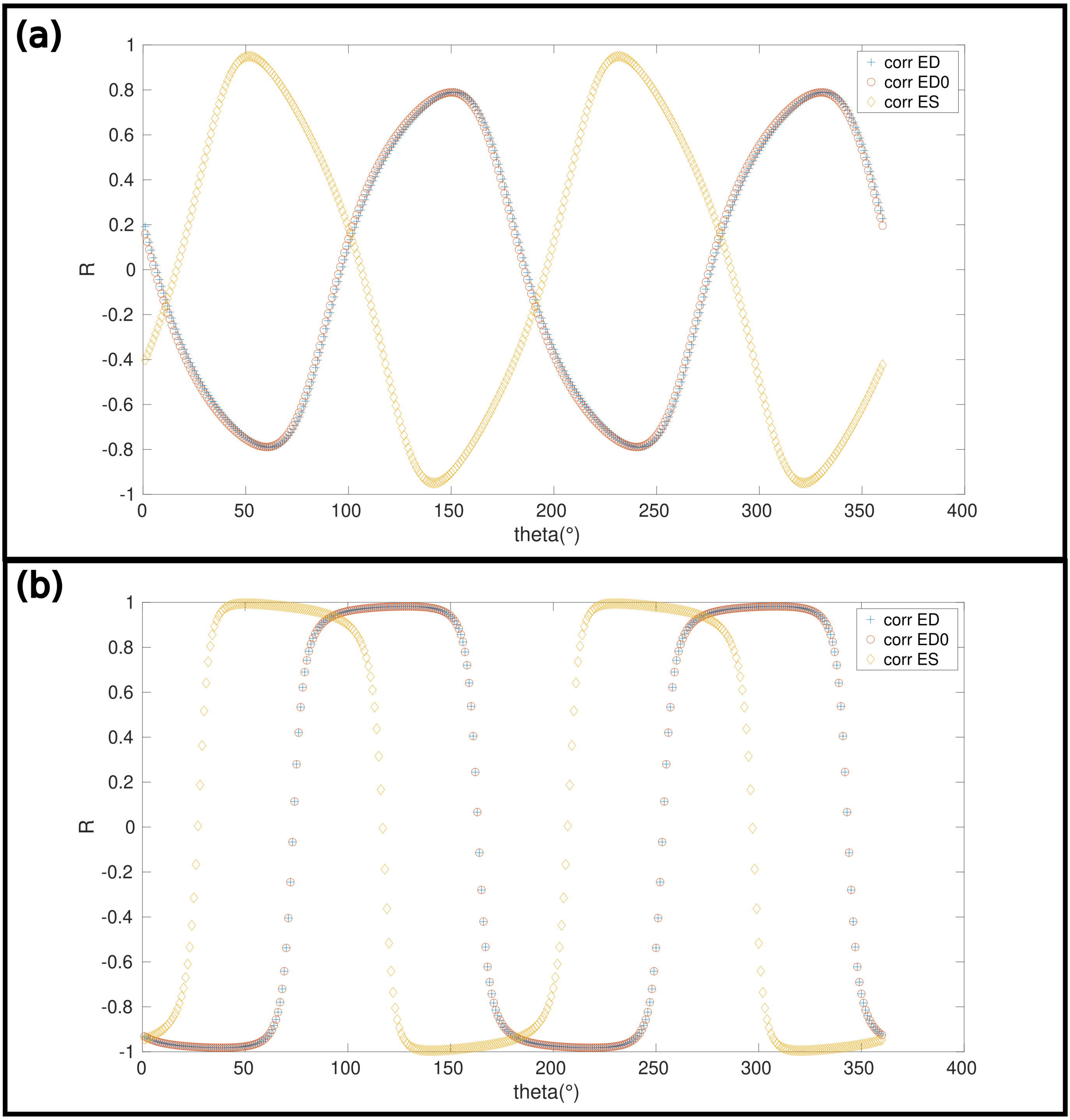

Figure 4.6. Example of the procedure adopted to correct for the instrument azimuth (Section 3.4.1), for (a) CINT and (b) TAIS. Blue crosses mark the correlation between theoretical differential strain and ED, orange circles mark the correlation with ED_0 and yellow diamonds mark the correlation between theoretical engineering strain and ES.

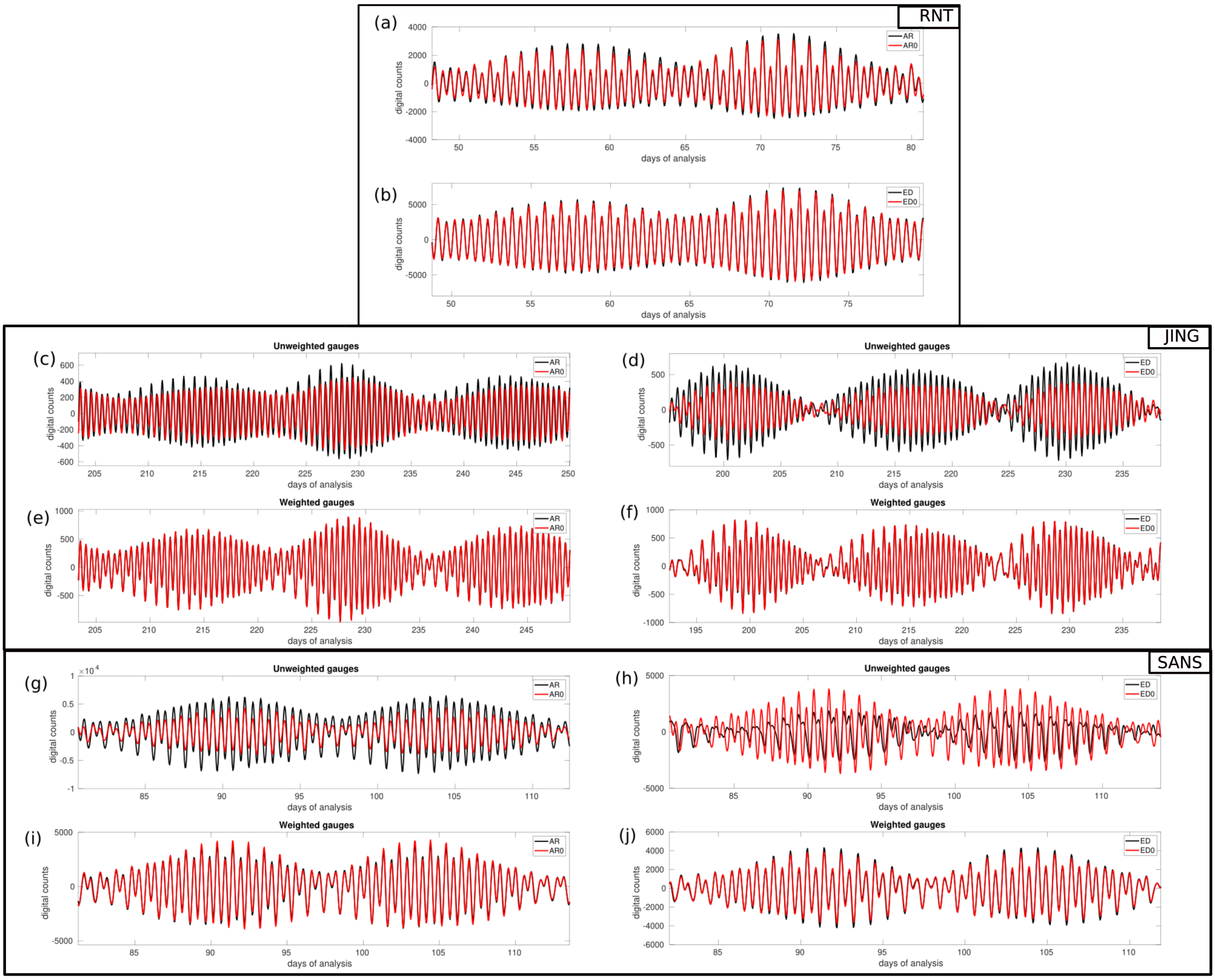

Figure 4.7. Examples of the weighting of gauges described by equation 4.1. In panels (a) and (b) respectively the comparison of the two ways areal and differential strain for RNT (weights of gauges $g_i = 1$, $i = 0, 1, 2, 3$). Panels (c),(e) and (g),(i) show areal strain before and after weighting the CH_i respectively for JING and SANS. Equivalently, panels (d),(f) and (h),(j) show weighting differential strain before and after weighting for the same sites.

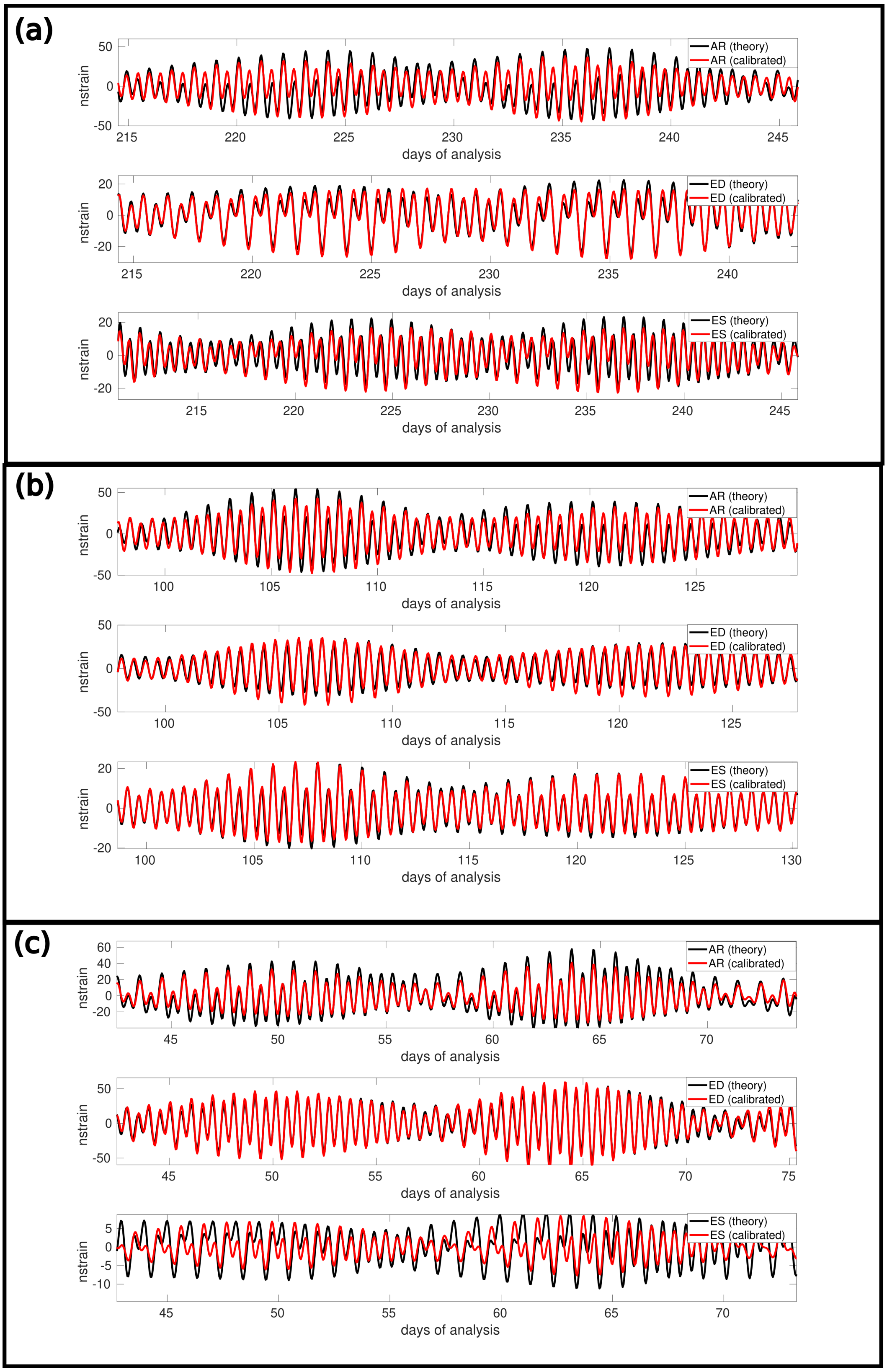

Figure 4.8. Areal (upper panels), differential (central panels) and engineering (lower panels) strain calibration for (a) TSUN, (b) DARB, (C) RST. Back lines represent the theoretical waveforms as computed through *Gotic2*, red lines the calibrated strain components.

Station	**R(unweighted)** areal strain diff. strain	g_i	**R(weighted)** areal strain diff. strain	**variance reduction** (%)
RNT	0.9889 0.9977	1 1 1 1	\	\
RST	0.9921 0.9765	1 1 1 1	\	\
DARB	0.9969 0.9677	0.10 1 0.87 0.10	0.9944 0.9943	98
TAIS	0.8411 0.9767	0.13 1 0.28 0.35	0.9994 1.0000	99
TSUN	0.9849 0.9720	1.63 1 1.84 1	0.9889 0.9920	90
PFMT	0.0398 0.9962	2.09 1 2.09 1	0.9266 0.9949	87
BMMT	0.9963 0.9804	0.51 1 0.52 0.82	0.9999 1.0000	99
SANS	0.9723 0.4719	0.39 0.29 1 0.83	0.9927 0.9930	98
JING	0.8530 0.9477	1.44 1 3.65 2.68	0.9994 0.9992	99
SLIN	0.9936 0.9330	0.10 1 0.68 0.18	0.9922 0.9911	75
CINT	0.9434 0.9311	0.53 1 2.20 0.95	0.9937 0.9932	91

Table 4.3. In table the weights g_i, the correlation coefficients R between the two ways areal and differential strain before and after the weighting of gauges, and the variance reduction.

Station	**R(areal strain)** (%)	**R(diff. strain)** (%)	**R(eng. strain)** (%)
RNT	98.7 ± 0.2	97.3 ± 0.3	64
RST	98.1 ± 0.5	97.7 ± 0.8	68
DARB	94 ± 1	94.6 ± 0.8	98
TAIS	49.7 ± 0.2	98.21 ± 0.01	95
TSUN	87 ± 3	95.8 ± 0.4	89
PFMT	90 ± 5	93 ± 1	84
BMMT	96.15 ± 0.17	98.17 ± 0.05	78
SANS	90 ± 2	78.7 ± 0.3	9
JING	95.2 ± 0.2	70.0 ± 0.2	32
SLIN	92 ± 1	91.0 ± 0.3	16
CINT	76.7 ± 0.2	79.0 ± 0.1	89

Table 4.4. In table the Pearson correlation coefficients R among the calibrated strain components through Method 1 and theoretical ones are summarized.

Station	$C_{q-iso}\left(\frac{nstrain}{counts}\right)$	$D_{dif}\left(\frac{nstrain}{counts}\right)$	$D_{eng}\left(\frac{nstrain}{counts}\right)$	θ (°)
RNT	0.0169 ± 0.0009	0.007 ± 0.003	0.0037	14.5 ± 1.5
RST	0.026 ± 0.009	0.011 ± 0.001	-0.0024	113 ± 7
DARB	$-0.02930 \pm 2 \times 10^{-5}$	0.026 ± 0.004	-0.0175	7 ± 4
TAIS	0.1416 ± 0.0001	$0.0555000 \pm 3 \times 10^{-7}$	-0.0268	128
TSUN	-0.0538 ± 0.0011	0.0273 ± 0.0015	-0.0162	149 ± 1
PFMT	0.0640 ± 0.0016	0.0114 ± 0.0002	-0.0044	60 ± 1
BMMT	$-0.0449 \pm 2 \times 10^{-6}$	$0.026000 \pm 4 \times 10^{-6}$	-0.0092	70
SANS	-0.0087 ± 0.0004	0.0049 ± 0.0001	-5.68×10^{-4}	56.5 ± 1.5
JING	$-0.04780 \pm 2 \times 10^{-5}$	0.0239 ± 0.0001	-0.002	112
SLIN	-0.0464 ± 0.0014	0.0354 ± 0.0011	-0.0038	43.5 ± 1.5
CINT	-0.0149 ± 0.0003	0.0103 ± 0.0004	-0.0060	150.5 ± 0.5

Table 4.5. In table the calibration coefficients and the azimuth of CH_1 for the 11 GTSMs are summarized.

4.2.2 Method 2

Following the approach presented in Figure 3.3, we notice from Table 4.4 that for six strainmeters (i.e., RNT, RST, TAIS, SANS, JING and SLIN) at least one of the strain components is weakly (Pearson coefficient< 70%) correlated with theory. For this reason we believe that a calibration with a more complex model is needed. Hence we completely relax the isotropic assumption and we proceed with the methodology of Section 3.4.2. In this section calibration results obtained following Method 2 (Section 3.4.2) will be given, and in particular it will be shown the calibration matrix, which relates the observed elongations e_i and the strain components (equation 3.25).

Results of calibration are summarized in Table 4.6. For JING and SANS strainmeters, as an example, the graphical solution of equation 3.24 is provided (Figures 4.9 and 4.10). For the same sites, in Figures 4.11 and 4.12, the final comparison of the calibrated time series (i.e., the linear system expressed by equation 3.25) is shown. We can observe from Table 4.7 a general improvement in the correlation among the measured strain components and the modeled ones. This is likely due to the greater flexibility that Method 2 offers, even though this requires the addition of further complexities to our model. A comparison and discussion of the results of Method 1 and 2 will be detailed in Section 4.3.

Station	$C_{non-iso}\left(\frac{nstrain}{counts}\right)$	$D^{dif}_{non-iso}\left(\frac{nstrain}{counts}\right)$	$D^{eng}_{non-iso}\left(\frac{nstrain}{counts}\right)$
RNT	0.0039	0.0098	-0.0021
	0.0197	0.0004	0.0101
	0.0135	-0.0101	0.0034
	0.0054	-0.0041	-0.0016
RST	0.0022	-0.0040	0.0054
	0.0188	-0.0155	-0.0018
	0.0003	0.0087	-0.0026
	0.0188	-0.0046	0.0059
TAIS	-0.0246	-0.0123	-0.0068
	-0.0828	0.0300	-0.0434
	-0.0962	0.0476	-0.0252
	0.0196	-0.0054	0.0254
SANS	-0.0196	0.0297	-0.0187
	0.0031	0.0162	0.0090
	-0.0056	-0.0140	-0.0016
	-0.0044	0.0051	-0.0043
JING	-0.0134	0.0085	0.0168
	-0.0438	-0.0524	0.0176
	-0.0857	-0.0134	-0.0071
	-0.0772	-0.0032	-0.0024
SLIN	-0.0473	0.0525	-0.0520
	-0.0255	0.0716	-0.0052
	0.0212	-0.0833	0.0615
	0.0127	-0.0869	0.0427

Table 4.6. In table the calibration coefficients retrieved using Method 2 are summarized (see equation 3.25).

Station	**R(areal strain)** (%)	**R(diff. strain)** (%)	**R(eng. strain)** (%)
RNT	98.2	99.5	99.0
RST	98.6	98.2	97.1
TAIS	98.7	99.2	99.5
SANS	97.4	70.2	79.7
JING	98.8	97.8	98.8
SLIN	99.4	74.5	79.0

Table 4.7. In table the Pearson correlation coefficients R among the calibrated strain components through Method 2 and theoretical ones are summarized.

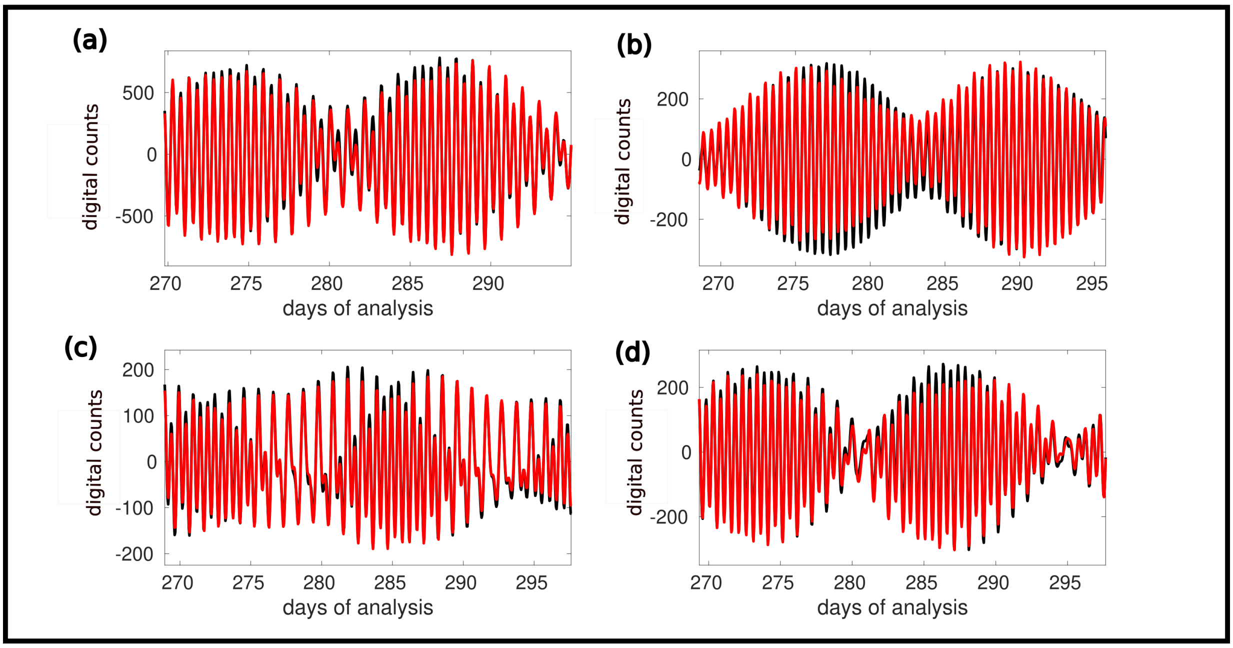

Figure 4.9. Elongation e_i, $i = 0, 1, 2, 3$, of JING (respectively panels (a), (b), (c), (d)). Black lines represent the observed elongations (left-side hand of equation 3.24) while red lines the theoretical ones (right-side hand of equation 3.24).

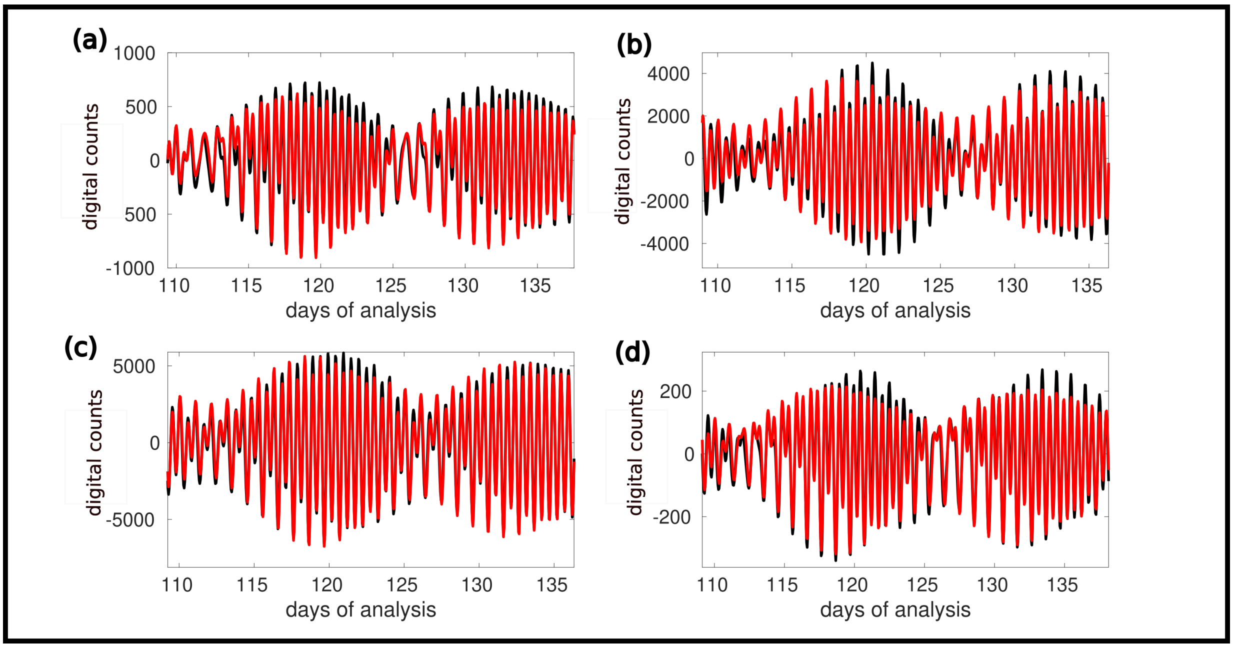

Figure 4.10. Same as figure 4.9 for SANS strainmeter.

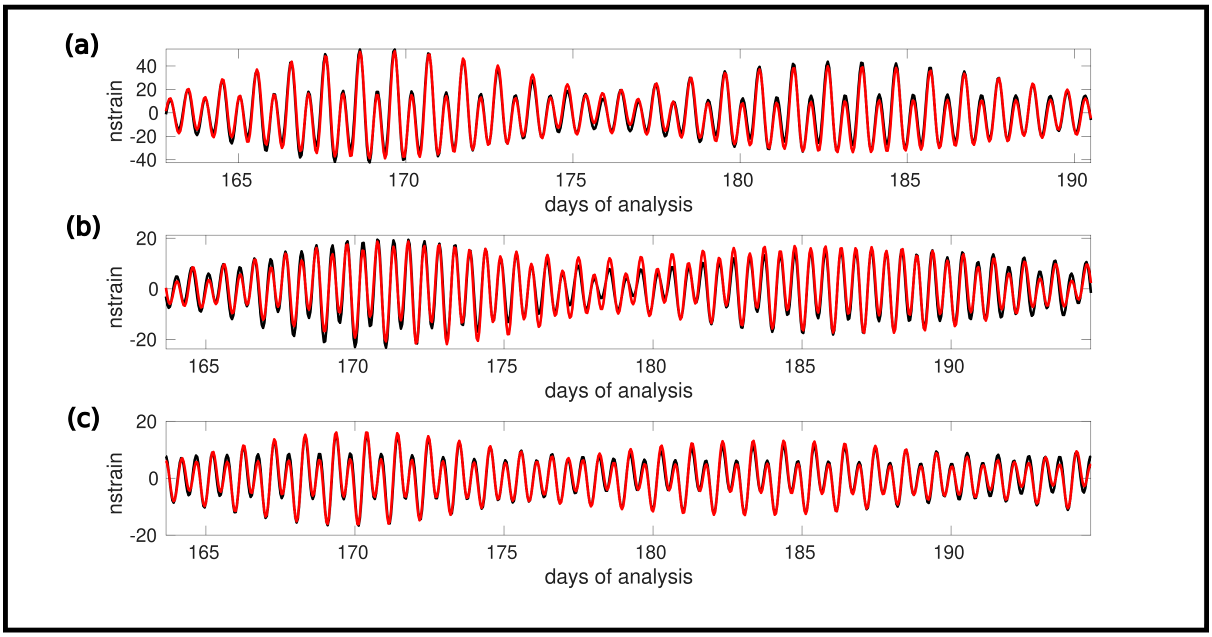

Figure 4.11. (a) Areal strain, (b) differential strain and (c) engineering strain calibration of JING following Method 2 (Section 3.4.2). Red lines represent the theoretical waveforms as computed through *Gotic2*, black lines the calibrated strain components.

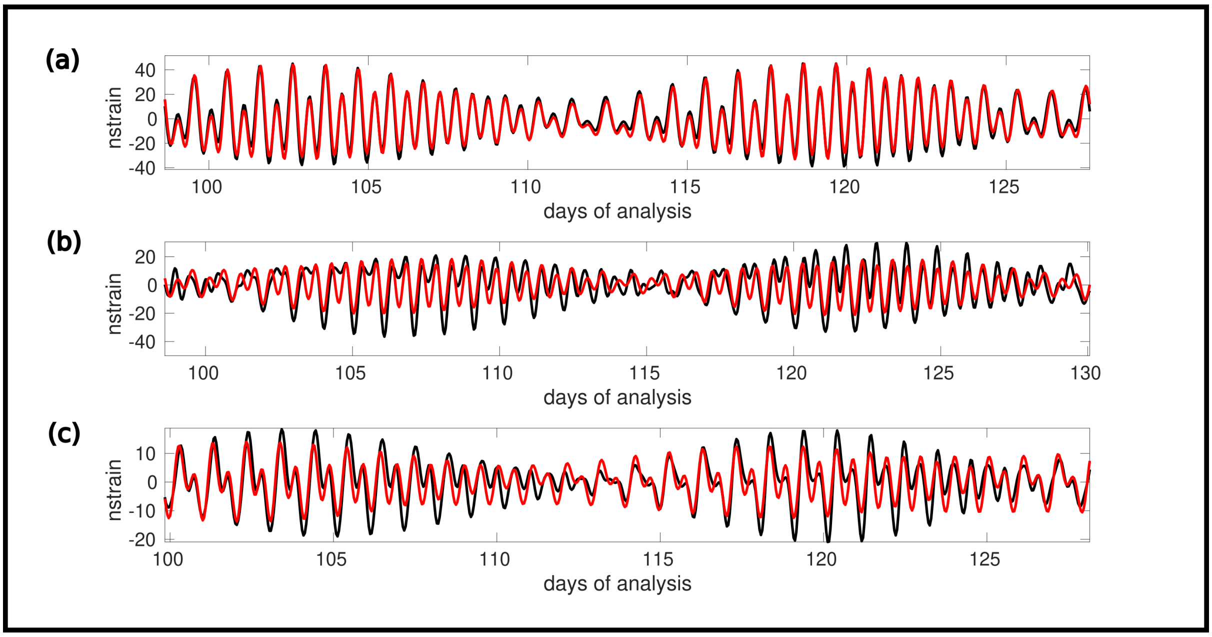

Figure 4.12. Same as figure 4.11 for SANS strainmeter.

4.3 Comparison between methods

In this section we will discuss the differences between the calibration carried out following Method 1 and Method 2. If, on the one hand, the two ways calibration of Method 1 (Section 3.4.1) are expected to give a similar result as they rely on the same assumptions, on the other hand Method 2 might lead to a different outcome, mainly due to the further relaxation of the condition of isotropy. A comparison among the areal strain is straightforward, however the calibration of the shear components also includes the azimuthal direction, namely the reference system we put ourselves in. As a matter of fact, Method 2 relates our observations and the strain components in the rock formation in a reference system NS-EW (equation 3.25). On the other hand, since in Method 1 the theoretical shear components are rotated before being compared with the observed ones (equation 3.20), they are referred to the reference system defined by CH_1 and CH_3.

Before carrying out any graphical comparison, we firstly need to notice that the dominant signal in the strainmeter time series is the long term trend of the perturbed local stress field due to the drilling. As acknowledged by Barbour in his PhD dissertation (Barbour, 2014), the secular trend is generally modeled through the sum of decaying exponentials. However, in many cases during the drilling of the borehole, a circulation of fluids is triggered causing further pore-fluid pressure transient perturbations (Day-Lewis, 2007). The latter long term behaviour can be observed, for instance, in BMMT areal strain time series (upper panel Figure 4.13a), whereas the former one in JING areal strain time series (lower panel of Figure 4.13a). For a clearer comparison, in Figure 4.13b, we show a zoom of the first ~ 60 days of the time series shown in Figure 4.13a. Due to the different magnitude of the relaxation, areal strain in Figure 4.13b are normalized. In order to better compare the strainmeter time series, data need to be detrended subtracting a decay in the form proposed by Gwyther et al. (1996):

$$f(t) = C + mt + A_1 e^{\frac{t}{\tau_1}} + A_2 e^{\frac{t}{\tau_2}} \tag{4.2}$$

However, we sometimes have observed a residual quadratic term in the time series detrended through equation 4.2, which we deem to be related to the functional form used to remove the trend rather than an actual strain signal. Hence, to obtain a more accurate detrending of the time series, for such sites, we will use a functional form like:

$$f(t) = C + mt + A_1 e^{\frac{t}{\tau_1}} + A_2 e^{\frac{t}{\tau_2}} + Bt^2 \tag{4.3}$$

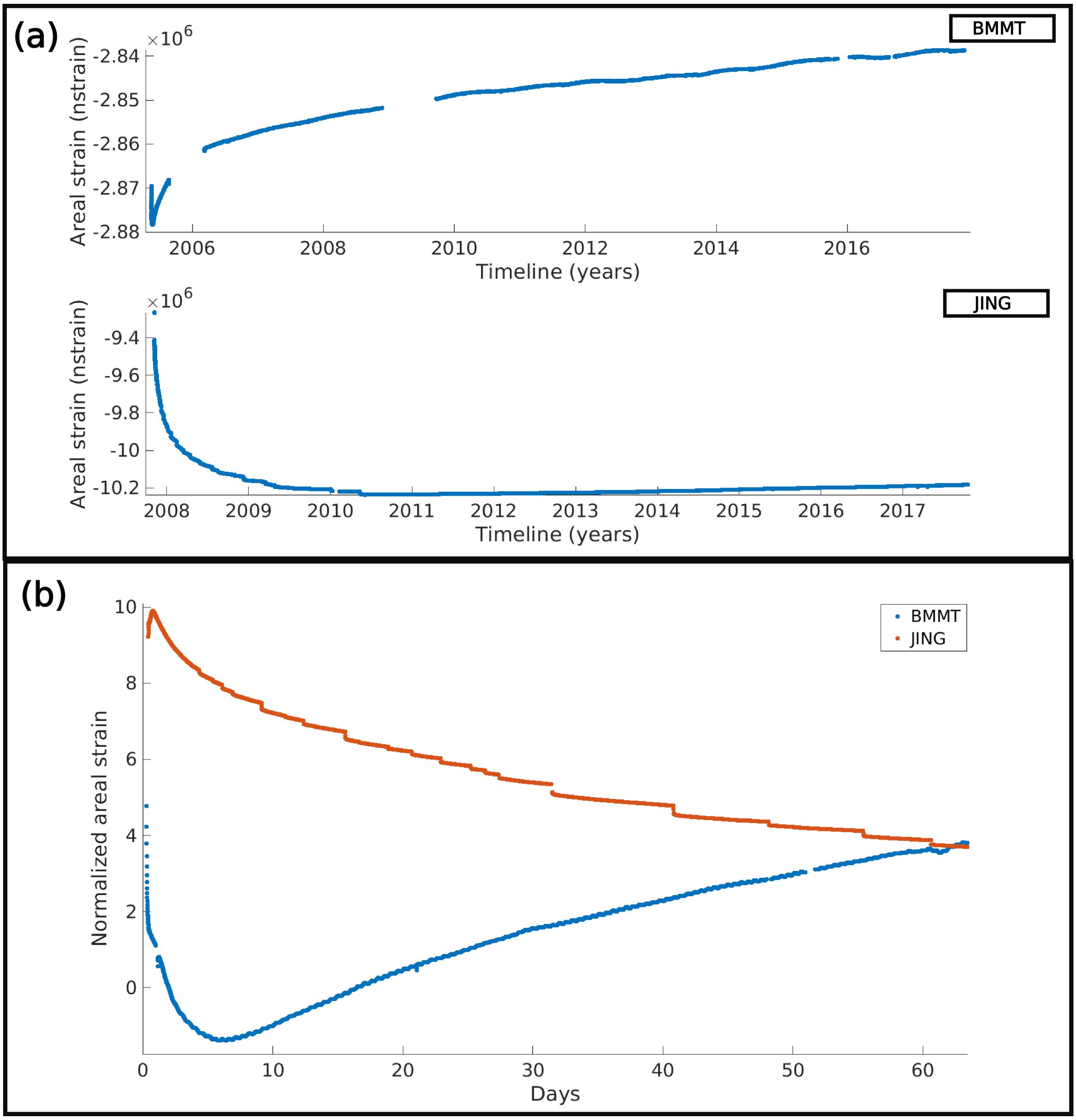

Figure 4.13. In Figure (a) *AR* following Method 1 for BMMT JING GTSMs is shown (respectively upper and lower panel). Figure (b) is a zoom of the first $\sim$ 60 of (a), *AR* time series are normalized to have mean value = 0 and standard deviation = 1. The non-monotonic trend of BMMT is representative of a pore-fluid pressure redistribution (Barbour, 2014).

Starting off with a comparison between the two ways areal strain is computed following Method 1, we can observe that there is a general good agreement with correlations $> 90\%$ for eight of the eleven strainmeters (second column of Table 4.8). Strainmeters that make exception are CINT and SANS. Looking at the third column of Table 4.8, we notice that high correlation holds also for the two ways differential strain, with just RST and CINT making exception. RST, SANS and CINT case will be analyzed more in detail later on in this Section. The high coherence of the two-ways areal and differential strain confirms the good weighting of the gauges carried out through the tidal content of the time series (reported in Table 4.3), and in fact Table 4.8 shows that such a good agreement is kept even when we are comparing the whole time series.

Station	R($AR^{Meth.1}; AR_0^{Meth.1}$) (%)	R($ED^{Meth.1}; ED_0^{Meth.1}$) (%)
RNT	99.9	99.9
RST	99.9	-97.1
DARB	99.2	99.2
TAIS	99.3	98.9
TSUN	70.5	69.4
PFMT	98.9	99.7
BMMT	97.7	93.2
SANS	-53.6	99.5
JING	98.0	99.6
SLIN	98.6	99.7
CINT	-87.3	21.6

Table 4.8. In table the Pearson correlation coefficients R among the areal and differential strain (respectively in the second and third column) calibrated following Method 1 (Section 3.4.1). R values have been computed considering the whole duration of the time series.

It has to be noticed that TSUN site shows, for both areal and differential strain, a weaker correlation with respect to the other sites. For this strainmeter, correlation between AR and AR_0 of Method 1 decreases with the length of time span considered, reaching $\sim 70\%$ when the whole time series is considered (Table 4.8, see upper panel of Figure 4.14a). However, R($AR^{iso}; AR_0^{iso}$) can be enhanced to 83.1% if we limit the time span to the first 2200 days, and up to 85.2% if we limit it to the first 1500 days, namely before large data gaps begin lower panel of Figure 4.14a. Contextually, Pearson coefficient between ED and ED_0 can be enhanced to $\sim 97\%$ on the same time spans (Figure 4.14b).

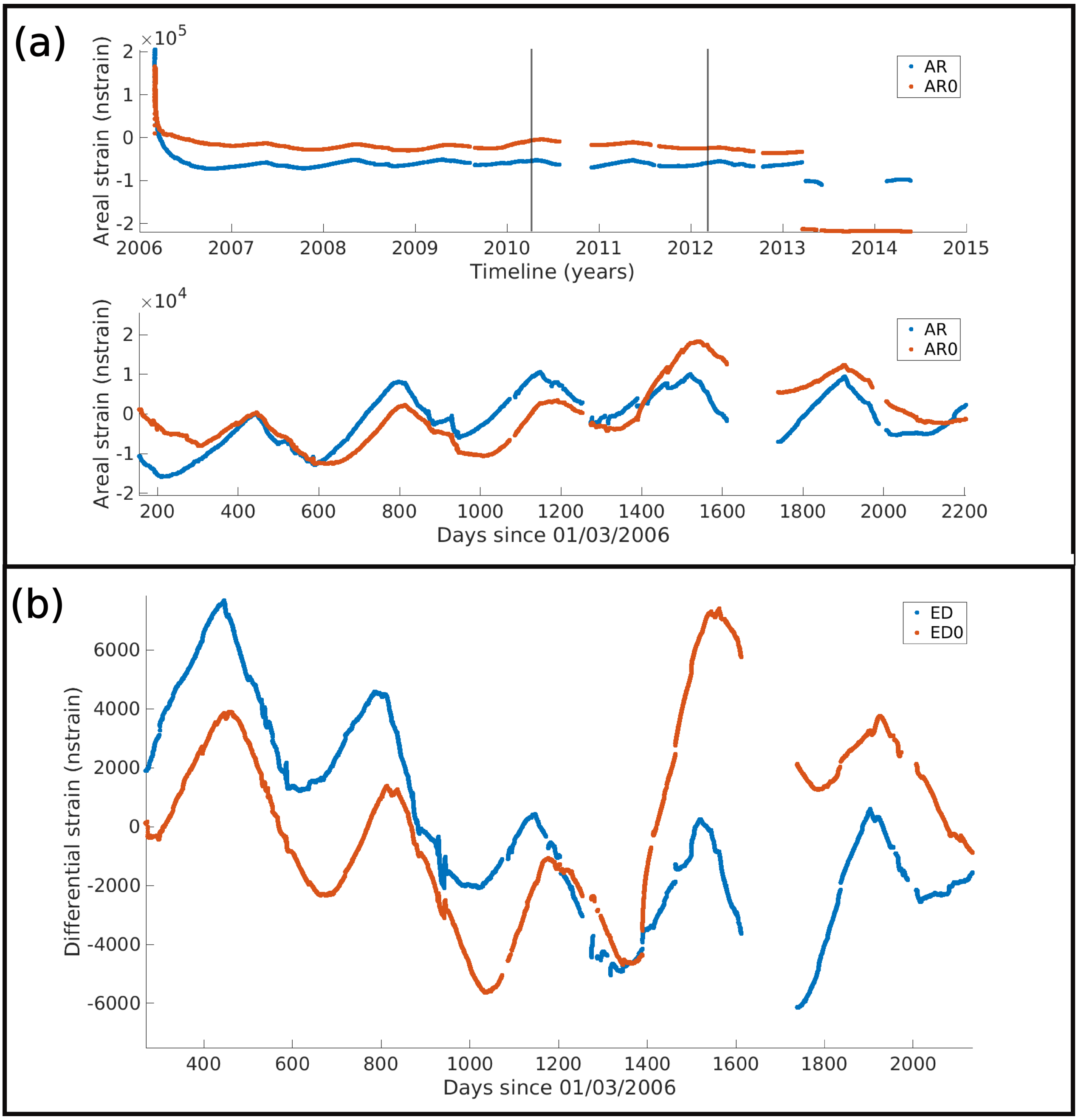

Figure 4.14. (a): in the upper panel comparison of the whole TSUN areal strain time series (blue line for AR, orange line for AR_0). Vertical lines mark the period over which the zoom of the lower panel is done. (b): comparison of the whole TSUN differential strain time series (blue line for ED, orange line for ED_0). For both lower panel of (a) and for (b), curves are detrended with function of equation 4.2

For CINT strainmeter, when we compute the Pearson coefficient between the whole time series of AR and AR_0 from Method 1, we find almost an anticorrelation, whereas the two ways differential strain show a weak agreement. However, looking at Figure 4.15a we observe that the main difference between AR and AR_0 is on the long term (upper panel), with the former measuring an expansion and the latter a contraction. In the lower panel of Figure 4.15a we focus on a shorter time scale (marked by the vertical lines of the upper panel), and we notice that after the removal of the secular trend the two curves give comparable results. We want to stress here that the detrendization of the time series through either equation 4.2 or equation 4.3 proves to be a challenging task and a residual trend remains in the data. A graphical comparison of the two ways differential strain (Figure 4.15b) confirms that the calibrated ED and ED_0 are satisfactorily in agreement.

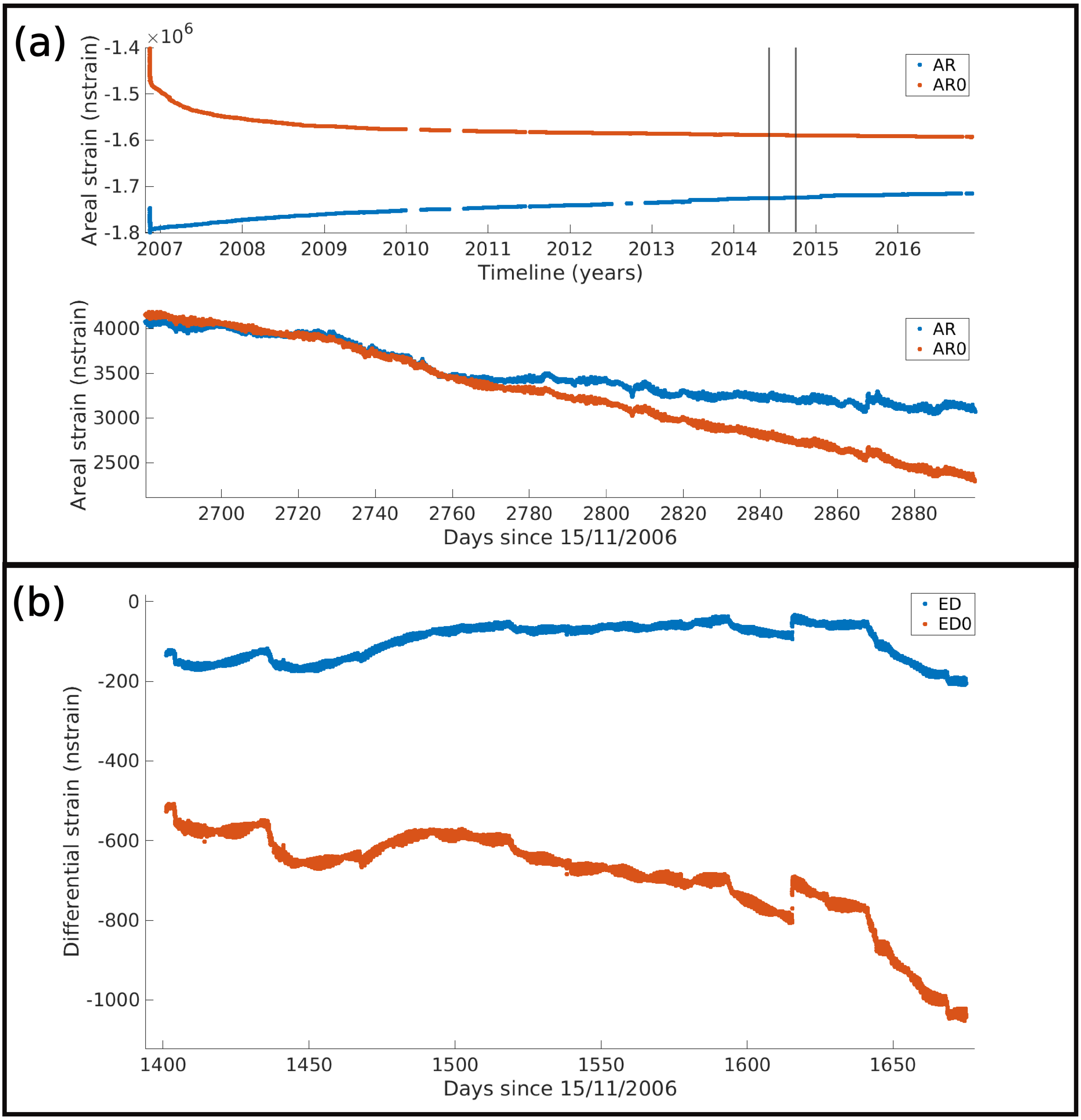

Figure 4.15. Same as Figure 4.14 for CINT strainmeter

Among the eleven strainmeters, six (RNT, RST, TAIS, SANS, SLIN and JING) have been calibrated also following Method 2 (Section 4.2.2), and our aim here is to compare the results of the two methods. As already claimed, a comparison between the areal strain is straightforward as they do not depend on the reference system. On the other hand, before comparing the shear components, we need to rotate the azimuth of each strainmeter so that the direction of CH_1 and CH_3 coincides respectively with the east and north directions. In order to do that, we start from the strain tensor in the CH_1 and CH_3 reference system $\epsilon_{i'j'}$ (see equation 3.20):

$$\begin{cases} \epsilon_{x'x'} & = \frac{AR+ED}{2} \\ \epsilon_{y'y'} & = \frac{AR-ED}{2} \\ \epsilon_{x'y'} & = \frac{1}{2}ES \end{cases} \tag{4.4}$$

Having the strain field in CH_1 and CH_3 reference system, we can re-obtain ϵ_{ij} in the E-N reference system by applying to $\epsilon_{i'j'}$, a rotation of an angle $-\theta$:

$$\epsilon_{ij} = R^T(-\theta)\epsilon_{i'j'}R(-\theta) \tag{4.5}$$

where θ is the azimuth of CH_1. Taking the resulting strain components of equation 4.5, we get the strain field from Method 1 in the E-N reference system. In Table 4.9 we compare the strain components obtained from Method 1 and Method 2:

Station	R($AR^{meth1}; AR^{meth2}$) (%)	R($ED^{meth1}; ED^{meth2}$) (%)	R($ES^{meth1}; ES^{meth2}$) (%)
RNT	96.5	88.0	99.8
RST	99.9	-75.7	4.2
TAIS	-99.5	22.0	95.6
SANS	-90.0	94.9	98.6
JING	98.5	-72.1	-89.3
SLIN	-58.4	-18.8	90.7

Table 4.9. In table the Pearson correlation coefficients R among the strain components calibrated through Method 1 and 2. R for areal, differential and engineering strain are respectively reported in the second, third and fourth column.

Starting off the comparison between Method 1 and 2 with the strainmeters belonging to the Tsengwen Reservoir array, namely RST and RNT, we notice that CH_1 of the former site has been active for a very short time, with a large data gap between $\sim$ March 2006 and January 2017 (Figure 4.16). Ominously Method 2 relies on the measurements of all of the four gauges, and it cannot be employed in case of malfunctioning of one channel. Therefore, for RST, we can say that although

Method 2 provides a more accurate waveform reproduction (Table 4.7) it is of no use for this strainmeter. On the other hand Method 1 provides satisfying results for the areal and differential strain waveform reproduction, and a lower agreement is found for the engineering strain component (Table 4.4). A thorough comparison of the two methods is limited by the short strain time series available ($\sim$ 500 days), and it is not of particular relevance. Hence, for RST the tidal analysis demonstrates to be robust enough for the calibration of the instrument despite the short time series length. For such a site, the redundancy of observations provided by Method 1 proves to be essential for the usage of this strainmeter.
Considering RNT, we find a good agreement among the results of Method 1 and 2, with Pearson coefficients>$\sim$ 90%. Calibration through Method 1 already resulted in good tidal correlation for areal and differential strain, and a weaker correlation for engineering strain (Table 4.4). However, the differences on the tidal part of the time series do not heavily affect the general calibration as the high correlation between the total time series of Table 4.9 testifies. Hence we deem the further complication of Method 2 to be unnecessary for RNT strainmeter.

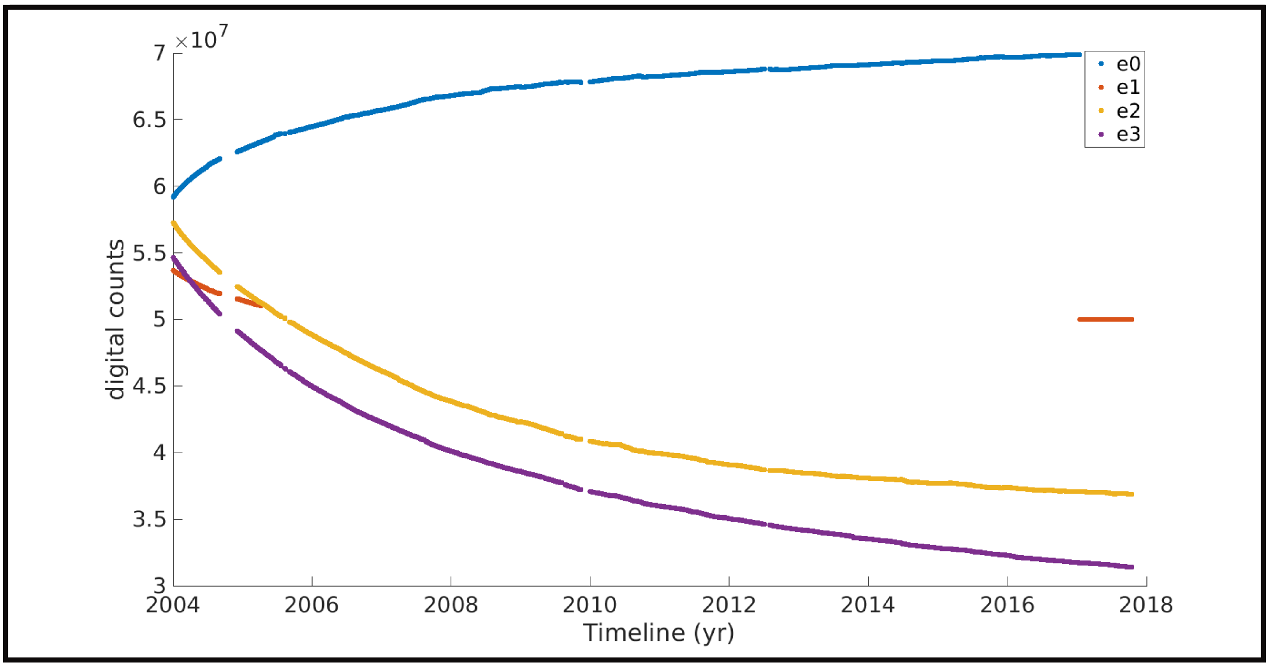

Figure 4.16. In Figure the four raw time series (e_i, $i = 1, 2, 3, 4$, respectively in blue, orange, yellow and purple) measured at RST site.

Regarding SANS, Method 1 provides good results for areal strain and satisfying results for differential strain (Table 4.4). However, as Table 4.8 shows, we do not observe a good agreement between AR and AR_0 of Method 1 when we compare the whole time series. We impute this fact to a difference in the long term trend (Figure 4.17a), which is due to the different relaxation the gauges experience. In fact, such a discrepancy is not maintained on shorter time scales: computing the Pearson coefficient on the more stable period between 1200 and 1700 days after installation of the instrument (Figure 4.17b), we get a correlation of $R = 92.2\%$. Hence the main difference between AR and AR_0 is in the long term trend, namely expansion for the former and contraction for the latter. Applying Method 2, we can significantly improve the calibration of engineering strain (Table 4.7). Comparing the whole calibrated series from the two methods (Table 4.9), we observe a high correlation among the results of Method 1 and 2 for the shear components. The only exception is the areal strain for which we find almost an opposition of phase. Since Method 2 allow us to find a significant correlation for all of the strain field components, while Method 1 is not capable of properly model the engineering strain tidal waveform, we suggest Method 2 as the most reliable for SANS strainmeter.

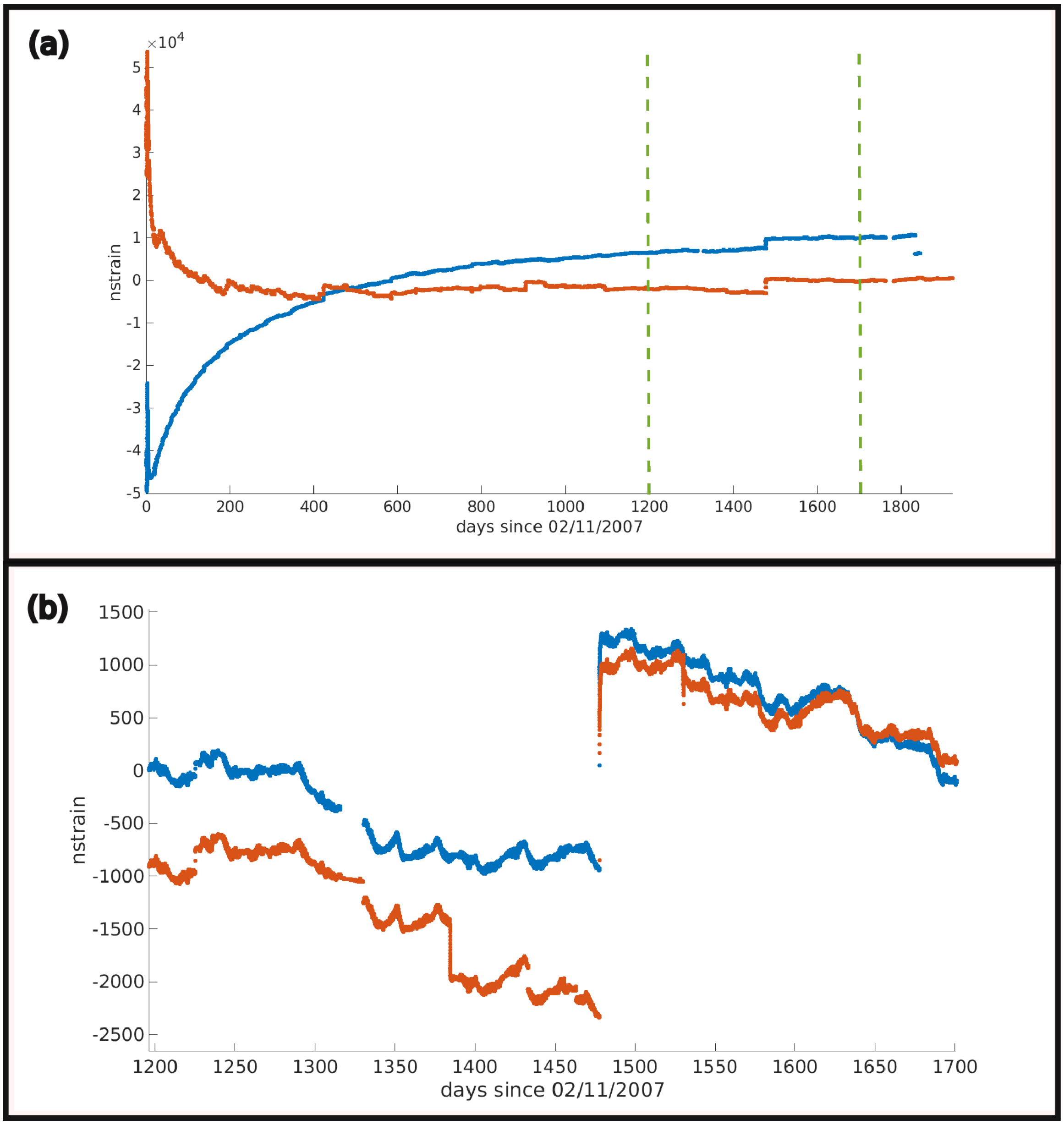

Figure 4.17. In figure comparison of areal strain from Method 1 for SANS GTSM. (a): comparison of the whole time series, blue line for AR and orange line for AR_0. Vertical dashed lines mark the epochs mentioned in the text. (b): Zoom of the above plot in the time span 1200 - 1700 days since installation, after the detrending with equation 4.2. Curves colors as in panel (a).

The application of Method 1 to JING site produces similar results as for SANS GTSM (Table 4.4). However, conversely to this latter, a good agreement is kept even when we compare the whole time series (Table 4.8). The low ($\sim$ 32%) Pearson coefficient

of the engineering strain tidal modelization led us to the application of Method 2 as well. From Table 4.7 we notice that the second calibration approach is capable of reproducing almost perfectly the tidal waveforms, with $R \sim 98 - 99\%$. Comparing Method 1 and 2 (Table 4.9) we observe that the areal strain time series is similar for the two methodologies, whereas the shear components are closer to an anticorrelation.
SLIN strainmeter, for which a good areal and differential strain calibration following Method 1 is found (Tables 4.4 and 4.8), has on the other hand a poor engineering strain tidal waveform reproduction. Applying Method 2, we can significantly improve results for engineering strain, at the expense of a lower reproduction of the differential strain (Table 4.7). For JING and SLIN GTSMs, due to the very low engineering tidal waveform reproduction of Method 1 (respectively $\sim 32\%$ and $\sim 16\%$) we propose Method 2 as more suitable for the calibration of these sites.

The last strainmeter we will discuss is TAIS site, for which the lowest correlation of areal strain following Method 1 is found (Table 4.4), but at the same time we observe a high coherence among the waveforms of Method 1 and 2 (Table 4.9). Areal strains from Method 1 and 2 bear an opposition of phase which is hard to explain only through a difference in the long term behaviour. As it can be observed from Figure 4.18, TAIS has a very weak secular trend compared to the other GTSMs, and its long term behaviour is almost completely dominated by a periodical signal which will be discussed in Section 4.5. In fact, Table 4.4 confirms that TAIS's low coherence is independent of the time span considered for computing the correlation, as a very low agreement ($\sim 50\%$) between the theoretical and observed waveforms is detectable also on tidal time scales. However such low coherence should not be associated with a bad waveform reproduction but to a time shift of $\sim 11h$ between theoretical and measured tidal induced strain. This time shift can be corrected through an appropriate combination of the four CH_i, which is why it is not present in the areal strain from Method 2. In order to check which is the areal strain actual sign, and hence which calibration method carries the best result, we exploit the instrument response to heavy rainfall (Figure 4.19). Among the rain gauges present in Taiwan, we select those in the rectangle defined by the coordinates $23° \leq latitude \leq 24°$ and $120.1° \leq longitude \leq 121.1°$ (Figure 4.21), and we stack the results. As in Chen (2021) we suggest that the response of the GTSM to heavy rainfall is represented by areal strain from Method 1 (red lines in Figure 4.19): the undeformed conditions (*phase (i)*, Figure 4.19(b)) are followed by a quick contraction (*phase (ii)*, Figure 4.19(b)) during which the medium can be considered to respond in an elastic way. After that, expansion of the borehole during a transient phase related to fluid diffusion in the poro-elastic medium (phase *(iii)* in Figure 4.19(a)), and a contraction due to the draining process of the medium (phase *(iv)* in Figure 4.19(a)). Therefore we explain TAIS peculiar behaviour suggesting that *Gotic2* software poorly predicts the theoretical tides for TAIS. As Method 2 showed, through an appropriate combination it is still possible to match the (non poro-elastic) tide-induced strain, however the quick response of the instrument to rainfall suggests that Method 1 brings the correct results for TAIS.

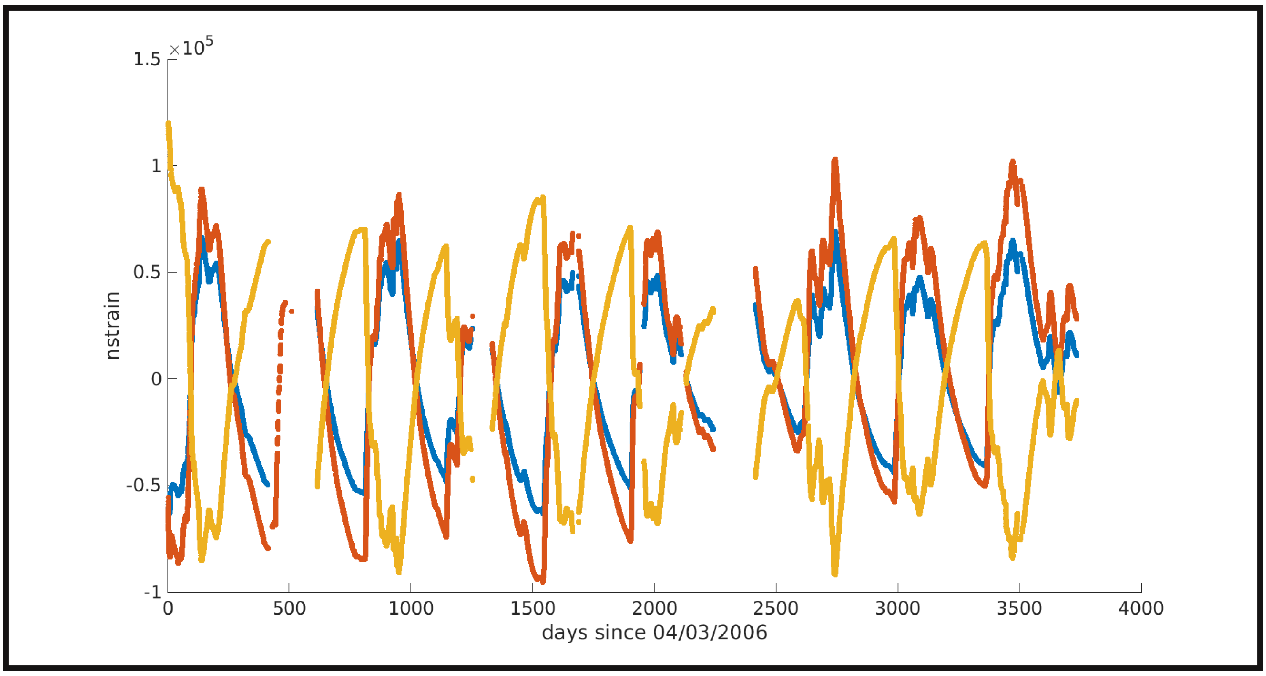

Figure 4.18. In Figure comparison of areal strain from Method 1 and 2 for TAIS GTSM. Blue and orange lines represent AR and AR_0 from Method 1, while yellow line represents AR from Method 2.

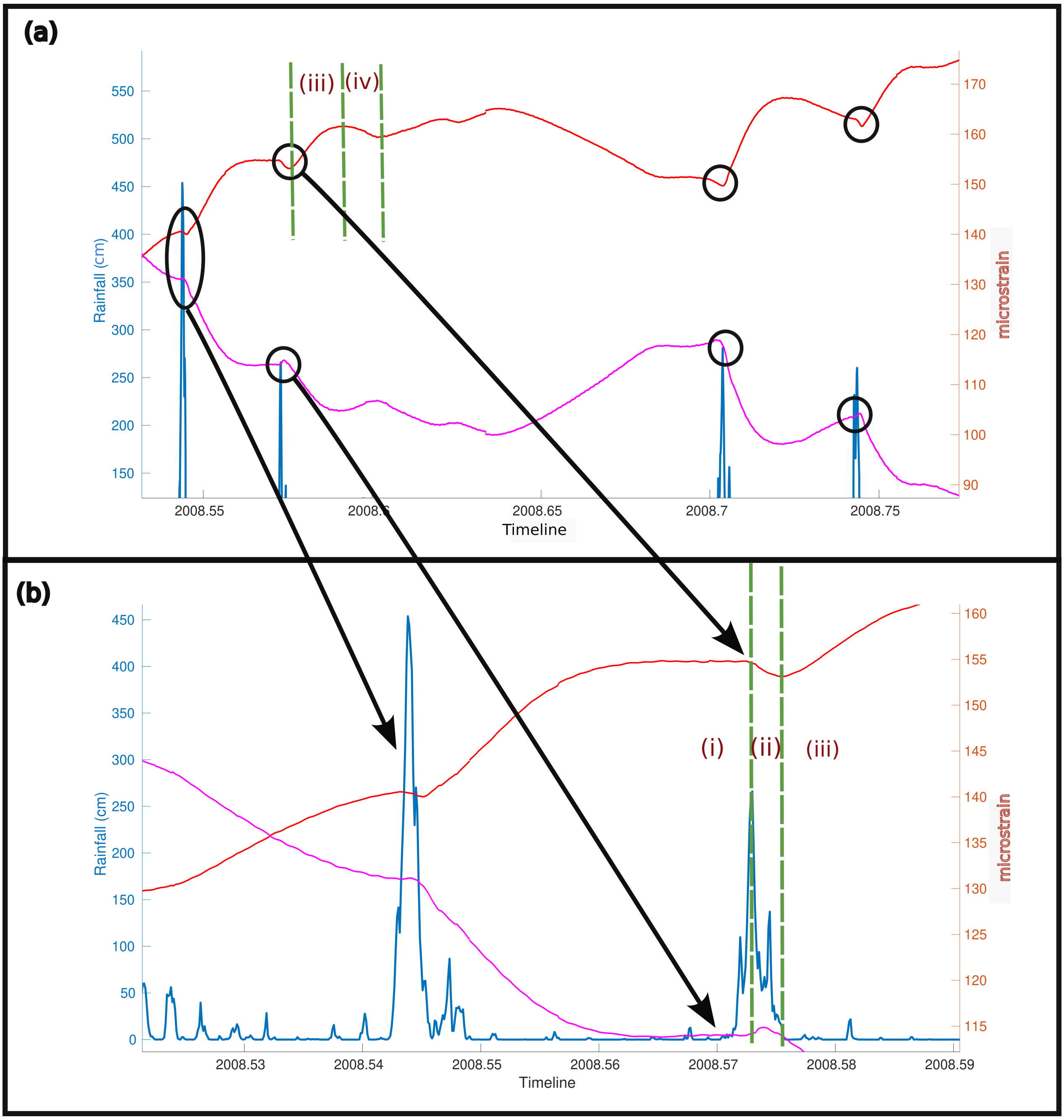

Figure 4.19. (a): In Figure comparison of areal strain from Method 1 (red line) and 2 (magenta line) for TAIS GTSM, and stacked rainfall in the time period 19 June - 30 September 2008. (b): focus on the first two heavy rainfall events. Vertical green dashed lines mark the four different phases of the response of the GTSM: (i) undeformed condition; (ii) elastic effect during rainfall; (iii) increase of pore fluid pressure in transient conditions (diffusive penetration of precipitation), iv) decrease of fluid pore pressure in transient conditions to drain the fluid.

4.4 Taiwan GTSMs calibration summary

We apply the calibration methods developed in this thesis on the Gladwin strainmeters deployed in Taiwan. Hart et al. (1996) already acknowledged that calibration of strainmeters, and in particular tensor ones, is nontrivial, and an accurate estimation of the calibration coefficients is hard to obtain. The high precision of these instruments provides precious information for the characterization of deformation sources, on the other hand it can make the interpretation of the recorded signals very difficult to achieve. This proves to be particularly true for the Taiwanese GTSMs array for which complicated deformation patterns are observed: as a matter of fact, we often find that gauges of the same strainmeter record substantially different deformation time series, thus pointing towards a complicated medium and/or installation. This is also testified by the different long term contraction/expansion that an instrument sees, depending on which combination of gauges we use to compute areal strain: as we notice, for instance for SANS and CINT sites (Figure 4.17 and upper panel of Figure 4.15a), the two-ways areal strain determined through Method 1 show different long term behaviour which we know to be representative of the stress state of the rock prior to the strainmeter's installation and the of poro-mechanical response of the local rock formation (Barbour, 2014). Strainmeters in Taiwan are generally installed in regions where the topography matters (Table 4.1) and close to hydrological sources of deformation (e.g., rivers, reservoirs...). Moreover, the tropical climate of the island, characterized by high seasonal rainfall and significant water content in the ground, pushes away the installation environment from the desired one (see Section 3.2). This is particularly true, for instance, for TAIS site in Section 4.3, where hydrology can heavily affect the calibration up to a sign inversion (Figure 4.18). In such cases, we demonstrate that the integration of further data sets can help in selecting the most reasonable method to follow (Figure 4.19).

The calibration methods here proposed (Sections 3.4.1 and 3.4.2) are capable of providing coefficients that satisfactorily reproduce the tidal waveforms. As highlighted in Canitano et al. (2018), the waveform modelization should produce more robust coefficients, especially for the shear strain components that are generally more affected by cross-coupling effects due to inhomogeneities (Hart et al., 1996). It must be said that a quantitative comparison between the methodology developed in this thesis and the "standard" calibration (e.g., Hodgkinson et al., 2013) is limited by some factors. In Hodgkinson et al. (2013) coefficients are adjusted to fit the phases and amplitudes of M2/O1, assuming the orientation of the instrument measured during installation to be correct. On the other hand, we use a larger number of tidal constituents and we estimate the azimuth of the instrument during calibration. Therefore, to directly compare our methodology with Hodgkinson et al. (2013)s', we need to extract only M2/O1 from our data at each azimuth with step of 2°, in order to keep into account the effect of a wrong azimuth estimation at installation. However, if we used the corrected azimuth in eq. 8 of Hodgkinson et al. (2013), we would expect to get comparable results as M2/O1 are by far the most influent tidal constituents. To sum up, a quantitative comparison between methodologies proves to be a hard task due to: (1) a different instrument's orientation; (2) a different number of tidal constituents, this latter deemed to have little effect on the results. However, we can claim that an improvement of our methodology lies in an estimate of the actual orientation of the strainmeter, as well as a visual control of the quality of the calibration through waveforms modelization.

We suggest that for seven strainmeters out of eleven the simpler case of Method 1 is suitable to reproduce the Earth's tides waveforms (results summarized in Table 4.4). For such a method we find calibration coefficients common to the four gauges though allowing for different shear coefficients. For the remaining four sites, mainly due to the difficulty of properly reproducing the tidal shear components, we completely relax the condition of isotropy of the rock and we propose Method 2 as the most suitable (results summarized in Table 4.4). In Table 4.10 we sum up what we suggest to be the most adapt method for each strainmeter.

Station	Method 1	Method 2
RNT	x	
RST		x
DARB	x	
TAIS	x	
TSUN	x	
PFMT	x	
BMMT	x	
SANS		x
JING		x
SLIN		x
CINT	x	

Table 4.10. In table a summary of the calibration approach that we suggest to be the most suitable for each of the GTSMs deployed in Taiwan.

4.5 Hydrology of southern Taiwan

As highlighted in Section 4.3, TAIS strainmeter shows a peculiar long term behaviour dominated by a periodical signal (Figure 4.18), which is in contrast with the typical trend observed for these instruments (e.g., Figure 4.13). Given the periodical form, we deem some hydrological source of deformation to be dominating TAIS time series, and we aim at investigating it.

The straightforward question that follows is: can we consider TAIS's behaviour a site effect or can such a hydrological signal be observed in other GTSMs too? In order to answer, we try to point out the same signal in the closest neighbors, namely DARB and TSUN sites, which are located at a distance < 15 km. In Figure 4.20 we show the comparison of the detrended areal strain time series, and we notice that the periodical signal recorded by TAIS is strongly attenuated moving eastward. As a matter of fact, TSUN time series is magnified by a factor $\times 10$ and DARB time series by a factor $\times 50$, in Figure 4.20. Moreover, it has to be stressed that TAIS areal strain has an opposite phase with respect to DARB and TSUN. On the other hand, we are not capable of finding it in the next closests strainmeters (i.e., RNT an RST). Despite the differences in sign and amplitude, Figure 4.20 confirms that such a periodical signal is not just a local effect.

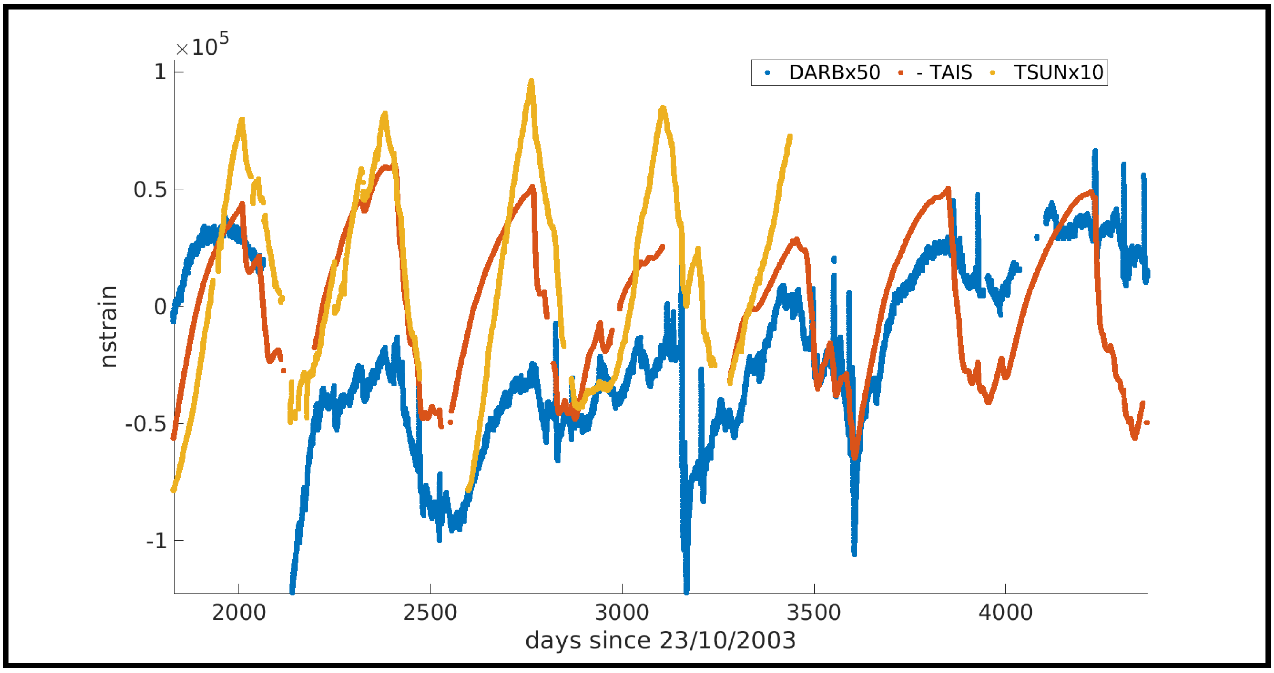

Figure 4.20. Comparison of areal strain for DARB, TAIS and TSUN GTSMs (respectively in blue, orange and yellow). Remarkably, TAIS sign has been reversed, whereas TSUN and DARB time series have been magnified by a factor 10 and 50 respectively.

Strainmeters can only provide a punctual measurement of the strain field in few locations. In order to better characterize the intensity and spatial distribution of such a source of deformation, we exploit the GNSS network deployed in the area. Here we are mainly interested in hydrological sources, hence we take advantage of the GNSS time series provided by the Central Weather Bureau (CWB) of Taiwan (http://tgm.earth.sinica.edu.tw). We consider time series from which the tectonic signal, represented at first order by a linear term, was removed. As Figure 4.20 points out, the hydrological signal under study is quickly damped moving away from TAIS location. Hence, keeping also into account the higher strainmeters' sensitivity, we first need to check whether the researched signal can be found in GNSS time series as it can be easily hidden by other sources of deformation. To do so, we select the six GNSS stations in the area of the three strainmeters and we compute the deformation from the displacement time series exploiting the *PyTAGS* Python package for GNSS time series analysis (Crowell, 2019). Deformation from the GNSS is assessed in a triangulated mode, namely taking sub-networks of three sites and computing the strain in their barycentre. Among the five possible combinations, two sub-networks showed a periodical deformation similar to the one observed in the strainmeters time series. From now on, they will be referred to as *sub-network 1*, formed by GS63, GS66, GS07 sites, and *sub-network 2*, formed by GS63, JHCI, GS07 sites (respectively black and magenta dashed triangles in Figure 4.21). In Figure 4.22 we plot the detrended areal strain at TAIS, DARB and TSUN sites, against the areal strain of sub-networks 1 and 2. As for Figure 4.20 DARB and TSUN time series have been magnified to help the visual comparison. GNSS deformation time series have been detrended and smoothed with a gaussian sliding window of 7 days, and then magnified by a factor $\times 20$. Figure 4.22 confirms the polarity of the areal strain recorded by TAIS.

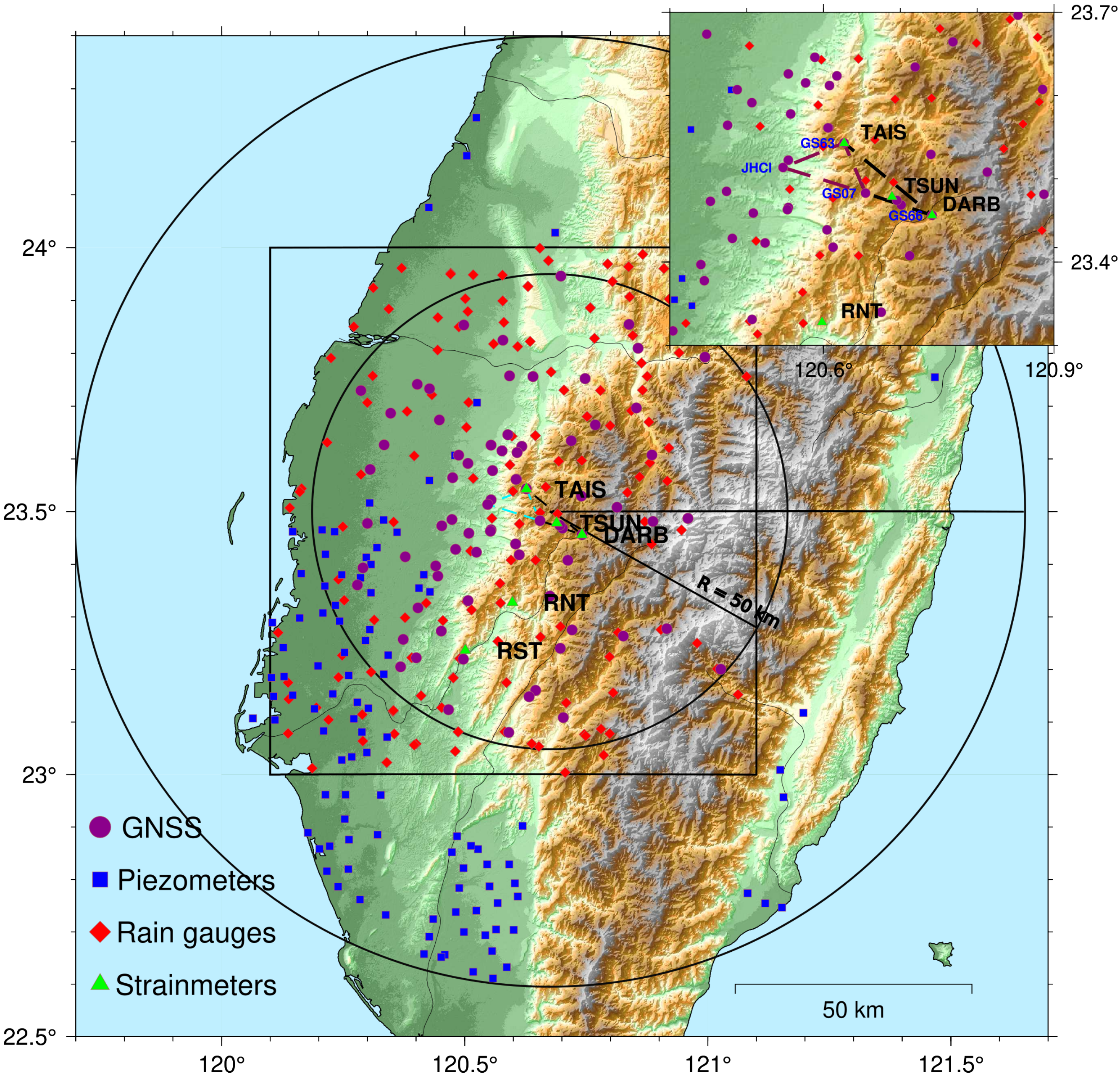

Figure 4.21. In Figure the data set employed to study the hydrological sources in southern Taiwan. Large black circumference marks the area within the piezometers (blue squares) have been selected; small black circumference marks the area within the GNSS stations (magenta circles) have been selected; large black square marks the area within the rain gauges (red diamonds) have been selected. Small green triangles mark the location of the strainmeters considered (names in Figure). Insert: small dashed black and magenta triangles mark respectively GNSS sub-network 1 and sub-network 2 used for the strain calculation (see text).

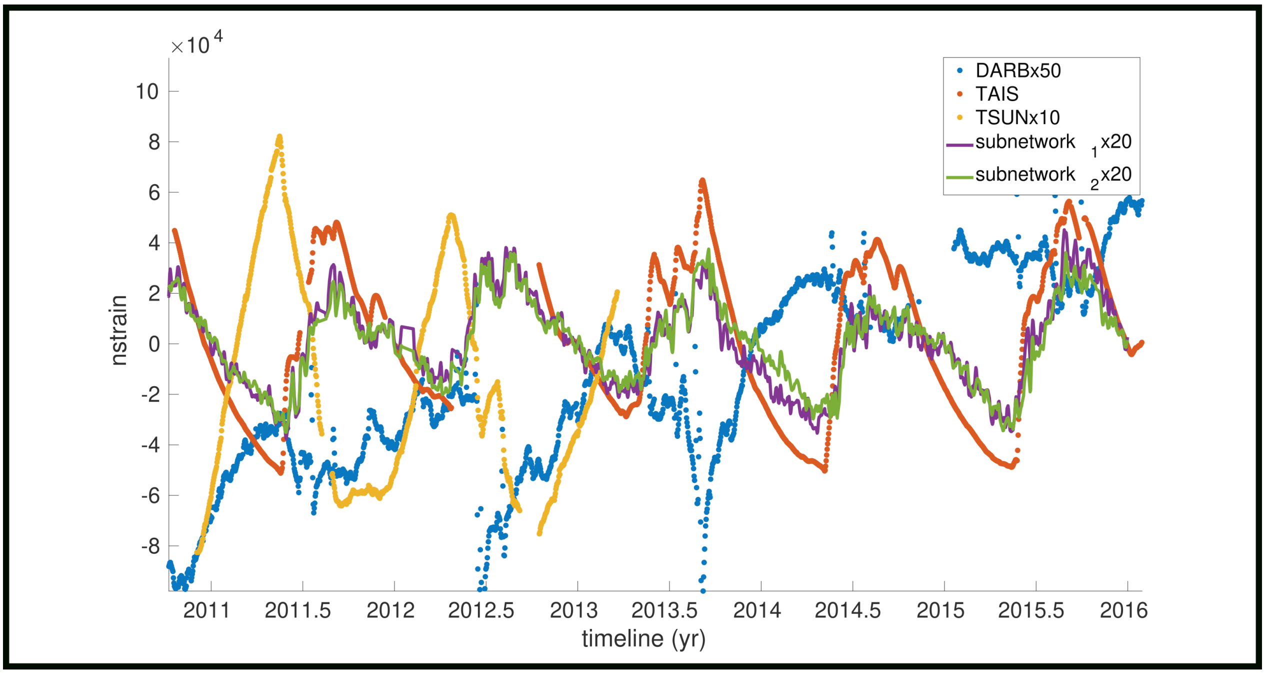

Figure 4.22. Comparison of areal strain for DARB, TAIS and TSUN GTSMs (respectively in blue, orange and yellow), with the GNSS deformation of sub-networks 1 and 2 (respectively in purple and green). As for Figure 4.20, TSUN and DARB time series have been magnified by a factor 10 and 50 respectively, while the GNSS time series by a factor 20. On the other hand, TAIS sign is here unchanged.

After having checked that the hydrological source of deformation under study has affected the GNSS network, we exploit its wider and denser distribution. We analyze the GNSS displacement time series through the *vbICA* technique (see Section 2.2.1) to retrieve the different independent sources of deformation in the area. We focus on the time span 2009-2015, which is slightly larger than the one where the three strainmeters have few data gaps, and we select the stations within a radius of 50 km from the location with coordinates longitude = 120.675°, latitude = 23.5° (Figure 4.21). We detrend the time series to enhance the decorrelation of the data set in a similar way as Section 2.2, and we carry out the decomposition fixing a number of sources $L = 5$. In Figure 4.23(a-e) we report the temporal (V) evolution of the sources of deformation acting on the GNSS network, while in Figure 4.24 the corresponding GNSS stations' spatial response.

We repeat the analysis on the groundwater measurements, this time including all the piezometers within a radius $R < 100$ km (blue square, Figure 4.21). We take a larger study area due to the scarce presence of wells on the central mountain chain, so that enough data are available for the vbICA. Piezometers provide time series of groundwater level changes, hence we perform a 1D ICA and we limit the number of components to $L = 1$. This choice is mainly driven by the fact that we seek for a common signal in the groundwater time series and, as a matter of fact, a decomposition with just one IC is already sufficient for explaining $\sim \frac{2}{3}$ of the data set variance. Moreover, tests run on vbICA decompositions with $L > 1$ suggest that the addition of further components does not lead to the extraction of common signals that help the interpretation of the regional hydrological deformation observed at the strainmeter and GNSS sites. In Figure 4.25 we report the temporal (panel (a)) and spatial part (panel (b)) of the IC1 of the analysis on the piezometers.

As we are interested in hydrological sources, we exploit the $GRACE$ products (see also Section 2.3.2) which allow us to estimate the liquid water equivalent thickness (LWE). We selected the area delimited by coordinates $22° \leq lat \leq 25°$ and $120° \leq lon \leq 122°$, and the time span 2009-2015. The area considered for the estimation of the LWE is slightly larger than the study area, given the lower spatial resolution of GRACE.

Lastly, we include in our study the large number of rain gauges available, limiting the data set to the instruments in the area included in the square with coordinates $23° \leq lat \leq 24°$ and $120.1° \leq lon \leq 121.1°$ (red diamonds in Figure 4.21). Rain measurements in the area are stacked, cumulated in the time period 2009-2015, and afterwards detrended. The results of the analysis on these two latter data sets will be presented in Section 4.5.1.

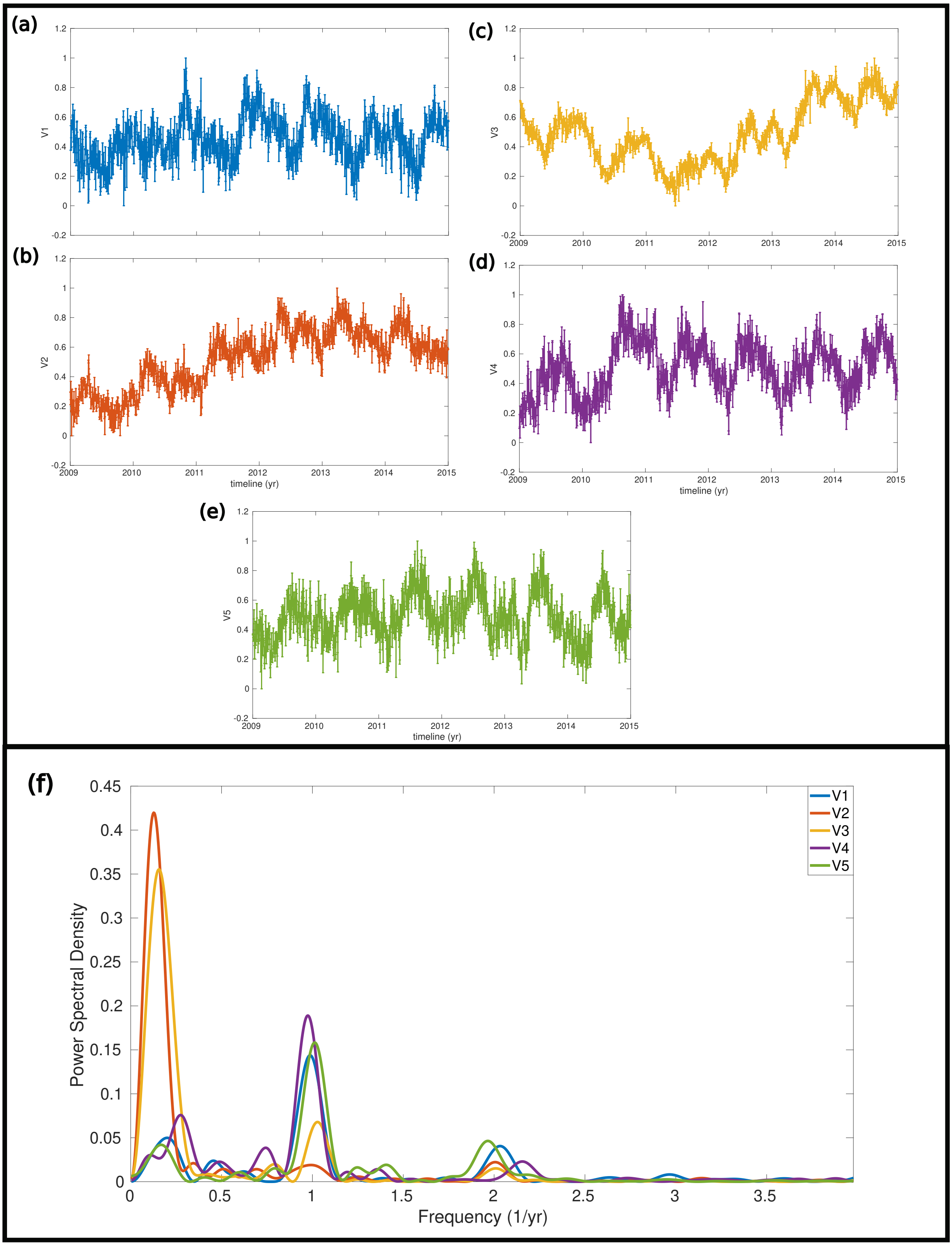

Figure 4.23. Temporal evolution V of the five ICs (panels (a) to (e)) retrieved from the analysis on the GNSS displacement time series. The V are normalized to be $\in [0, 1]$. Panel (f) shows the power spectral density of the five components

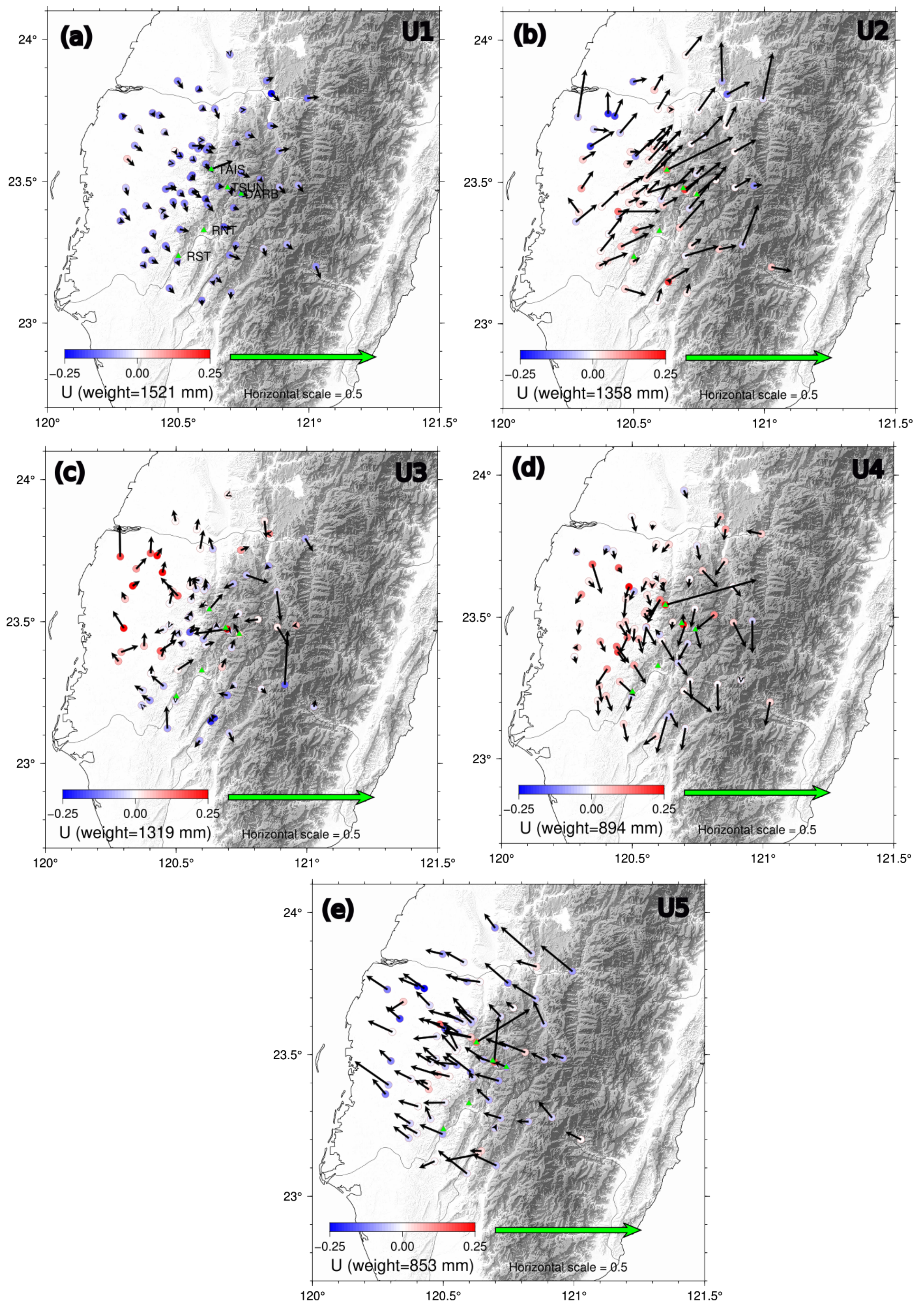

Figure 4.24. (Caption next page.)

Figure 4.24. Spatial response U of the GNSS stations to the five ICs retrieved from the analysis on the displacement time series. The relative weight in mm of each component is provided. Circles mark the position of the GNSS sites with a $r < 50$ km from the point longitude = 120.675°, latitude = 23.5°; green triangles the five strainmeters deployed in the area.

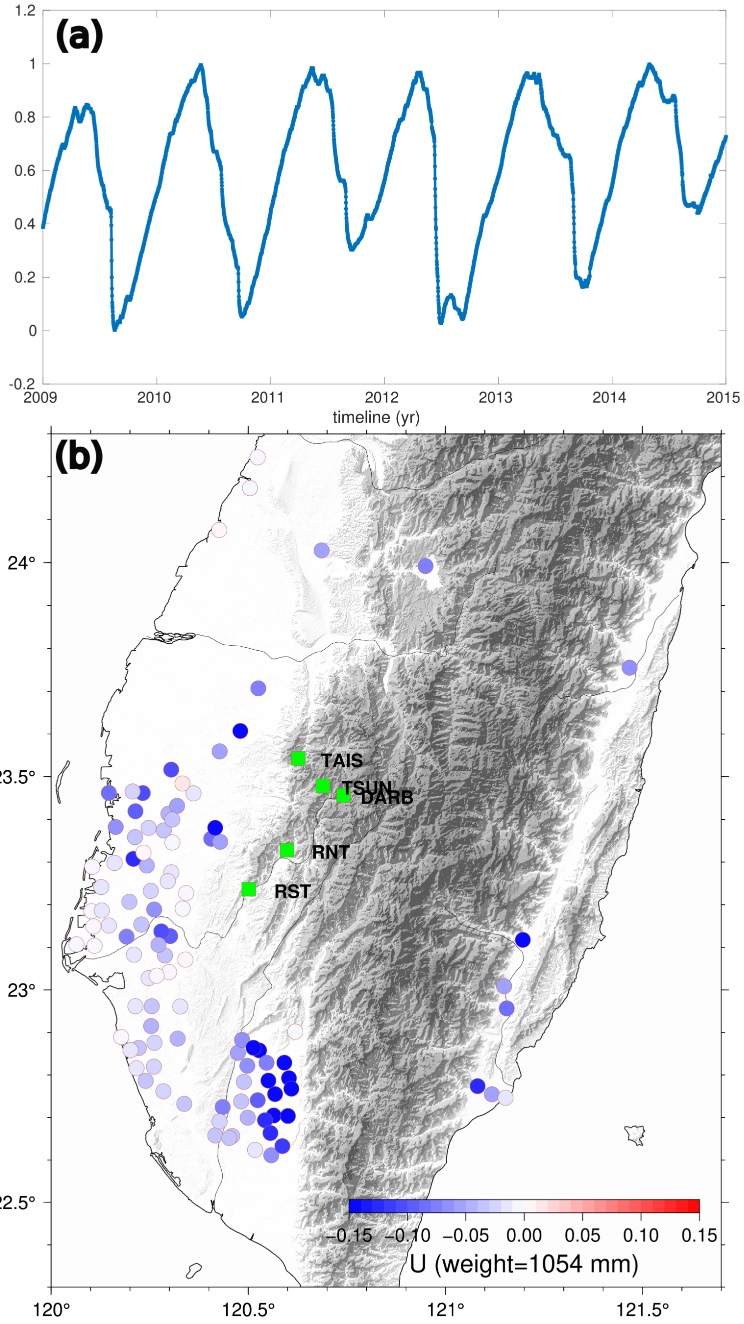

Figure 4.25. Panel (a): temporal evolution V of the IC retrieved from the analysis on the groundwater level. V are normalized to be $\in [0, 1]$. Panel (b): spatial response of the wells (circles). Weight in mm of the IC is provided. Green squares mark the strainmeters' position.

4.5.1 Interpretation of the hydrological sources

In this Section we aim at providing a justification for the sources of deformation, highlighted in the different data sets, that were previously presented.

The IC1 retrieved from the GNSS shows a periodical pattern with periodicity of roughly 1 year (Figure 4.23(f)), and it affects mainly the vertical component of the GNSS (Figure 4.24a). Combining the temporal evolution and spatial response, the effect of the IC1 on the GNSS network is of maximum subsidence in correspondence with the maxima of the V1, followed by maximum uplift during the minima of the V1 (Figure 4.23a). As already observed in literature (e.g., Amos et al., 2014; Argus et al., 2014; Borsa et al., 2014; Dong et al., 2002; Tregoning, 2005), and in Section 2.3.1 for Central Italy, this is coherent with loading from mass redistribution on the shallow portion of the Earth's crust. In particular, the increased loading during rain season at the Earth's surface produces a coherent common subsidence for the whole data set. In order to confirm this interpretation, we compare the temporal evolution of the IC1, with an estimation of the total water content of the ground (i.e., the LWE). From Figure 4.26 we observe that the two curves follow roughly the same time evolution. Some differences are not surprising as the LWE spatial resolution does not allow accurate estimates on lands with limited extension such as Taiwan. Moreover GRACE products are averaged monthly, and we deem this smaller temporal resolution to influence the differences observed. Despite some discrepancies, since the V1 of the GNSS follows the LWE time evolution and the spatial response is coherent with hydrological loading (Figure 4.24a), we interpret the IC1 on the GNSS as due to a total content of water in the ground.

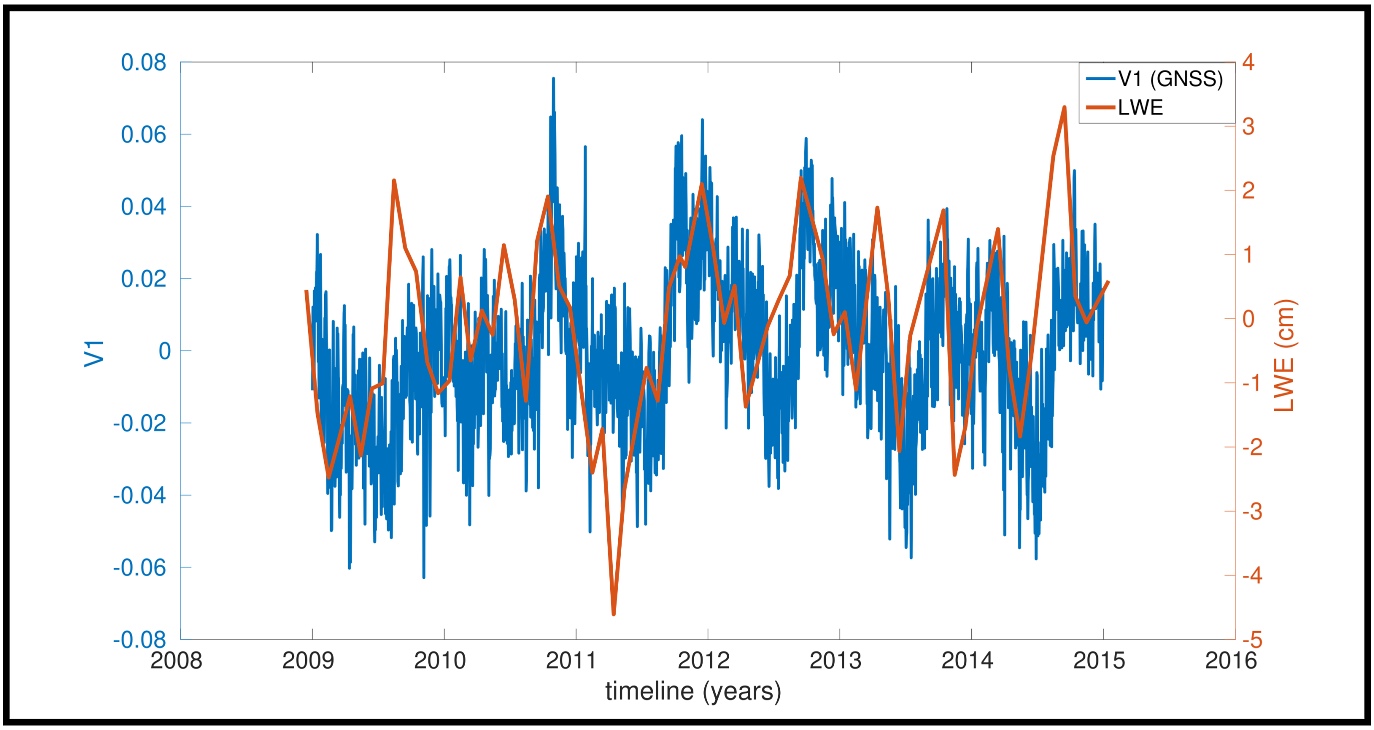

Figure 4.26. Comparison of the V1 retrieved from the analysis on the GNSS (blue) and the LWE derived from GRACE measurements (orange).

The IC2 retrieved from the GNSS appears to be a long term signal with a high content of low frequencies (Figure 4.23(f)), with a dominant N-E displacement common to all the GNSS sites (Figure 4.24(b)). To rule out the possibility of a remaining secular trend in the time series, we carry out the vbICA, extending the period of analysis until the 2020. Among the extracted ICs, in this second analysis (of which we do not show the complete results), we focus on the third IC, as it shows a similar behavior with respect to the IC2 (Figure 4.27, black curve) within the common time interval. The black curve in Figure 4.27 reaches its maximum around the year 2014, thereafter a multi-annual descent begins. Hence we believe that the IC2 retrieved from the analysis on the time span 2009-2015 should not be associated with the residual of a secular trend in the time series. However, it is not possible to infer further interpretations of this IC as the characteristic time of such deformation signal appears to be larger than the length of the available GNSS time series.

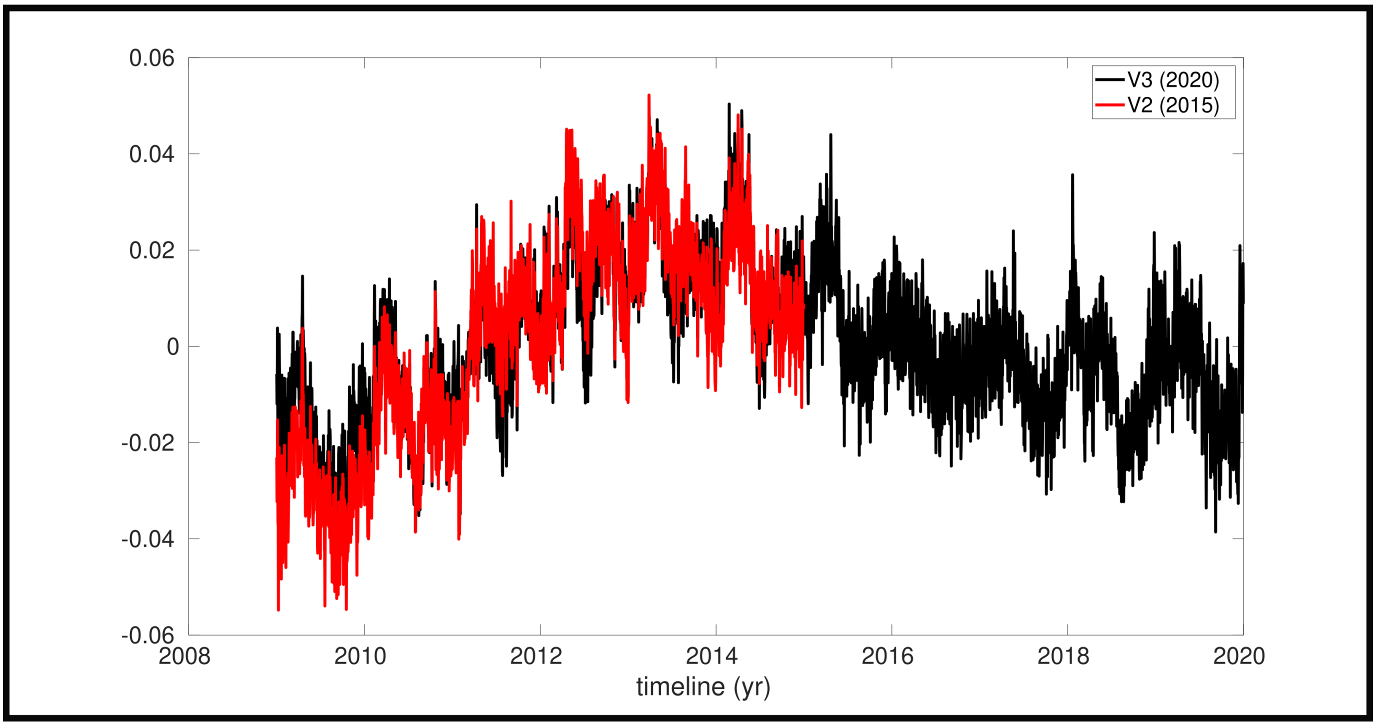

Figure 4.27. Comparison of the V3 retrieved from the analysis on the GNSS on the time period 2009-2020 (black curve) and the V2 from the analysis on the time period 2009-2015 (red curve).

Looking at the IC3 retrieved from the GNSS, we notice a content of low frequencies mainly, combined with traces of a periodical signature with characteristic time ~ 1 year (Figure 4.23(f)). The spatial response U3 (Figure 4.24(c)) does not show any particular horizontal common pattern. On the other hand, the vertical response of the GNSS network seems to be characterized by a slight opposition of phase moving from west to east. Stations located on the plain (i.e., on the west of the study area) appear to be in uplift when stations on the mountainous area (i.e., on the east) generally record subsidence. This is in agreement with the findings relative to the Northern Italy area of Nespoli et al. (2021), who related GNSS stations subsidence to a water level increase on the Apennines mountain chain, while GNSS in the Po Plain observed uplift. This is consistent with an elastic response of GNSS stations in mountainous area and a dominant poro-elastic response of GNSS sites in the plain area (Nespoli et al., 2021). We compare the IC3 acting on the GNSS with the rain gauges measurements. From Figure 4.28 we notice that the temporal evolution of the IC3 is in good agreement with the detrended cumulated rainfall in the area, and we therefore interpret this component of the vbICA analysis on the GNSS data as due to the water content in the first meters of the ground.

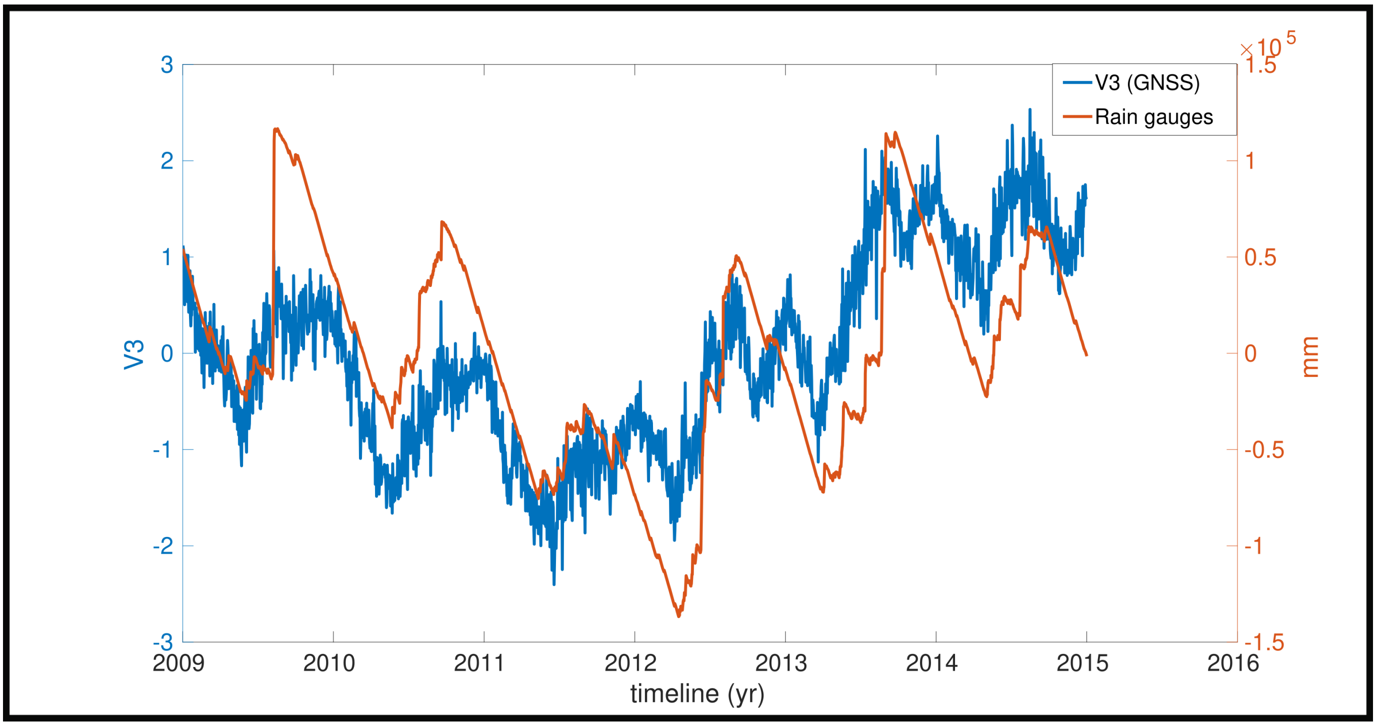

Figure 4.28. Comparison of the V3 retrieved from the analysis on the GNSS (blue curve) and the cumulated and detrended rain (orange curve). For visual comparison, V3 has been scaled to have zero mean and standard deviation = 1.

Regarding IC4 retrieved from the GNSS, the signal is prevalently dominated by $\sim$ 1 year periodicity (Figure 4.23(f)), mainly producing on the GNSS network an effect of uplift on the vertical, and a S-E displacement on the horizontal (Figure 4.24(d)). To explain this component, we compare its temporal evolution (i.e., the V4) with the V retrieved with the vbICA on the piezometers (Figure 4.25(a)). Results are provided in Figure 4.29: it has to be noticed that the sign of the V derived from groundwater has been reversed. As a matter of fact, the spatial response U of the piezometers shows a negative sign (Figure 4.25(b)), meaning that the minimum water level of the wells corresponds to the maximum of the V and vice versa. Coherently, the GNSS spatial response is generally of uplift, meaning that maximum uplift corresponds to the maximum of the V and vice versa. This means that a maximum content of groundwater recorder by piezometers corresponds to a maximum of subsidence in GNSS displacement time series. We therefore associate the IC4 of the GNSS with a deeper water content of the ground.

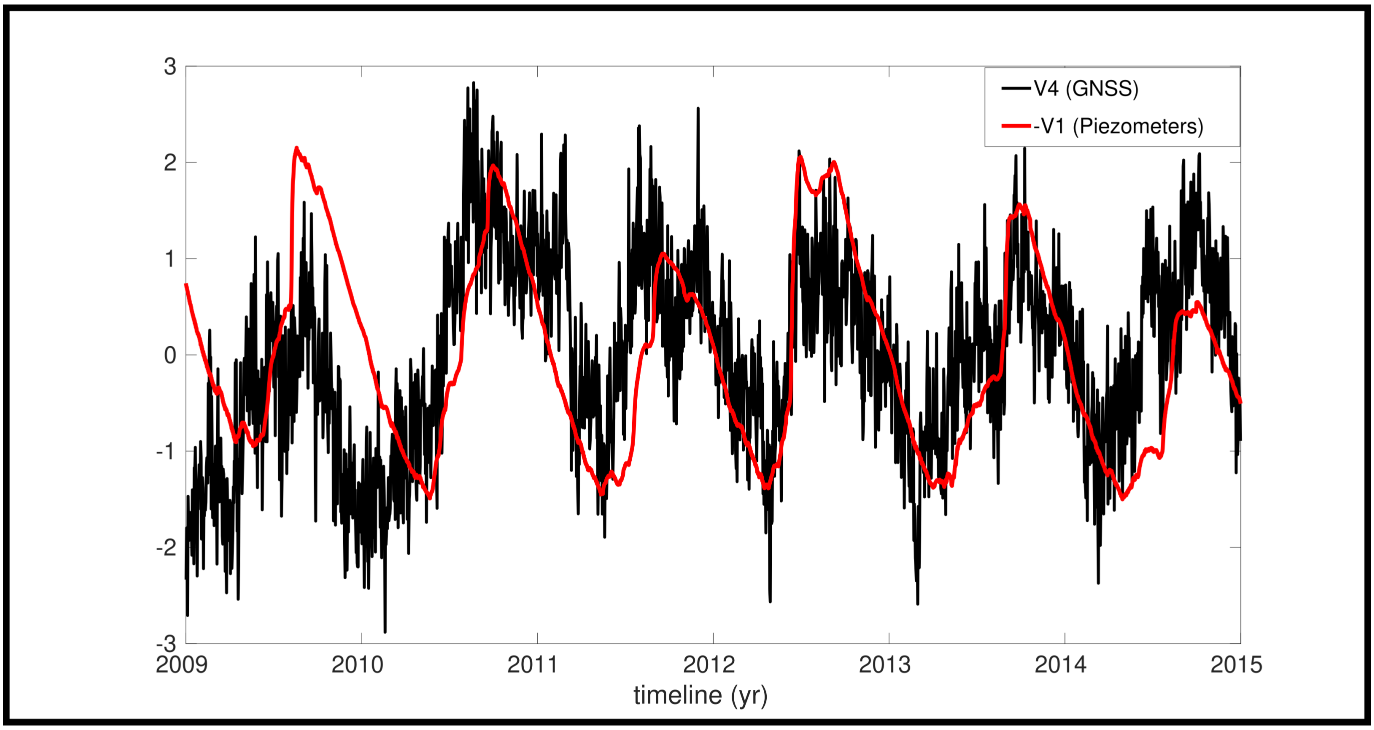

Figure 4.29. Comparison of the V4 retrieved from the analysis on the GNSS (black curve) and the V from the analysis on the piezometers (red curve). The sign of the piezometers is reversed. Both curves have been scaled as in Figure 4.28

The interpretation of the IC5 retrieved from the GNSS is less straightforward: the frequency content of this signal is very similar to the one of the IC1 and IC4 (Figure 4.23(f)), and the U5 shows a weak general subsidence of the GNSS network. On the other hand, the horizontal displacement associated with the U5 is more marked that the one of the U1, with a prevalent N-W direction (Figure 4.24(e)). Conversely to the IC1-4 already described, we could not directly relate the IC5 to any deformation signal observed through other types of data. However a few considerations can be made: its temporal and spatial parts (respectively Figures 4.23(e) and 4.24(e)) are not compatible with the deep water content of the ground that we associate with the IC on the piezometers (Figure 4.25). Comparing the V5 and the LWE from GRACE, we do not observe an agreement as good as for the IC1 (Figure 4.26) as long as we consider the whole time span analyzed (Figure 4.30(a)). On the other hand, focusing on first ~ 2 years of analysis (Figure 4.30(b)) we notice that the V5 may be related to the LWE. This might explain the similarity among the frequency content of V1 and V5, and the vertical component of U1 and U5 abovementioned. Although the weight of IC5 in explaining the variance of the data is only $\sim 56\%$ of that of IC1, it is possible that a certain cross-talk among these components exists.

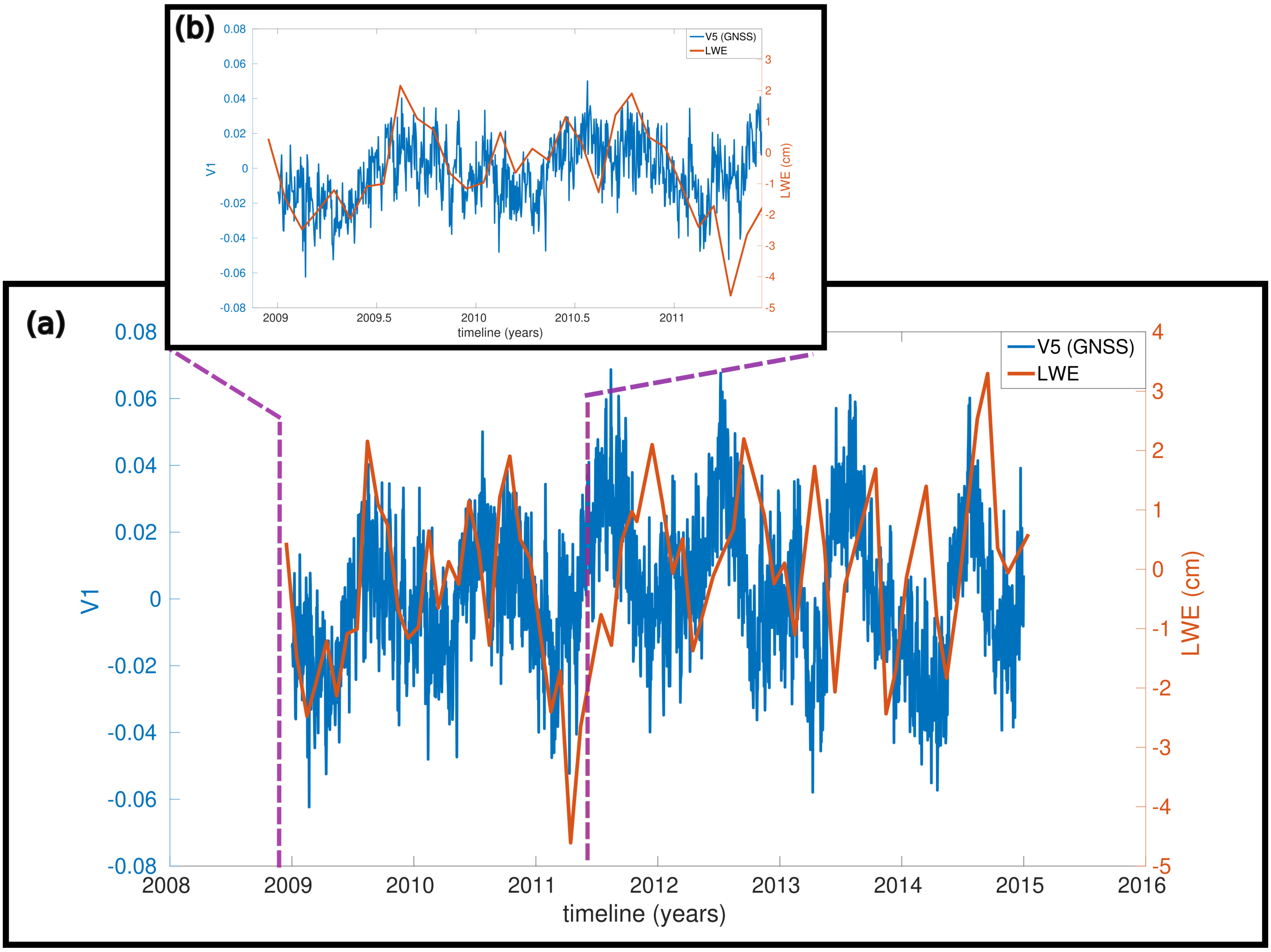

Figure 4.30. Panel (a): comparison of the V5 retrieved from the analysis on the GNSS (blue) and the LWE derived from GRACE measurements (orange). Purple dashed lines mark the zoomed time span depicted in panel (b).

Having recognized the main hydrological sources of deformation affecting the GNSS network in the area, we can now focus on the station (GS63) co-located with the strainmeter and the piezometer (10040111) closest to it. In Figure 4.31 we compare the time evolution of the areal strain measured by TAIS, with the horizontal displacement components of GS63 and the water level measurements of 10040111. As we can observe, the horizontal components of GS63 follow the same evolution as the areal strain, and of water levels in 100400111 piezometer. Comparing it with the rain measurements in the area (in blue, Figure 4.31), we notice that TAIS experiences expansion during the wet season and contraction during the dry season, hence showing a behavior consistent with the piezometer response to rain, namely an increase of strain during times of high rainfall and a decrease of strain related to a water discharge during drier periods. In Figure 4.32 we also compare TAIS areal strain with mean monthly temperature. Thermal fluctuations show rough correlation with changes in areal strain if a phase lag is assumed (with temperature anticipating strain of about 1 month), as expected for thermoelastic effects on strain (e.g. Figure 4 by Ben Zion e Leary, 1986). On the other hand, the areal strain resembles the behaviour of piezometer 10040111 (Figure 4.31). For this reason, keeping also into account the limited thermal excursion this area experiences (Figure 4.32), we believe hydrological-related effects to be the dominant forcing, similarly to what has been found by Mouyen et al. (2017) for Taiwan, even though some minor effects ($\sim$microstrain, e.g. Ben Zion and Allard, 2017) related to temperature variations cannot be ruled out. Therefore we infer that the areal strain time evolution measured by TAIS reflects strong poro-elastic features of the medium it is installed in (e.g., Nespoli et al., 2021), which responds to a greater content of water in the ground expanding, and to a water discharge contracting. Since TAIS is installed at $\sim$ 200 m depth, we can infer that it is either located very close to an aquifer, or already inside it. The presence of a shallow aquifer is partly corroborated by the strong (in the order of the cm), coherent horizontal response of the GNSS station co-located. As a matter of fact, GS63 time series is largely explained by the IC4 and IC5 retrieved from the vbICA decomposition, namely a deep content of water in the ground (see Table 4.11). Although this might explain the piezometer-like behavior of TAIS strainmeter and the GNSS in this location (and their strong response to water level in the ground), it is not possible to make further inferences due to a lack of precise information on the siting of these instruments. A more thorough investigation might be derived only through a site inspection.

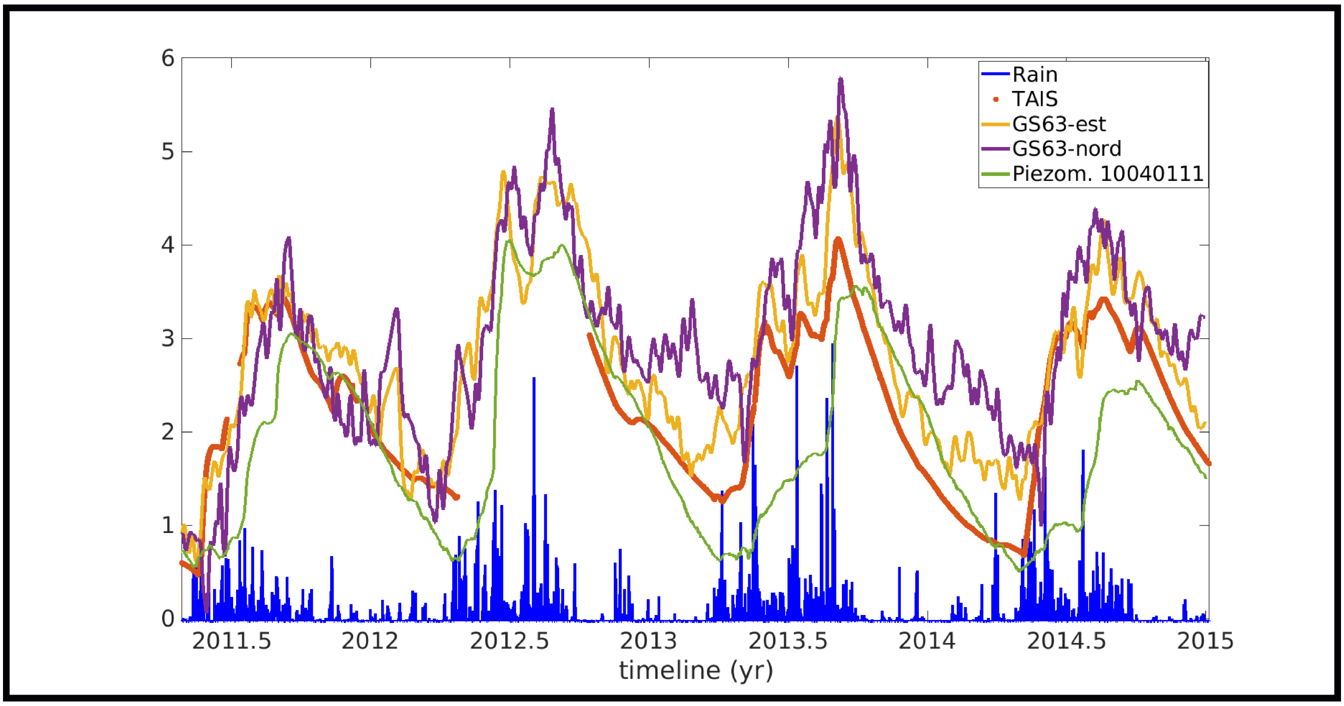

Figure 4.31. Comparison among the normalized time series of TAIS areal strain (orange); the horizontal components of GNSS station GS63 (yellow and purple, respectively for the east and north components) and the water level measured by the 10040111 piezometer (green). In blue the daily stacked rain.

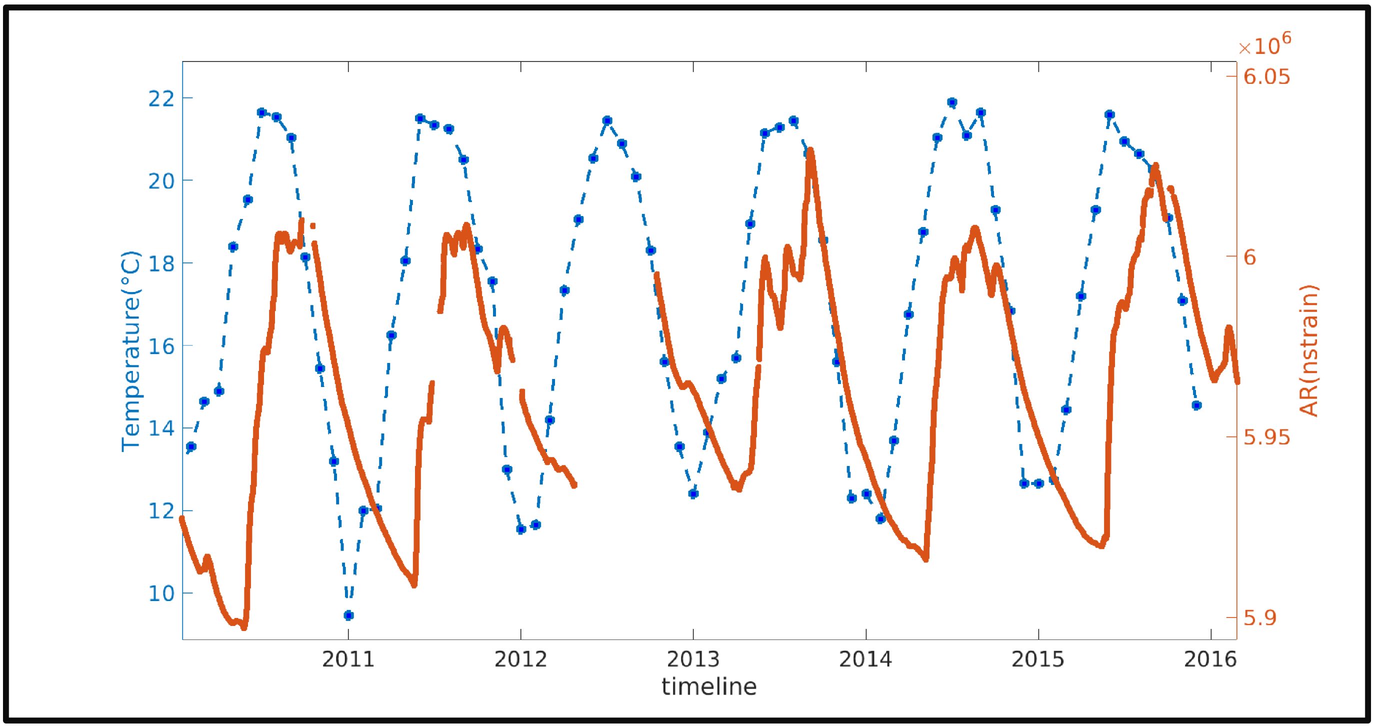

Figure 4.32. Comparison among the areal strain time series of TAIS (orange) and mean monthly temperature measurement. Gridded temperature recordings are provided by Climatic Research Unit (available at https://cds.climate.copernicus.eu/)

GS63	Tot. Variance explained	IC4+5 Variance explained-
East	95 %	78 %
North	76 %	48 %
Up	70 %	52 %

Table 4.11. In table the total data variance of the GNSS GS63 station co-located with TAIS strainmeter explained by the vbICA (second column), and the variance explained only by the IC4 and IC5 (third column).

To conclude, in this section we show the importance of a multiparametric analysis, which includes hydrological, satellite and geodetic data sets, to correctly interpret non-tectonic sources of deformation. The relevance of the interpretation of signals unrelated to tectonic origins lies in multiple factors:

1. the first, straightforward reason concerns the characterization of the hydrological processes ongoing in the area, with possible interest for the management of water

resources and the assessment of hydrological hazard. As acknowledge by Clements and Denolle (2018), monitoring hydrological resources requires the use of multiple types of data sets. A precise monitoring of the hydrological processes is needed to properly manage water supplies, especially in the frame of climate change (Taylor et al., 2012).

2. A second factor lies in the well documented relationship existing between observed deformation and hydrological sources (e.g., Devoti et al., 2015,; Serpelloni et al., 2018; Pintori et al., 2021), with effects on the earthquakes occurrence. Hainzl et al. (2006) proposed that the water cycle may produce pore-fluid pressure changes at seismogenic depths, whereas seismicity rates in phase with groundwater cycle suggest a direct effects of fluids in stressing faults (e.g., D'Agostino et al., 2018). Hence the study of hydrological processes is essential if we want to achieve a thorough characterization of the behaviour of faults.

3. Lastly, a proper interpretation of non-tectonic signals is of primary importance for an accurate study of tectonic sources of deformation. This proves to be particularly true for the borehole strainmeter case, due to their high sensitivity to strain variations. In fact, if we are interested in studying tectonic processes, hydrology and environmental effects raise the "noise" level of the data, possibly hiding faint seismic signals (Chen et al., 2021). If on the one hand the high sensitivity of borehole strainmeters allows us to downscale the intensity of the measurable tectonic processes, on the other hydrological signals can become a relevant and/or dominant signal in strain time series. Hence the importance of a multiparametric analysis which aims at discriminating environmental signals from the tectonic signals of interest.

Chapter 5

Central Italy GTSM array

In this Chapter the Gladwin strainmeters array deployed on the Alto Tiberina Fault (ATF, Figure 5.1a), Central Italy, will be presented. GTSMs in the area have recently been installed as part of the *STrainmeter ARray* project (STAR, https://www.icdp-online.org/projects/world/europe/northern-apennines-italy/details/), to complement the existing Near Fault Observatory (NFO) TABOO project (http://taboo.rm.ingv.it/) belonging to the European Plate Observing System (EPOS, https://www.epos-ip.org/), with the aim of enhancing the spectrum of the detectable tectonic phenomena.

The calibration methods presented in Section 3.4 will also be applied and preliminary results will be provided: as a matter of fact, due to the recent installation of these instruments (late 2021), calibration results may be subjected to revision in future analyses.

5.1 Geology of the area and Instrumentation

Between Fall 2021 and early Summer 2022, six Gladwin Tensor strainmeters have been installed in the Umbria Marche sector of the Northern Apennines, Italy (see Table 5.1 and Figure 5.1b). The extension rate of $\sim 2-3$ mm/yr (Serpelloni et al., 2006; D'Agostino et al., 2009; Bennett et al., 2012) that characterizes this area is currently accommodated through a complex normal fault system, which results from the Quaternary extensional phase. The tectonic setting is furtherly complicated by the presence of thrust and folds which resulted from the upper Miocene-lower Pleistocene compressional phase (Anderlini et al., 2016). In the past 40 years, at least three main seismic sequence occurred in this area, respectively in 1984 (Gubbio seismic sequence), in 1997 (Colfiorito seismic sequence), and in 1998 (Gualdo Tadino seismic sequence) (Chiaraluce et al., 2004). The Alto Tiberina fault, described in detail in Chiaraluce et al. (2007), appears to serve as a structural control on the high angle normal fault system located in its hanging wall, though its role is still debated since no large event has been attributed to it (Rovida et al., 2011). In fact, both the 1984 Gubbio and 1998 Gualdo Tadino seismic sequences occurred directly in the hanging wall of the ATF, and we have no evidence of historical earthquakes within the past 1000 years rupturing the whole ATF length, which would result in very large earthquakes.

The ATF is a Low Angle Normal Fault (LANF), dipping with an angle of $\sim 15° - 30°$ eastwards, which extends for $\sim$ 60 km along strike with depths between 4 and 16 km. It is a $\sim$ 1.5 km thick fault zone made of multiple sub-parallel slipping planes, and a complex network of synthetic and antithetic higher-angle structures located on its hanging wall can be traced along strike for $\sim$ 35 km (Valoroso et al., 2017). Whether or not LANFs are capable of originating moderate to large magnitude earthquakes is widely discussed in the literature (e.g., Wernicke, 1995 and references therein; Axen, 2004), and such a debate goes by the name of *LANF paradox*. The LANF paradox is hardly explained by the classical Andersonian theory of faulting since, from a physical point of view, in an extensional tectonic setting characterized by a vertical principal stress, no slip is expected on faults dipping less than 30° with a friction coefficient ranging between 0.6 and 0.85 (Byerlee 1978). The ATF shows a mixed slip behaviour, as microseismicity activity (Vadacca et al., 2016), creeping (Anderlini et al., 2016) and transient slip (Gualandi et al., 2017) have all been detected. This is consistent with the creeping rate of the unlocked deepest portions of the ATF modeled by Anderlini et al. (2016), while the locked, shallower, portion ATF fault system may represent a seismic gap capable of producing a large magnitude ($M_w \sim 7$) earthquake over time periods of $\sim 10^3$ years.

Hence the ATF is an ideal natural laboratory to study a wide range of the fault slip spectrum. The area hosts a Near Fault Observatory (NFO) equipped with seismological, geodetic and geochemical data sets part of the TABOO project (Figure 5.1b). Six GTSMs have recently been installed as part of the *STAR* project with the aim of better investigating the spatio-temporal pattern of slip on time scales of minutes to days-months that appears to characterize transient aseismic slip. Moreover, thanks to the GTSMs increased capability of measuring strain, we aim at better resolving features of the minor, long-lasting seismic sequences (with $3.0 \leq M_W \leq 3.9$ mainshocks), which characterize this area and have been poorly resolved until now, as they are usually below the detection threshold of surface GPS instruments.

Hence the six GTSMs promise to shed some light on the low-intensity seismic sequences occurring in this area, and on the spatio-temporal characteristics of creep on the ATF, including the possible triggering of larger earthquakes on the high angle normal faults on its hanging wall, which is a key issue to address for the seismic hazards and risk assessment community. The strainmeters will also help in answering questions about the relationship between seismic and aseismic slip (see also Chapter 1), allowing us to actively observe transient deformation and microseismic swarms, and the physics that allows for both seismic and aseismic slip on a single fault patch.

In this thesis we focus on the calibration of the available GTSMs of the STAR project, applying the two methodologies of Section 3.4.1 and 3.4.2. At the time of this work, only

3 strainmeters are suitable for calibration, namely they have time series long enough for a tidal analysis. Time is a key factor for a proper calibration of the STAR instruments (see Section 4.2), both for the 3 younger sites and for those already suitable for calibration. In the future, longer time series will surely help in better constraining the calibration coefficients of these instruments. Finally (Section 5.4) we present an example of the potential of the strainmeters in detecting with high accuracy the dynamics of short-term deformation signals.

Site	**Lat(°)**	**Lon(°)**	**Alt.(m)**	**Instal. depth(m)**	**1^{st} available epoch**	**Lithology**	**State of health**
TSM1	43.34536	12.597621	553	131	11/10/2021	Limeston & calcareous marl	Long term contract. $\surd$ Tides recording $\surd$ Seismic recording $\surd$
TSM2	43.39619	12.489944	630	158	02/11/2021	Red limeston & calcareous marl	Long term contract. $\surd$ Tides recording $\surd$ Seismic recording $\surd$
TSM3	43.38298	12.354506	341	79	13/11/2021	Marly-arenaceous fm.	Long term contract. $\times$ Tides recording $\surd$ Seismic recording $\surd$
TSM4	43.3087	12.3046	270	99	13/05/2022	Marly-arenaceous fm.	Not functioning
TSM5	43.479691	12.60252	379	116	26/05/2022	Schlier fm.	Long term contract. $\times$ Tides recording $\surd$ Seismic recording $\surd$
TSM6	43.47246	12.33275	402	116	14/06/2022	Marly-arenaceous fm.	Long term contract. $\surd$ Tides recording $\surd$ Seismic recording $\surd$

Table 5.1. In table the details of the installation environment and location of the six GTSMs installed in Central Italy

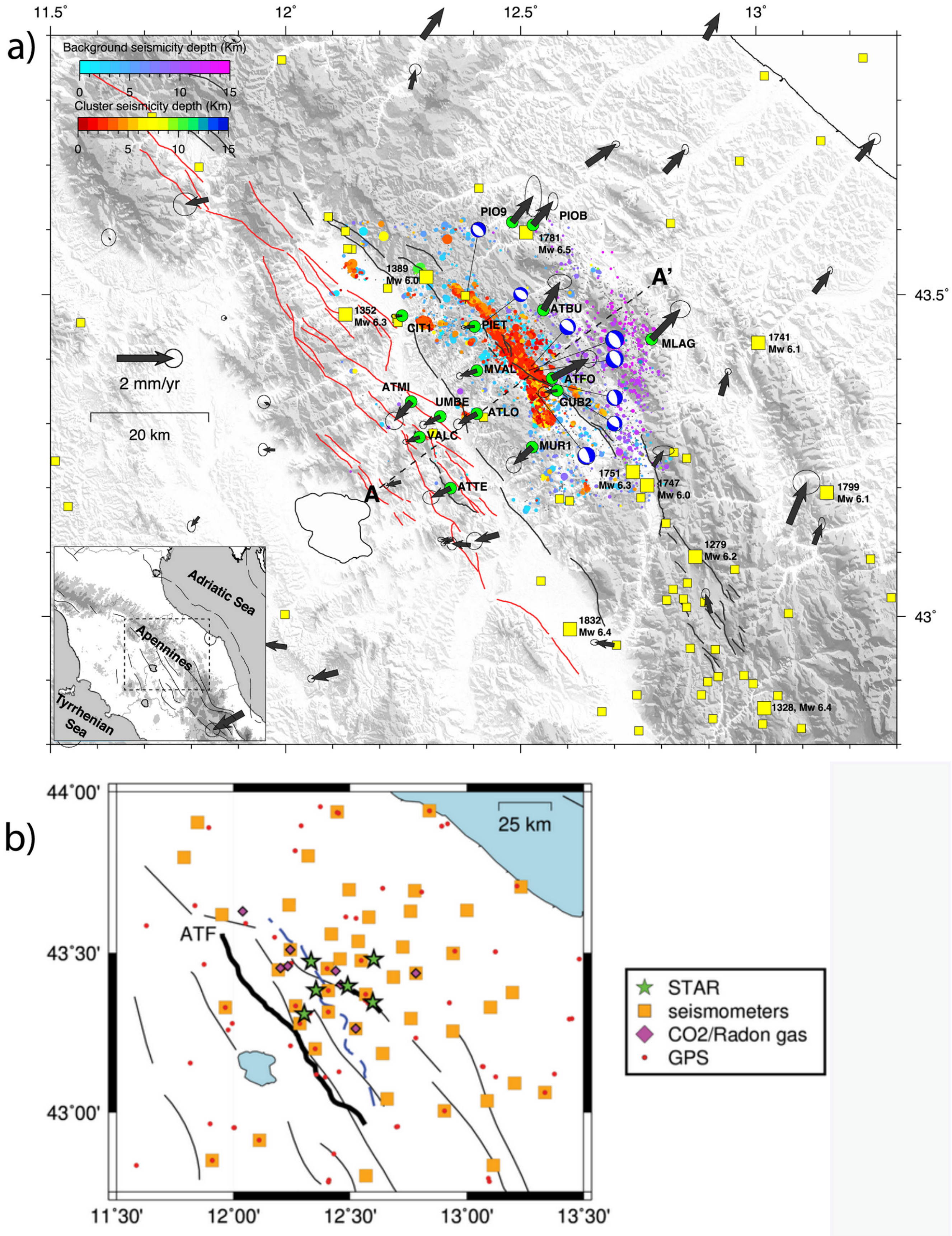

Figure 5.1. (Caption next page.)

Figure 5.1. Map of the Umbria Marche sector of the Northern Apennines. Panel (a): green circles mark the location of the GPS stations analyzed in Gualandi et al. (2017), arrows show the residual velocities after removing the Eurasian-fixed velocity field. Mapped faults traces of the area are represented by red and black lines, respectively for eastward/westward dipping faults (http://ccgm.free.fr). Seismicity is represented by gray dots, whereas cold and rainbow dots are respectively the background and clustered seismicity with $1.55 \leq M_w$. Focal mechanisms from http://cnt.rm.ingv.it/tdmt. Historical seismicity from Rovida et al. (2016) with $5 \leq M_w$ is represented by yellow squares (year and magnitude is also reported for $6 \leq M_w$. Panel (a) has been taken from Gualandi et al. (2017). Panel (b): map of the NFO deployed on the ATF (black line). Red dots mark the position of the GPS stations; yellow squares the position of the seismic network; purple diamonds the position of the geochemical stations; green stars the position of the recently installed Gladwinn strainmeters. Figure has been taken from the UNAVCO website (https://www.unavco.org/news/borehole-project-in-italy-will-help-answer-questions-about-enigmatic-faults/).

5.2 Calibration results

In this section we will reapply the calibration methods of Sections 3.4.1 and 3.4.2 following the same approach as for the Taiwan arrays.

We start off by comparing Baytap08 analysis results with the recorded data in the periods of interest, namely around the 12 and 24 hours (respectively Figure 5.2a and 5.2b). $TSM1-3$ correctly record tidal deformations, which confirms the good state of health of these instruments (Section 3.2). Although only a few months of data are available, Baytap08 has proven to be capable of a robust tidal analysis, providing tidal signals compatible with the raw time series (Figure 5.2).

Next, following the same path as for the Taiwanese GTSMs, we start applying the simplest model which assumes the isotropy of the medium. As for the Taiwanese array, a single coefficient for the shear components cannot be found, hence we directly present results for a quasi-isotropic medium (i.e., Method 1). As in Section 3.4.1, we run the consistency check on the two-ways areal and differential strain, and we find a good agreement for $TSM1-2$, in both phase ($> 98\%$, see table 5.2) and amplitude (Figure 5.3(a-d)). This suggests us that for these sites a weighting of the gauges in unnecessary. On the other hand, $TSM3$ shows a very weak agreement between the two-ways areal strain which can be readjusted applying some weighting factors g_i, $i = 0, 1, 2, 3$, to the CH_i (Table 5.2). Figure 5.3(g,h) shows that the use of weighted gauges effectively reduces the differences between AR and AR_0 (Figure 5.3(e)), while keeping the good agreement between ED and ED_0 (Figure 5.3(f)).

We continue by checking the azimuth of CH_1 applying the approach described in Section 3.4.1. From Figure 5.4a we notice that for TSM1 the shear components have low correlations $\forall\theta \in [0, 2\pi]$, with maximum Pearson coefficient $R < 80\%$. For the engineering strain of TSM2 we can find an azimuth which allows a good correlation with theory, whereas lower coherence is found for the differential strain (respectively yellow and orange/blue markers in Figure 5.4b). The opposite situation is observed for TSM3 (Figure 5.4c), for which maximum $R(diff.strain) \sim 90\%$ and $R(eng.strain) \sim 50\%$.

Station	**R(unweighted)** areal strain diff. strain	g_i	**R(weighted)** areal strain diff. strain	**variance reduction** (%)
TSM1	0.9858 0.9989	1 1 1 1	\	\
TSM2	0.9951 0.9991	1 1 1 1	\	\
TSM3	0.6754 0.9972	0.14 1 0.10 0.50	0.9840 0.9963	83

Table 5.2. In table the weights g_i, the correlation coefficients R between the two ways areal and differential strain before and after the weighting of gauges, and the variance reduction are reported.

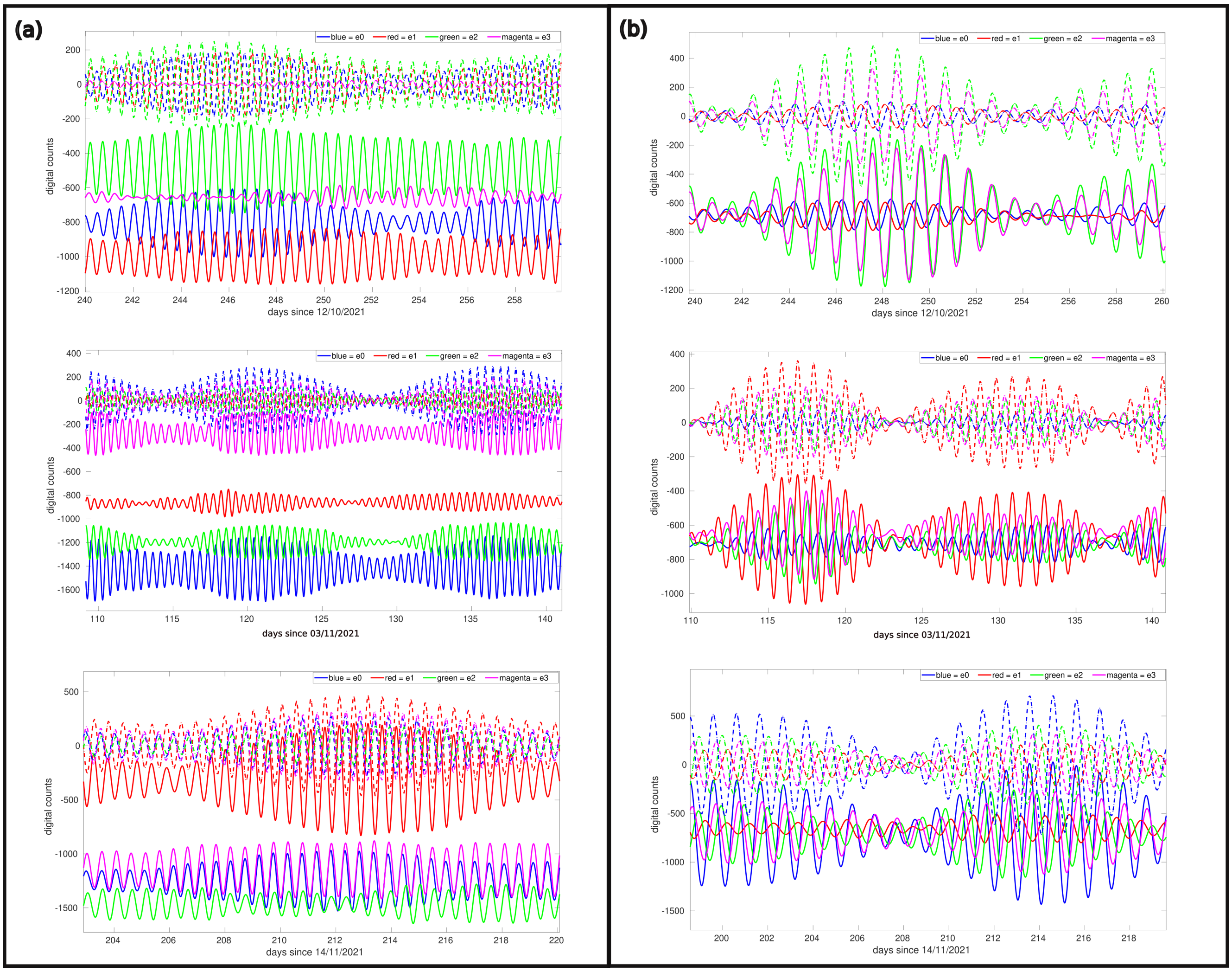

Figure 5.2. (a): comparison of a 12h pass-band filter applied to raw data (solid lines) and to tidal signals outputted from Baytap08 (dashed lines) respectively for TSM1 (upper panel), TSM2 (central panel) and TSM3 (lower panel). (b): same as (a) for a 24h pass-band filter.

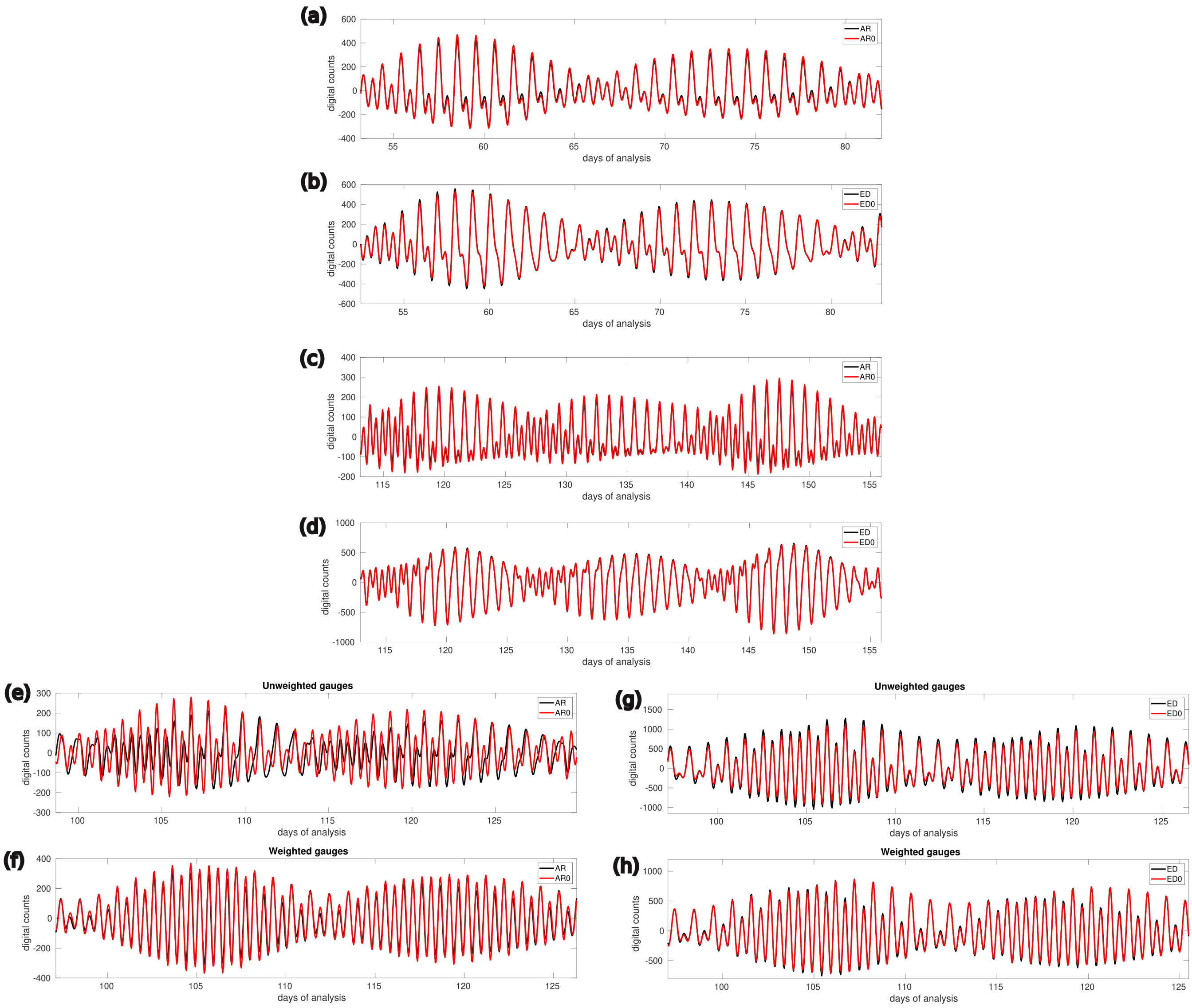

Figure 5.3. Examples of the weighting of gauges described by equation 4.1. In panels (a,b) and (c,d) respectively the comparison of the two ways areal and differential strain for TSM1 and TSM2 (weights of gauges $g_i = 1$, $i = 0, 1, 2, 3$). Panels (e),(f) show areal strain respectively before and after weighting the CH_i for TSM3. Equivalently, panels (g), (h) show differential strain respectively before and after weighting for the same sites.

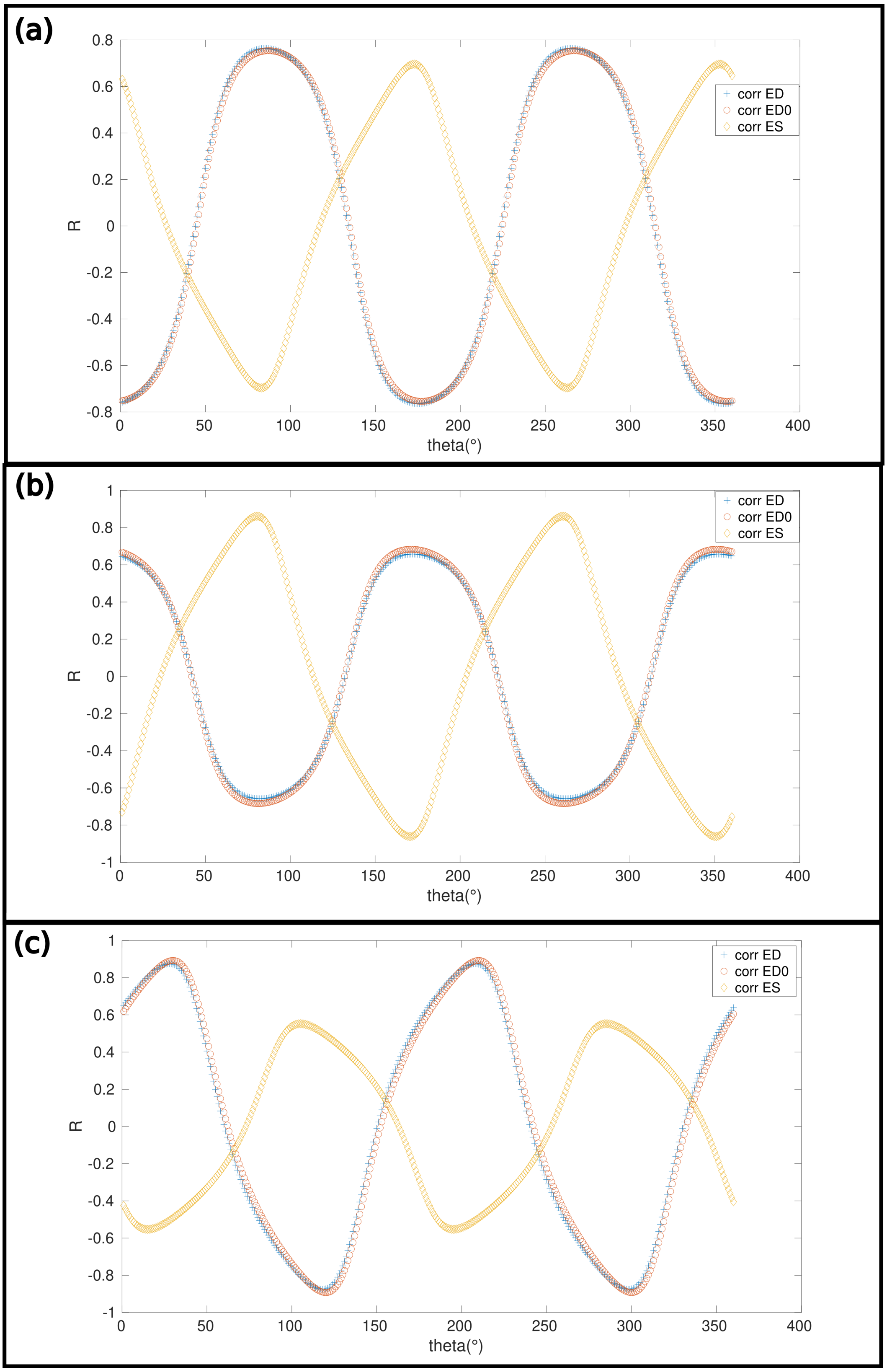

Figure 5.4. Same as Figure 4.6 for (a) TSM1, (b) TSM2 and (c) TSM3.

Having an estimation of the azimuth of the instruments, we can proceed with the comparison with the theoretical waveforms computed using *Gotic2* software. Figures 5.5(a,b) show that areal strain (upper panels) are well estimated applying Method 1 on $TSM1$ and $TSM2$ strainmeters. Good correlation among the theoretical and observed waveforms is found for these strain components (table 5.3), with $R \sim 88 - 93\%$. However, it can be remarked that poorer results are found for engineering strain for $TSM1$ (lower panel of Figure 5.5(a)) and differential strain of $TSM2$ (central panel of Figure 5.5(b)), with $R < 70\%$. As a matter of fact, shear strains are often the least robust components to model (Canitano et al., 2018) but we deem that with a bigger amount of data available and more time for the strainmeters to settle (i.e., with longer time series), better results will be achieved. On the other hand, $TSM3$ keeps on bearing some issues with the areal strain, as a very poor agreement $R \sim 56\%$ is found during calibration (table 5.3). In upper and lower panels of Figure 5.5(c) we can observe that, through Method 1, it is not possible to satisfyingly reproduce the areal and engineering strain for this site. Conversely, better results are obtained for the differential component (central panel of Figure 5.5(c)), with correlations $R > 88\%$ (table 5.3).

Station	**R(areal strain)** (%)	**R(diff. strain)** (%)	**R(eng. strain)** (%)
TSM1	88.7 ± 0.6	75.9 ± 0.8	69.2
TSM2	92.6 ± 0.4	67.1 ± 0.1	85.9
TSM3	56 ± 4	88.4 ± 0.9	50.4

Table 5.3. In table the Pearson correlation coefficients R among the calibrated strain components through Method 1 and theoretical ones are summarized.

Station	$C_{q-iso}\left(\frac{nstrain}{counts}\right)$	$D_{dif}\left(\frac{nstrain}{counts}\right)$	$D_{eng}\left(\frac{nstrain}{counts}\right)$	θ (°)
TSM1	0.111 ± 0.002	0.0390 ± 0.0009	-0.0066	86 ± 1
TSM2	0.168 ± 0.007	0.0210 ± 0.0003	-0.0118	171.5 ± 0.5
TSM3	$-0.0633 \pm 9 \times 10^{-4}$	$0.0188 \pm 1 \times 10^{-4}$	-0.0360	29 ± 1

Table 5.4. In table the calibration coefficients and the azimuth of CH_1 for the 3 GTSMs are summarized.

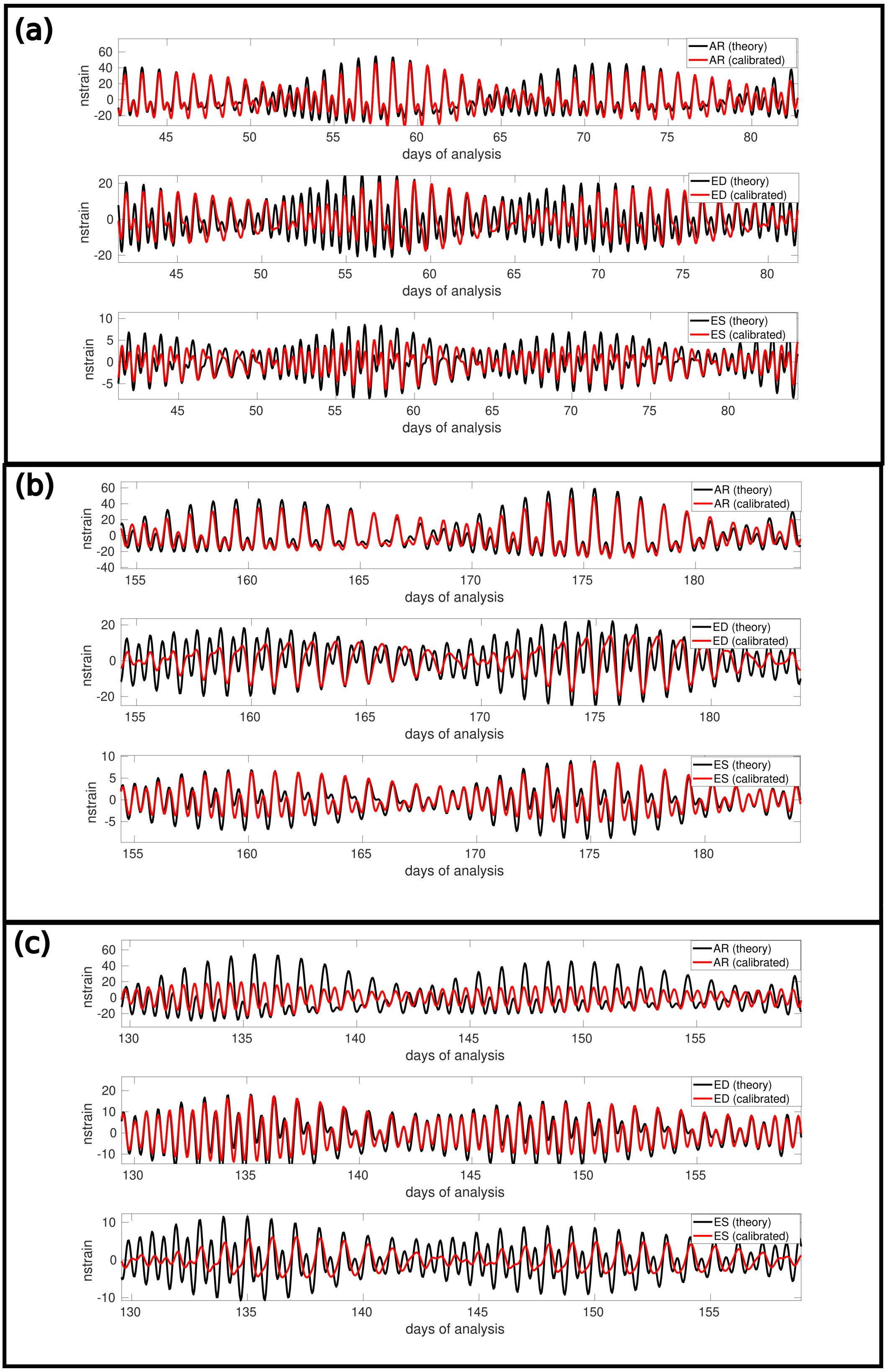

Figure 5.5. Graphical results of calibration through Method 1: areal strain (upper panels), differential strain (central panels) and engineering strain (lower panels) for (a) TSM1, (b) TSM2 and (c) TSM3. Black lines represent the theoretical strain components whereas red lines the observed ones.

Since Method 1 provides unsatisfactory results for at least one of the shear components of $TSM1-2$ and for areal and engineering strain of $TSM3$ (Figure 5.5), we furtherly relax the isotropy assumption and apply Method 2.

Fitting elongations for the four gauges e_i (Figure 5.8), we can estimate the coupling coefficients whose pseudo-inverse gives the calibration matrix (equation 3.25). Results are summarized in table 5.5. In Figures 5.6, 5.7 and 5.8 we show how the high flexibility of Method 2 allows us to reproduce the tidal waveforms that each gauge of the strainmeters measures. As already done for the Taiwanese array, we apply the calibration matrix to our observations to check whether they match the theoretical strain waveforms. From Figure 5.9 we can observe that Method 2 provides good results for all of the GTSMs considered. The good graphical comparison is also corroborated by the high Pearson coefficients that we find (Table 5.6), with values $R >\sim 90\%$.

Station	$C_{non-iso}\left(\frac{nstrain}{counts}\right)$	$D^{dif}_{non-iso}\left(\frac{nstrain}{counts}\right)$	$D^{eng}_{non-iso}\left(\frac{nstrain}{counts}\right)$
TSM1	0.1080	-0.0105	0.0352
	0.1594	-0.1094	0.0324
	0.0434	-0.0020	-0.0084
	0.0780	0.0112	0.0145
TSM2	0.0704	-0.0455	-0.0068
	0.1675	-0.0230	0.0212
	0.0871	-0.0296	0.0316
	0.0890	-0.0552	0.0164
TSM3	-0.0092	0.0266	-0.0093
	-0.1699	0.0774	-0.0222
	-0.0972	0.0085	-0.0151
	-0.1155	0.0349	-0.0234

Table 5.5. In table the calibration coefficients retrieved using Method 2 are summarized (see equation 3.25).

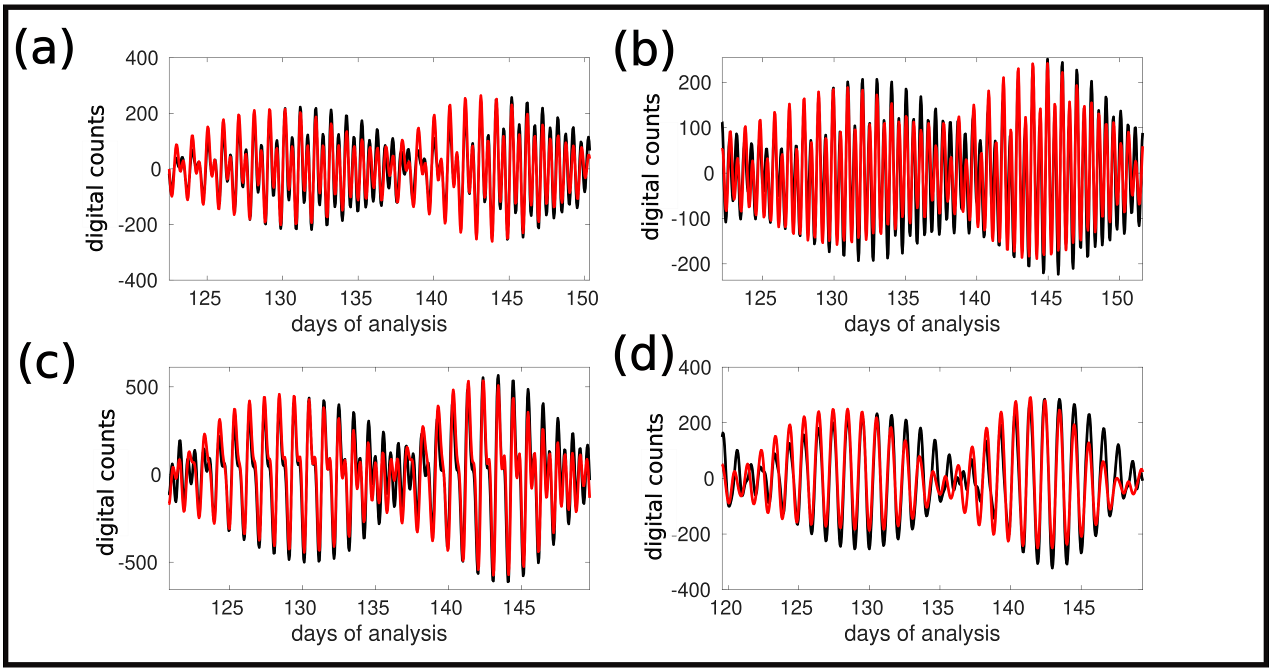

Figure 5.6. Elongation e_i, $i = 0, 1, 2, 3$, of TSM1 (respectively panels (a), (b), (c), (d)). Black lines represent the observed elongations (left-side hand of equation 3.24) while red lines the theoretical ones (right-side hand of equation 3.24).

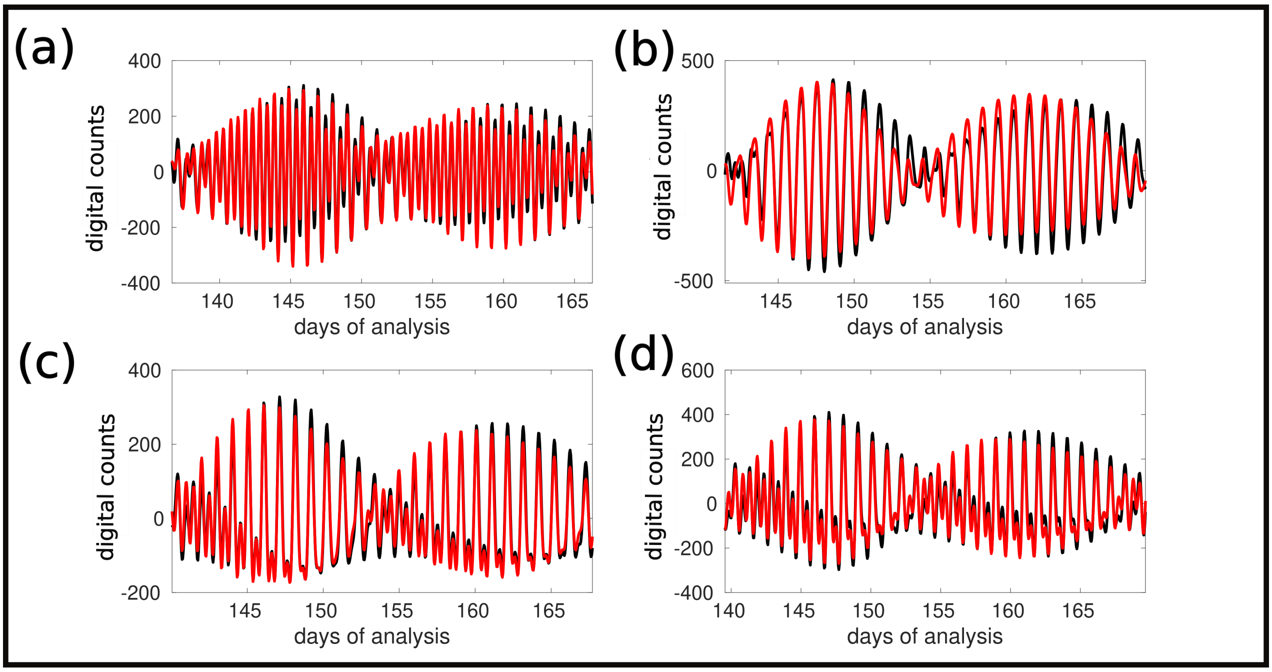

Figure 5.7. Same as Figure 5.6 for TSM2 strainmeter.

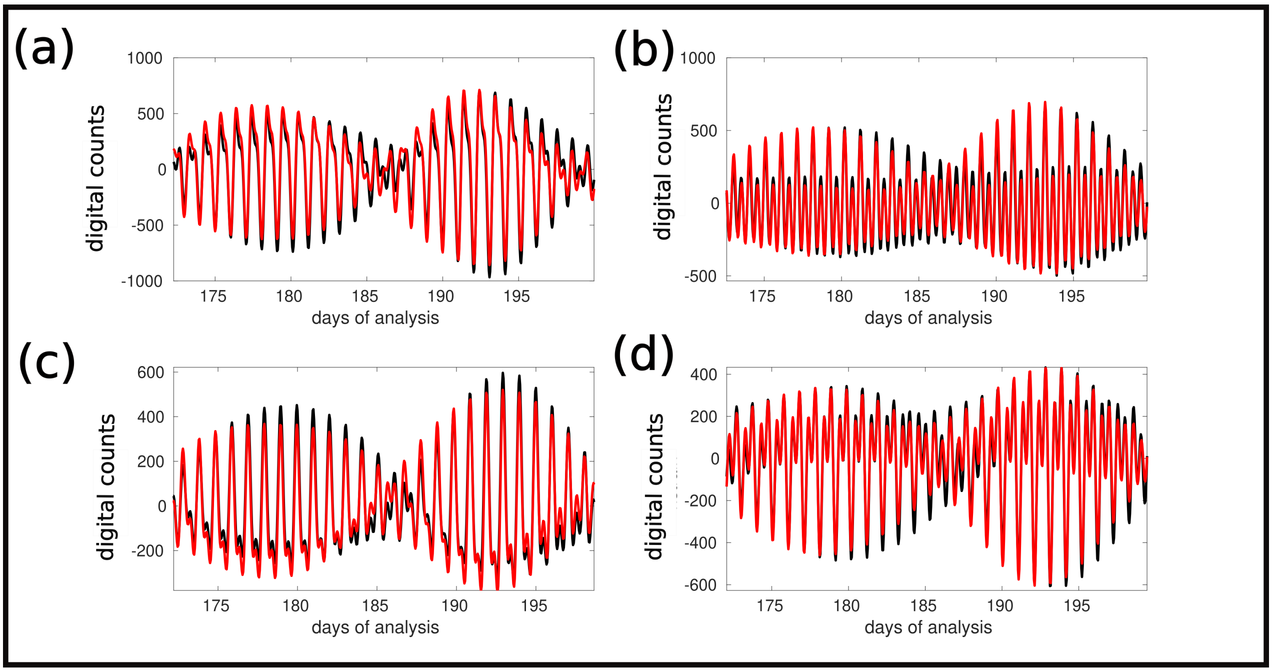

Figure 5.8. Same as Figure 5.6 for TSM3 strainmeter.

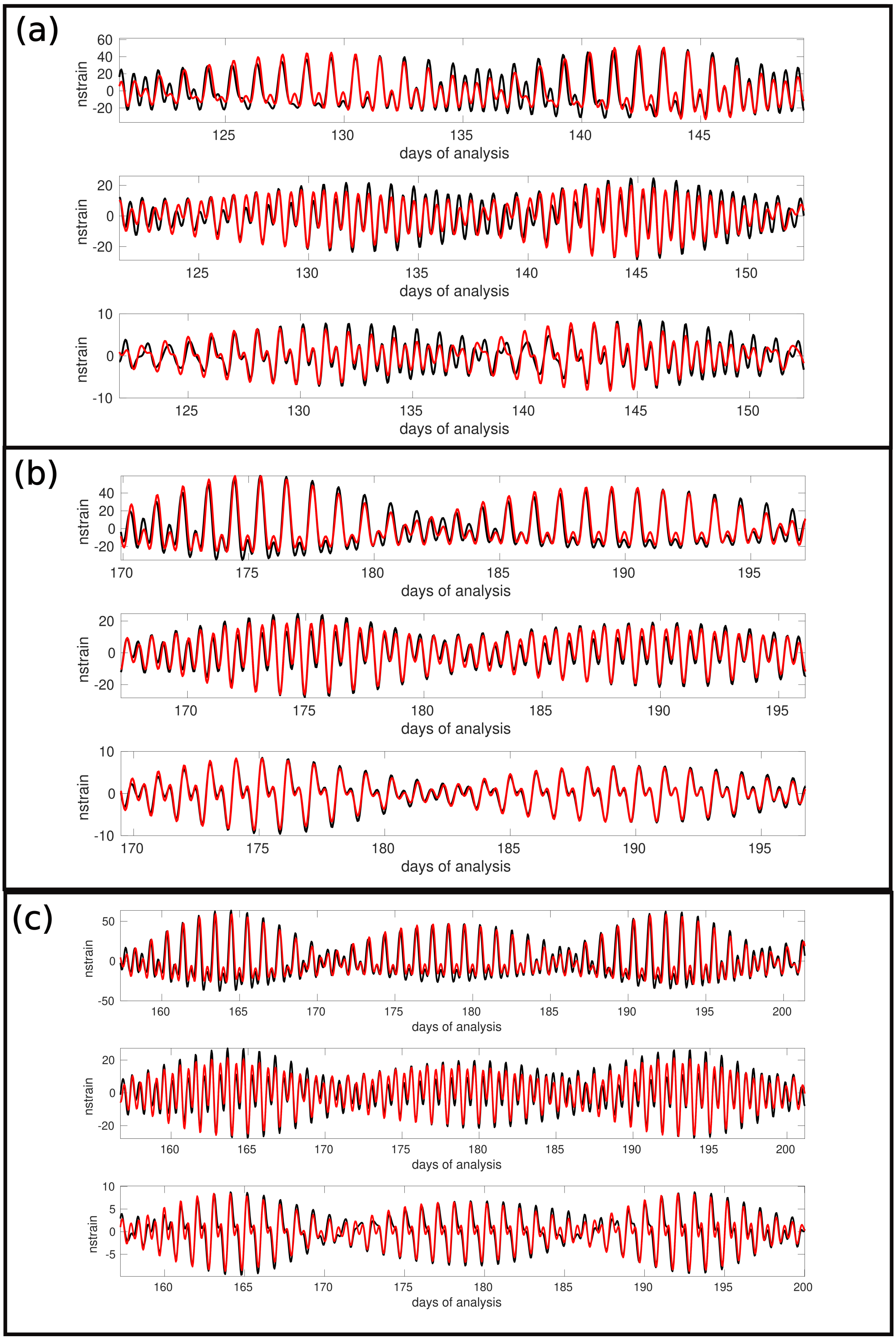

Figure 5.9. Graphical results of calibration through Method 2: areal strain (upper panels), differential strain (central panels) and engineering strain (lower panels) for (a) TSM1, (b) TSM2 and (c) TSM3. Black lines represent the theoretical strain components whereas red lines the observed ones.

Station	R(areal strain) (%)	R(diff. strain) (%)	R(eng. strain) (%)
TSM1	89.4	91.3	90.8
TSM2	92.6	96.7	97.2
TSM3	89.3	93.8	93.8

Table 5.6. In table the Pearson correlation coefficients R among the calibrated strain components through Method 2 and theoretical ones are summarized.

5.3 Comparison between methods and Summary

In this chapter, we tested the calibration methodologies developed on the Glawdin strainmeters recently installed in Central Italy. Despite the limited length of the data set, $TSM1-3$ prove to record Earth's tides sufficiently well (Section 5.2), showing their good state of health. The weighting of gauges carried out through the tidal content of the time series appears to be good enough even when we consider the whole time series (Table 5.7), with the sole exception of the differential strain of $TSM2$. As a matter of fact, shear components are less robust and might require more time for a better characterization. Method 1 provides good results for the areal strain of $TSM1-2$ (Table 5.3). On the other hand at least one of the shear components for these two GTSMs appears to be poorly modeled by this method. Calibration following Method 1 does not appear to be suitable for $TSM3$, the strainmeter most recently installed.

Station	R($AR^{Meth.1}$; $AR_0^{Meth.1}$) (%)	R($ED^{Meth.1}$; $ED_0^{Meth.1}$) (%)
TSM1	94.0	86.0
TSM2	89.6	29.5
TSM3	99.3	99.6

Table 5.7. In table the Pearson correlation coefficients R among the areal and differential strain (respectively in the second and third column) calibrated following Method 1 (Section 3.4.1). R values have been computed considering the whole duration of the time series.

Calibration carried out with Method 2 provides very good results for all of the GTSMs (Table 5.6). A comparison among the results of the two methods gives back a good agreement for the areal strain and a poor correlation of the shear components of $TSM1-2$. Comparable results are found for the differential strain of $TSM3$, whereas engineering strain (poorly modeled through Method 1) for this site points towards an anticorrelation (Table 5.8).

Since Method 1 does not provide strain components sufficiently robust, we propose Method 2 as the proper calibration to follow for these GTSMs. However, we are aware that strainmeters require some time to properly couple with the rock formation they are installed in. Therefore, we do not completely rule out the possibility that further attempts with Method 1 in the future may give a more reliable calibration and therefore a simplification of the model. Nevertheless, for the moment, we suggest calibration coefficients of Table 5.5 as the most appropriate, and in Figures 5.10, 5.11 and 5.12 we show the resulting strain field time series. We report the calibrated time series before (upper panels of (a), (b) and (c)) and after the removal of the secular trend (lower panels), performed considering the whole length of the time series. The very initial weeks follow an evolution, related to the thermal effects of the curing of the cement used to install the strainmeters, which is hard to model through some functional form (such as those of equations 4.2 or 4.3) and reduce the quality of the estimated trend. This explains the curvature that we observe in the detrended time series (lower panels of Figures 5.10, 5.11 and 5.12 (a,b,c)). Our aim here is to present the whole time series, however for a more thorough detrending we suggest to focus on limited periods of data, and as an example, we show the comparison of the calibrated areal (Figure 5.13a), differential (Figure 5.13b) and engineering strain (Figure 5.13c) for $TSM1-3$ time series limited to summer 2022. TSM1 and TSM2 show comparable areal strain time series while differences are observed for TSM3. This is expected as the strainmeters are deployed at a close distance, on the other hand differences for TSM3 might reflect some peculiar characteristic of the installation site, as also testified by the long term expansion that this strainmeter experiences (Figure 5.12a), opposed to the expected contraction observed for $TSM1-2$ (Figures 5.10a and 5.11a). Remarkably, we observe in $TSM2-3$ a sharp peak around September 2022 which is however not evidently present in TSM1 areal strain time series (Figure 5.13a). This signal, which proves to be an interesting example of the potential improvement in deformation's monitoring brought along by these instruments, will be presented and discussed in Section 5.4. An exact comparison among shear components is less straightforward, as they are more subject to inhomogeneities of the ground and are more heavily affected by the specific properties of the rock formation, therefore sharper differences among the time series are expected (Figure 5.13b,c).

Station	R($AR^{meth1}; AR^{meth2}$) (%)	R($ED^{meth1}; ED^{meth2}$) (%)	R($ES^{meth1}; ES^{meth2}$) (%)
TSM1	99.4	63.8	-17.6
TSM2	98.0	-78.7	13.8
TSM3	97.3	94.7	-79.5

Table 5.8. In table the Pearson correlation coefficients R among the strain components calibrated through Method 1 and 2. R for areal, differential and engineering strain are respectively reported in the second, third and fourth column.

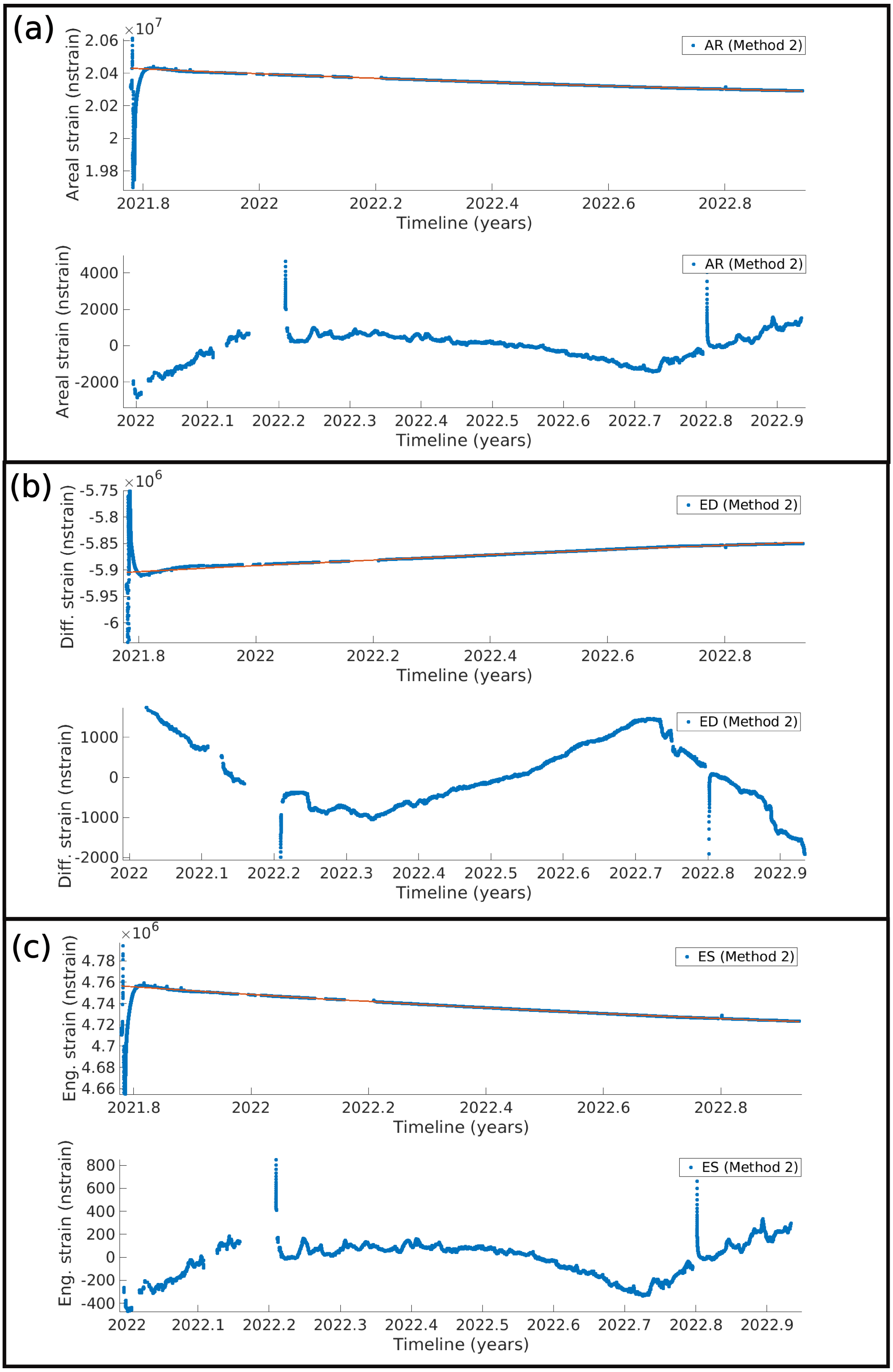

Figure 5.10. In Figure areal strain calibrated time series (a), (b) differential strain and (c) engineering strain before (upper panels) and after detrending (lower panels) for $TSM1$ GTSM. Results are obtained through Method 2. The detrending function is described by equation 4.3, and represented in orange in the upper panels.

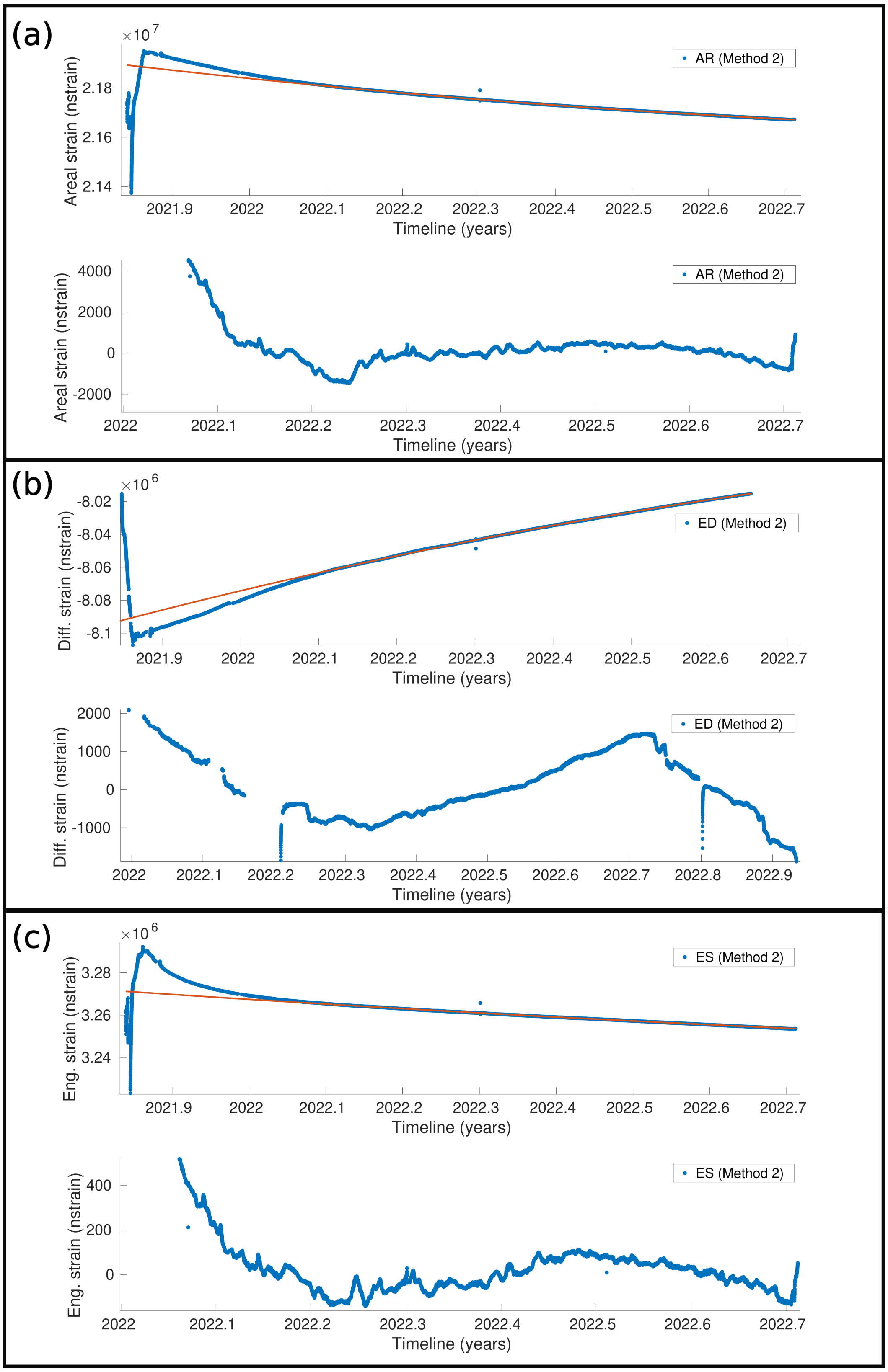

Figure 5.11. Same as Figure 5.10 for TSM2 GTSM.

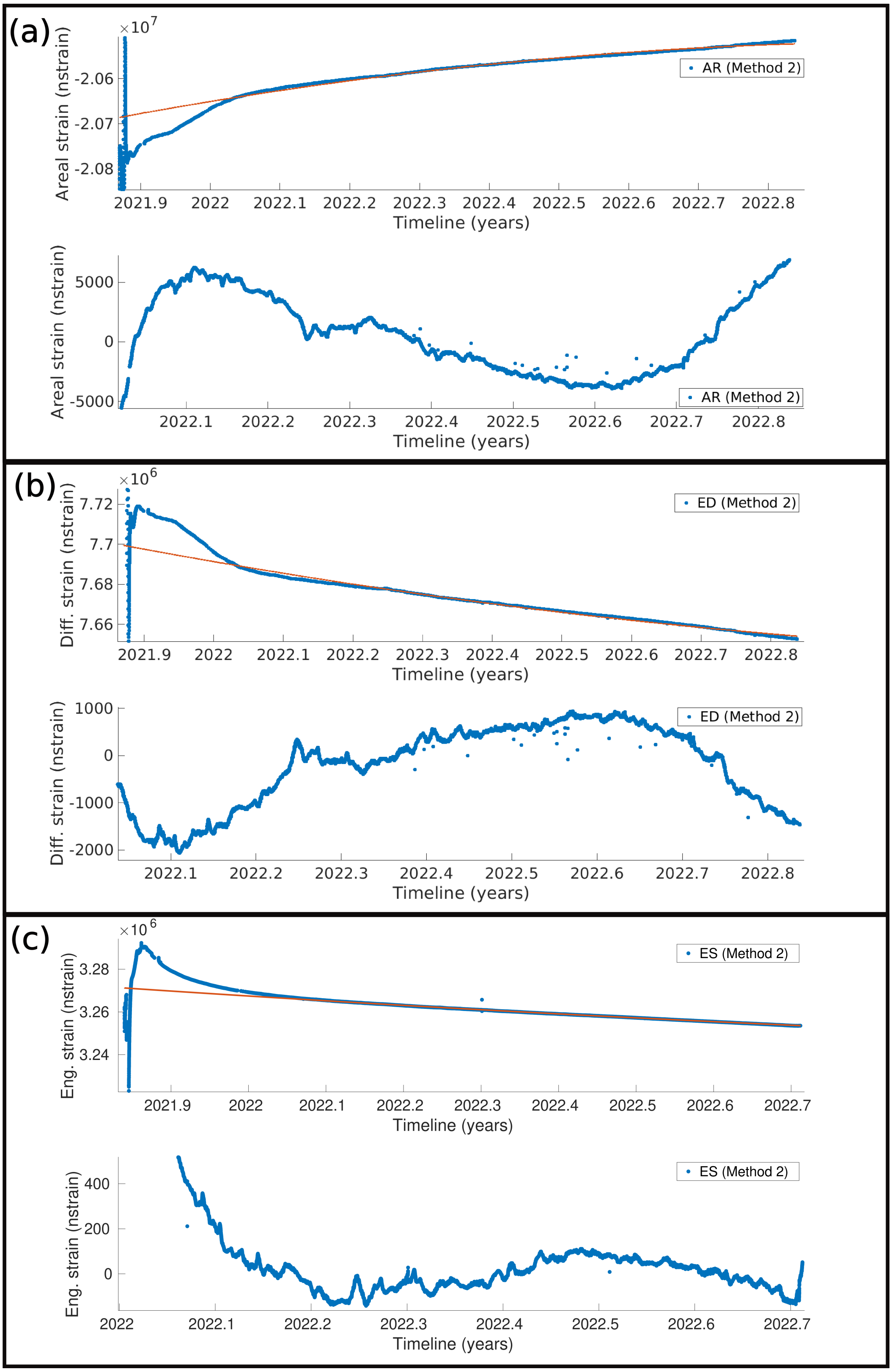

Figure 5.12. Same as Figure 5.10 for TSM3 GTSM.

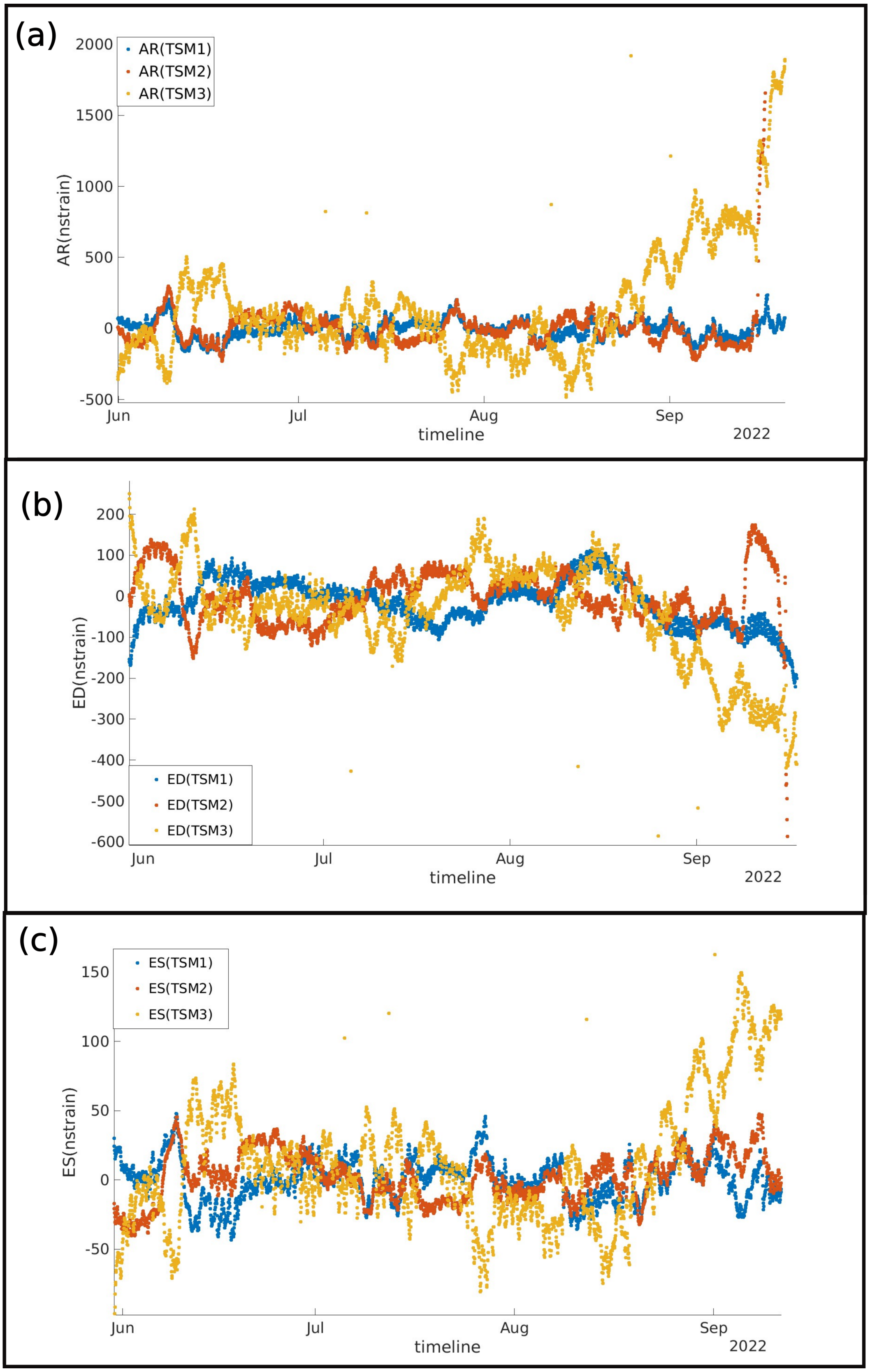

Figure 5.13. In figure the comparison among the areal (panel a), differential (panel b) and engineering (panel c) strain components, for $TSM1-3$ (respectively in blue, orange and yellow). We focus on the summer period between June and September 2022.

5.4 Short-term strain interpretation

In this section, we are willing to provide a demonstration of the potential of the strainmeters in increasing our capability of detecting short-term signals, focusing on the storm that hit the Umbria and Marche (Central Italy) regions between the 15^{th} and 16^{th} September 2022. In the evening of the 15^{th} September a self-regenerating thunderstorm remained for a few hours practically stationary, self-feeding, in the Cantiano area (Figure 5.14) in the province of Pesaro and Urbino (Marche). The thunderstorms that originate in mountainous areas move with the currents at high altitude towards the plains or the sea where they discharge. However, due to the abnormally high temperature of the Adriatic sea, warm and humid winds reinvigorated and blocked the storm in the area between Gubbio and Ancona (Figure 5.14a). Such an extreme event produced in just 7 hours, more than 400 mm of rainfall, with peaks of 90 mm in an hour in the Cantiano and Monte Cucco area, which is half of the total annual rainfall this area normally experiences. The subsequent floods, which struck predominantly the villages and towns towards the Adriatic sea, caused 12 fatalities and heavily damaged the hit communities.

The three strainmeters discussed in Section 5.3, which are deployed in the Gubbio area, actively recorded the passage of the storm. We consider strain data sampled at 10 minutes, which is sufficient to observe the evolution of the storm in the study area. In particular, we focus on the recorded areal strains, since rainfall affects the water content of the soil mainly causing areal variations (see also Figure 5.13). We consider the time span around the peak of the storm (i.e., the 15^{th} of September) and we compare the recorded areal variations of $TSM1-3$ (Figure 5.15). Since the barometric pressure plays an important role on strain measurements during heavy storms (e.g., Mouyen et al., 2017), we firstly remove their effect from areal measurements. To this aim we exploit Baytap08 software: in Figure 5.16(a) we show the estimated areal strain response to barometric pressure while panel (b) shows the residual of this processing, namely the areal strain related to the load carried by rainfall. In Figure 5.17, we compare the areal strain due to rainfall and the corresponding co-located rain gauges measurements. The time series show the features of the typical response to rainfall already discussed for TAIS site in Taiwan (see Figure 4.18). In particular it is well evident for $TSM1-2$ the elastic contraction during rainfall (Figure 5.17a,b). On the other hand, $TSM3$ shows an opposite behaviour as already observed for the barometric pressure (Figure 5.16b) and on longer time scales (Figure 5.13). We generally observe a larger response of $TSM3$ to barometric pressure which is, according to Roeloff et al. (2010), a strong indication of a greater sensitivity to vertical strain. As discussed in that study, for some strainmeters, the degree of coupling with vertical strain might be as significant as to reverse the sign of the areal strain (equation 7 of Reoloff et al., 2010). An indication of this behaviour of $TSM3$ is given by the negative calibration coefficients for areal strain (Table 5.5).

Thanks to the accurate spatio-temporal measurements of the strainmeters, we are capable of following the dynamics of the perturbation, and to separate the two opposed effects of barometric pressure and rainfall. Moreover, we notice from Figure 5.14a that the storm is characterized by a prevalent E-W stretched shape, and it only partially affects the area south of Gubbio and north of Città di Castello. Palette in Figure 5.14a describes the Vertical Maximum Intensity (VMI), which is proportional to the number of drops per unit volume and the sixth power of drops' diameter and it is used to estimate the rain or snow intensity (Yau and Rogers, 1989). The VMI spatial distribution is confirmed by the rain gauges daily measurements which are very heterogeneous in space: as a matter of fact we observe a N-S symmetry of daily water accumulation, with peaks of $\sim$ 200 mm at Pieve di Saddi and S. Benedetto Vecchio (rain gauges 3 and 4 in Figure 5.14b). The rain gauges to the north (Cerbara and Città di Castello, respectively 6 and 7 in Figure 5.14b), and to the south (Gubbio, M. Cucco and Torre dell'Olmo, respectively 1, 2 and 5 in Figure 5.14b) record in the same 24h a maximum of water accumulation $\sim$ 50 mm. This is reflected in the significantly different areal strain variations measured by $TSM1$ (in the order ~ 0.15 $\mu strain$) with respect to $TSM2-3$, (~ 0.8 $\mu strain$), as it is evident from Figure 5.17.

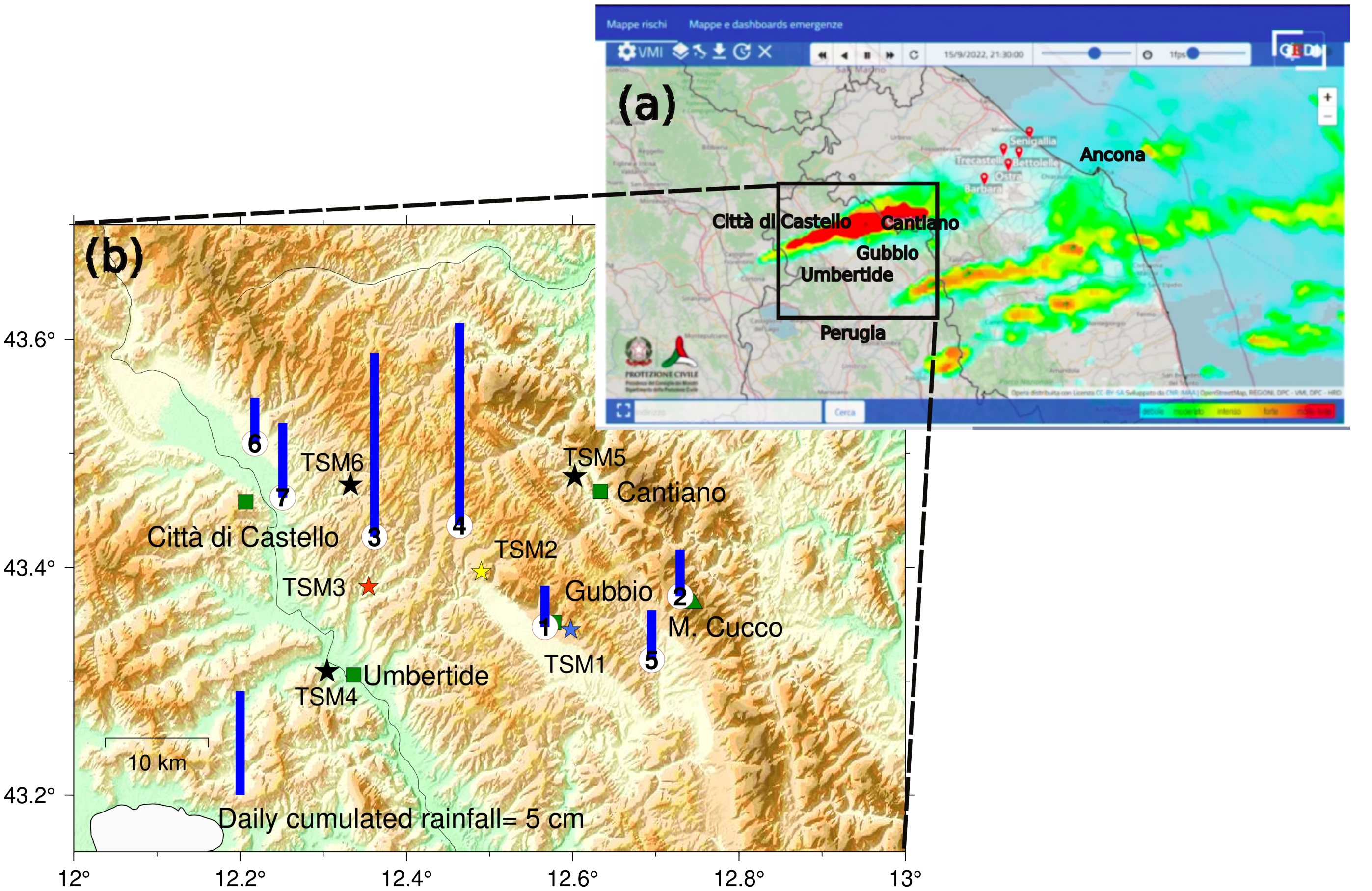

Figure 5.14. In the panel (a) a screenshot of the radar VMI (Vertical Maximum Intensity) recording of the 15^{th} September 2022 storm, taken from the Dipartimento della Protezione Civile website (https://mappe.protezionecivile.gov.it/it/mappe-rischi/piattaforma-radar). Palette color goes from weak (light blue) to very strong (red) intensity. Panel (b) shows a zoom of the area included in the black square of upper figure. Stars show the location of the six strainmeters, black stars for the strainmeters not yet suitable for calibration, colored stars for the calibrated strainmeters. For these latter, color as in Figure 5.13. Cities shown in upper panel are represented by green squares. White circles show the position of the seven rain gauges in the area, blue bars show the measured daily total rainfall for the 15^{th} September. Numbers from 1 to 7 inside white circles correspond respectively to Gubbio, M. Cucco, Pieve di Saddi, S. Benedetto Vecchio, Torre dell'Olmo, Cerbara and Città di Castello rain gauges (data from https://annali.regione.umbria.it/)

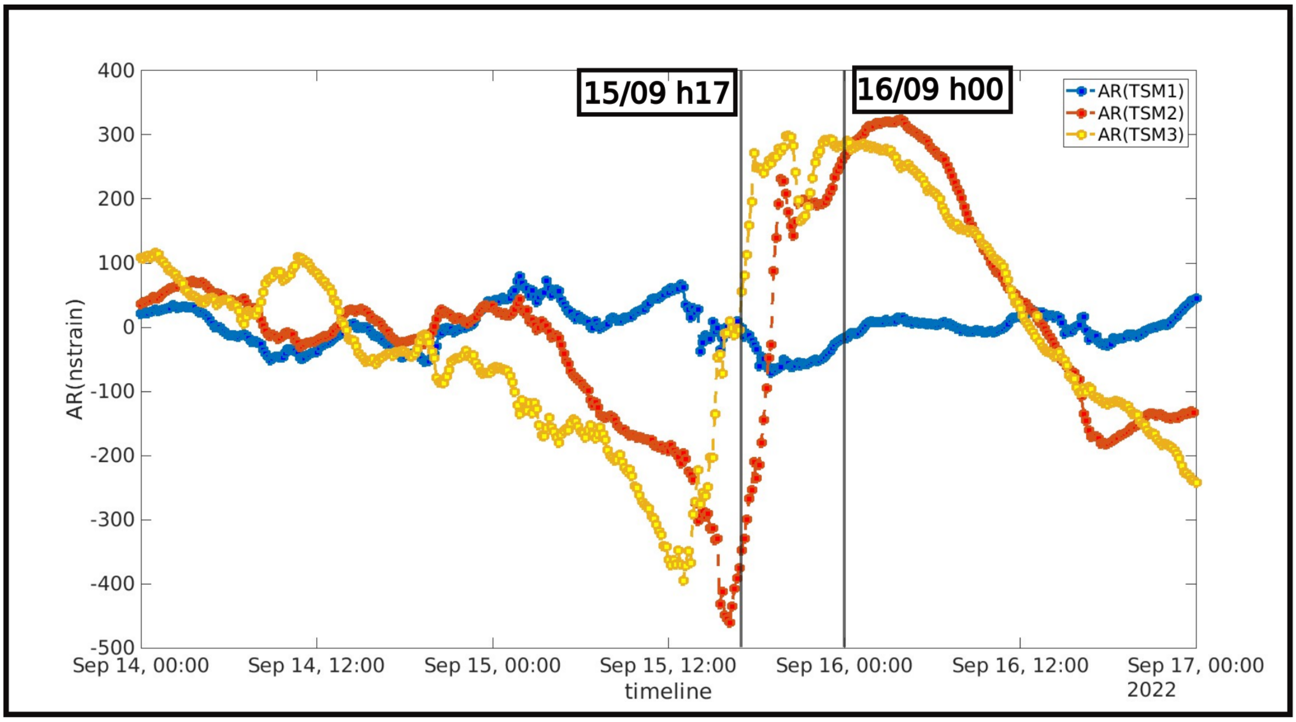

Figure 5.15. In Figure, a zoom of the areal strain time series of $TSM1-3$ (colors as in Figure 5.14b) in the time period $14^{th}-17^{th}$ of September. Vertical lines mark the time window of maximum intensity of the storm.

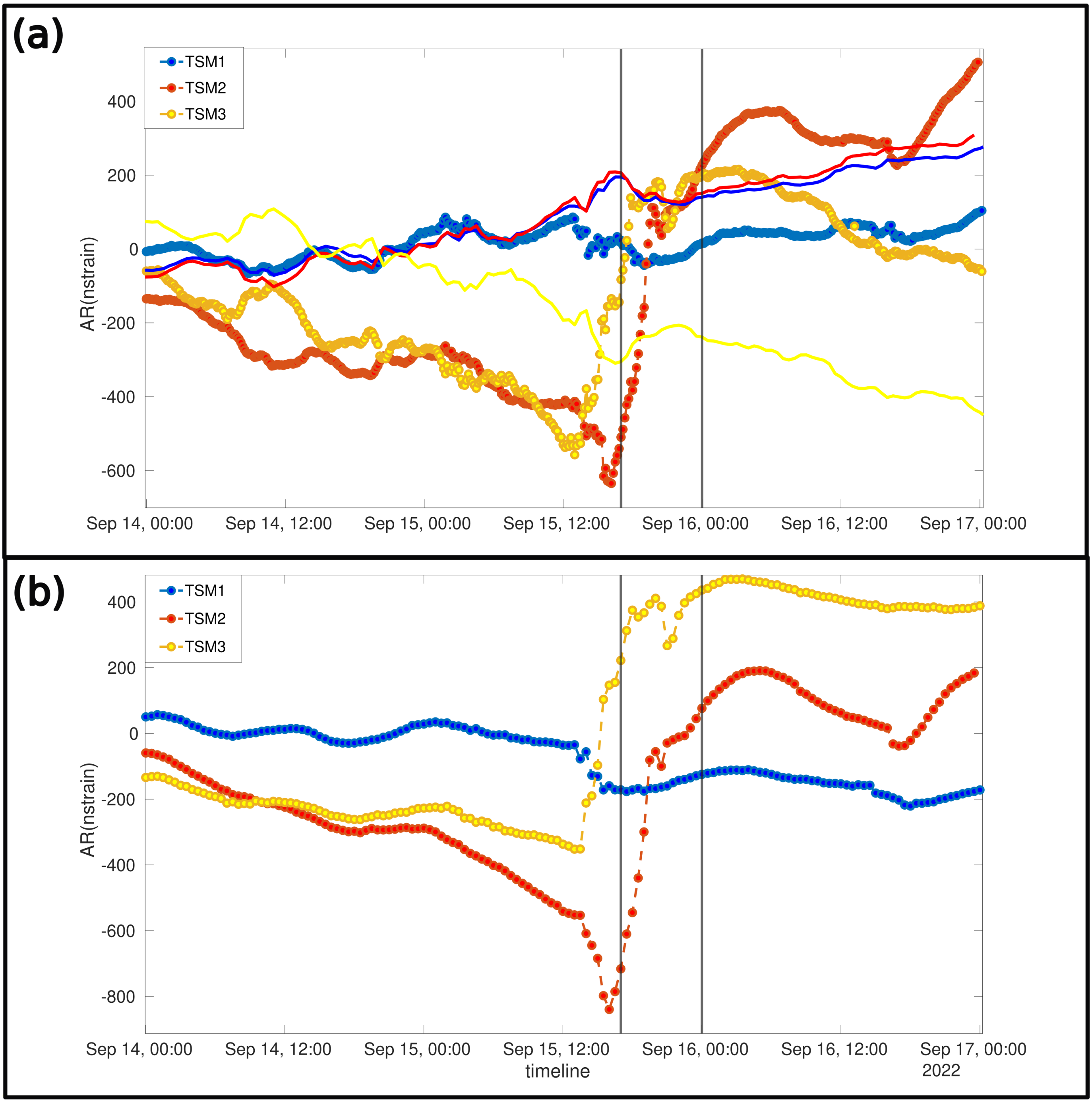

Figure 5.16. Panel (a): same areal strain time series of $TSM1-3$ as in Figure 5.15 (thicker lines) and the estimated areal strain due to barometric pressure (thinner lines). Panel (b): residual of the areal strain removed of the barometric effect. Vertical lines mark as in Figure 5.15.

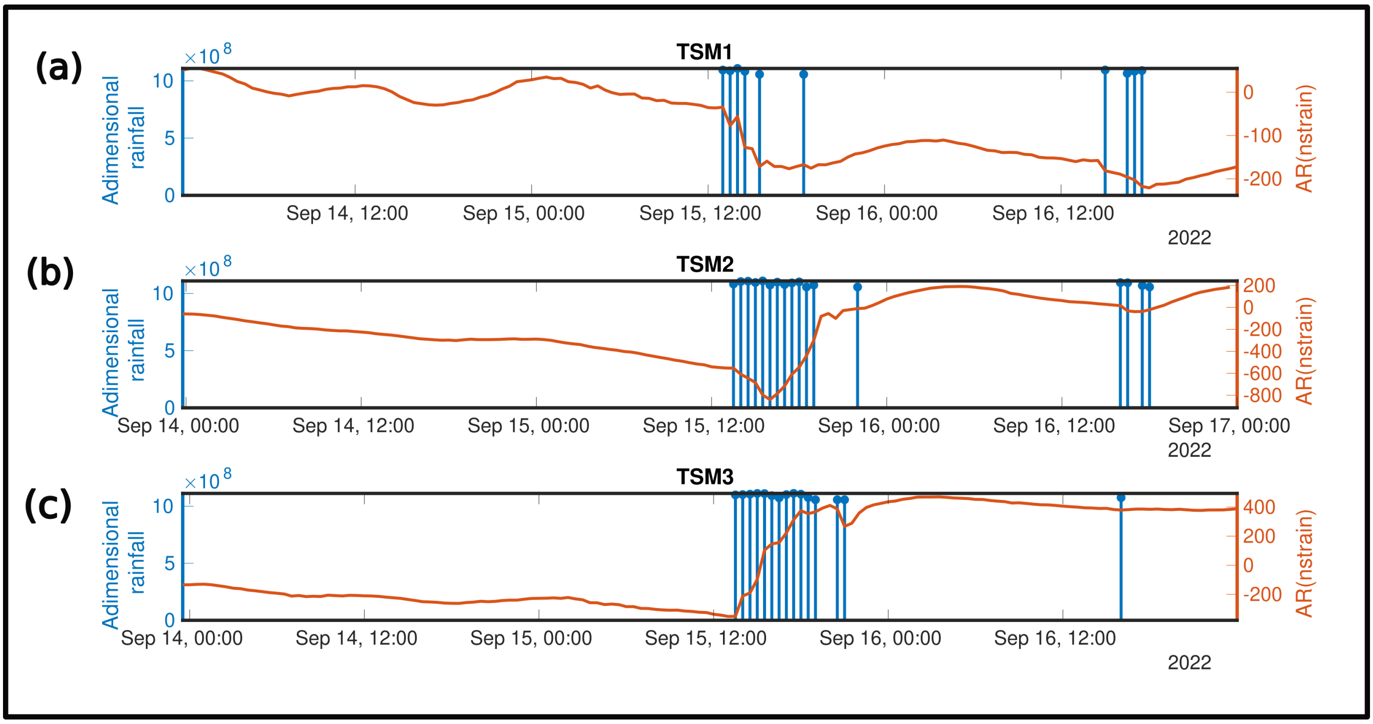

Figure 5.17. Areal strain as in Figure 5.16 and the measured rainfall from the co-located rain gauges, for (a) $TSM1$, (b) $TSM2$ and (c) $TSM3$.

The recordings of the thunderstorm that hit the Umbria-Marche area provide a good opportunity to test the state of health of the recently installed GTSMs. The three strainmeters suitable for calibration at the time of the editing of this manuscript prove to have sensibly recorded the perturbation, and the occurrence of the storm confirmed the calibration results for $TSM1$ and $TSM2$. On the other hand, $TSM3$ shows an opposite behaviour to the other sites, and it might be interpreted in the light of a strong vertical coupling as proposed by Roeloff et al. (2010). This is also confirmed by the negative calibration coefficients retrieved for this site (Table 5.5). Thanks to the high sampling rate of the deformation measured by the GTSMs, we highlight the potential of these new instruments in bettering our capability of detecting deformation signals, hence showing that it is possible to follow the dynamics of processes occurring with characteristic time $\sim hour$. On top of that, as already reported in literature, hydrological sources affect seismicity rates in various tectonic settings altering the state of stress of the crust (e.g., Bettinelli et al., 2008; Craig et al., 2017; Johnson et al., 2020; Lowry, 2006). In the Italian context, seismic activity modulated by groundwater storage has been observed on the Alps (Pintori et al., 2021), while transient deformations related to variations of the groundwater content on the Apennines (Silverii et al., 2016), and to precipitations on the Alps (Devoti et al., 2015; Serpelloni et al., 2018), are well documented. We show here the relevance of the strainmeters in the detection of subtle strain variations, such as the passage of heavy storms, which are known to be capable of inducing, for example, slow earthquakes on faults close to the failure condition (Liu et al., 2009). Furthermore, as it has been acknowledged by Hsu et al. (2015) and discussed in Section 4.5 of this manuscript, when downscaling our detection capability, it is important to distinguish strain changes induced by environmental factors (i.e., of hydrological and/or barometric origins) from those of tectonic origin. Hence the need of properly assessing and interpreting strain changes which are hydrologically induced, an example of which is here provided for the Central Italy area.

Conclusion and Perspectives

During this work of thesis we study time dependent deformation, of both tectonic and non-tectonic origin, through more "classic" GNSS measurements and less commonly used borehole strainmeter measurements, integrated with hydrological and meteo-climatic data sets. Exploiting precise GPS daily displacement time series, we have been able to characterize the temporal evolution and spatial pattern of the post-seismic slow deformation transient that followed the mainshocks of the 2016-2017 Central Italy seismic sequence (Chapter 2). The analysis of the measured post-seismic relaxation pointed out the occurrence of multiple post-seismic mechanisms (i.e., afterslip on faults and a viscoelastic relaxation of the lower crust, discussed respectively in Section 2.5.1 and 2.5.2) driving the geodetic displacement. The 2016-2017 seismic sequence most energetic mainshock, namely the M_w 6.5 Norcia event, was a moderate size earthquake, nevertheless we show in this thesis that the GPS, on the time scales of months, is capable of detecting the mm-scale tectonic signal associated with the viscoelastic relaxation of the lower crust. As we discuss in Section 2.3.3, although the accuracy of the measurement method represents a key factor while trying to highlight such faint signals, it is also fundamental to correctly separate and interpret the different signals present in the time series. The applied methods, and in particular the variational bayesian ICA, proves to be a valuable analysis technique to distinguish tectonic deformation processes (in the order of a few mm far from the epicentral area) from the hydrological ones, despite the sparse distribution of the GPS stations in the study area. Such a thorough analysis on the time series allows us to infer the occurrence of aseismic slip on the Paganica fault, which was responsible for the 2009 M_w 6.1 L'Aquila earthquake, but did not experience significant earthquake ruptures during the 2016-2017 seismic sequence. This result provides an example of the importance of increasing our detection capability, as this clearly affects the evaluation of the recurrence time of significant events on fault segments and therefore impacts the hazard assessment of the area.

On the other hand, through the available GPS measurements we are not able to detect any signal associated with the preparation of the first shock of the seismic sequence (i.e., the August 24^{th} Amatrice earthquake, Section 2.2.3). Borehole strainmeters, thanks to their higher sensitivity, may help to shed some light on the processes that can accompany the nucleation of moderate or large earthquakes. In particular, the six Gladwin strainmeters installed in Central Italy (Chapter 5) promise to provide answers to the mechanics of the Alto Tiberina fault and the associated seismogenic faults on its hanging wall. To this aim, a joint analysis which includes geodetic, satellite, geochemical and seismic data will be indispensable in the future. However, as we already pointed out for the Amatrice-Visso-Norcia earthquakes, with the downscaling of the observational capability, the correct interpretation of the wider spectrum of deformation signals will become more and more essential. This proves to be particularly true for the Glawdin strainmeters as we show, for instance, in Section 5.4 for the instruments deployed in Central Italy, with the detection of microstrain deformations associated with the storm that struck the Umbria-Marche region in mid September 2022, clearly visible in our data (Figure 5.13a).

Besides the comparison with models, the interpretation of deformation signals requires necessarily the joint analysis of various data sets, and in this thesis we give examples of the relevance of the integration of geodetic and hydrological data sets. Sometimes hydrology can play a key role, being the most important source of seasonal and non-seasonal deformation in our data as, for instance, in the case of strainmeters in Southern Taiwan (Section 4.5). Whether hydrology is the dominant process that causes the observed deformation as it is for TAIS site, or it is just a concurring one as it is for the strainmeters close by (i.e., TSUN and DARB), we show how the joint analysis of hydrological and geodetic data sets allows us to give an interpretation of the recorded time series. In light of either characterizing the hydrological processes or investigating their relationships with the seismic activity (i.e., an hydromechanical coupling), the integration of different kind of data sets represents a clear path to follow in the future.

Furthermore, in this thesis, we exploit independent sources of data to correctly choose the most suitable calibration method for GTSMs (Section 4.3). Owing to their high sensitivity, borehole strainmeters, and in particular GTSMs, require a flexible approach to meet the complexity that is usually observed in strain time series. An innovative, completely data driven, approach to calibrate the GTSMs (Section 3.4) relies on the waveform reproduction of Earth tides induced deformation, and should provide robust shear calibration results (Canitano et al., 2018). The proposed methodology can account for an increasing level of complexity (i.e., Method 1 of Section 3.4.1 and Method 2 of Section 3.4.2) depending on the quality of the data. We deem this to be an advantage with respect to the classical approaches followed to calibrate this type of strainmeter (e.g., Roeloff et al., 2010; Hodkginson et al., 2013), which adjust amplitude and phase of the observed tidal coefficients to those predicted in theory, though one have to bear in mind that a direct comparison among different methods is difficult (see Section 4.4). The workflow proposed in this thesis (Figure 3.3) allows us to keep under control step by step the calibration procedure and, in case of uncertain results (e.g., TAIS areal calibration, Section 4.3), we demonstrate how comparisons with other data sets provide independent constraints to evaluate its quality.

In the future, we plan to apply such a methodology to the remaining GTSMs installed in Central Italy, and thanks to the highly dense instrumentation available at the TABOO

Near Fault Observatory (Figure 5.1) to validate and/or complement the calibration procedure tested during this work of thesis.

References

- Albano, M., Barba, S., Bignami, C., Carminati, E., Doglioni, C., Moro, M., Saroli, M., Samsonov, S., Stramondo, S., (2020). Numerical analysis of interseismic, coseismic and post-seismic phases for normal and reverse faulting earthquakes in Italy, Geophysical Journal International, Volume 225, Issue 1, April 2021, Pages 627–645, https://doi.org/10.1093/gji/ggaa608

- Altamimi, Z., Collilieux, X., and Métivier, L. (2011). ITRF2008: An improved solution of the international terrestrial reference frame. Journal of Geodesy, 85, 457–473. https://doi.org/10.1007/s00190-011-0444-4

- Amato, A., Azzara, R., Chiarabba, C., Cimini, G. B., Cocco, M., Di Bona, M., et al. (1998). The 1997 Umbria-Marche, Italy, Earthquake Sequence: A first look at the main shocks and aftershocks. Geophysical Research Letters, 25(15), 2861–2864. https://doi.org/10.1029/98GL51842

- Amos, C. B., Audet, P., Hammond, W. C., Bürgmann, R., Johanson, I. A., and Blewitt, G. (2014). Uplift and seismicity driven by groundwater depletion in central California. Nature, 509(7501), 483–486. https://doi.org/10.1038/nature13275

- Anderlini, L., E. Serpelloni, and M. Belardinelli (2016), Creep and locking of a low-angle normal fault: Insights from the Altotiberina fault in the Northern Apennines (Italy), Geophys. Res. Lett., 43, 221–4329, doi:10.1002/2016GL068604

- Argus, D. F., Fu, Y., and Landerer, F. W. (2014). Seasonal variation in total water storage in California inferred from GPS observations of vertical land motion. Geophysical Research Letters, 41(6), 1971–1980. https://doi.org/10.1002/2014GL059570

- Axen, G.J. (2004), Mechanics of low-angle normal faults. In: Karner, G.D., Morris, J.D., Driscoll, N.W., Silver, E.A. (Eds.), Rheology and Deformation of the Lithosphere at Continental Margins: MARGINS Theoretical and Experimental Earth Science Series, pp. 46–91

- Barani, S., Mascandola, C., Serpelloni, E., Ferretti, G., Massa, M., and Spallarossa, D. (2017). Time–space evolution of seismic strain release in the area shocked by the august 24–october 30 central italy seismic sequence. Pure and Applied Geophysics, 174(5), 1875–1887. https://doi.org/10.1007/s00024-017-1547-5

- Barbot, S., and Fialko, Y. (2010). A unified continuum representation of post-seismic relaxation mechanisms: semi-analytic models of afterslip, poroelastic rebound and viscoelastic flow. Geophysical Journal International, 182(3), 1124–1140. https://doi.org/10.1111/j.1365-246X.2010.04678.x

- Barbour, A. J., Investigations of fluid-strain interaction using Plate Boundary Observatory borehole data, Ph.D. thesis, University of California, San Diego, 2014.

- Bawden, G. W, Thatcher, W., Stein, R. S., Hudnut, K. W., and Peltzer, G. (2001). Tectonic contraction across Los Angeles after removal of groundwater pumping effects. Nature, 412(6849), 812–815. https://doi.org/10.1038/35090558

- Ben-Zion, Y., and Allam, A. A. (2013). Seasonal thermoelastic strain and postseismic effects in Parkfield borehole dilatometers. Earth and Planetary Science Letters, 379, 120–126. https://doi.org/10.1016/j.epsl.2013.08.024

- Bennett, R. A., et al. (2012), Syn-convergent extension observed using the RETREAT GPS network, Northern Apennines, Italy, J. Geophys. Res., 117, B04408, doi:10.1029/2011JB008744

- Bettinelli, P., Avouac, J.-P., Flouzat, M., Bollinger, L., Ramillien, G., Rajaure, S., and Sapkota, S. (2008). Seasonal variations of seismicity and geodetic strain in the Himalaya induced by surface hydrology. Earth and Planetary Science Letters, 266, 332–344. https://doi.org/10.1016/j.epsl.2007.11.021

- Bevis, M., Brown, A., 2014. Trajectory models and reference frames for crustal motion geodesy. J Geodesy 88, 283–311. doi:10.1007/s00190-013-0685-5

- Bilham, R. (1989). Surface slip subsequent to the 24 November 1987 Superstition Hills, California, earthquake monitored by digital creepmeters. Bulletin of the Seismological Society of America, 79(2), 424–450.

- Boehm, J., Heinkelmann, R., and Schuh, H. (2007). Short note: A global model of pressure and temperature for geodetic applications. Journal of Geodesy, 81, 679–683. https://doi.org/10.1007/s00190-007-0135-3

- Bonaccorso, A., Linde, A., Currenti, G., Sacks, S., and Sicali, A. (2016), The borehole dilatometer network of Mount Etna: A powerful tool to detect and infer volcano dynamics, J. Geophys. Res. Solid Earth, 121, 4655– 4669, doi:10.1002/2016JB012914.

- Boncio, Paolo and Lavecchia, Giusy. (2000). A geological model for the Colfiorito earthquakes (September-October 1997, central Italy). Journal of Seismology. 4. 345-356. 10.1023/A:1026509717771.

- Boncio, P., Lavecchia, G., and Pace, B. (2004). Defining a model of 3D seismogenic sources for Seismic Hazard Assessment applications: The case of central Apennines (Italy). Journal of Seismology, 8(3), 407–425.

  https://doi.org/10.1023/B:JOSE.0000038449.78801.05

- Borsa, A. A., Agnew, D. C., and Cayan, D. R. (2014). Remote Hydrology. Ongoing drought-induced uplift in the western United States. Science, 345(6204), 1587–1590. https://doi.org/10.1126/science.1260279

- Bruhat, L., Barbot, S., and Avouac, J.-P. (2011). Evidence for postseismic deformation of the lower crust following the 2004 Mw 6.0 Parkfield earthquake. Journal of Geophysical Research, 116, B08401. https://doi.org/10.1029/2010JB008073

- Byerlee, J. Friction of rocks. PAGEOPH 116, 615–626 (1978).

  https://doi.org/10.1007/BF00876528

- Canitano, A., Hsu, Y. J., Lee, H. M., Linde, A. T., and Sacks, S. (2015). Near-field strain observations of the October 2013 Ruisui, Taiwan, earthquake: source parameters and limits of very short-term strain detection. Earth, Planets and Space, 67(1), 1-15.

- Canitano, A., Hsu, YJ., Lee, HM. et al. Calibration for the shear strain of 3-component borehole strainmeters in eastern Taiwan through Earth and ocean tidal waveform modeling. J Geod 92, 223–240 (2018). https://doi.org/10.1007/s00190-017-1056-4

- Carannante, S., Monachesi, G., Cattaneo, M., Amato, A., and Chiarabba, C. (2013), Deep structure and tectonics of the northern-central Apennines as seen by regional-scale tomography and 3-D located earthquakes, J. Geophys. Res. Solid Earth, 118, 5391– 5403, doi:10.1002/jgrb.50371.

- Carcione, J. M., Poletto, F., Farina, B., and Craglietto, A. (2014). Simulation of seismic waves at the earth's crust (brittle–ductile transition) based on the Burgers model. Solid Earth, 5(2), 1001–1010. https://doi.org/10.5194/se-5-1001-2014

- Carminati, E., Toniolo Augier, F. and Barba, S. (2001) Dynamic modelling of stress accumulation in Central Italy: role of structural heterogeneities and rheology. Geophys. J. Int., 144, 373390. doi:10.1046/j.1365-246x.2001.00323.x

- Chanard, K., Fleitout, L., Calais, E., Rebischung, P., and Avouac, J.-P. (2018). Toward a Global Horizontal and Vertical Elastic Load Deformation Model Derived from GRACE and GNSS Station Position Time Series. Journal of Geophysical Research: Solid Earth, 123(4), 3225–3237. https://doi.org/10.1002/2017JB015245

- Chan, K., Lee, T.-W., and Sejnowski, T. J. (2003). Variational Bayesian Learning of ICA with Missing Data. Neural Computation, 15(8), 1991–2011.

  https://doi.org/10.1162/08997660360675116

- Chaussard, E., Milillo, P., Bürgmann, R., Perissin, D., Fielding, E. J., and Baker, B. (2017). Remote sensing of ground deformation for monitoring groundwater management practices: Application to the Santa Clara Valley during the 2012–2015 California drought. Journal of Geophysical Research: Solid Earth, 122, 8566–8582. https://doi.org/10.1002/2017JB014676

- Cheloni, D., Serpelloni, E., Devoti, R., D'Agostino, N., Pietrantonio, G., Riguzzi F., Anzidei, M., Avallone, A., Cavaliere, A., Cecere, G., D'Ambrosio, C., Esposito, A., Falco, L., Galvani, A., Selvaggi, G., Sepe, V., Calcaterra, S., Giuliani, R., Mattone, M., Gambino, P., Abruzzese, L., Cardinale, V., Castagnozzi, A., De Luca, G., Massucci, A., Memmolo, A., Migliari, F., Minichiello, F., Zarrilli, L. (2016). GPS observations of coseismic deformation following the 2016, August 24, Mw 6 Amatrice earthquake (central Italy): data, analysis and preliminary fault model.

- Cheloni, D., De Novellis, V., Albano, M., Antonioli, A., Anzidei, M., Atzori, S., et al. (2017). Geodetic model of the 2016 Central Italy earthquake sequence inferred from InSAR and GPS data. Geophysical Research Letters, 44(13), 6778–6787. https://doi.org/10.1002/2017GL073580

- Cheloni, D., Falcucci, E., and Gori, S. (2019). Half-graben rupture geometry of the 30 october 2016 mw 6.6 mt. vettore-mt. bove earthquake, central italy. Journal of Geophysical Research: Solid Earth, 124(4), 4091–4118. https://doi.org/10.1029/2018JB015851

- Cheloni, Daniele, D'Agostino, N., Scognamiglio, L., Tinti, E., Bignami, C., Avallone, A., et al. (2019a). Heterogeneous Behavior of the Campotosto Normal Fault (Central Italy) Imaged by InSAR GPS and Strong-Motion Data: Insights from the 18 January 2017 Events. Remote Sensing, 11(12), 1482. https://doi.org/10.3390/rs11121482

- Chen, Chih-Yen, Jyr-Ching Hu, Chi-Ching Liu, and Chun-Ying Chiu. (2021). "Abnormal Strain Induced by Heavy Rainfall on Borehole Strainmeters Observed in Taiwan" Applied Sciences 11, no. 3: 1301. https://doi.org/10.3390/app11031301

- Chiaraluce, L., Ellsworth, W. L., Chiarabba, C., and Cocco, M. (2003). Imaging the complexity of an active normal fault system: The 1997 Colfiorito (central Italy) case study. Journal of Geophysical Research, 108(B6). https://doi.org/10.1029/2002JB002166

- Chiaraluce, Lauro; Amato, Alessandro; Chiarabba, Claudio; Selvaggi, G.; Bona, M.; Piccinini, Davide; Deschamps, Anne; Margheriti, Lucia; Courboulex, Françoise; Ripepe, Maurizio (2004) - Complex Normal Faulting in the Apennines Thrust-and-Fold Belt: The 1997 Seismic Sequence in Central Italy. Volume 94. doi:10.1785/0120020052 - Bulletin of the Seismological Society of America

- Chiaraluce L., C. Chiarabba, C. Collettini, D. Piccinini, and M. Cocco (2007), Architecture and mechanics of an active low-angle normal fault: Alto Tiberina Fault, Northern Apennines, Italy, J. Geophys. Res., 112, B10310, doi:10.1029/2007JB005015

- Chiaraluce, L. (2012). Unravelling the complexity of Apenninic extensional fault systems: A review of the 2009 L'Aquila earthquake (Central Apennines, Italy). Journal of Structural Geology, 42, 2–18. https://doi.org/10.1016/j.jsg.2012.06.007

- Chiaraluce, L., Di Stefano, R., Tinti, E., Scognamiglio, L., Michele, M., Casarotti, E., et al. (2017). The 2016 central italy seismic sequence: A first look at the mainshocks, aftershocks, and source models. Seismological Research Letters, 88(3), 757–771. https://doi.org/10.1785/0220160221

- Chiaraluce, L., Barchi, M. R., Carannante, S., Collettini, C., Mirabella, F., Pauselli, C., and Valoroso, L. (2017). The role of rheology, crustal structures and lithology in the seismicity distribution of the northern Apennines. Tectonophysics, 694, 280–291. https://doi.org/10.1016/j.tecto.2016.11.011

- Choudrey, R. (2002). Bayesian Independent Component Analysis.

- Civico, R., Pucci, S., Villani, F., Pizzimenti, L., De Martini, P. M., Nappi, R., and the Open EMERGEO Working Group. (2018). Surface ruptures following the 30 October 2016M w 6.5 Norcia earthquake, central Italy. Journal of Maps, 14(2), 151–160. https://doi.org/10.1080/17445647.2018.1441756

- Clements, T., and Denolle, M. A. (2018). Tracking groundwater levels using the ambient seismic field. Geophysical Research Letters, 45, 6459– 6465.

  https://doi.org/10.1029/2018GL077706

- Craig, T. J., Chanard, K., and Calais, E. (2017). Hydrologically-driven crustal stresses and seismicity in the New Madrid Seismic Zone. Nature Communications, 8, 2143. https://doi.org/10.1038/s41467-017-01696-w

- Crowell, B.W. (2019), PyTAGS: A Python package for the temporal analysis of GNSS strains, V1.0, doi:10.5281/zenodo.2634525.
- D'Agostino, N., S. Mantenuto, E. D'Anastasio, A. Avallone, M. Barchi, C. Collettini, F. Radicioni, A. Stoppini, and G. Fastellini (2009), Contemporary crustal extension in the Umbria–Marche Apennines from regional CGPS networks and comparison between geodetic and seismic deformation, Tectonophysics, 476(1-2), 3– 12, doi:10.1016/j.tecto.2008.09.033
- D'Agostino, N. (2014). Complete seismic release of tectonic strain and earthquake recurrence in the Apennines (Italy). Geophysical Research Letters, 41(4), 1155–1162. https://doi.org/10.1002/2014GL059230
- D'Agostino, N., Silverii, F., Amoroso, O., Convertito, V., Fiorillo, F., Ventafridda, G., and Zollo, A. (2018). Crustal deformation and seismicity modulated by groundwater recharge of karst aquifers. Geophysical Research Letters, 45, 12253–12262. https://doi. org/10.1029/2018GL079794
- Davis, J. L., Wernicke, B. P., and Tamisiea, M. E. (2012). On seasonal signals in geodetic time series. Journal of Geophysical Research, 117(B1). https://doi.org/10.1029/2011JB008690
- Day-Lewis, A., Characterization and Modeling of In Situ Stress Heterogeneity, Ph.D. thesis, Stanford University, 2007.
- Dee, D. P., Uppala, S. M., Simmons, A. J., Berrisford, P., Poli, P., Kobayashi, S., et al. (2011). The ERA-Interim reanalysis: configuration and performance of the data assimilation system. Quarterly Journal of the Royal Meteorological Society, 137(656), 553–597. https://doi.org/10.1002/qj.828
- Devoti, R., D'Agostino, N., Serpelloni, E., Pietrantonio, G., Riguzzi, F., Avallone, A., et al. (2017). A combined velocity field of the mediterranean region. Annals of Geophysics, 60(2). https://doi.org/10.4401/ag-7059
- Devoti, R., Riguzzi, F., Cinti, F.R., Ventura, G. (2018); Long-term strain oscillations related to the hydrological interaction between aquifers in intra-mountain basins: A case study from Apennines chain (Italy), Earth and Planetary Science Letters, 501, 1-12, https://doi.org/10.1016/j.epsl.2018.08.014.
- Devoti, R., Zuliani, D., Braitenberg, C., Fabris, P., Grillo, B. (2015); Hydrologically induced slope deformations detected by GPS and clinometric surveys in the Cansiglio Plateau, southern Alps, Earth and Planetary Science Letters, 419, 134-142, https://doi.org/10.1016/j.epsl.2015.03.023.

- Di Stefano, R., E. Kissling, C. Chiarabba, A. Amato, and D. Giardini (2009), Shallow subduction beneath Italy: Three-dimensional images of the Adriatic-European-Tyrrhenian lithosphere system based on high-quality P wave arrival times, J. Geophys. Res., 114, B05305, doi:10.1029/2008JB005641

- Dong, D., Fang, P., Bock, Y., Cheng, M. K., and Miyazaki, S. (2002). Anatomy of apparent seasonal variations from GPS-derived site position time series. Journal of Geophysical Research, 107(B4), ETG 9-1-ETG 9-16. https://doi.org/10.1029/2001JB000573

- Dong, D., Fang, P., Bock, Y., Webb, F., Prawirodirdjo, L., Kedar, S., and Jamason, P. (2006). Spatiotemporal filtering using principal component analysis and Karhunen-Loeve expansion approaches for regional GPS network analysis. Journal of Geophysical Research, 111, B03405. (B4),2075 https://doi.org/10.1029/2005JB003806

- Dong, D., Herring, T., and King, R. (1998). Estimating regional deformation from a combination of space and terrestrial geodetic data. Journal of Geodesy, 72(4), 200–214. https://doi.org/10.1007/s001900050161

- Dresen, G., Kwiatek, G., Goebel, T., and Ben-Zion, Y. (2020). Seismic and aseismic preparatory processes before large stick–slip failure. Pure and Applied Geophysics, 177(12), 5741-5760.

- EMERGEO W.G. : Pucci, S., De Martini, P.M., Civico, R., Nappi, R., Ricci, T., Villani, F., Brunori, C.A., Caciagli, M., Sapia, V., Cinti, F.R. , Moro, M., Di Naccio, D., Gori, S., Falcucci, E., Vallone, R., Mazzarini, F., Tarquini, S., Del Carlo, P., Kastelic, V., Carafa, M., De Ritis, R., Gaudiosi, G., Nave, R., Alessio, G., Burrato, P., Smedile, A., Alfonsi, L., Vannoli, P., Pignone, M., Pinzi, S., Fracassi, U., Pizzimenti, L., Mariucci, M.T., Pagliuca, Sciarra, N., A., Carluccio, R., Nicolosi, I., Chiappini, M., D'Ajello Caracciolo, F., Pezzo, G.,Patera, A. , Azzaro, R., Pantosti,D., Montone, P., Saroli, M., Lo Sardo, L., Lancia, M.. Coseismic effects of the 2016 Amatrice seismic sequence: first geological results. Annals of Geophysics (2016). https://doi.org/10.4401/ag-7195

- Fan, Y., and van den Dool, H. (2008). A global monthly land surface air temperature analysis for 1948–present. Journal of Geophysical Research, 113(D1). https://doi.org/10.1029/2007JD008470

- Falcucci, E., Gori, S., Galadini, F., Fubelli, G., Moro, M., Saroli, M., (2016) Active faults in the epicentral and mesoseismal Ml 6.0 24, 2016 Amatrice earthquake region, central Italy. Methodological and seismotectonic issues, Annals of Geophysics. https://doi.org/10.4401/ag-7266

- Farrell, W. E., Deformation of the Earth by Surface Loads, Reviews of Geophysics and Space Physics, Vol. 10, No. 3, PP. 761-797, AvevsT (1972)

- Fayon, A. K., Peacock, S. M., Stump, E., and Reynolds, S. J. (2000). Fission track analysis of the footwall of the Catalina detachment fault, Arizona: Tectonic denudation, magmatism, and erosion. Journal of Geophysical Research, 105(B5), 11047–11062. https://doi.org/10.1029/1999JB900421

- Ferrarini, F., Lavecchia, G., de Nardis, R., and Brozzetti, F. (2015). Fault Geometry and Active Stress from Earthquakes and Field Geology Data Analysis: The Colfiorito 1997 and L'Aquila 2009 Cases (Central Italy). Pure and Applied Geophysics, 172(5), 1079–1103. https://doi.org/10.1007/s00024-014-0931-7

- Frank, W. B., and Brodsky, E. E. (2019). Daily measurement of slow slip from low-frequency earthquakes is consistent with ordinary earthquake scaling. Science Advances, 5(10), eaaw9386.

  https://doi.org/10.1126/sciadv.aaw9386

- Freed, A.M. and Burgmann, R., (2004). Evidence of power-low flow in the Mojave desert mantle, Nature, 430, 548–551.

- Freed, A. M., Bürgmann, R., Calais, E., Freymueller, J., and Hreinsdóttir, S. (2006). Implications of deformation following the 2002 Denali, Alaska, earthquake for postseismic relaxation processes and lithospheric rheology. Journal of Geophysical Research, 111(B1). https://doi.org/10.1029/2005JB003894

- Fukuda, M., Sagiya, T. and Asai, Y. A causal relationship between the slow slip event and deep low frequency tremor indicated by strain data recorded at Shingu borehole station. Eos 89 (suppl.), U33A-0033 (2008)

- Galadini, F., Falcucci, E., Gori, S., Zimmaro, P., Cheloni, D., and Stewart, J. P. (2018). Active faulting in source region of 2016–2017 central italy event sequence. Earthquake Spectra, 34(4), 1557–1583. https://doi.org/10.1193/101317EQS204M

- Galli, P., Galadini, F., Pantosti, D.; Twenty years of paleoseismology in Italy, Earth-Science Reviews, Volume 88, Issues 1–2, (2008), Pages 89-117, ISSN 0012-8252, https://doi.org/10.1016/j.earscirev.2008.01.001.

- Galloway, D. L., and Hoffmann, J. (2007). The application of satellite differential SAR interferometry-derived ground displacements in hydrogeology. Hydrogeology Journal, 15(1), 133–154. https://doi.org/10.1007/s10040-006-0121-5

- Galvani, A., Anzidei, M., Devoti, R., Esposito, A., Pietrantonio, G., Pisani, A.R., Riguzzi, F., Serpelloni, E., (2013). The interseismic velocity field of the central Apennines from a dense GPS network. Ann Geophys-Italy 55. doi:10.4401/ag-5634

- Gegout, P., Boy, J. P., Hinderer, J., and Ferhat, G. (2010). Modeling and Observation of Loading Contribution to Time-Variable GPS Sites Positions. In S. P. Mertikas (Ed.), Gravity, Geoid and Earth Observation: IAG Commission 2: Gravity Field, Chania, Crete, Greece, 23-27 June 2008 (Vol. 135, pp. 651–659). Berlin, Heidelberg: Springer Berlin Heidelberg. https://doi.org/10.1007/978-3-642-10634-7-86

- Gladwin, M. T., High precision multi component borehole deformation monitoring, Rev. Sci. Instrum., 55, 2011-2016, 1984

- Gladwin, Michael T., and Rhodes Hart. "Design parameters for borehole strain instrumentation." pure and applied geophysics 123.1 (1985): 59-80.

- Gomberg, J., Wech, A., Creager, K., Obara, K., and Agnew, D. (2016). Reconsidering earthquake scaling. Geophysical Research Letters, 43, 6243–6251. https://doi.org/10.1002/grl.54609

- Gualandi, Adriano, Avouac, J.-P., Galetzka, J., Genrich, J. F., Blewitt, G., Adhikari, L. B., et al. (2016). Pre- and post-seismic deformation related to the 2015, Mw7.8 Gorkha earthquake, Nepal. Tectonophysics. https://doi.org/10.1016/j.tecto.2016.06.014

- Gualandi, A, Serpelloni, E., and Belardinelli, M. E. (2014). Space-time evolution of crustal deformation related to the Mw 6.3, 2009 L'Aquila earthquake (central Italy) from principal component analysis inversion of GPS position time-series. Geophysical Journal International, 197(1), 174–191. https://doi.org/10.1093/gji/ggt522

- Gualandi, A, Serpelloni, E., and Belardinelli, M. E. (2016). Blind source separation problem in GPS time series. Journal of Geodesy, 90(4), 323–341.

  https://doi.org/10.1007/s00190-015-0875-4

- Gualandi A., Nichele C., Serpelloni E., Belardinelli M. E., Chiaraluce L., Anderlini L., Latorre D. and Avouac J.-P. . Aseismic deformation associated with an earthquake swarm in the northern Apennines (Italy). Geophysical Research Letters

- Gualandi, A, Liu, Z., and Rollins, C. (2020). Post-large earthquake seismic activities mediated by aseismic deformation processes. Earth and Planetary Science Letters, 530, 115870. https://doi.org/10.1016/j.epsl.2019.115870

- Gwyther, R. L., M. T. Gladwin, M. Mee, and R. G. Hart (1996), Anomalous shear strain at Parkfield during 1993-94, Geophys. Res. Lett., 23, 2425–2428.

- Hainzl, S., Kraft, T., Wassermann, J., Igel, H., and Schmedes, E. (2006). Evidence for rainfall-triggered earthquake activity. Geophysical Research Letters, 33, L19303. https://doi.org/10.1029/2006GL027642

- Harrison, J. C. (1976), Cavity and topographic effects in tilt and strain measurement, J. Geophys. Res., 81(2), 319– 328, doi:10.1029/JB081i002p00319.
- Hart, R. H. G., et al. "Tidal calibration of borehole strain meters: Removing the effects of small-scale inhomogeneity." Journal of Geophysical Research: Solid Earth 101.B11 (1996): 25553-25571.
- Hawthorne, J. C., and Bartlow, N. M. (2018). Observing and modeling the spectrum of a slow slip event. Journal of Geophysical Research: Solid Earth, 123, 4243–4265. https://doi.org/10.1029/2017JB015124
- Herring, T. A., King, R. W., Floyd, M. A., and McClusky, S. C. (2018). Introduction to GAMIT/GLOBK, Release 10.7. Retrieved from http://geoweb.mit.edu/gg/Intro-GG.pdf
- Hetland, E. A., and Zhang, G. (2014). Effect of shear zones on post-seismic deformation with application to the 1997 Mw 7.6 Manyi earthquake. Geophysical Journal International, 198(1), 259–269. https://doi.org/10.1093/gji/ggu127
- Hodgkinson, K., Langbein, J., Henderson, B., Mencin, D., and Borsa, A. (2013), Tidal calibration of plate boundary observatory borehole strainmeters, J. Geophys. Res. Solid Earth, 118, 447– 458, doi:10.1029/2012JB009651.
- Hsu, M.-T. (1980), Earthquake Catalogues in Taiwan (From 1644 to 1979) (in Chinese), 77 pp., Natl. Taiwan Univ., Taipei.
- Hsu, Y.-J., Chang, Y.-S., Liu, C.-C., Lee, H.-M., Linde, A. T., Sacks, S. I., Kitagawa, G., and Chen, Y.-G. (2015), Revisiting borehole strain, typhoons, and slow earthquakes using quantitative estimates of precipitation-induced strain changes. J. Geophys. Res. Solid Earth, 120, 4556– 4571. doi: 10.1002/2014JB011807.
- Huang, Y.T.; Chen, K.H.; Yang, M. (2000) Estimation of Taiwan Vertical Velocity Field Using TWVD2001 Leveling Data. J. Taiwan Land Res. 2000, 13, 28.
- Huang, M., Fielding, E. J., Liang, C., Milillo, P., Bekaert, D., Dreger, D., and Salzer, J. (2017). Coseismic deformation and triggered landslides of the 2016 M 6.2 Amatrice earthquake in Italy. Geophysical Research Letters, 44(3), 1266–1274. https://doi.org/10.1002/2016GL071687
- Ide, S., Beroza, G. C., Shelly, D. R. and Uchide, T. A scaling law for slow earthquakes. Nature 447, 76–79 (2007)
- Ishiguro, M., H. Akaike, M. Ooe, and S. Nakai (1981), A Bayesian approach to the analysis of earth tides, in Proc. Ninth Internat. Symp. Earth Tides, pp. 283–292, E. Schweizerbart'sche Verlag, Stuttgart, Germany.

- Ishiguro, M., T. Sato, Y. Tamura, and M. Ooe (1984), Tidal data analysis: an introduction to BAYTAP (in Japanese), Proc. Inst. Statis. Math., 32, 71–85.
- Ishiguro, M., and Y. Tamura (1985), BAYTAP-G in TIMSAC-84, in Computer Science Monographs, vol. 22, Institute of Statistical Mathematics, Tokyo.
- Jaeger, J. C., and N. G. W. Cook (1976), Fundamentals of Rock Mechanics, Halsted Press, New York.
- Ji, K. H., and Herring, T. A. (2012). Correlation between changes in groundwater levels and surface deformation from GPS measurements in the San Gabriel Valley, California. Geophysical Research Letters, 39, L01301. https://doi.org/10.1029/2011GL050195
- Johnson, C., Fu, Y., and Bürgmann, R. (2017). Seasonal water storage, stress modulation, and California seismicity. Science, 356(6343), 1161–1164.

  https://doi.org/10.1126/science.aak9547
- Johnson, C. W., Fu, Y., Bürgmann, R. (2020). Hydrospheric modulation of stress and seismicity on shallow faults in southern Alaska. Earth and Planetary Science Letters, 530, 115904. http://dx.doi.org/10.1016/j.epsl.2019.115904.
- Jolivet, L., Labrousse, L., Agard, P., Lacombe, O., Bailly, V., Lecomte, E., et al. (2010). Rifting and shallow-dipping detachments, clues from the Corinth Rift and the Aegean. Tectonophysics, 483(3–4), 287–304. https://doi.org/10.1016/j.tecto.2009.11.001
- Jolivet, R and Frank, W. B. (2020). The transient and intermittent nature of slow slip. AGU Advances, 1, e2019AV000126. https://doi.org/10.1029/2019AV000126
- King, G. C. P., Bilham, R. G., Campbell, J. W., McKenzie, D. P., and Niazi, M. (1975). Detection of elastic strainfields caused by fault creep events in Iran. Nature, 253(5491), 420–423.
- King, N. E., Argus, D., Langbein, J., Agnew, D. C., Bawden, G., Dollar, R. S., et al. (2007). Space geodetic observation of expansion of the San Gabriel Valley, California, aquifer system, during heavy rainfall in winter 2004–2005. Journal of Geophysical Research, 112, B03409. https://doi.org/10.1029/2006JB004448
- Kodaira, S., T. Idaka, A. Kato, J. Park, and Y. Kaneda (2004), High pore pressure may cause silent slip in the Nankai Through, Science, 304, 1295–1298.
- Kositsky, A. P., and Avouac, J. P. (2010). Inverting geodetic time series with a principal component analysis-based inversion method. Journal of Geophysical Research, 115(B3). https://doi.org/10.1029/2009JB006535

- Lagler, K., Schindelegger, M., Böhm, J., Krásná, H., and Nilsson, T. (2013). GPT2: Empirical slant delay model for radio space geodetic techniques. Geophysical Research Letters, 40, 1069–1073. https://doi.org/10.1002/grl.50288
- Langbein J (2015) Borehole strainmeter measurements spanning the 2014 M w 6.0 South Napa Earthquake, California: the effect from instrument calibration. J Geophys Res Solid Earth doi:10.1002/2015JB012278
- Lavecchia, Giusy and Federica, Ferrarini and Brozzetti, Francesco and Nardis, Rita and Boncio, Paolo and Chiaraluce, Lauro. (2012). From surface geology to aftershock analysis: Constraints on the geometry of the L'Aquila 2009 seismogenic fault system. Italian Journal of Geosciences. 131. 330-347. 10.3301/IJG.2012.24.
- Lavecchia, G., Castaldo, R., de Nardis, R., De Novellis, V., Ferrarini, F., Pepe, S., et al. (2016). Ground deformation and source geometry of the 24 August 2016 Amatrice earthquake (Central Italy) investigated through analytical and numerical modeling of DInSAR measurements and structural-geological data. Geophysical Research Letters, 43(24), 12,389-12,398. https://doi.org/10.1002/2016GL071723
- Lienkaemper, J. J., McFarland, F. S., Simpson, R. W., Bilham, R. G., Ponce, D. A., Boatwright, J. J., and Caskey, S. J. (2012). Long-term creep rates on the Hayward Fault: Evidence for controls on the size and frequency of large earthquakes. Bulletin of the Seismological Society of America, 102(1), 31–41
- Lin, K.-C., Hu, J.-C., Ching, K.-E., Angelier, J., Rau, R.-J., Yu, S.-B., Tsai, C.-H., Shin, T.-C., and Huang, M.-H. (2010), GPS crustal deformation, strain rate, and seismic activity after the 1999 Chi-Chi earthquake in Taiwan, J. Geophys. Res., 115, B07404, doi:10.1029/2009JB006417.
- Liu, C. C., A. T. Linde, and I. S. Sacks (2009), Slow earthquakes triggered by typhoons, Nature, 459, 833–836.
- Lowry, A. R. (2006). Resonant slow fault slip in subduction zones forced by climatic load stress. Nature, 442, 802–805. https://doi. org/10.1038/nature05055
- Lyard, F., Lefevre, F., Letellier, T., and Francis, O. (2006). Modelling the global ocean tides: Modern insights from FES2004. Ocean Dynamics,56, 394–415. https://doi.org/10.1007/s10236-006-0086-x
- Mandler, E., Pintori, F., Gualandi, A., Anderlini, L., Serpelloni, E., and Belardinelli, M. E. (2021). Post-seismic deformation related to the 2016 Central Italy seismic sequence from GPS displacement time-series. Journal of Geophysical Research: Solid Earth, 126, e2021JB022200. https://doi.org/10.1029/2021JB022200

- Maubant, L., Socquet, A., Hollingsworth, J., Pathier, E., and Pousse-Beltrán, L. (2017). The Seismic Sequence of the Norcia Earthquake, Italy 2016, seen by geodesy. In Cargese, 2nd of October – 6th of October 2017. France.
- Matsumoto, K., T. Sato, T. Takanezawa, and M. Ooe, GOTIC2: A Program for Computation of Oceanic Tidal Loading Effect, J. Geod. Soc. Japan, 47, 243-248, 2001.
- McCausland, W. A., Roeloffs, E. and Silver, P. New insights into Cascadia slow slip events using Plate Boundary Observatory borehole strainmeters. Eos 89 (suppl.), G21B-0691 (2008)
- Michele, M., Chiaraluce, L., Di Stefano, R., and Waldhauser, F. (2020). Fine-scale structure of the 2016–2017 central italy seismic sequence from data recorded at the italian national network. Journal of Geophysical Research: Solid Earth, 125(4). https://doi.org/10.1029/2019JB018440
- Michel, S., Gualandi, A., and Avouac, J.-P. (2018). Interseismic coupling and slow slip events on the Cascadia megathrust. Pure and Applied Geophysics, 1–25. https://doi.org/10.1007/s00024-018-1991-x
- Miller, S. A., C. Collettini, L. Chiaraluce, M. Cocco, M. Barchi, and B. J. P. Kaus (2004), Aftershocks driven by a high-pressure CO2 source at depth, Nature, 427, 724–727.
- Molinari, I., and Morelli, A. (2011). EPcrust: a reference crustal model for the European Plate. Geophysical Journal International, 185(1), 352–364.

  https://doi.org/10.1111/j.1365-246X.2011.04940.x
- Molinari, I., J. Verbeke, L. Boschi, E. Kissling, and A. Morelli (2015), Italian and Alpine three-dimensional crustal structure imaged by ambient-noise surface-wave dispersion, Geochem. Geophys. Geosyst., 16, 4405–4421, doi:10.1002/2015GC006176.
- Mouyen, M., Canitano, A., Chao, B. F., Hsu, Y.-J., Steer, P., Longuevergne, L., and Boy, J.-P. (2017). Typhoon-induced ground deformation. Geophysical Research Letters, 44, 11,004–11,011. https://doi.org/10.1002/2017GL075615
- Munafò, I., Malagnini, L., and Chiaraluce, L. (2016). On the Relationship betweenM w andM L for Small Earthquakes. Bulletin of the Seismological Society of America, 106(5), 2402–2408. https://doi.org/10.1785/0120160130
- Nespoli, M., Belardinelli, M. E., and Bonafede, M. (2019). Fault dip variations related to elastic layering. Geophysical Journal International.

  https://doi.org/10.1093/gji/ggz505

- Nespoli M., Cenni N., Belardinelli M. E., Marcaccio M. (2021) The interaction between displacements and water level changes due to natural and anthropogenic effects in the Po Plain (Italy): The different point of view of GNSS and piezometers, Journal of Hydrology, Volume 596, 2021, 126112, ISSN 0022-1694, https://doi.org/10.1016/j.jhydrol.2021.126112.

- Nur, A., and J. Booker (1972), Aftershocks caused by pore fluid flow? Science, 175, 885–887.

- Obi E. O., Abong A. A, Ogbeche J. U. Empirical Study of the Frequency and Severity of Earthquakes in Taiwan. Journal of Geosciences and Geomatics. 2017; 5(4):167-172. doi: 10.12691/jgg-5-4-1.

- Palano, M., Pezzo, G., Serpelloni, E., Devoti, R., D'Agostino, N., Gandolfi, S., et al. (2020). Geopositioning time series from offshore platforms in the Adriatic Sea. Scientific Data, 7(1), 373. https://doi.org/10.1038/s41597-020-00705-w

- Papadopoulos, G. A., Ganas, A., Agalos, A., Papageorgiou, A., Triantafyllou, I., Kontoes, C., et al. (2017). Earthquake Triggering Inferred from Rupture Histories, DInSAR Ground Deformation and Stress-Transfer Modelling: The Case of Central Italy During August 2016–January 2017. Pure and Applied Geophysics, 174(10), 3689–3711. https://doi.org/10.1007/s00024-017-1609-8

- Peng, Z., and Gomberg, J. (2010). An integrated perspective of the continuum between earthquakes and slow-slip phenomena. Nature Geoscience, 3(9), 599–607. https://doi.org/10.1038/ngeo940

- Perfettini, H., and Avouac, J. P. (2007). Modeling afterslip and aftershocks following the 1992 Landers earthquake. Journal of Geophysical Research, 112(B7). https://doi.org/10.1029/2006JB004399

- Petrie, E. J., King, M. A., Moore, P., and Lavallée, D. A. (2010). Higher-order ionospheric effects on the GPS reference frame and velocities. Journal of Geophysical Research, 115, B03417. https://doi.org/10.1029/2009JB006677

- Pintori, F., Serpelloni, E., Longuevergne, L., Garcia, A., Faenza, L., D'Alberto, L., et al. (2021). Mechanical response of shallow crust to groundwater storage variations: inferences from deformation and seismic observations in the eastern southern alps, italy. Journal of Geophysical Research. Solid Earth, 126(2). https://doi.org/10.1029/2020JB020586

- Pizzi, A., Galadini, F. Pre-existing cross-structures and active fault segmentation in the northern-central Apennines (Italy). Tectonophysics, Volume 476, Issues 1–2, 2009, Pages 304-319, ISSN 0040-1951, https://doi.org/10.1016/j.tecto.2009.03.018.

- Pizzi, A., Di Domenica, A., Gallovič, F., Luzi, L., and Puglia, R. (2017). Fault segmentation as constraint to the occurrence of the main shocks of the 2016 central italy seismic sequence. Tectonics. https://doi.org/10.1002/2017TC004652

- Platt, J. P., Behr, W. M., and Cooper, F. J. (2015). Metamorphic core complexes: windows into the mechanics and rheology of the crust. Journal of the Geological Society, 172(1), 9–27. https://doi.org/10.1144/jgs2014-036

- Porreca, M., Minelli, G., Ercoli, M., Brobia, A., Mancinelli, P., Cruciani, F., et al. (2018). Seismic Reflection Profiles and Subsurface Geology of the Area Interested by the 2016-2017 Earthquake Sequence (Central Italy). Tectonics, 37(4), 1116–1137. https://doi.org/10.1002/2017TC004915

- Pousse-Beltran, L., Socquet, A., Benedetti, L., Doin, M., Rizza, M., and D'Agostino, N. (2020). Localized afterslip at geometrical complexities revealed by insar after the 2016 central italy seismic sequence. Journal of Geophysical Research: Solid Earth, 125(11). https://doi.org/10.1029/2019JB019065

- Prejean, S. G., et al. (2004), Remotely triggered seismicity on the United States west coast following the Mw 7.9 Denali Fault earthquake, Bull. Seismol. Soc. Am., 94, 348–359.

- Pucci, S., De Martini, P. M., Civico, R., Villani, F., Nappi, R., Ricci, T., et al. (2017). Coseismic ruptures of the 24 August 2016, M 6.0 Amatrice earthquake (central Italy). Geophysical Research Letters, 44(5), 2138–2147. https://doi.org/10.1002/2016GL071859

- Pushpalatha, R., Perrin, C., Le Moine, N., Mathevet, T., and Andréassian, V. (2011). A downward structural sensitivity analysis of hydrological models to improve low-flow simulation. Journal of Hydrology, 411(1–2), 66–76.

  https://doi.org/10.1016/j.jhydrol.2011.09.034

- Rabillard, A., Jolivet, L., Arbaret, L., Bessière, E., Laurent, V., Menant, A., et al. (2018). Synextensional granitoids and detachment systems within cycladic metamorphic core complexes (aegean sea, greece): toward a regional tectonomagmatic model. Tectonics, 37(8), 2328–2362. https://doi.org/10.1029/2017TC004697

- Radiguet, M., Cotton, F., Vergnolle, M., Campillo, M., Valette, B., Kostoglodov, V., and Cotte, N. (2011). Spatial and temporal evolution of a long term slow slip event: the 2006 Guerrero Slow Slip Event. Geophysical Journal International, 184(2), 816–828. https://doi.org/10.1111/j.1365-246X.2010.04866.x

- Ragon, T., Sladen, A., and Simons, M. (2019). Accounting for uncertain fault geometry in earthquake source inversions – II: application to the Mw 6.2 Amatrice earthquake, central Italy. Geophysical Journal International, 218(1), 689–707. https://doi.org/10.1093/gji/ggz180

- Reuveni, Y., Kedar, S., Owen, S. E., Moore, A. W., and Webb, F. H. (2012), Improving sub-daily strain estimates using GPS measurements, Geophys. Res. Lett., 39, L11311, doi:10.1029/2012GL051927

- Riva, R. E. M., Borghi, A., Aoudia, A., Barzaghi, R., Sabadini, R., and Panza, G. F. (2007). Viscoelastic relaxation and long-lasting after-slip following the 1997 Umbria-Marche (Central Italy) earthquakes. Geophysical Journal International, 169(2), 534–546. https://doi.org/10.1111/j.1365-246X.2007.03315.x

- Roberts, S., and Choudrey, R. (2003). Data decomposition using independent component analysis with prior constraints. Pattern Recognition, 36(8), 1813–1825. https://doi.org/10.1016/S0031-3203(03)00002-5

- Rodell, M., Houser, P. R., Jambor, U., Gottschalck, J., Mitchell, K., Meng, C. J., et al. (2004). The global land data assimilation system. Bulletin of the American Meteorological Society, 85(3), 381–394. https://doi.org/10.1175/BAMS-85-3-381

- Rovida, A., R. Camassi, P. Gasperini, and M. Stucchi (2011), CPTI11, the 2011 version of the Parametric Catalogue of Italian Earthquakes. Istituto Nazionale di Geofisica e Vulcanologia, Milano, Bologna. DOI: http://doi.org/10.6092/INGV.IT-CPTI11

- Rovida, A., M. Locati, R. Camassi, B. Lolli, and P. Gasperini (2016), CPTI15, the 2015 Version of the Parametric Catalogue of Italian Earthquakes, Istituto Nazionale di Geofisica e Vulcanologia, doi:10.6092/INGV.IT

- Rovida, A. N., Locati, M., Camassi, R. D., Lolli, B., and Gasperini, P. (2019). Catalogo Parametrico dei Terremoti Italiani CPTI15, versione 2.0.

  https://doi.org/10.13127/CPTI/CPTI15.2

- Sacks S, Suyehiro S, Evertson DW, Yamagishi Y (1971) Sacks–Evertson strainmeter, its installation in Japan and some preliminary results concerning strain steps. Pap Meteorol Geophys 22:195–208

- Sani, F., Vannucci, G., Boccaletti, M., Bonini, M., Corti, G., and Serpelloni, E. (2016). Insights into the fragmentation of the Adria Plate. Journal of Geodynamics, 102, 121–138. https://doi.org/10.1016/j.jog.2016.09.004

- Schmid, R., Rothacher, M., Thaller, D., and Steigenberger, P. (2005). Absolute phase center corrections of satellite and receiver antennas. GPS Solutions, 9, 283–293. https://doi.org/10.1007/s10291-005-0134-x

- Schmid, R., Steigenberger, P., Gendt, G., Ge, M., and Rothacher, M. (2007). Generation of a consistent absolute phase-center correction model for GPS receiver and satellite antennas. Journal of Geodesy, 81, 781–798. https://doi.org/10.1007/s00190-007-0148-y Tape, C., Musé, P., Simons, M., Dong, D., Webb, F., 2009. Multiscale estimation of GPS velocity fields. Geophysical Journal International 179, 945–971. doi:10.1111/j.1365-246X.2009.04337.x

- Scognamiglio, L., Tinti, E., Casarotti, E., Pucci, S., Villani, F., Cocco, M., et al. (2018). Complex fault geometry and rupture dynamics of the mw 6.5, 30 october 2016, central italy earthquake. Journal of Geophysical Research: Solid Earth, 123(4), 2943–2964. https://doi.org/10.1002/2018JB015603

- Scuderi, M. M., Tinti, E., Cocco, M., and Collettini, C. (2020). The role of shear fabric in controlling breakdown processes during laboratory slow-slip events. Journal of Geophysical Research: Solid Earth, 125, e2020JB020405.

  https://doi.org/10.1029/2020JB020405

- Serpelloni, Enrico, Faccenna, C., Spada, G., Dong, D., and Williams, S. D. P. (2013). Vertical GPS ground motion rates in the Euro-Mediterranean region: New evidence of velocity gradients at different spatial scales along the Nubia-Eurasia plate boundary. Journal of Geophysical Research: Solid Earth, 118(11), 6003–6024. https://doi.org/10.1002/2013JB010102

- Serpelloni, E, Pintori, F., Gualandi, A., Scoccimarro, E., Cavaliere, A., Anderlini, L., et al. (2018). Hydrologically Induced Karst Deformation: Insights From GPS Measurements in the Adria-Eurasia Plate Boundary Zone. Journal of Geophysical Research: Solid Earth, 123(5), 4413–4430. https://doi.org/10.1002/2017JB015252

- Serpelloni, E., Casula, G., Galvani, A., Anzidei, M., and Baldi, P. (2006). Data analysis of Permanent GPS networks in Italy and surrounding region: application of a distributed processing approach. Annales de Geophysique, 49, 897–928. https://doi.org/10.4401/ag-4410

- Shimada, Seiichi, Shoji Sakata, and Shin'ichi Noguchi. "Coseismic strain steps observed by three-component borehole strainmeters." Tectonophysics 144.1-3 (1987): 207-214.

- Shin, T.; Kuo, K.; Lee, W.; Teng, Tzuyun; Tsai, Y.. (2000). A Preliminary Report on the 1999 Chi-Chi (Taiwan) Earthquake. Seismological Research Letters. 71. 24-30. 10.1785/gssrl.71.1.24.

- Shin, T.-C. (2004). An Overview of the 1999 Chi-Chi, Taiwan, Earthquake. The Bulletin of the Seismological Society of America. 91. 1377-1377. 10.1785/0120000745.

- Shyu H., Sieh, K., Chen, Y.-G., and Liu, C.-S. (2005), Neotectonic architecture of Taiwan and its implications for future large earthquakes, J. Geophys. Res., 110, B08402, doi:10.1029/2004JB003251

- Shyu H., Bruce J., Kerry Sieh, Yue-Gau Chen, Ling-Ho Chung (2006); Geomorphic analysis of the Central Range fault, the second major active structure of the Longitudinal Valley suture, eastern Taiwan. GSA Bulletin 2006; 118 (11-12): 1447–1462. doi: https://doi.org/10.1130/B25905.1

- Silverii, F., D'Agostino, N., Métois, M., Fiorillo, F., and Ventafridda, G. (2016). Transient deformation of karst aquifers due to seasonal and multiyear groundwater variations observed by GPS in southern Apennines (Italy). Journal of Geophysical Research: Solid Earth, 121(11), 8315–8337. https://doi.org/10.1002/2016JB013361

- Stacey, F. D., J. M. W. Rynn, E. C. Little, and C. Croskell, Displacement and tilt transducers of 140 dB range, J. Phys. E: Sci. Instrum., 2 (11), 945–949, doi:10.1088/0022-3735/2/11/310, 1969.

- Tamura, Y., T. Sato, M. Ooe, and M. Ishiguro (1991), A procedure for tidal analysis with a Bayesian information criterion, Geophys. J. Internat., 104, 507–516

- Tarantola, A., 2005. Inverse Problem Theory and Methods for Model Parameter Estimation. SIAM.

- Taylor, R. G., Scanlon, B., Döll, P., Rodell, M., van Beek, R., Wada, Y., et al. (2012). Ground water and climate change. Nature Climate Change, 3(4), 322–329. https://doi.org/10.1038/nclimate1744

- Tesauro, M., M. K. Kaban, and S. A. P. L. Cloetingh (2008), EuCRUST-07: A new reference model for the European crust, Geophys. Res. Lett., 35, L05313, doi:10.1029/2007GL032244.

- Tinti, E., Scognamiglio, L., Michelini, A., and Cocco, M. (2016). Slip heterogeneity and directivity of the M 6.0, 2016, Amatrice earthquake estimated with rapid finite-fault inversion. Geophysical Research Letters, 43(20), 10,745-10,752. https://doi.org/10.1002/2016GL071263

- Tregoning, P. (2005). Effects of atmospheric pressure loading and seven-parameter transformations on estimates of geocenter motion and station heights from space geodetic observations. Journal of Geophysical Research, 110(B3).

  https://doi.org/10.1029/2004JB003334

- Vadacca, Luigi; Casarotti, Emanuele; Chiaraluce, Lauro; Cocco, Massimo. (2016). On the mechanical behaviour of a low angle normal fault: the Altotiberina fault (Northern Apennines, Italy) system case study. Solid Earth Discussions. 1-21. 10.5194/se-2016-48

- Valoroso, L., Chiaraluce, L., Piccinini, D., Di Stefano, R., Schaff, D., and Waldhauser, F. (2013). Radiography of a normal fault system by 64000 high-precision earthquake locations: The 2009 L'Aquila (Central Italy) case study. Journal of Geophysical Research: Solid Earth, 118(3), 1156-1176. https://doi.org/10.1002/jgrb.50130

- Valoroso, Luisa; Chiaraluce, Lauro; Di Stefano, Raffaele; Monachesi, Giancarlo. (2017). Mixed-Mode Slip Behavior of the Altotiberina Low-Angle Normal Fault System (Northern Apennines, Italy) through High-Resolution Earthquake Locations and Repeating Events: Seismic activity of low-angle ATF system. Journal of Geophysical Research: Solid Earth. 122. 10.1002/2017JB014607

- Verdecchia, A., Pace, B., Visini, F., Scotti, O., Peruzza, L., and Benedetti, L. (2018). The Role of Viscoelastic Stress Transfer in Long-Term Earthquake Cascades: Insights After the Central Italy 2016-2017 Seismic Sequence. Tectonics, 37(10), 3411–3428. https://doi.org/10.1029/2018TC005110

- Vičič, B., Aoudia, A., Borghi, A., Momeni, S., and Vuan, A. (2020). Seismicity rate changes and geodetic transients in central apennines. Geophysical Research Letters, 47(22). https://doi.org/10.1029/2020GL090668

- Villani, F., Civico, R., Pucci, S., Pizzimenti, L., Nappi, R., De Martini, P. M., and Open EMERGEO Working Group. (2018). A database of the coseismic effects following the 30 October 2016 Norcia earthquake in Central Italy. Scientific Data, 5, 180049. https://doi.org/10.1038/sdata.2018.49

- Vuan, A., Sugan, M., Chiaraluce, L., and Di Stefano, R. (2017). Loading rate variations along a midcrustal shear zone preceding the m 6.0 earthquake of 24 august 2016 in central italy. Geophysical Research Letters, 44(24).
https://doi.org/10.1002/2017GL076223

- Walters, R. J., Gregory, L. C., Wedmore, L. N. J., Craig, T. J., McCaffrey, K., Wilkinson, M., et al. (2018). Dual control of fault intersections on stop-start rupture in the 2016 Central Italy seismic sequence. Earth and Planetary Science Letters, 500, 1–14. https://doi.org/10.1016/j.epsl.2018.07.043

- Wang, CS; Huang, Tzu-Hua ; Yen, I-Chin ; Wang, Su-Long ; Cheng, Win-Bin. (2000). Tectonic Environment of the 1999 Chi-Chi Earthquake in Central Taiwan and its Aftershock Sequence. Terrestrial, Atmospheric and Oceanic Sciences. 11. 661-678. 10.3319/TAO.2000.11.3.661(CCE)

- Wang, L., Gao, H., Feng, G., and Xu, W. (2018). Source parameters and triggering links of the earthquake sequence in central Italy from 2009 to 2016 analyzed with GPS and InSAR data. Tectonophysics, 744, 285–295.

  https://doi.org/10.1016/j.tecto.2018.07.013

- Watkins, M. M., Wiese, D. N., Yuan, D.-N., Boening, C., and Landerer, F. W. (2015). Improved methods for observing Earth's time variable mass distribution with GRACE using spherical cap mascons. Journal of Geophysical Research: Solid Earth, 120(4), 2648–2671. https://doi.org/10.1002/2014JB011547

- Wech, A. G., Creager, K. C., Houston, H., and Vidale, J. E. (2010). An earthquake-like magnitude-frequency distribution of slow slip in northern Cascadia. Geophysical Research Letters, 37, L22310. https://doi.org/10.1029/2010GL044881

- Wernicke, B. (1995), Low-angle normal faults and seismicity: A review, J. Geophys. Res., 100(B10), 20159-20174, doi:10.1029/95jb01911

- Xu, G., Xu, C., Wen, Y., and Jiang, G. (2017). Source Parameters of the 2016–2017 Central Italy Earthquake Sequence from the Sentinel-1, ALOS-2 and GPS Data. Remote Sensing, 9(11), 1182. https://doi.org/10.3390/rs9111182

- Yau, M. K. and Rogers, R. R. (1989). Short Course in Cloud Physics, Third Edition. Butterworth-Heinemann. p. 190. ISBN 0750632151.

- Yu S.-B, Kuo L.-C (2001) Present-day crustal motion along the Longitudinal Valley Fault, eastern Taiwan. Tectonophysics 333:199–217

- Yu, S.-B., H.-Y. Chen, and L.-C. Kuo (1997), Velocity field of GPS Stations in the Taiwan area, Tectonophysics, 274, 41–59, doi:10.1016/S0040-1951(96)00297-1.

- Yu, S.-B., L.-C. Kuo, R. S. Punongbayan, and E. G. Ramos (1999), GPS observation of crustal deformation in the Taiwan-Luzon region, Geophys. Res. Lett., 26, 923–926, doi:10.1029/1999GL900148.

- Zhuang, J., Chang, C.-P., Ogata, Y., and Chen, Y.-I. (2005), A study on the background and clustering seismicity in the Taiwan region by using point process models, J. Geophys. Res., 110, B05S18, doi:10.1029/2004JB003157.